Plasticity and strength of metal oxide high-temperature superconductors (Review)

S. V. Lubenets,* V. D. Natsik, and L. S. Fomenko

B. Verkin Institute for Low Temperature Physics and Engineering, National Academy of Sciences of Ukraine, pr. Lenina 47, Kharkov 61103, Ukraine

(Submitted August 20, 2003; revised November 24, 2003)
Fiz. Nizk. Temp. **30**, 467–508 (May 2004)

The results of research on the plasticity and strength of a wide class of metal oxide perovskite-like compounds which have the property of high-temperature superconductivity or which can be used as base compounds for making high-temperature superconductors (HTSCs) are systematized and presented from a unified point of view. The mechanical properties of materials with different morphology—single crystals, polycrystals, and composites,—measured by different methods of mechanical testing in the low-temperature, room-temperature, and high-temperature regions, are discussed. The characteristic defects of the crystal structure for these compounds are considered, the crystallography of two modes of plastic deformation—slip and twinning—is described, and the stress-induced structural rearrangement of the twin structure that appears at a high-temperature phase transformation is discussed. The features of plastic deformation and fracture of metal oxide materials due to structural microdefects (dislocations, impurities, twin and grain boundaries) and macrodefects (voids, cracks, heterophase inclusions) are noted, and the role of heavy-cation diffusion in the kinetics of high-temperature deformation is discussed. The influence of structural phase transformations and the superconducting transition on the mechanical properties of metal oxides is considered. This review is a continuation of a review of the elastic and acoustic properties of HTSCs published earlier by the authors in Fiz. Nizk. Temp. **21**, 475 (1995) [Low Temp. Phys. **21**, 367 (1995)]. [DOI: 10.1063/1.1739131]

INTRODUCTION

Almost two decades have passed since Bednorz and Müller's discovery[1] of superconductivity with an unusually high critical temperature $T_c \simeq 35$ K in $La_{2-x}Ba_xCuO_4$ ceramics. This observation opened up a new subfield in the problem of superconductivity—high-temperature superconductivity. In the years since then, considerable progress has been achieved in research both on the physical nature of phenomenon of high-temperature superconductivity itself and on the practical application of materials possessing this property. The enormous efforts of physicists, chemists, and materials scientists around the world have largely focused on the search for new materials with ever higher values of T_c (see the diagram in Fig. 1), and T_c has been pushed to 164 K (a mercury-based HTSC under pressure).[6] An important achievement in recent years has been the discovery of superconductivity of magnesium diboride,[7] which has the highest value of the critical current.

Besides metal oxide compounds with the perovskite lattice and magnesium diboride, high-temperature superconductivity with $T_c \sim 40$ K has also been observed in a new allotropic form of carbon—C_{60} fullerite doped with alkali metals[8] (this system is sometimes called the first organic HTSC). The injection of holes into C_{60} crystals has made it possible to raise T_c to 52 K,[9] and the introduction of tribromomethane has given a record high $T_c = 116$ K.[10] Superconductivity has also been observed in carbon nanotubes.[11]

The wide application of metal oxide HTSCs is greatly impeded by their poor mechanical properties. These compounds are hard and brittle and are difficult to make in the form thin wires and ribbons. One of the main problems of HTSC materials sciences is therefore to optimize the mechanical and superconducting properties. This problem is solved by using various technological treatments of the base metal oxide compounds: doping, special thermomechanical treatments, fabrication of composites or thin films based on HTSCs, etc.

Intensive research in the field of HTSC materials science continues, directed mainly toward improving the functional properties of these materials. New achievements in this direction are reflected in the reports at recent international forums: 1) 13th International Symposium on Superconductivity (ISS 2000), Oct. 14–16, Advances in Superconductivity XIII, Tokyo, Japan; 2) 14th International Symposium on Superconductivity (ISS 2001), Sept. 25–27, Advances in Superconductivity XIV, Kobe, Japan; 3) 5th European Conference on Applied Superconductivity (EUCAS 2001), Aug. 26–30, Lyngby, Denmark; 4) Workshop on High-T_c Superconductivity, Williamsburg, Virginia, June 7–8, 2002; 5) Topical Conference of the International Cryogenic Materials Conference ICMC 2000 ''Superconductors for Practical Applications,'' Xi'an, China, June 16–20, 2002.

As a rule, metal oxide HTSCs are prepared from powders of the initial components by various ceramic technologies and are therefore often called HTSC ceramics, the term ''ceramics'' being used in the broad sense without regard to the details of the morphology of the samples.

One of the important subfields of the physical materials science of HTSCs is the study of the plasticity and strength properties of these materials. Such studies are done over a

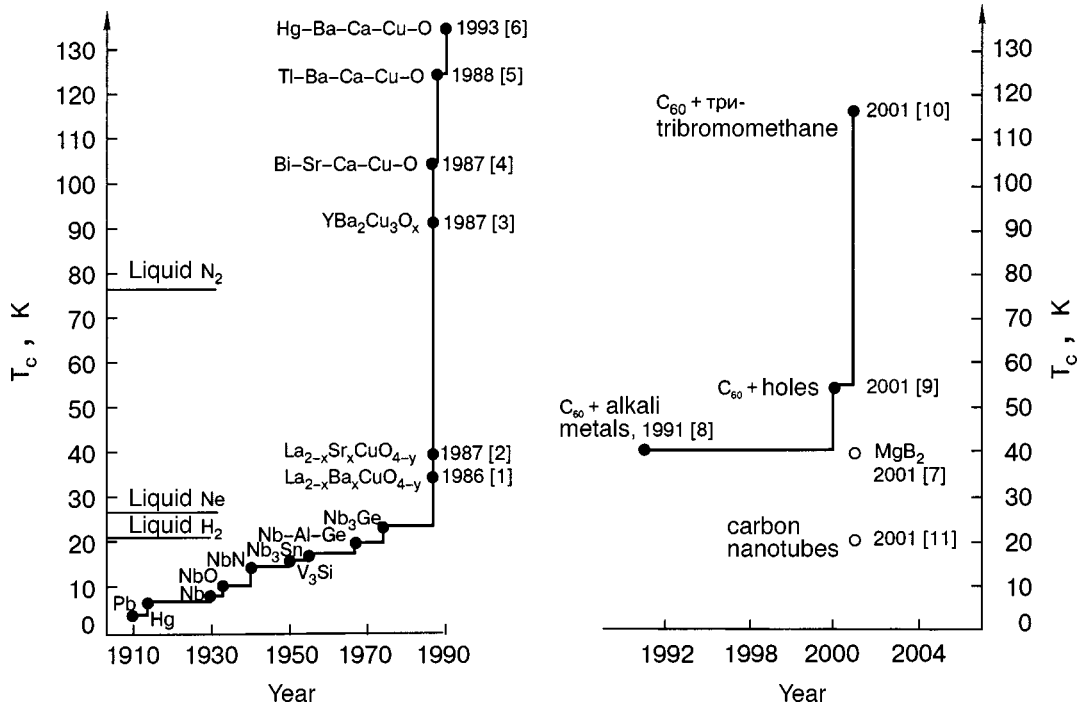

FIG. 1. Chronology of the increase of the critical temperature T_c of superconductors.

wide range of temperatures, from helium to pre-melting, and the experimental objects are bulk samples with various morphology: single crystals, polycrystals, and grain-oriented samples obtained from the melt; granular/porous structures (polycrystals) prepared by the methods of solid-phase sintering of oxide powders; composites obtained by the introduction of particles of metals or simple oxides into metal oxide materials and also by the conjoining of bulk elements of such systems. Less studied are the mechanical properties of several special types of HTSC samples which are of importance from an applied standpoint: fine (micron and nanometer) wires and ribbons, films, heterostructures, etc. Information about the mechanical properties is important both for devising and perfecting methods of manufacturing high-quality objects and for estimating their reliability of operation. It is also of great interest to elucidate the microscopic mechanisms of plastic deformation and fracture of this new class of materials. The natural brittleness of perovskite-like metal oxides is a hindrance to both the preparation and application of HTSCs. In materials of this type the formation of cracks is the final step in the relaxation of the internal stresses due to the preliminary pressing of the oxide powders prior to their sintering and also due to the phase transformations, the strong anisotropy of the thermal expansion coefficients, and temperature gradients. Microcracking has a substantial influence on the final structure of a ceramic, its stability, mechanical strength, and superconducting and other physical properties. The search for ways of combatting this undesirable phenomenon involves a deeper study of the mechanisms of plastic deformation of metal oxides.

Metal oxide ceramics have a weakly expressed plasticity even in the region of moderately low temperatures, and it increases noticeably upon heating. The occurrence of plastic deformation is attested to, for example, by the formation of clear impressions of an indenter on the surface of the samples in hardness measurements,[12–15] detwinning in the neighborhood of the impression of an indenter,[15–18] and microcreep.[19–21] Reliable measurements of the yield point of a ceramic can be made under conditions of hydrostatic pressure, which prevents the development of brittle cracks.[22] In some cases the plasticity of polycrystals is due to intragrain slip of lattice dislocations, and at elevated temperatures a ceramic will manifest significant plasticity[23–28] and even superplasticity, which are due to dislocation-diffusion processes[24,27,28] and grain-boundary slip.[24,25]

This review is devoted to generalizing the main results of research on the plasticity and fracture of metal oxide HTSCs, and it can be considered to be the second part of a review of the elastic properties of these materials published in 1995.[29] For the main metal oxide HTSCs and several of the corresponding base compounds we present the results of research by the methods of microindentation, microcreep, and active deformation in the low-, room-, and high-temperature regions.

1. CRYSTAL STRUCTURE OF THE MAIN METAL OXIDE HTSCs

The plasticity and strength of crystals is largely determined by defects of the crystal structure, some of which are the elementary carriers of plasticity while others are obstacles to plastic slip. It is found, by various methods, that all HTSC single crystals and polycrystals are characterized by the presence of a large number of defects of various types: twins, stacking faults, dislocations, impurity atoms, vacancies, grain boundaries, voids and cracks, heterophase inclusions, atomic segregations near voids and grain boundaries, etc. These defects have a substantial influence on the plasticity, strength, and other physical properties of HTSCs, including their superconductivity. Nonuniformities of the composi-

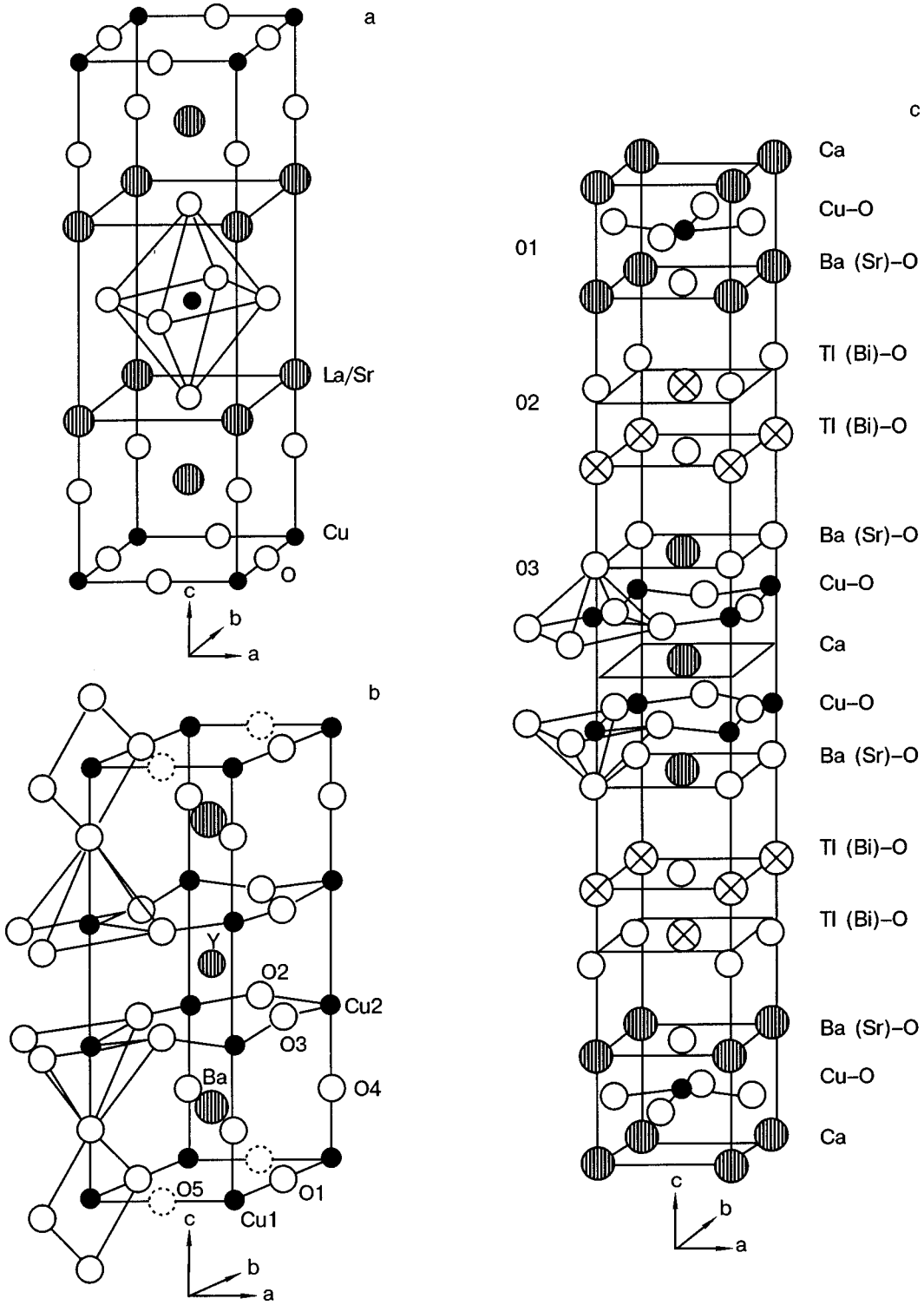

FIG. 2. Structures of the unit cells of the main metal oxide HTSC compounds: $(La,Sr)_2CuO_4$ (a), $YBa_2Cu_3O_7$ (b), and Bi(Tl)-2212 (c).

tion, internal boundaries (in particular, twin boundaries), and the elastic fields of dislocations act as pinning centers for Abrikosov vortices and lead to a change in the critical parameters of the HTSC. Local superconductivity with higher T_c can exist at twin boundaries (the mechanism for this in conventional superconductors is described in Refs. 30 and 31), or T_c may be lower owing to a lower oxygen concentration at a boundary.[32]

For better understanding of the structure and properties of elementary defects of metal oxide HTSCs it is advisable to start with a brief characterization of the crystal structure of several of the main materials of this type which will be discussed most thoroughly in this review. The lattice structures of all perovskite-like metal oxides have been studied in detail and discussed in numerous original papers, review, and monographs (see, e.g., Refs. 33–38). Here the well-known schemes of the unit cells for the compounds of interest to us are presented in Fig. 2 in a form convenient for the subsequent discussion; the space group and lattice parameters are taken from a review.[36] The figures show the coordination

polyhedra of the copper ion; the shapes of the coordination polyhedra of the remaining cations can be seen in Refs. 34 and 35. The lattice parameters are taken from a table presented in Ref. 36, where citations to the original papers can be found.

The structure of the compounds $(La,Sr)_2CuO_4$ is shown in Fig. 2a. At the center of the unit cell is the coordination polyhedron of the copper ion, which, together with the adjacent La/Sr ions forms the characteristic structure of the perovskite family ABO_3 (named after the mineral $CaTiO_3$). Elements of the perovskite structure are contained in the lattices of all metal oxide HTSCs, i.e., they are perovskite-like. $(La,Sr)_2CuO_4$ has space group $I4/mmm$, with lattice parameters $a=b=3.7793$ Å and $c=13.2260$ Å.

The unit cell of the superconducting orthorhombic $YBa_2Cu_3O_7$ phase is more complex (Fig. 2b). Its space group is $Pmmm$, and the lattice parameters are $a=3.8177$ Å, $b=3.8836$ Å, and $c=11.6827$ Å. A distinctive feature of the unit cell of this phase is the presence of two types of oxygen environment of the copper ions: a four-sided pyramid in the CuO_2 planes and a rhombus in the basal planes containing CuO chains. In the nonsuperconducting tetragonal $YBa_2Cu_3O_6$ phase the oxygen positions O1 are vacant, while in the $YBa_2Cu_3O_8$ phase oxygen also occupies the O5 positions, and the Cu1 copper ion is found at the center of a coordination octahedron.

Finally, the crystal structure of Bi(Tl)-HTSCs is shown in Fig. 2c. The 2212 phase has space group $I4/mmm$. The lattice parameters of Bi-2212 are $a=5.4095$ Å, $b=5.4202$ Å, and $c=30.9297$ Å, and those for Tl-2212 are $a=b=3.8558$ Å and $c=29.2596$ Å. The Bi-2201 phase does not have the Ca and Cu(O_{Cu}) layers, and its parameter c is accordingly smaller and its superconducting transition temperature is lowered to $T_c=10$ K. In the Bi-2223 phase additional Ca and Cu(O_{Cu}) layers appear between the $Cu1(O_{Cu1})_2$ and SrO_{Sr}/BaO_{Ba} layers (see Ref. 36 for a diagram of the structure); the parameter c increases, and the critical temperature reaches its highest value for the compounds of this family: $T_c=110$ K.

2. SLIP AND TWINNING IN CRYSTALS OF METAL OXIDE HTSCs

In this Section we discuss those defects having a direct relation to plasticity: we shall discuss the elementary ''carriers'' of the two modes of plastic deformation—twinning and slip.

2.1. Slip systems

Electron microscope studies of the dislocation structure of deformed crystals of the $YBa_2Cu_3O_{7-\delta}$ family[39–44] have led to the following conclusions. The sole slip plane in $YBa_2Cu_3O_{7-\delta}$ crystals at any values of δ is the basal plane (001), and their plastic deformation is governed by dislocations with Burgers vectors $a[100]$ and $b[010]$. In the complex lattice of this compound (Fig. 2b) there are three possible shear planes of the (001) type: BaO/CuO_2, CuO_2/Y, and BaO/CuO. Direct observation on a high-resolution electron microscope showed that the core of the $\langle 100\rangle(001)$ dislocations lies in the CuO plane between BaO layers.[45] For a shear between the BaO and CuO layers it is natural for the degree of splitting of the dislocation to depend on the direction of the Burgers vector—[100] or [010]—along which the O-Cu-O chains lie.[39–41] A strong influence of the oxygen concentration on the mechanical properties (see Sec. 7.1 below) also attests to a shear in the BaO/CuO plane, since it is in the CuO plane that the main changes occur upon variation of the oxygen index; in particular, the magnitude of the Burgers vectors of the dislocations changes smoothly with changing lattice parameters.

The splitting of complete dislocations into partial dislocations occurs according to the reactions[40,41] $[100]\rightarrow 1/2[100]+1/2[100]$ and $[010]\rightarrow 1/2[010]+1/2[010]$. The $a[100]$ dislocations are split more strongly than the $b[010]$ dislocations.

In both the orthorhombic[22,40] and tetragonal[45] phases a small density of dislocations with Burgers vectors in the $\langle 110\rangle$ direction are observed, which form according to the reaction $[100]+[010]\rightarrow[110]$ when the main dislocations intersect; this leads to the formation of plane hexagonal networks.[43] The $\langle 110\rangle(001)$ slip system can be effective in high-temperature deformation.

In dynamically compacted samples of YBCO, additional slip systems have been observed:[45] $[110](1\bar{1}0)$ and $[010]\times(100)$. The edge components of such dislocations are parallel to the [001] axis. Dislocations with a Burgers vector component in the direction of the [001] axis are practically never encountered.

The influence of the oxygen index δ on the mechanical properties of YBCO crystals may be a consequence of changes in the structure of the core of the gliding dislocations and their ionic charge upon changes in the oxygen index and, accordingly, in the character of the atomic ordering in the basal plane.[46]

The slip systems in crystals of Bi-containing HTSCs are the same as in crystals of the YBCO system.[47] However, the more complex crystal structure of Bi(Pb)–Sr–Ca–Cu–O superconductors (Fig. 2c) admits two types of possible slip planes parallel to the basal plane: between the CuO_2 and Ca layers, and between two BiO layers.[47] It turns out that stacking faults lying in such planes will have low and somewhat different surface energies. Of the three types of dislocations with Burgers vectors [100], [010], and [110], the last type of dislocations are the least stable and always split into partial dislocations according to the reaction $[110]\rightarrow 1/3[120]+1/3[210]$. Practically no splitting of [010] dislocations has been observed.

2.2. Twinning systems and the structure of twin boundaries

The most detailed and complete studies of twins have been done for the orthophase of the systems $ReBa_2Cu_3O_{7-\delta}$ (Re=Y, Sm, Eu, Gd, Dy, Ho, Er). This phase is always twinned (see, e.g., some of the first papers[48–50] and references to original papers in the review[51] and monograph[52]). The crystallography of this structure admits the existence of both twins of rotation and twins of reflection. We shall not discuss twins of rotation (axial twins),[53,54] since they do not actively take part in plastic deformation processes and can only act as strong obstacles for the slip of perfect and

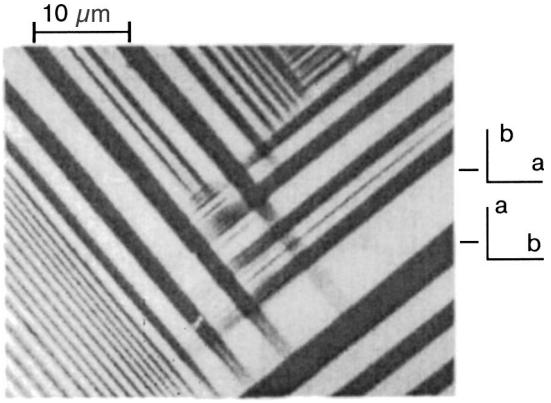

FIG. 3. Polarization-optical micrograph of twin structure in the orthorhombic phase of YBCO.[59]

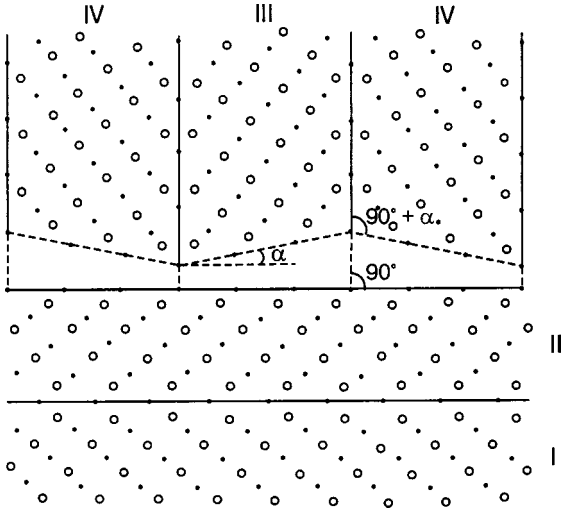

FIG. 4. The four possible orientations of twins in the orthorhombic phase of YBCO: oxygen atoms (○), copper atoms (●), $\alpha = 0.89°$ (Ref. 60).

twinning dislocations. At the same time, the twins of rotation and other defects do influence the parameters of superconducting HTSC metal oxides.

During the high-temperature phase transformation of the tetragonal to the orthorhombic phase which occurs at temperatures between 750 and 500 °C in the presence of an oxygen atmosphere,[55] a polydomain twin structure arises which consists of two equiprobable families of reflection twins which are coherent over most of their length. The exact value of the transition temperature is determined by the oxygen partial pressure; the transition is due to the simultaneous occurrence of an atomic ordering reaction in the oxygen sublattice and a martensitic type of shear transformation of the whole crystal lattice.[56–58] The elastic stresses arising as a result of the transformation relax by twinning deformation of the orthophase. Under observation in polarized light in the (001) plane the domain structure of the crystals appears as a system of alternating bright and dark fringes parallel to the ⟨110⟩ direction (Fig. 3); the coloration of the domains varies as the analyzer is rotated.[59]

The two families of twins (Fig. 3) intersect at right angles, since the crystallographic plane {110} is an invariant for the tetra-ortho transformation.[59] Being nucleated at different places in a grain, these families of twins form regions of four orientations, I, II, III, and IV, which are shown schematically in Fig. 4.[48,60] The interface at which the two orthogonal families of twins meet is incoherent and consists of an alternation of twin boundaries and low-angle grain boundaries.[48,60]

The fine structure of the twin boundaries depends on the local oxygen concentration and oxygen ordering in the boundary region and on the presence of impurity atoms. Coherent twin boundaries parallel to the {110} planes pass through the O1 oxygen ions in the CuO layers (anion boundaries) if $\delta = 0$ (Refs. 61–63) or through the copper ions (cation boundaries) in those layers if the oxygen concentration is lower, e.g., $\delta \simeq 0.4$.[61,62] Aluminum and iron impurities apparently lower the energy of the twin boundary if it passes through the cations. Above a certain Al or Fe concentration the twin boundaries form at lattice cations even at a high oxygen concentration ($\delta = 0$). Structural models of the two types of boundary are shown in Fig. 5.[63] Observations of $YBa_2Cu_3O_7$ with a high-resolution electron microscope revealed twinning dislocations and dislocations at the junction of anion and cation boundaries.[62]

Upon variations the oxygen and impurity concentrations the mean distance between twin boundaries varies between 100 Å and 1000 Å (Refs. 49 and 63–67) but it may even reach several microns.[59,64] In the vicinity of the twin boundaries there are transition zones along which the crystallographic parameters of one twin orientation go over smoothly and continuously to the parameters of the other orientation. The widths of the transition zones have been measured in electron microscope studies: in YBCO crystals they consist of 5–10 cells for coherent joining[68] and 100–300 cells for incoherent joining.[69] The smooth change of the parameters is

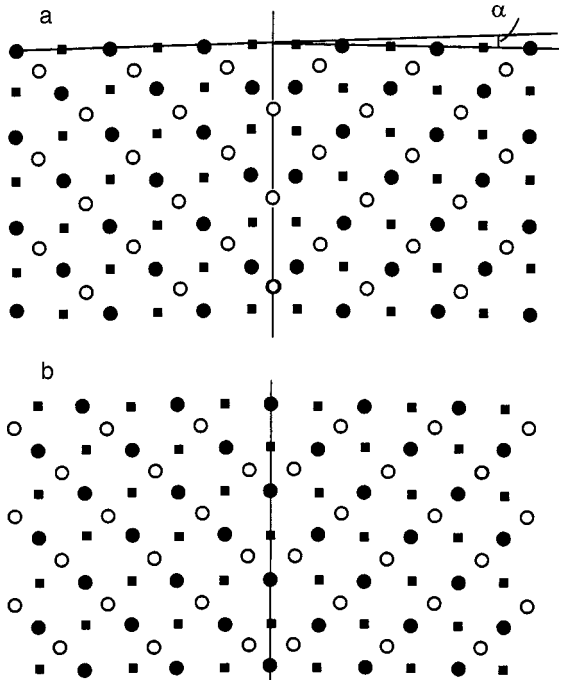

FIG. 5. Structural models of twin boundaries in the orthorhombic phase of YBCO: "anionic" boundary (a), "cationic" boundary (b). Oxygen atoms (○), Cu atoms (■), Ba (Y) atoms (●).[63]

due to ordering of the oxygen along the transition zone and not to variation of the oxygen concentration.[70]

Twinning in $YBa_2Cu_3O_7$ crystals can be caused by mechanical loading; it is brought on by a shear along the crystallographic systems $[1\bar{1}0](110)$ and $[110](1\bar{1}0)$. The crystal geometry of the twins is characterized by the following parameters: the specific shear s, the angle β between the $[100]$ directions in the initial lattice and in the twin, the distance d_{110} between the twinning planes, and the magnitude b_t of the Burgers vector of the twinning dislocation. The values of these parameters are given in terms of the lattice parameters a and b by the following formulas:

$$s=\frac{(b/a)^2-1}{b/a}, \quad d_{110}=\frac{b}{[1+(b/a)^2]^{1/2}},$$

$$\beta=2\ \mathrm{arctg}\left(\frac{a}{b}\right), \quad b_t=d_{110}s.$$

Taking $a=3.82$ Å and $b=3.88$ Å,[60] we obtain the value $s=0.031$, and from the data of direct observation of twins we obtain the estimate $s\simeq 0.036$;[71] for the other parameters we have $\beta=89.1°$, $d_{110}=2.72$ Å, and $b_t=0.084$ Å.

The energy γ_{tw} of a twin boundary in the orthorhombic phase of YBCO was estimated in Refs. 72–78. The most systematic discussion of this question is given in Ref. 78. There the twin structure formed as a result of the high-temperature phase transition and the shape of the residual twins in the large grains of polycrystalline samples of YBCO were investigated in detail by transmission electron microscopy. Samples with 40% and 30% Y211+0.05 wt.% Pt were used. An estimate of the energy of the twin boundaries was made by two independent methods: 1) from the distance between twins in columns of twins (the conventional method used previously in Refs. 72 and 74–77); 2) from the form of wedge-shaped twins and a comparison of that shape with the equations of the dislocation theory of thin twins, developed by Boyko and Kosevich.[52,78,79] For γ_{tw} the values obtained were 46.5 mJ/m^2 (estimated by the first method) and (60.0 $\pm$21.0) mJ/m^2 (estimated by the second method). The admixture of platinum decreases the energy of twin boundaries to values 18.3 mJ/m^2 (estimated by the first method) or (26.8$\pm$9.5) mJ/m^2 (estimated by the second method). Appropos of this the authors of Ref. 78 called attention to the following important fact: according to the results of their studies, the admixture of Pt leads not only to a decrease of γ_{tw} (i.e., to a thinning of the twins and an increase in their density) but also to a more uniform distribution of the particles of the second phase Y211. This explains the increase in the density of pinning centers and, consequently, in the critical current density in such samples.

Estimates of γ_{tw} obtained in Ref. 78 are basically in agreement with the data of other studies.[76,77] We note that even the calculation of γ_{tw} in Ref. 73 in the theory of elastic twins[52,79] (which, as was pointed out in Ref. 78, is incorrect, since only residual and not elastic twins have been observed in YBCO) gives a reasonable value of 20 mJ/m^2 (instead of the extreme overestimate 1000 mJ/m^2) if the correct value of the Burgers vector of the twinning dislocation, $b_t\simeq 0.02a$, is used in the calculations instead of the lattice parameter a.

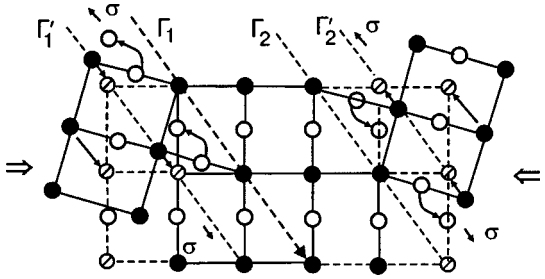

FIG. 6. Displacement of atoms during detwinning of orthorhombic YBCO crystals under the influence of a compressive stress.[69]

In simple one-atom structures the trajectory of the displacement of atoms in the twinning process is a uniform shear in the twinning plane and in the twinning direction.[80] The atomic rearrangements are more complicated in the case of polyatomic lattices. In nonstoichiometric YBCO crystals with $\delta>0$, where the {110} twin boundaries pass through cations, the rearrangement on twinning does not reduce to only a uniform deformation of the lattice. In addition to that there also occurs a hop of the oxygen anions in the twinning plane by a distance $(-1/2[110]+b_t/2)$ in the direction counter to the twin shear.[22,57,81] A diagram of these displacements in the (001) plane is shown in Fig. 6:[69] under the influence of a uniaxial compressive stress the boundaries Γ_1 and Γ_2 change their position along the trajectories shown by the arrows ($\Gamma_1\rightarrow\Gamma_1'$ and $\Gamma_2\rightarrow\Gamma_2'$). The displacement of the anion boundaries requires a displacement of all the cations by a distance of the order of 1/2[110],[81] and is apparently not realized under mechanical stresses.

Experimental studies of the twinning process in YBCO crystals under the influence of the residual internal stresses in the region of the impression of an indenter have shown that the rate of rearrangement of the twin structure is governed by the short-range diffusion of oxygen along the twin boundaries.[16,17]

The above-described features of the motion of atoms in the core of a moving twinning dislocation in YBCO crystals suggest that pseudotwins can form, within which the oxygen atoms occupy nonequilibrium positions. Under conditions such that there is insufficient time for the disrupted atomic order to be restored during the heating-cooling cycle,[51,52] the samples can exhibit pseudoelastic behavior. This effect has not yet been observed, but its realization is possible in single crystals in the region of moderate and low temperatures, where the diffusive displacement of oxygen is sluggish.

The role of twinning dislocations as carriers of plastic deformation in YBCO crystals is extremely small on account of the small value of the crystallographic shear. Upon complete retwinning of a single crystal the change of its dimensions cannot exceed 3.1% at $\delta=0$ and it decreases with increasing δ. Therefore the main carriers of the plastic deformation are gliding dislocations and diffusive mass transport, although a small twinning contribution to the plasticity of the ceramics has been detected.[41] Evidence for twin-boundary mobility has been obtained in experiments on detwinning in the region of an indenter impression[16–18] and also in a study of the defect structure of dynamically compacted YBCO samples.[45]

The twin structure in Bi-containing HTSC crystals is

qualitatively different from that inherent to $YBa_2Cu_3O_7$ crystals. Twins are planar defects of the type including stacking faults and interphase boundaries and are observed in abundance along with the latter in high-resolution electron microscope studies in samples prepared by the standard technology.[82] There are no data on deformation twins in Bi-containing HTSCs.

Twinning systems in the lattice of lanthanum superconductors (the crystal lattice of which is shown in Fig. 2c) are the same as in the $YBa_2Cu_3O_{7-\delta}$ lattice. $La_{2-x}Sr_xCuO_4$ crystals are easily brought to the single-domain state at room temperature by means of mechanical loading,[75] whereas such a procedure in the case of YBCO is possible only at elevated temperatures.[16,17,84–88]

Coherent twin boundaries are rather strong obstacles to the motion of gliding dislocations.[40,45] This is due to the fact that relatively immobile twinning dislocations ''chip off'' from the twin boundaries at their intersections with dislocations. In addition, the regions adjacent to the twin boundaries are enriched with impurities.[22] However, microindentation experiments have revealed no noticeable change in microhardness at the tetra→ortho transition, which results in the formation of a domain (twin) structure—neither in $La_{1.85}Sr_{0.15}CuO_4$ on decreasing temperature ($T_{TO} \simeq 180$ K)[18] nor in $YBa_2Cu_3O_{7-\delta}$ crystals with changing oxygen concentration. The values of the microhardness of twinned and mechanically detwinned crystals of $YBa_2Cu_3O_{7-\delta}$ also turn out to be equal.[89] At the same time, twins present an appreciable resistance to the propagation of microcracks, so that the fracture toughness of twinned crystals has been found to be approximately 12% higher than that of detwinned crystals.[89]

3. REARRANGEMENT OF THE DOMAIN STRUCTURE UNDER MECHANICAL STRESS

The initial polydomain structure formed as a result of the high-temperature tetra→ortho transition in metal oxide HTSCs and compounds related to them can be restructured under the influence of mechanical stresses. This makes it possible to obtain completely detwinned orthorhombic single crystals of $YBa_2Cu_3O_{7-\delta}$, which are needed for studies of anisotropic phenomena and parameters: the critical magnetic fields, thermal conductivity, thermopower, elasticity, and conductivity. To bring them to a single-domain state the as-grown single crystals were compressed along the (100) direction by a certain load at an elevated temperature: in Ref. 84 the detwinning was done at a temperature of 325 °C and a stress of 50 MPa, and in Ref. 86, at a higher temperature of 450 °C, the crystal was brought completely to a single-domain state in one minute by a stress of ~25 MPa. A similar method was used to bring $YBa_2Cu_3O_{7-\delta}$ crystals to a single-domain state in a large cycle of studies reported in Bondarenko's dissertation.[90]

In Ref. 78 the force of friction S_{fr} of a twinning dislocation in YBCO crystals was estimated from the shape of the twins on the basis of the minimum thickness of stable twins. The values obtained, 20 MPa$\leqslant S_{fr} \leqslant$50 MPa, are seen to be in good agreement with the detwinning stresses given above.

The kinetics of the motion of twin boundaries in $YBa_2Cu_3O_{7-\delta}$ crystals in the temperature interval 40–160 °C was obtained in Refs. 16 and 17 by an optical method with the use of measurements of the time dependence of the change in intensity of light reflection on a part of the crystal containing a group of indenter impressions. An exponential character of the temperature dependence of the detwinning time was found, which permitted estimation of the activation energy of the process: it turned out to be sensitive to the oxygen concentration and the presence of Mn, Ca, and Si impurities[17] and ranged from 0.48 to 1.62 eV. It was noted[17] that these values are in good agreement with the value of the activation energy for the diffusion of oxygen in $YBa_2Cu_3O_{7-\delta}$ at the same values of the oxygen index (see, e.g., Refs. 91 and 92). This agreement is considered to be an argument in favor of the model for twin-boundary motion in which the motion of twinning dislocations occurs as a result of diffusive hopping of the oxygen atoms (Fig. 6).

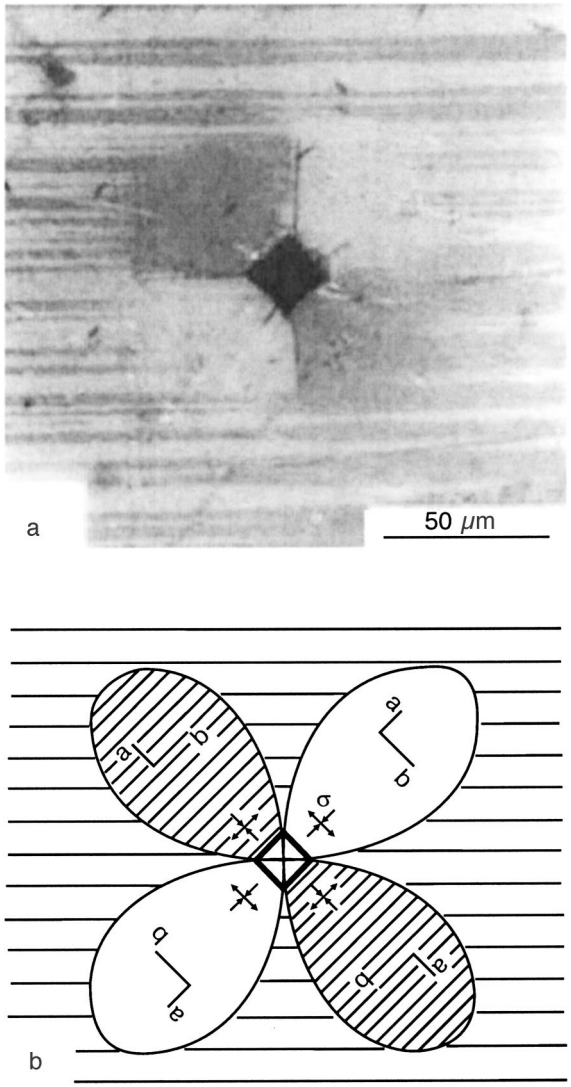

FIG. 7. Polarization-optical micrograph of twin structure in the (001) plane of La_2CuO_4 crystals (a) and a diagram of the stresses acting near an indenter impression (b).[18]

An example of the rearrangement of the domain structure in the crystal La_2CuO_4 in the vicinity of an indenter impression is shown in Fig. 7a.[18] The direction of motion of the domain boundaries, leading to growth of the bright or dark domains, is governed by the sign of residual stresses acting inside the indenter impression (see the diagram in Fig.

7b): the bright domains expand and absorb the dark domains in the first and third quadrants, while in the other two quadrants the opposite effect is observed. The rearrangement of the domain structure occurs over a time of the order of a minute even at room temperature, a fact which is indicative of high mobility of the domain boundaries. In Refs. 83 and 93 it was observed that La_2CuO_4 crystals were brought partially or completely to a single-domain state under the influence of uniform external stresses and also on heating or cooling in the column of an electron microscope.[94]

The motion of the domain boundaries in La_2CuO_4 is governed by the reorientation of the CuO_6 octahedra.[95] The high mobility of twin boundaries in La_2CuO_4 in comparison with YBCO means that the activation energy for reorientation of the CuO_6 octahedra is lower than the activation energy for the diffusion of oxygen in $YBa_2Cu_3O_{7-\delta}$.

Owing to the presence of domains and their switching under mechanical stresses in $YBa_2Cu_3O_{7-\delta}$ and La_2CuO_4, these crystals can be classed as ferroelastics.[96] In both cases the twins arise at a structural phase transition from the more symmetric tetragonal (paraelastic) phase to the less symmetric orthorhombic (ferroelastic) phase. A complete crystallographic analysis of the domain structure of La_2CuO_4 is carried out in Refs. 96–100. The connection between the instability of the domain structure and anomalous acoustic properties in HTSC compounds has been discussed in a review.[29]

4. MICROHARDNESS AND MICROBRITTLENESS OF SINGLE CRYSTALS, AND ANISOTROPY OF THE MECHANICAL PROPERTIES

The use of single crystals in studies of the physical properties began almost immediately after the discovery of the high-temperature superconductivity of perovskite-like metal oxides. The first single crystals of the compound YBCO were in the form thin slabs with dimensions of approximately 1×1 mm in the (001) plane and a thickness of 0.1–0.2 mm in the direction of the [001] axis. Various methods of obtaining bulk single crystals of many metal oxides have now been developed (see review[101]), making it possible not only to expand the base of research on these materials but also to realistically consider the prospects for their practical application.

The small size and the shape of single crystals limited the methodological possibilities for their experimental study. In particular, studies of the mechanical properties of such samples were most often done by the method of microindentation, which remains basic to the study of the plasticity and strength of HTSCs. While being comparatively simple, it is useful for comparing the mechanical behavior of different materials, enabling one to study the anisotropy of the mechanical properties of single crystals, and it also gives information about the local mechanical characteristics in the case of a structurally nonuniform material (hardness and crack-resistance of adjacent phases, grains, and grain boundaries). The presence of high hydrostatic pressure under a blunt indenter makes for plastic deformation at lower temperatures than are possible in the case of other methods of mechanical testing and also in brittle materials such as metal oxide HTSCs.

Although the physical interpretation of the microindentation results is difficult,[102,103] this method is effective thanks to the presence of certain correlations between the values of the microhardness H_V and the yield stress σ_y and also between the values of the critical stress intensity factor as measured according to the length of a radial crack in the region of an indenter impression and as determined by the standard macroscopic methods[103–107] (see Sec. 6.3 for more details).

The microindentation method is based on formulas relating the load P on the indenter, the length $2a$ of the diagonal of the indenter impression, and the length c of the radial crack around the indenter impression with the values of the Vickers microhardness H_V and the stress intensity factor K_{1c} at the tip of the crack:[108–110]

$$H_V = 1.854\frac{P}{(2a)^2}, \tag{1}$$

$$K_{1c} = 0.016\left(\frac{E}{H_V}\right)^{1/2}\frac{P}{c^{3/2}}. \tag{2}$$

Here E is Young's modulus in the direction perpendicular to the surface of the crack. For a number of materials the empirical relation $E/H_V \simeq 40$ is well satisfied, and it is convenient to determine K_{1c} using the simplified formula

$$K_{1c} = 0.1\frac{P}{c^{3/2}} \tag{3}$$

Since the penetration of the indenter into the material at a constant load is a form of kinetic process, viz., creep,[111–113] the loading time should not exceed the time of completion of the plastic deformation, when the impressions take on steady, equilibrium sizes. In the case of brittle materials and/or low temperatures, 5 or 10 s are sufficient for this.

According to the scaling law derived for a cone and confirmed experimentally for a pyramid,[114] the microhardness H_V should not depend on the load P. However, in the majority of cases that law is broken in the region of small loads.[114–118] The authors of Ref. 116 expressed the opinion that it is more correct to determine the hardness H_V and the fracture toughness K_{1c} with allowance for a threshold load P_{th} at which the plastic deformation under the indenter begins, and in that case the load P in formulas (1), (2), and (3) should be replaced by the difference $(P-P_{\text{th}})$. The results of measurements are conveniently plotted in the coordinates $(2a)^2-P$ and $c^{3/2}-P$, making it possible to find the threshold value of P_{th}.

Figure 8 shows the results obtained in the indentation of the basal plane (001) of a $YBa_2Cu_3O_{7-\delta}$ single crystal.[13] At $P>0.5$ N a strong cracking of the indented volume occurs, and at $P>0.7$ N, as a rule, fracture of the samples occurs. Measurements the geometric parameters of the straight lines on the $(2a)^2-P$ plot and using formulas (1)–(3), we obtain for the given indentation surface the following values: $P_{\text{th}} = 0.03-0.04$ N, $H_V \simeq 9.75$ GPa, and $K_{1c} \simeq 0.4$ MPa·m$^{1/2}$; these values are typical for ytterbium HTSC crystals.[12–15,89,119] The micromechanical characteristics of other rare-earth cuprates grown under identical conditions vary over rather wide limits and for the majority of them are found at the level of the lower values of H_V and K_{1c} for the ytterbium samples: $P_{\text{th}} \simeq 0.01-0.03$ N, $H_V \simeq 5-7$ GPa, and

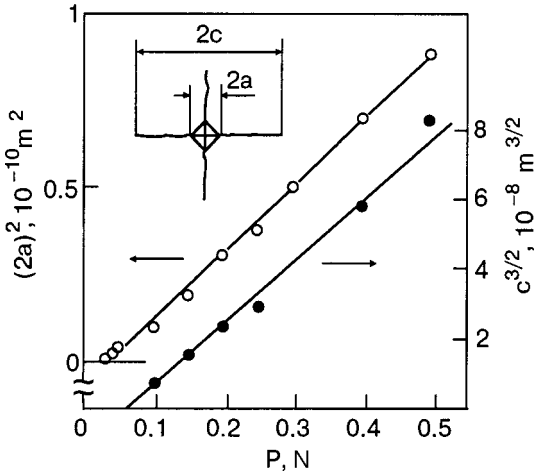

FIG. 8. Length of the diagonal of the impression and length of the radial crack versus load in the indentation of the (001) plane of a $YBa_2Cu_3O_{7-\delta}$ single crystal. The diagonals of the impression are parallel to the $\langle 100\rangle$ directions, and $T=290$ K.[13]

$K_{1c}\simeq 0.3-0.5$ MPa·m$^{1/2}$ (Ref. 14). Table I permits a comparison of the micromechanical characteristics of HTSC single crystals, a series of solid oxides, and silicon: according to the classification that is accepted in the literature, HTSC metal oxides belong to the group of solid materials having a high tendency toward brittle fracture.

TABLE I. Values of the microhardness H_V and critical stress intensity factor K_{1c} for single crystals of YBaCuO, BiSrCaCuO, LCO, and LSCO (indentation of the basal plane (001)) and also for several typically brittle oxide materials and silicon at room temperature.

Crystal	T_c, K	H_V, GPa	Direction of indenter diagonal	K_{1c}, MPa·m$^{1/2}$	Ref.
$YBa_2Cu_3O_{7-\delta}$	60	8.7	<100>	0.74	[12]
		9.7	<100>	0.43	[13]
BiSrCaCuO					
phase (2212)	85	2.5	<110>		[120]
	85	0.8	<100>		[120]
phase (2212)	85	0.69		0.22	[121]
phase (2223)*	> 100	1.27*	<110>		[122]
	> 100	0.9*	<100>		[122]
La_2CuO_4		7.44	<110>	0.96	[18]
		8.05	<100>		[18]
$La_{1.85}Sr_{0.15}CuO_4$	25	9			[18]
$BaTiO_3$		5.9		0.59	[12]
Si		9.0		0.70	[12]
MgO		7.7		0.76	[12]
SiO_2 (glass)		6.3		0.81	[12]

Note: *Knoop hardness.

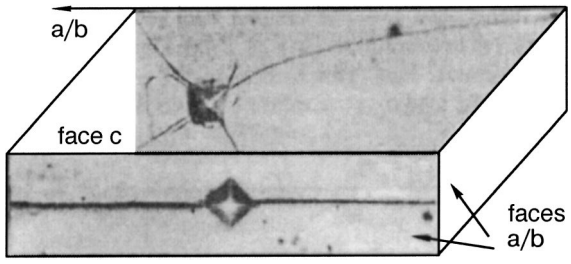

FIG. 9. Shape of microcracks formed around an indenter impression on different faces of $ReBa_2Cu_3O_{7-\delta}$ crystals.[14,125]

The micromechanical characteristics of $YBa_2Cu_3O_{7-\delta}$ crystals depend on the purity of the initial oxides, the type and concentration of dopants, the crucible material, and the gaseous composition of the surrounding medium and are highly sensitive to the microstructure defects and the crystallographic orientation. Let us present some data on how the microhardness and fracture toughness are influenced by the lattice anisotropy, twin structure, and moisture.

The pronounced anisotropy of all metal oxide HTSCs is due to their layered structure. A study of the mechanical anisotropy was done for single-crystal samples with thicknesses of 0.2–0.3 mm[14,89] and $\sim$1 mm[123] and also on large elongated grains of a polycrystalline sample.[89] The microhardness of $YBa_2Cu_3O_{7-\delta}$ crystals of the orthorhombic modification is the same in air and in water[89] and is practically isotropic: within the error limits the values of H_V on all three basal faces $\{100\}$ are equal and independent of the direction of the diagonal of the impression,[14] and are the same for twinned and detwinned crystals.[89] Meanwhile, a number of other studies have revealed substantial anisotropy of the micromechanical characteristics. Anisotropy of the first kind, wherein the measured value of H_V depends on the direction of the diagonal of the indenter with respect to the crystallographic direction on the chosen plane [100], has been observed in orthorhombic YBCO crystals,[15] and in the oxygen-saturated crystals the ratio $(H_V^{\langle 100\rangle}-H_V^{\langle 110\rangle})/H_V^{\langle 110\rangle}$ reached 50–80%. The anisotropy of the second kind, wherein H_V depends on the plane of indentation, was characterized by the following values:[123] $H_V^{(001)}$ was approximately 20% smaller than $H_V^{(100)/(010)}$, and in the tetragonal modification these differences reached 50%. On highly textured (aligned) samples a value $H_V^{(100)/(010)}/H_V^{(001)}\simeq 0.6$ was obtained,[124] probably because of the influence of the pronounced cracking along the (001) planes. One of the most likely causes of the microhardness anisotropy of metal oxide crystals is the anisotropy of the development of plastic shears in them.

The length and direction of propagation of cracks are extremely sensitive to the crystallography of the indentation.[14,125,126] Cracks propagate easily along planes of the $\{100\}$ type, and their direction therefore coincides with the direction of the diagonal of the impression when the latter is oriented along $\langle 100\rangle$. In other cases the cracks turn out to be shorter and noncoincident in direction with the diagonal of the impression; sometimes they smoothly change direction to coincidence with $\langle 100\rangle$ (Fig. 9), and a tendency toward the development of secondary cracks is observed. In the case of indentation of the (001) plane the cracks had the

same lengths in the mutually perpendicular directions [010] and [100]. When indentations were made on the (100)/(010) planes, strong anisotropy of the nucleation and propagation of cracks around the impression was observed. As is seen in Fig. 9, cracks develop predominantly in the basal plane (001), for which the surface energy is apparently minimal. This agrees with the observed growth habits of crystals in the form of thin slabs parallel to the (001) plane. A similar picture of crack development was observed in Ref. 116 in the indentation of the (001) and (100)/(010) surfaces of samples cut from highly aligned polycrystalline $YBa_2Cu_3O_{7-\delta}$ grown by a melt technology.

Measurement of the fracture toughness of detwinned crystals showed[84] that there is a small anisotropy of K_{1c} between the *a* and *b* directions: the average value of K_{1c} in the direction of the [100] axis is approximately 25% larger than in the direction of the [010] axis (0.59 and 0.47 MPa $\cdot m^{1/2}$). The ratio of the K_{1c} values for cracks propagating perpendicular to and parallel to the basal plane is equal to two. Twin boundaries have an appreciable influence on the propagation of cracks: the average value of K_{1c} in the (001) plane is approximately 25% larger for the twinned crystals than for the detwinned. The increase of the fracture toughness in the twinned material is due to dissipation of the crack energy upon the intersection of twin boundaries and, possibly, on account of the motion of these boundaries under the influence of the stress field of the crack.

A water medium leads to a substantial decrease of the crack resistance; the average value of K_{1c} is 35% lower for indentation in water than for indentation in air[124] (meanwhile, in Ref. 89 no noticeable influence of moisture on K_{1c} was observed). The study of the interaction of HTSC materials with surrounding media has important practical value in situations where it is necessary to ensure stability of the properties of corresponding device elements. This problem must be considered separately in each specific case.

Thus the crystallographic and structural factors and also the surrounding medium have a sensitive influence on the mechanical properties of $YBa_2Cu_3O_{7-\delta}$ crystals and, in particular, can be the cause of the scatter of the results of measurements of different investigators if those factors are not controlled.

5. INFLUENCE OF STRUCTURAL DEFECTS ON THE MECHANICAL PROPERTIES OF METAL OXIDES

Defects of the crystal structure of metal oxides have a significant influence on the physical/mechanical properties. Especially noticeable is the negative influence of structural defects on the plasticity of HTSCs—they enhance the innate tendency of these materials toward brittleness. The main aspects of the influence of defects on the dynamic and static elastic properties of HTSCs have been described in a review.[29] Below we present information about the influence of doping, grain boundaries, porosity, and heterophase nature on the plasticity and strength of polycrystals and single crystals of some HTSCs.

5.1. Impurity hardening

It is known that the admixture of impurities increases the mechanical strength of crystalline materials for several reasons. In the dislocation mechanism of plastic deformation, the motion of dislocations is impeded by individual impurity atoms. If the impurity concentration exceeds the solubility limit, precipitates can form which are also effective obstacles to the motion of dislocations. Impurities lead to solid-solution and precipitate hardening. In addition, impurities or their complexes can fill the intergrain space, thereby altering the coupling between granules. On the basis of what we have said above, numerous attempts have been undertaken to improve the mechanical characteristics of HTSC ceramics by doping with various impurities to take advantage of various hardening mechanisms. Let us discuss some of the results in this area.

Significant hardening of polycrystalline YBCO upon doping with the substitutional impurities Zn and Li was found in Ref. 127: a linear increase of H_V with increasing impurity concentration was observed. Since optical microscopy and x-ray diffraction have not revealed the appearance of extraneous phases upon doping, this effect has been interpreted as being a consequence of solid-solution hardening of the grains, which to a first approximation is proportional to the relative difference of the ionic radii of copper and the dopant elements and to their concentration. No effect of those impurities on the strength properties of the grain boundaries were observed. Furthermore, the difference of the charges of the Cu and Li ions was not reflected in the hardening of the ceramic.

Polycrystals based on $YBa_2Cu_3O_{7-\delta}$ with admixtures of rare-earth metal oxides Re_y ($y \leqslant 0.02$) were studied in Ref. 128. The doping admixture was incorporated in the structure of the orthorhombic 123 phase, partly substituting for the Ba^{2+} ions and forming a compound of the form $YBa_{2-y}Re_yCu_3O_{7-\delta}$; doping strengthened the grain and increased the density and microhardness while leaving T_c unaffected.

The mechanical and superconducting properties have been improved[129] by sintering a 0.2 wt. % platinum powder with YBCO. Further increase in the Pt concentration improved the properties (H_V increased by approximately a factor of 2 when the Pt concentration was increased from 0 to 0.5 wt. %), but the higher density of the ceramic reduced its permeability to oxygen and decreased the superconducting fraction and the critical current density.

In the case of La_2CuO_4, substitution of part of the La atoms by Sr led to an appreciable increase in H_V: for example, in $La_{1.85}Sr_{0.15}CuO_4$ crystals at room temperature the effect was $\sim 20\%$.[18] This result does not completely agree with the data of Ref. 130: although the authors of that paper[130] spoke of the hardening effect of doping, their measurements registered a decrease of H_V on going from LCO ($H_V = 9.24$ GPa) to LSCO ($H_V = 8.94$ GPa). An increase of the grain size of the ceramic was noted, and that could have caused the softening.

For polycrystalline $Bi_{2-x}Pb_xSr_2Ca_2Cu_3O_y$ a close-to-linear growth of H_V with increasing lead concentration was observed[131] in the interval $x = 0.2-0.5$, which is assumed to be the result of solid-solution hardening. At $x = 0.6$ a deviation from the linear dependence to the side of higher H_V was noted, which may be due to precipitate hardening by segregates of the new phase Ca_2PbO_4 (see Sec. 5.4).

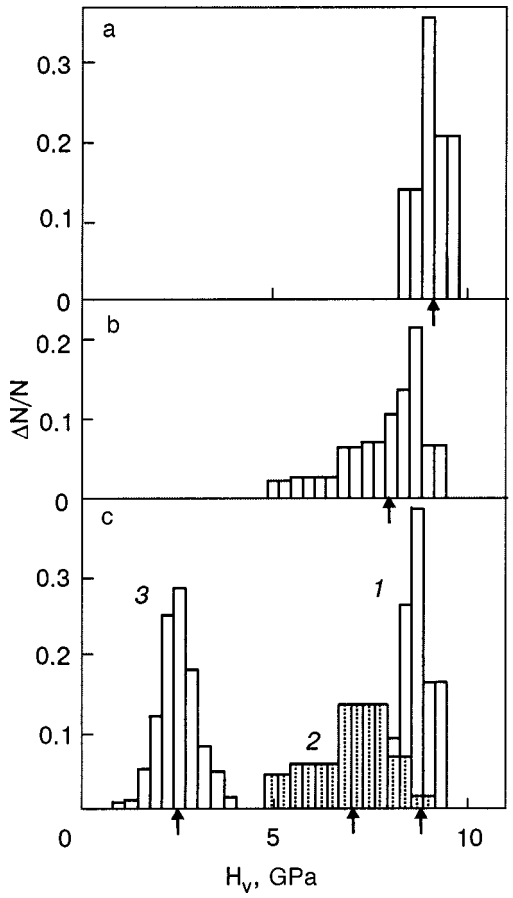

FIG. 10. Histograms of the microhardness of YBCO: single crystals, $P=0.15$ N (a); coarse-grained polycrystal, $P=0.15$ N, continuous indentation (b); histogram "b" after separation of the data for crystallites (*1*) and grain boundaries (*2*), and the histogram of a fine-grained polycrystal (*3*), $P=2$ N (c); the arrows indicate the average values of the microhardness.[133]

5.2. The softening role of grain boundaries in polycrystals

Grain boundaries in polycrystalline samples are sites of segregation of impurities and impurity phases and localization of voids and microcracks, and they should therefore play an important role in the mechanical behavior of these materials. For example, it has been observed[132] that the sound velocity in YBCO samples obtained by hydrostatic pressing of the powder increased significantly after a thermochemical treatment (annealing in oxygen at 873 K) that did not affect the density.

To study the influence of grain boundaries on the plasticity and strength of YBCO ceramics we used the method of microindentation, which permits measurement of the local plastic compliance: the values of the microhardness of single crystals and of the central and boundary regions of grains in polycrystals were determined and compared.[133] Histograms of the H_V values for 50–500 impressions obtained on single crystals and polycrystals at room temperature are shown in Fig. 10. The scatter of H_V for the single crystals (Fig. 10a) is found within the error limits of the optical measurements. The histogram in Fig. 10b was constructed from the results of indentation of the surface of a coarse-grained polycrystal (average grain size $d\simeq 40$ μm) at equal intervals of 50 μm (continuous indentation). One notices the asymmetry of the latter histogram (the broadening to lower values of H_V), which may be due to the contribution of the grain boundaries. When the body of data is divided into two groups, one of which pertains to impressions within a grain and the other to impressions in the region of the grain boundaries, the histogram separates into two bell-shaped parts (histograms *1* and *2* in Fig. 10c): the first of them is close to the histogram for single crystals (Fig. 10a), while the second attests to the lower values and appreciable variance of the microhardness in the region of the boundaries between crystallites. Consequently, the defects responsible for the lowering of H_V are concentrated mainly at the grain boundaries.

The softening role of the grain boundaries is manifested especially clearly in measurements with a large load on the indenter for a fine-grained sample,[126,133] as is reflected in histogram *3* in Fig. 10c. A comparison of histograms *1* and *3* indicates an almost threefold difference between the mean values of H_V of the polycrystal and single crystal. Apparently, in the case of the polycrystal the condition of H_V with increasing load on the indenter is due to an increase in the number of defect regions in the area of the impression of the indenter and to enhancement of the intergrain cracking. In Ref. 134 an increase of H_V was observed in polycrystalline samples with increasing number of grinding-pressing cycles; the authors of that paper interpret this as evidence of growth in the strength of the bonds between crystallites on account of activation of the contact surfaces of the particles.

The results show that the inhomogeneity of the mechanical characteristics of polycrystalline HTSCs and their low strength as compared to single crystals are due mainly to the grain boundaries. The structure of the grain boundaries is one of the decisive factors determining the physical-mechanical and functional properties of a majority of the items made from metal oxide HTSCs.

5.3. Influence of the porosity of the samples on the plasticity and strength

The microhardness of polycrystalline YBCO was studied[14] on samples of different density from $\rho/\rho_R=0.33$ to $\rho/\rho_R=0.92$, where $\rho_R=6.38$ g/cm^3 is the x-ray density. The dependence of the mechanical properties of a ceramic on the relative density ρ/ρ_R at room temperature is shown in Fig. 2 of Ref. 29, which presents data on the influence of porosity of YBCO ceramics on the microhardness[14,135,136] ultimate strength, and static Young's modulus.[137] The results of the measurements are described satisfactorily by the empirical formula[138]

$$M=M_0\exp[-np],\quad p=1-\rho/\rho_R, \tag{4}$$

where M stands for the microhardness H_V, ultimate strength σ_f, or Young's modulus E, and p is the porosity. The parameter n has values typical of conventional ceramics:[138] $n\simeq 4.6$ (Refs. 14, 135, and 136) in the case of $H_V(p)$, $n=5.7$ (Ref. 137) and $n\simeq 11$ (Ref. 139) in the case of $\sigma_f(p)$, and $n\simeq 7.8$ for $E(p)$ (Ref. 137).

The value of the pre-exponential factor $H_{V0}\simeq 4.5$ GPa is at the level of the mean hardness of single crystals of the ReBaCuO family but turned out to be lower by a factor of two than the microhardness of yttrium-based single crystals. This indicates that in polycrystalline HTSCs the local defor-

mation under the indenter is determined not only by microvoids at the boundary but also by other defects (grain boundaries and microcracks).

We note that the density of the ceramic also influences the fracture toughness. The strong increase of K_{1c} with increasing density was attributed in Ref. 140 to a significant increase in the grain size upon compaction of the material, which makes the propagation path of an intergrain crack more tortuous.

The results presented show that with increasing density of metal oxide ceramics one observes an improvement in their mechanical characteristics. However, for $\rho \to \rho_R$ one can observe the opposite effect: enhancement of the cracking upon cooling of the ceramics, which is due to anisotropy of the coefficient of linear expansion. The cracking can be suppressed by decreasing the grain size and also by optimizing the cooling conditions in the process of saturation with oxygen.[141]

5.4. Features of the mechanical properties of heterophase Bi-containing HTSCs

This class of HTSC materials merits separate discussion because of their amenity to fabrication and the realistic hope of obtaining superconductors with improved critical parameters. An x-ray analysis shows that an important feature of Bi-containing HTSCs[142,143] is their tendency toward multiphase behavior. The superconducting phases in this system, 2201, 2212, and 2223, are usually described by the general formula $Bi_2Sr_2Ca_{n-1}Cu_nO_y$, where n is the number of CuO_2 planes.[144]

The difference of the physical properties of the phases is manifested in mechanical experiments. In the study of the microhardness of Bi–Sr–Ca–Cu–O single crystals with $T_c = 82$ K, the authors of Ref. 145 observed a strong inhomogeneity of the micromechanical properties (significant scatter in the value of H_V) even within a single optically homogeneous sample, but an even larger scatter of H_V was observed in a study of different samples. Measurements made on a series of single crystals showed that H_V is grouped around three characteristic values: 0.5, 1.1, and 3.1 GPa, which are considerably lower than the values obtained on Re–Ba–Cu–O single crystals ($H_V \simeq 5-10$ GPa).

Inhomogeneity of the mechanical properties was also manifested in a measurement[145] of the microhardness of polycrystalline samples of Bi–Pb–Sr–Ca–Cu–O. Observation of polished surfaces of the samples under an optical microscope revealed the presence of at least two types of crystallites with different reflectivities, bright and dark, which had different hardness. Figure 11 shows histograms of the size distribution of the impressions, obtained under selective indentation of the surface of the sample in the bright (Fig. 11a) and dark (Fig. 11b) crystallites and at random places (Fig. 11c). The maxima in Fig. 11c are also well apparent in Fig. 11a and 11b. The values of the microhardness at the maxima ($H_V = 3.8$ GPa in Fig. 11a and $H_{V1} = 1.08$ GPa and $H_{V2} = 0.43$ GPa in Fig. 11b) are rather close to the values obtained on single crystals. As an averaged characteristic for a polycrystalline ceramic one should apparently consider the mean value $H_V = 1.1$ GPa calculated on the basis of the histogram in Fig. 11c.

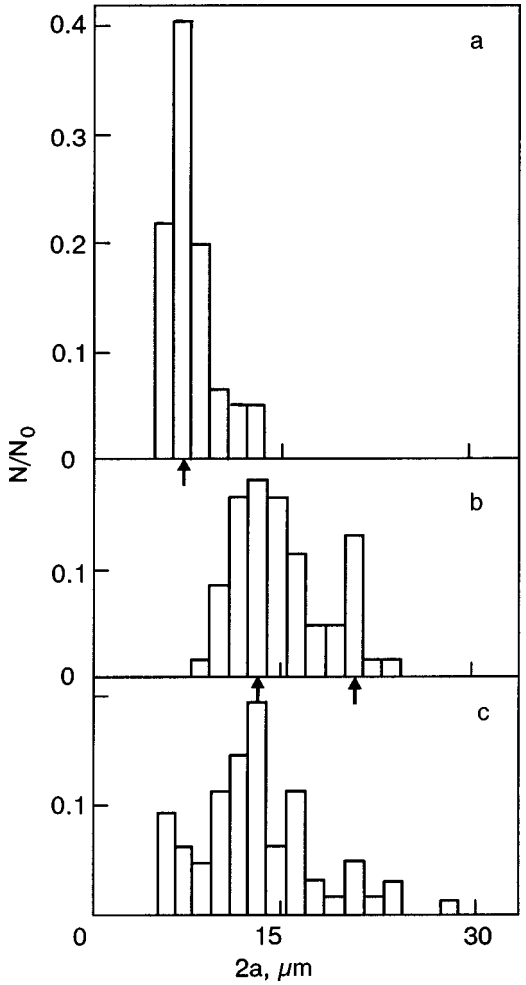

FIG. 11. Histograms of the size distribution of indenter impressions on the surface of a polycrystalline sample of Bi-Pb-Sr-Ca-Cu-O for a load on the indenter of $P = 0.1$ N: bright regions (a); dark regions (b), random places (c). The arrows denote the values of the impression diagonals corresponding to the maxima on the histograms.[145]

Unfortunately, the authors were unable to link the microhardness values obtained to specific phases. However, some conjectural identifications can be made on the basis of the following data. A value $H_V = 0.69$ GPa was obtained in Ref. 121 and a value $H_V = 0.63$ GPa in Ref. 146 for single crystals of the 2212 phase at room temperature (with a load $P \gtrsim 0.5$ N on the indenter). The critical temperature of this phase $T_c = 85$ K, which is close to the value $T_c = 82$ K for the samples studied in Ref. 145. It may be thought that the hardness value $H_V = 1.1$ GPa (1.08 GPa for the polycrystal) in Ref. 145 corresponds to regions of the 2212 phase, which on average determines the properties of both the single crystal and polycrystal. Measurements of the Knoop microhardness H_K showed that for a single crystal of the 2223 phase ($T_c = 100-110$ K)[122] the maximum value of H_K is almost a factor of 2 lower than for the 2212 phase[120] (the basal plane of indentation): 1.3 GPa as against 2.5 GPa. A correlation was noted between the values of $\max H_K$ and T_c: the lower the value of T_c, the larger the value of $\max H_K$. An analogous correlation has been observed for other HTSCs;[147] this agrees with the idea that T_c increases with decreasing compactness of the crystal structure. The results presented above permit the assumption that the samples studied in Ref. 145

contained three phases, with the characteristic hardness values $H_V = 0.43-0.5$ GPa (2223); $H_V = 1.1-1.08$ GPa (2212), and $H_V = 3.1-3.8$ GPa (2201) (this last phase has a critical temperature $T_c = 10$ K; Ref. 148).

A large number of studies have been devoted to developing methods of preparing high-quality single-phase samples of the Bi–Sr–Ca–Cu–O system. In Ref. 149 a single-phase 2212 material was obtained by solid-phase synthesis under stringent control of the process parameters: the oxygen pressure, the maximum sintering temperature, the annealing time, and the cation stoichiometry.

In the early days of research on bismuth-based HTSCs[150] it was found that the high-temperature phase 2223 is stabilized by the partial substitution of Bi atoms by Pb atoms if a certain amount of lead oxide PbO is admixed to the initial components together with Bi_2O_3. In Refs. 151–155 the phase composition, density, porosity, critical temperature, and hardness H_V of polycrystalline samples of the system $Bi_{2-x}Pb_xSr_2Ca_2Cu_3O_y$ were studied as the conditions of solid-phase synthesis and the composition parameter $0 \leqslant x \leqslant 0.5$ were varied. The samples with $x = 0.3$ turned out to be optimal: they were distinguished by a higher volume fraction of the 2223 phase, a high critical temperature $T_c = 113$ K, minimal porosity $p = 0.23$, and maximal mean hardness $H_V = 0.325$ GPa,[155] which is close to the hardness of single crystals and polycrystals of this system.[137] Deviation from $x = 0.3$ to either side led to poorer-quality ceramics in terms of all parameters. It is clear that the influence of lead atoms on the properties of Bi-HTSCs is by no means confined to their strength characteristics. Partial substitution of Bi by Pb gives rise to new phases having a favorable influence on the stability of these materials and also promotes better conjoining of the grains.

A feature of Bi-HTSC crystals is their appreciable tendency toward brittle fracture: they have a low value of the critical stress intensity factor $K_{1c} = 0.11$ MPa·m$^{1/2}$ (Ref. 145; for crystals of the 2212 phase $K_{1c} = 0.22$ MPa·m$^{1/2}$; Ref. 121) and tend to develop secondary cracks in the basal planes (001) under the indenter. Figure 12 shows the result of such cracking—a raising of material in the form a ''roof'' which extends a considerable distance from the center of the indenter impression. The residual deformation of this fragment is of the order of 1%, which is large for a brittle metal oxide.

Nonuniformity of the mechanical properties due to the heterophase nature has also been observed in the case of Tl-containing HTSCs.[156] In a study of single crystals with the main phase $TlBa_2CaCu_2O_y$ ($T_c = 110$ K) two values of the microhardness were registered: $H_V = 0.2$ GPa and $H_V = (7.6 \pm 0.8)$ GPa. As studies of other phases in Tl-HTSCs have shown, the first value of H_V probably corresponds to the 2201 phase.

6. TEMPERATURE DEPENDENCE OF THE PLASTICITY AND STRENGTH OF METAL OXIDES

An important part of the groundwork for the preparation and practical application of HTSCs is to investigate the mechanical properties in detail over a wide range of temperatures. Deformation and thermomechanical treatment are among the most important technological means for preparing metal oxide HTSCs and items made from them (tablets, ribbons, wires, coils) having high pinning forces and good intergrain coupling, which are necessary for achieving high transport current densities. During use, parts of these items can be subjected to appreciable mechanical loading (e.g., the coils of magnets carrying high currents), and the internal stresses arising on cooling to the working temperatures and the subsequent heating can reach critical values, a situation which is extremely dangerous for the naturally brittle perovskite-like metal oxides. Data on the temperature dependence of the mechanical characteristics are also needed for developing the basic concepts of the physical nature of the processes that govern the elasticity, plastic deformation, and fracture of these samples at low temperatures (during use) and at high temperatures (during fabrication).

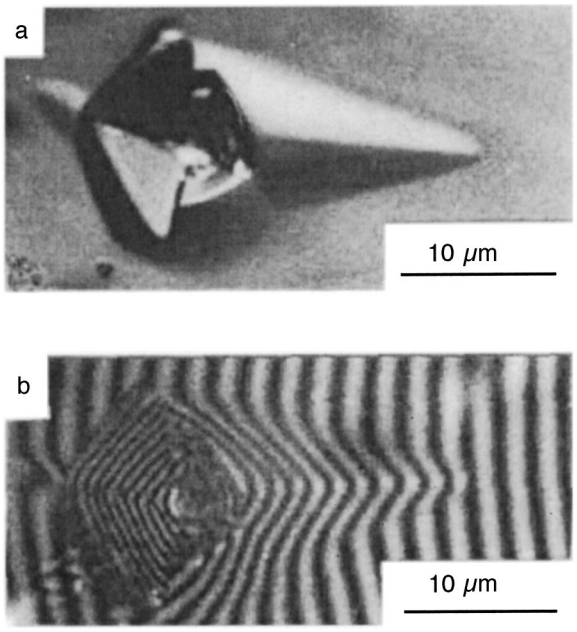

FIG. 12. Raised surfaces of a Bi-Sr-Ca-Cu-O crystal in the form of ''roofs;'' oblique illumination (a), interference pattern[145] (b).

6.1. Influence of temperature on the microhardness and fracture toughness of single crystals

The microhardness and fracture toughness of YBCO single crystals at room temperature depend on many factors (the conditions of preparation, the presence of impurities and admixtures of other phases, the oxygen index) and varies over rather wide limits: $H_V = 5-10$ GPa and $K_{1c} = 0.4-1.2$ MPa·m$^{1/2}$ (Refs. 12–15 and 157).

Figure 13[131,158] shows collected data on the temperature dependence of the microhardness in the interval from 77 to 1172 K, obtained on YBCO crystals of the orthorhombic and tetragonal modifications. The hardness of the ortho phase on cooling from $T = 300$ K increases linearly without any anomalies near $T_c \simeq 93$ K (curve *1*);[133] an analogous dependence is found for the softer crystals (curve *2*).[15] The increase in hardness at $T > 550$ K (curve *2*) is apparently due to a change in the oxygen stoichiometry in the surface layers of the sample during heating in air. Samples with the tetragonal structure have a lower hardness at room temperature, but their hardness increases rapidly with decreasing temperature (curve *3*), and in the vicinity of the temperature 200 K a

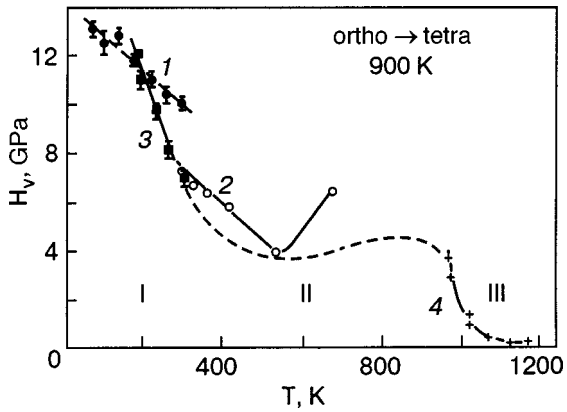

FIG. 13. Temperature dependence of the microhardness of YBCO single crystals: orthorhombic phase—$\delta=0.1$ (*1*, Ref. 133) and crystal after growth (*2*, Ref. 15); tetragonal phase—$\delta=0.9$ (*3*, Ref. 133), and $\delta=1$ (*4*, Ref. 159). I,II,III—temperature regions in which the controlling mechanisms of plastic deformation are presumably dislocation (I), dislocation-diffusion (II), and diffusion (III).

sharp transition from plastic deformation to brittle fracture under the indenter is observed.[133] In the high-temperature region 973–1173 K (curve *4*)[159] the hardness of the tetragonal phase falls off rapidly with increasing temperature, decreasing from 3.5 GPa to 0.05 GPa. This dependence was obtained with the aid of indentation by a three-sided pyramid made of zirconium oxide with a Y_2O_3 impurity; at the highest temperature a reaction of the pyramid material with the crystal was observed, and therefore the value at $T=1173$ K is questionable.

Figure 14[157] shows $H_V(T)$ in the temperature interval 40–293 K for a sample cut from a bulk pseudocrystal (highly aligned) with the composition Y123+40 mol. % Y211 +0.5 wt. % Pt, which was grown from the melt by a special technology (plane of indentation (001)). Against the significant scatter of the points one can discern an almost linear character of the dependence $H_V(T)$, the absence of features, and a significant increase in hardness with decreasing temperature: $H_V(40\text{ K})/H_V(293\text{ K})\simeq 3.5$ (this dependence is analogous to that shown in Fig. 13). The fracture of these samples is observed to be of a brittle character, as is evidenced by the behavior of the fracture toughness: K_{1c} is

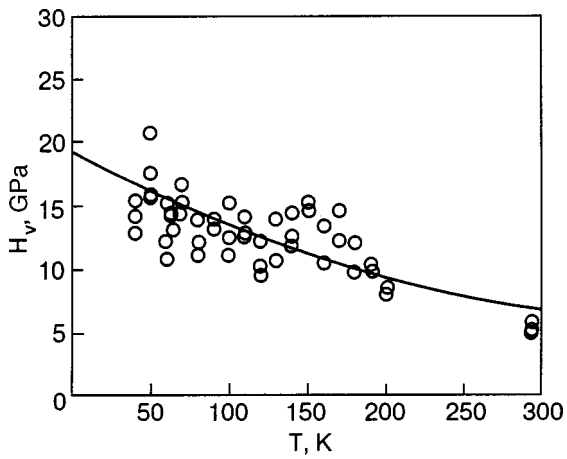

FIG. 14. Temperature dependence of the microhardness of a YBCO pseudosingle crystal.[157]

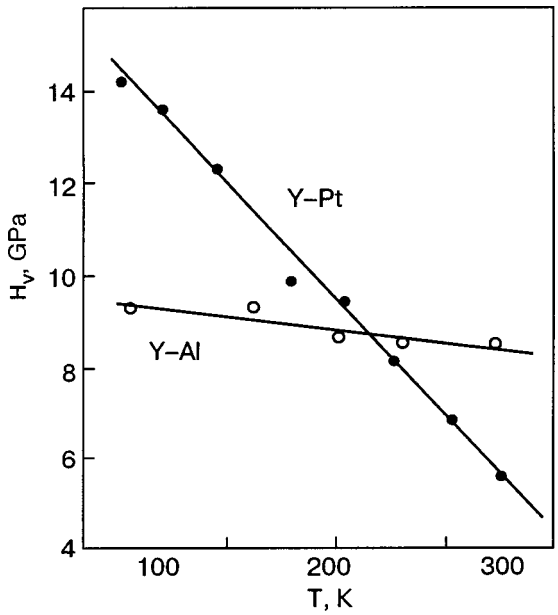

FIG. 15. Temperature dependence of the microhardness of YBCO single crystals of the Y–Pt and Y–Al series.[119]

independent of temperature or increases from 0.4 to 1.3 MPa·m$^{1/2}$ with increasing temperature. We note that the numerical values and temperature behavior of K_{1c} depend on the model used in the calculations to describe the crack under the indenter.

The value of K_{1c} registered in Ref. 157, which is higher than for other systems (see Table I), attests to the hardening role of particles of the second phase Y211, which is noticeably harder than the matrix. In measurements at room temperature by the method of nanoindentation[160] the following characteristics were obtained: for the Y211 phase—$E=213\pm5$ GPa, $H_V=14.4\pm2$ GPa; for the Y123 matrix—E=143 ±4 GPa, $H_V=10.0\pm1.9$ GPa for the (001) plane and $E=182\pm4$ GPa, $H_V=10.8\pm1.7$ GPa for the planes (100)/(010). A substantial hardening and improvement of the current-carrying properties of the Y123 phase upon the introduction of Y211 particles were also found in Refs. 161–163. The increase of K_{1c} of the matrix is due to dissipation of the energy of cracks at the interfaces and to blunting of the tip of the crack. Such a measure makes it possible to partially overcome the strong tendency of YBCO compounds toward brittle fracture and to increase the strength and fracture toughness.

The value and character of the temperature dependence of the mechanical characteristics of YBCO single crystals are extremely sensitive not only to the presence of second-phase particles in them or to the oxygen concentration δ but also to slight, often uncontrolled impurities entering during growth from the crucible material. The temperature dependence of $H_V(T)$ and $K_{1c}(T)$ of YBCO crystals of two series, Y–Al and Y–Pt, grown in alundum and platinum crucibles, respectively, were studied in Ref. 119. The crystals had close values of the oxygen index $\delta=0.3$–0.4 and critical temperature $T_c\simeq 60$ K but differed strongly in the values of H_V and K_{1c} and in the character of the temperature dependence of K_{1c} (Figs. 15 and 16). For crystals of the Y–Al series the hardness and fracture toughness depend weakly on temperature,

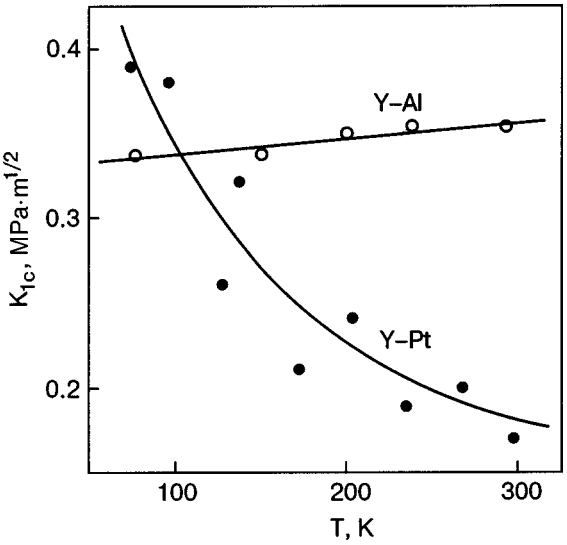

FIG. 16. Temperature dependence of the fracture toughness of YBCO single crystals of the Y–Pt and Y–Al series.[119]

while for the crystals of the Y–Pt series the hardness and fracture toughness increase substantially with decreasing temperature from 300 to 77 K. We note that in terms of hardness the pseudo-single crystals hardened by Y211 particles[157] are close to crystals of the Y–Pt series, but they are characterized by a $K_{1c}(T)$ dependence that is more similar to that for the crystals of the Y–Al series.

It is known that the temperature dependence of K_{1c} in different materials has the form of nonmonotonic curves with a maximum at the temperature of the brittle-plastic transition T_x (Fig. 17).[164,165] This parameter at low temperatures is determined by the interatomic forces (the model of an ideal crack) and therefore depends weakly on temperature (region I in Fig. 17),[164,165] while its growth in the vicinity of T_x (region II) is explained by the presence of plastic deformation.[164–168] Region III corresponds to the formation, at the tip of the crack, of a developed plastic zone where the crack is of a viscous character. The use of the formulas of linear mechanics of fracture for calculating K_{1c} under these conditions is incorrect, and it is necessary to take into account the thermally activated processes of plastic deformation, leading to a strong temperature dependence of K_{1c}.

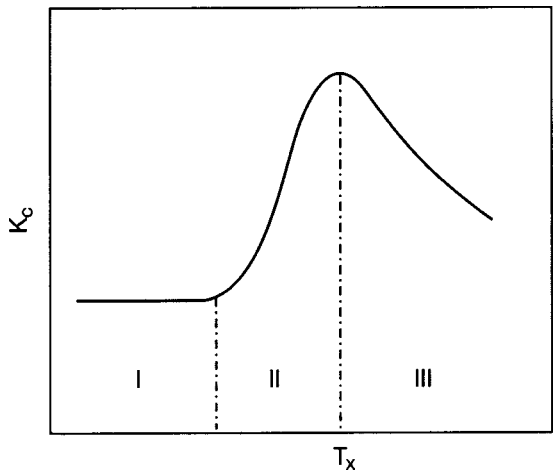

FIG. 17. Scheme of the temperature dependence of the fracture toughness K_{1c} for brittle materials near the temperature T_x of the brittle-plastic transition.[119]

The growth of K_{1c} with decreasing temperature for crystals of the series Y–Pt (Fig. 16) indicates that the measurements pertain to region III, and for them the temperature $T_x < 77$ K. Apparently the formation and development of cracks in these crystals are not due solely to the effect of the normal stresses under the indenter: processes of defect structure development in the region of the impression—in particular, the gliding of dislocations—also play a substantial role. Consequently, the values of K_{1c} given in Fig. 16 for crystals of the Y–Pt series characterize their tendency toward brittle fracture in only an approximate way.

The weak $K_{1c}(T)$ dependence for crystals of the Y–Al series (Fig. 15) gives reason to assume that the measurements for them pertain to region I in Fig. 17, in which K_{1c} is the basic characteristic of the brittleness and is determined solely by the fundamental constants of the crystal. For ideally brittle fracture of a crystal Griffiths-Orovan relation[165]

$$K_c^2 = 2\gamma E/(1-\nu^2), \tag{5}$$

where E is Young's modulus, ν is Poisson's ratio, γ is the surface energy for the plane of the mouth of the crack. Formula (5) can be used to estimate the surface energy γ if the values of the elastic moduli are known. Take $\nu = 0.3$, $E_{11} = E_{22} = 157$ GPa along the [100] and [010] axes and $E_{33} = 89$ GPa along [001].[29,89] Then for indentation of the (001) plane we have $\gamma_{100/010} \simeq 360$ erg/cm^2 ($K_{1c} \simeq 0.35$ erg/cm^2), while for indentation of the lateral surface we get $\gamma_{100/010} \simeq 1400$ erg/cm^2 ($K_{1c} \simeq 0.7$ erg/cm^2) and $\gamma_{001} \simeq 160$ erg/cm^2 ($K_{1c} \simeq 0.2$ MPa·m$^{1/2}$). As was to be expected, the cleavage plane (001) has a markedly lower energy in comparison with the other surfaces, and chipping occurs most easily along that plane. We note that the values of γ thus obtained are comparable to the values calculated theoretically for a number of ionic, metallic, and covalent crystals[169] or measured experimentally.[170]

The discussion above shows that the micromechanical characteristics of HTSCs are sensitive to the defect and impurity states of the material, i.e., technological factors which are not always known well enough.

The formation of the impression when an indenter is pressed into a solid under a certain load occurs in two stages.[107,111,112] In the first stage the indenter sinks rapidly into the sample, until the local stresses fall to a critical value below which the high-speed, nearly athermal deformation stops; in this stage the initial (zero-time) impression is formed. In the second stage the impression increases as a result of comparatively slow thermally activated plastic flow. While in the first stage the high local stresses are capable of activating dynamic processes of dislocation nucleation and multiplication, the second stage is governed by thermally activated motion of dislocations. In the region of high temperatures $T \sim 0.5T_m$ (T_m is the melting point) a direct relation between the kinetics of microplasticity under the indenter and the kinetics of macroscopic creep has been established for such diverse crystalline materials as In, Pb, Sn, Al, MgO, and silicon carbide;[111] for germanium the microplasticity is related to the mobility of individual dislocations.[113]

TABLE II. Values of the microhardness, its temperature sensitivity, and the empirical values of the parameters of the Arrhenius equation (6) for La_2CuO_4 (Ref. 18), $La_{2-x}Sr_xCuO_4$ (Ref. 18), $YBa_2Cu_3O_{7-\delta}$ (Refs. 119 and 173), and Ge (Ref. 171).

Crystal	Concentration of oxygen δ or of strontium x	parameters of the dependence $H_V(T)$			Thermal activation parameters	
		$H_V(T)$, GPa		$\delta H_V/\delta T$, 10^{-2} GPa/K		
		292 K	0 K		U_0, eV	$\gamma\cdot10^{30}$, m^3
La_2CuO_4	–	6.9	11.8	1.6	1.27	103.5
$La_{2-x}Sr_xCuO_4$	0.15	9.0	12.2	1.1	1.9	150.5
$YBa_2Cu_3O_{7-\delta}$ (Y–Pt)	0.1–0.3	9.9	14.65	1.6	1.57	103.5
$YBa_2Cu_3O_{7-\delta}$ (Y–Al)		9.8	14.6	1.6	1.6	103.5
$YBa_2Cu_3O_{7-\delta}$ (Y–Pt)	0.4	5.3	17.1	4	0.73	41.4
$YBa_2Cu_3O_{7-\delta}$ (Y–Al)		9.1	14.8	1.95	1.3	84.9
$YBa_2Cu_3O_{7-\delta}$ (Y–Pt)	0.9	4	16.45	4.25	0.66	39.0
$YBa_2Cu_3O_{7-\delta}$ (Y–Al)		6.75	20.4	4.6	0.8	36
Ge	–	7.5	19	4	1.5	80

Note: The values of $H_V(T=0)$ were obtained by extrapolation of the experimental curves; in the case of Ge the linearity of $H_V(T)$ breaks down at $T<550$ K.

In the case of HTSC crystals the relations governing the development of plastic deformation under the indenter are unknown, and the indentation data can serve only as indirect evidence of the mechanisms of macroplasticity. In the low-temperature region (region I in Fig. 13) the $H_V(T)$ dependence is substantially stronger than the temperature dependence of the Young's modulus: with decreasing temperature from 300 to 77 K the hardness increases by 25–35% or even by a factor of three,[119,158] while the increase of the elastic constants does not exceed 8%.[29] This attests to the thermally activated character of the formation of the plastic zone under the indenter.

To estimate the activational parameters of the process of microplastic deformation we use the approximate relation between microhardness and temperature,[171] which is a consequence of the Arrhenius equation for thermally activated deformation:

$$H_V=\frac{\beta \ln m}{\gamma}(U_0-kT). \tag{6}$$

Here U_0 is the characteristic activation energy of the process (the height of the potential barrier); γ is the activation volume, $\beta\simeq6$ is a factor that includes the Schmid factor and the coefficient of proportionality between the values of the microhardness and the yield stress; m is the ratio of the preexponential factor in the Arrhenius equation and the characteristic value of the rate of plastic deformation under the indenter, $\ln m\simeq20$ (Ref. 133). The results of an estimate are presented in Table II. It is seen that in terms of the absolute value and the character of the temperature dependence of $H_V(T)$ the YBCO, LCO, and LSCO single crystals are closest to the elemental semiconductors Si and Ge.[171] It can be assumed that the mechanisms of plastic deformation of these crystals are of a general nature, most likely the motion of dislocations in the Peierls relief. In the case of metal oxides the parameters of the relief are determined by the strong ionic-covalent bonds between components of the crystal lattice. There is also reason to assume that there can be a certain contribution to the formation of the impression from a crowdion mechanism of mass transport.[15,172]

The high-temperature deformation of crystals of the tetragonal phase (region III in Fig. 13; curve *4*)[159] is most likely due to diffusion processes; then the intermediate region II must be governed by mixed diffusion-dislocation mechanisms of plastic flow (see Sec. 6.4).

6.2. Temperature dependence of the microhardness and the ultimate strength of polycrystals of different density

As we mentioned previously, the indentation method is extremely efficient for estimating the structural inhomogeneity of materials owing to the possibility of precise localization of the impression of the indenter on the surface of the sample and to the sensitivity of the microhardness to the presence of defects. In particular, at sufficiently large values of the load P on the indenter the values of H_V can give some information on the macroscopic density of a ceramic. Figure 18 shows the temperature dependence of the microhardness in the interval 77–300 K for polycrystalline samples of YBCO with approximately equal mean grain size ($d\simeq5$ μm) but different densities ($\rho/\rho_R=0.73$, 0.91, and 0.98) at two values of the load on the indenter:[131] for $P_2=2$ N the area of the impression is several times larger than the area of an individual grain, while for $P_1=0.15$ N the grain size was comparable to the size of the impressions. The values of H_V obtained at the low load P_1 are close to the hardness of the grains, while those measured at the high load P_2 give an average hardness of the sample.

The substantial decrease of H_V with increasing load on the indenter is due to the contribution of weak grain boundaries and to the process of crack formation along grain boundaries. A close-to-linear growth of H_V with decreasing temperature, without noticeable anomalies, was reported in Ref. 133, along with a strong density dependence of the microhardness, described at all temperatures by the exponential

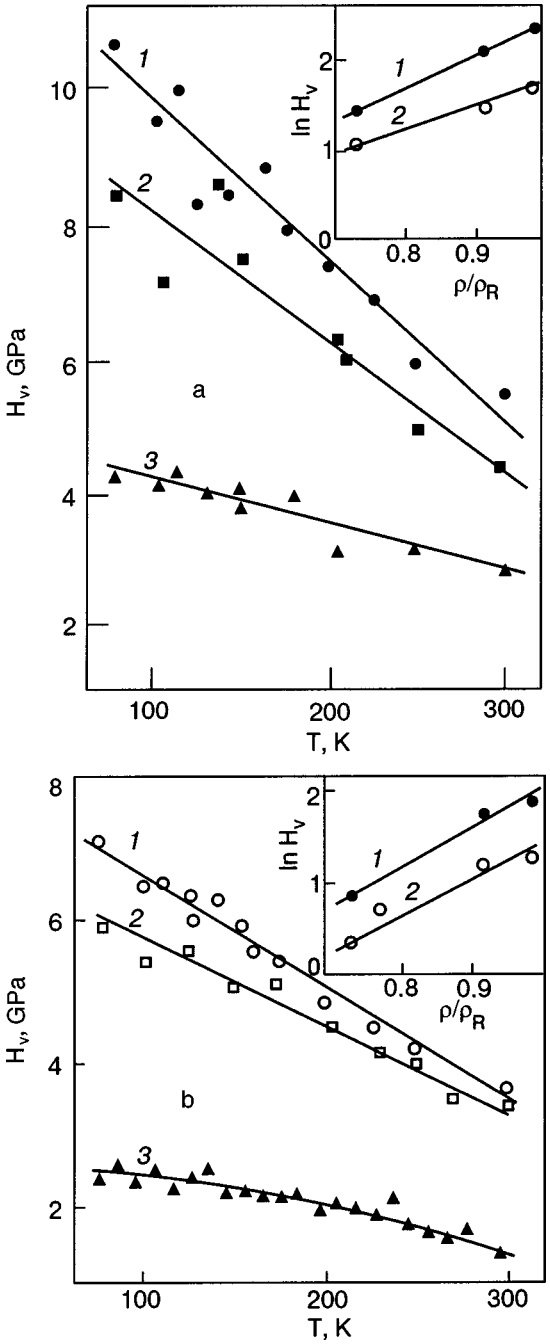

FIG. 18. Temperature dependence of the microhardness of YBCO ceramics for a load on the indenter of $P_1=0.15$ N (a) and $P_2=2$ N (b).[131] The relative densities $\rho/\rho_R=0.98$ (*1*), 0.91 (*2*), and 0.73 (*3*). The insets show $\ln H_V$ versus ρ/ρ_R for two temperatures T [K]: 77 (*1*) and 293 (*2*).

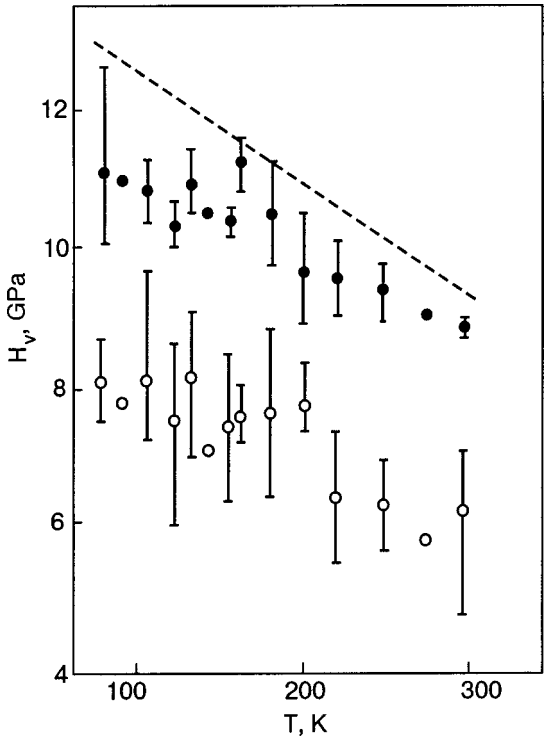

FIG. 19. The $H_V(T)$ dependence, averaged over several cycles of measurements on one sample, for the crystallites (●) and for grain-boundary regions (○) of coarse-grained polycrystalline YBCO. The dashed line shows the averaged data for several single crystals; the load on the indenter was $P=0.15$ N.[133]

law (4). The value of H_{V0} depends on temperature and on the load placed on the indenter: that parameter increases from 4.5 to 7.5 GPa with decreasing temperature at $P_2=2$ N and from 6.5 to 11 GPa at $P_1=0.015$ N.

At a load of $P_2=2$ N the coefficient in the argument of the exponential function in formula (4) had a value $n\simeq 4.6$ which remained unchanged in the entire temperature interval studied (this is seen from the parallelism of the straight lines in the inset to Fig. 18b), while at a load of $P_1=0.15$ N it increased from 2.6 at 300 K to 3.6 at 77 K (see the inset to Fig. 18a). The cause of the increase in n with decreasing temperature and increasing load on the indenter is probably the formation of microcracks at grain boundaries, which enhance the dependence of the hardness on the density (porosity) of the ceramic.

It is safe to assume that the main causes of the low values of H_V for polycrystalline samples of YBCO at temperatures of 77–300 K are the porosity and the weakened grain boundaries. The role of the boundaries is clearly demonstrated by the $H_V(T)$ curves for crystallites and grain-boundary regions, averaged over several series of measurements on a single sample of a coarse-grained ceramic (Fig. 19).[133] This figure also gives the averaged data (the dashed line) for several YBCO single crystals. At all temperatures the maximum values of H_V for the crystallites are close to the microhardness of the single crystals, while the values of H_V for the intergrain regions are considerably lower. The relatively large scatter of the data and the lower mean values of H_V for the crystallites in comparison with single crystals may be due to the deviation of the plane of indentation of the crystallites of the ceramic from the basal planes and also to the defect structure of the grain boundaries, which are the weakest structural element of the ceramic and are highly nonuniform. As we have said, the mechanical properties of polycrystals of the YBCO system can be improved by the introduction of silver or of the oxides ZrO_2 or HfO_2, which improve the coupling between grains without destroying the superconducting properties of the material.

A detailed investigation of the influence of density variations in the interval 3.6–5.5 g/cm^3 on the temperature behavior of the macroscopic ultimate strength of YBCO polycrystals was carried out in Ref. 137. The temperature dependence of the ultimate strength in compression, σ_f, is shown in Fig. 20. No influence of temperature on σ_f was seen for samples

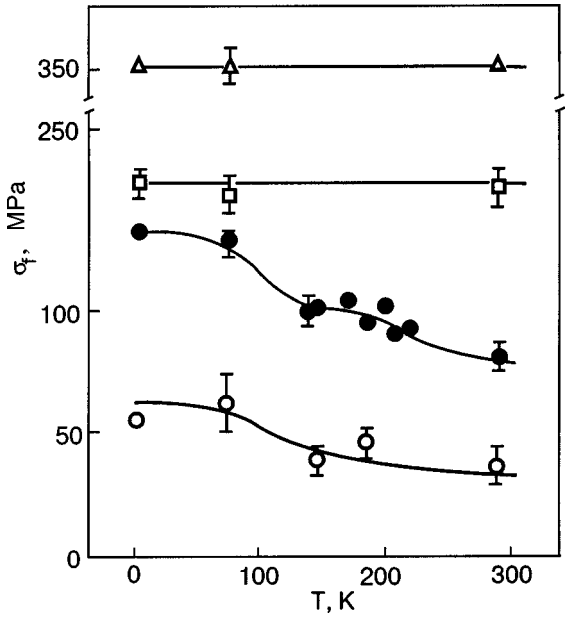

FIG. 20. Temperature dependence of the ultimate strength σ_f for YBCO samples of different density ρ [g/cm^3]: 3.6 (○), 4.6 (●), 5.2 (□), 5.9 (△).[137]

with $\rho \geqslant 5.2$ g/cm^3, but for less dense ceramics σ_f increased by 50% when the temperature was lowered from 300 to 77 K. The dependence of the static Young's modulus E and ultimate strength σ_f on the density is well described by relation (4) with the following empirical values of the parameters: $E_0 = 130$ GPa, $n = 7.8$ and $\sigma_{f0} \geqslant 4 \times 10^3$ GPa, $n = 11$. One notices the anomalously high value of σ_{f0}. Fractographic studies have established that with increasing density of the samples the intergranular character of the fracture gives way to a transcrystallite character, and the same occurs on decreasing temperature. For samples with a low density it was also noted that the temperature curves of σ_f have weak features in the region 60–200 K, which correlate with anomalies of the acoustic characteristics.[137] The insignificant influence of temperature on the value of σ_f for both porous and dense ceramics at $T < 300$ K is apparently due to the purely brittle character of the fracture under such conditions.

The low-temperature mechanical properties of polycrystalline Bi-HTSC ceramics have been studied in less detail. Figure 21 shows the temperature dependence of the microhardness of $Bi_{1.6}Pb_{0.4}Sr_2Ca_2Cu_3O_y$ (2223) (Fig. 21a)[131] and $Bi_2Sr_2CaCu_2O_y$ (2212) (Fig. 21b).[146] In both cases H_V increases linearly with decreasing temperature, and the value of the hardness of the 2212 phase is higher and has a considerably stronger temperature dependence in comparison with the 2223 phase. No anomalies near T_c were observed.

6.3. Comparison of the micro- and macromechanical characteristics

A theoretical analysis of the microindentation process was carried out in Ref. 107 for the model of an ideal elastoplastic solid and led to the relation $H_V \simeq 3\sigma_y$ between the microhardness H_V and the yield stress σ_y under simple compression/extension. This relation describes the properties of real materials with high values of σ_y but with a small reserve of plasticity. These are so-called "rigid-plastic" materials, for which fracture sets in after a small plastic deformation and the ultimate strength $\sigma_f \simeq \sigma_y$; they include, e.g., strongly cold-hardening metals. Certain dense YBCO and BSCCO metal oxide ceramics have analogous properties if the macroscopic mechanical testing is done under conditions of high hydrostatic pressure, which hinders the development of cracks. For example, for a YBCO ceramic with $\rho \simeq 0.92\rho_R$ one has $H_V = 4.3$ GPa at room temperature,[14] while for testing under conditions of hydrostatic pressure a value $\sigma_y = 1.25$ GPa was obtained;[22] consequently, $H_V/\sigma_y \simeq 3.2$.

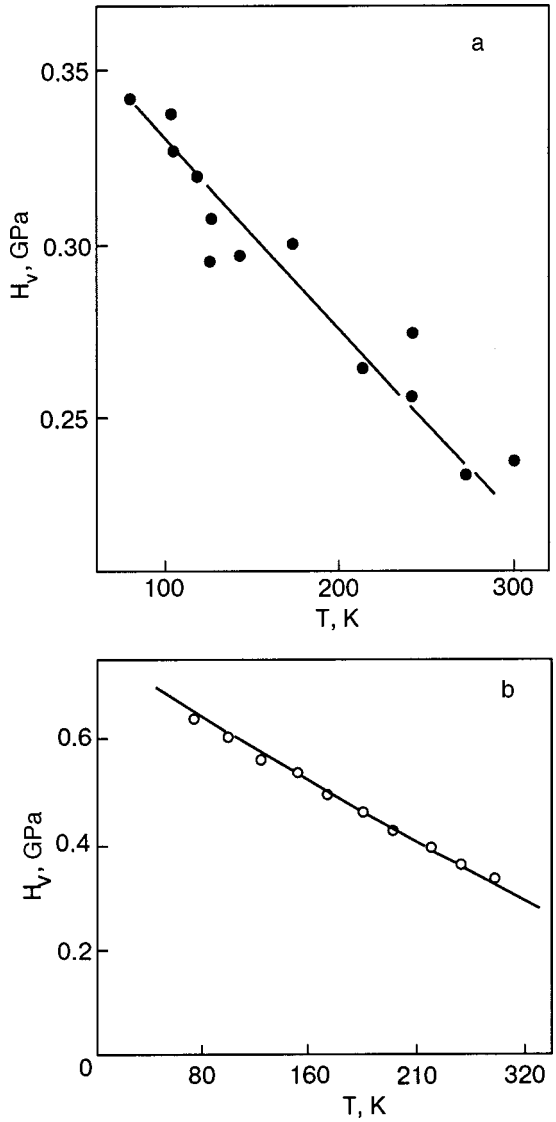

FIG. 21. Temperature dependence of the microhardness of polycrystalline Bi-2223 (a, Ref. 131) and Bi-2212 (b, Ref. 146).

The next class of materials can be conditionally called "plastic." Materials of this class have a low yield stress σ_y and a prolonged stage of plastic flow with a large work-hardening coefficient, as a result of which fracture sets in at stresses $\sigma_f > \sigma_y$. For these materials the ratio H_V/σ_y depends on many factors and is usually many times larger than three.[108] No analogs of such materials have been found among the metal oxide systems.

One can also identify a special class of "brittle-plastic" materials, which exhibit appreciable local plasticity under an indenter but which undergo brittle fracture in macrotesting.

For such materials it is easy to measure the ultimate strength σ_f, while the "potential" macroscopic yield stress $\sigma_y > \sigma_f$ remains unknown. In the study of such materials it is desirable to determine and analyze the ratio H_V/σ_f, for which the inequality $H_V/\sigma_f \gtrsim 3$ holds. Apparently the rather dense YBCO ceramics under conditions of normal pressures belong to this class of materials. In Ref. 137 a YBCO ceramic with a density $\rho \simeq 0.92\rho_R$ under compression at standard conditions experienced brittle fracture at a stress $\sigma_f = 0.35$ GPa, and for it $H_V/\sigma_f \simeq 12$.

Finally, some materials can be classified as "brittle." For them the impression of an indenter is made predominantly by the formation of microcracks, and in macrotesting the fracture is of a purely brittle character. These materials most often fracture at very high stresses of the order of the theoretical strength $[\sigma_f \simeq \sigma_T \sim (10^{-2} - 10^{-1})E]$, and for them the experimental data satisfy the inequalities $1 \lesssim H_V/\sigma_f < 3$. A number of single crystals of metal oxide compounds display the characteristic signs of materials of this class. For example, for crystals of the BSCCO 2212 system, room-temperature measurements of the hardness and of the fracture strength and Young's modulus of whiskers consisting of several single-crystal slabs have led to the values $H_V = 0.6$–1.1 GPa,[121,145,146] $\sigma_f = 0.94$ GPa, and $E = 92$ GPa.[174] In this case the relations $\sigma_f/E \simeq 10^{-2}$ and $H_V/\sigma_f \simeq 1$ hold, and the authors make special note of the fact that in the hardness measurements the material was observed to fracture under the indenter, and the fracture of the whiskers under tension occurred without any noticeable manifestations of plastic deformation.

For a $YBa_2Cu_3O_7$ single crystal at $T = 77$ K the hardness $H_V = 13.2$ GPa,[133] and the ultimate strength measured at this same temperature in a field ion microscope is $\sigma_f = 3.1$–5.4 GPa;[175–177] consequently, $H_V/\sigma_f \simeq 4.3 - 2.6$ and $\sigma_T/E_{33} = 1/16$–$1/30$, where E_{33} is Young's modulus in the [001] direction. A similar high value $\sigma_f \simeq 4.3 \pm 0.7$ GPa at 77 K was obtained for single-crystal whiskers of $LuBa_2Cu_3O_{7-\delta}$ in Ref. 174. In Ref. 159 the temperature dependence of the microhardness (see Fig. 12) and also that of the fracture stress σ_f in bending were obtained for YBCO single crystals under conditions of high temperatures 1023–1173 K: at 1073, 1123, and 1173 K the ratio of these quantities $H_V/\sigma_f \simeq 1$, while at $T = 1023$ K it has the value $H_V/\sigma_f \simeq 2.4$, and the ultimate strength varied from ~ 300 MPa at 1023 to ~ 30 MPa at 1173 K.

Thus single-crystal and polycrystalline metal oxide HTSCs in the majority of cases display the characteristic signs of brittle-plastic and brittle materials, and only some of them under special conditions (high pressure or high temperature; see the next Section) can be classified as rigid-plastic materials.

6.4. Features of the high-temperature plastic deformation

Heat treatment of metal oxide ceramics under conditions of high temperatures is the most important consituent of the technology of preparing HTSCs with the optimum combination of mechanical and superconducting properties; therefore the experimental investigation of high-temperature plasticity of these materials has been the subject of a large number of studies. The results of those studies are extremely diverse and contradictory, making it very difficult to systematize them and come up with a physical interpretation in terms of elementary mechanisms of inelastic deformation: atomic diffusion of individual chemical components, glide and climb of dislocations, development of microcracks, etc. The causes of these difficulties are understood: the diversity of methods of mechanical testing and experimental conditions, the complexity of the chemical composition and the diversity of crystal and defect structures of the materials studied, the fact that at high temperatures there are several elementary mechanisms of plastic deformation acting in combination, and because they are comparably effective it is difficult to separate them. In view of the practical importance of the problem discussed in this Section, we present below a number of experimental results obtained on the subject, without claiming any depth or rigor of the physical interpretation of the empirical material.

The usually brittle metal oxide systems can deform plastically owing to thermally activated mechanisms such as the glide and climb of dislocations, grain-boundary sliding, intragrain and grain-boundary diffusion, and recrystallization. This assertion will first be justified using the results for the YBCO system, and then other compounds will be discussed at the end of this Section.

Even the first studies of the mechanical properties of YBCO ceramics showed that on heating the orthorhombic and tetragonal phases one can observe transition from brittle fracture to plastic deformation in the temperature region 800–900 K.[159,178,179] However, the possibility of realizing such a transition apparently depends on the conditions and the heating regimen. In Ref. 180 the appearance of some residual strain was attributed not to plastic flow but to a slow cracking of the sample along grain boundaries. On the other hand, YBCO ceramics are plasticized on heating under conditions of hydrostatic pressure:[181] experiments on the compression of the orthorhombic phase Y123 upon application of a hydrostatic pressure of 1 GPa in the temperature region 750–950 °C revealed a deformation of up to 70%. Significant plastic deformations of YBCO ceramic samples are achieved under conditions of high-temperature creep.[25,182] If the rate of steady-state creep does not exceed $\dot{\varepsilon} \simeq 10^{-6}$ s^{-1}, then the value of the deformation without fracture can exceed 30%; here it is important that the critical parameters of the superconductivity of the material are practically unchanged.[182]

Heating of the ceramic leads to an extremely significant lowering of its yield stress. For example, in Ref. 181 at a strain rate $\dot{\varepsilon} \simeq 2 \times 10^{-5}$ s^{-1} a change in temperature from 1023 to 1223 K led to a decrease in the yield stress from 450 MPa to 90 MPa, and in Ref. 25 at $\dot{\varepsilon} \simeq 4 \times 10^{-5}$ s^{-1} the value of the yield stress was lowered from 160 MPa at $T = 1098$ K to 0.6 MPa at $T = 1248$ K. Furthermore, a substantial dependence of the plastic compliance on the strain rate is observed: in Ref. 181 a change in the yield stress in the range 150–1000 MPa was registered as $\dot{\varepsilon}$ was increased from 1.5×10^{-6} to 1.5×10^{-4} s^{-1} (deformation temperature 1023 K).

In the majority of cases the experimentally observed behavior of the plastic compliance in the variables "flow stress σ versus strain rate $\dot{\varepsilon}$ versus temperature T" is described by

a kinetic equation of the activation type (the Arrhenius equation):

$$\dot{\varepsilon} = A\sigma^n \exp(-U/kT). \quad (7)$$

Numerical values of the parameters of this relation (the activation energy U, exponent n, and pre-exponential factor A) depend on the type of HTSC compound, the conditions of the experiment, and the set of structure factors. In a number of cases the wide interval from room temperature to premelting temperatures is divided into several intervals with constant values of these parameters within an individual interval. Empirical estimates of the numerical values of the parameters U, n, and A have permitted researchers to conjecture with some degree of certainty about the physical nature of the mechanisms governing the plasticity of these materials under the conditions of a particular experiment. In some cases the conclusions reached are confirmed by the data of structural studies of the deformed materials by the methods of metallography and electron microscopy.

A study of the temperature dependence of the yield stress of Y123 polycrystals[25] showed that there are three temperature intervals with different values of the exponent n and activation energy U: 825–875 °C, where $n=2.5$ and $U=5\pm1$ eV; 925–975 °C, where $n=1.5$ and $U=10.4\pm1.5$ eV, and 875–925 °C, where n and U have intermediate values. In the authors' opinion such high values of U and the power-law dependence of the rate of strain on σ with an exponent $n\sim1-3$ are characteristic of purely diffusional or dislocation–diffusional processes in the volume or at the boundaries of the grains, which are controlled by the diffusion of the least mobile heavy cations, which form the frame of the crystal lattice of the metal oxides: Y, Ba, Sr, Ca. Meanwhile the study of the microstructure of the deformed samples attests to a certain participation in these processes of intragrain dislocation glide and grain-boundary sliding.

Y123 ceramics with submicron grain sizes have properties characteristic for superplastic materials:[183] at temperatures above 775 °C the samples deform plastically to 25–110%. At $T=850$ °C and $\dot{\varepsilon}=10^{-4}$ s^{-1} the microcracks are observed only after 50% deformation, and in some samples microcracks are absent even at 70%. During deformation the grain size did not change; the samples remained single-phase with $T_c\simeq88$ K after 50% deformation. The parameters of Eq. (7) ($n=2$ at 800 °C and $n=1.8$ at 850 °C, $U=7.5$ eV) are evidence that the superplasticity in this case is controlled by intergrain slip, which comes about by grain-boundary diffusion of heavy cations. These ideas are in agreement with the results of a study of the creep of fine-grained ceramics at temperatures of 800 and 850 °C.[182] In this regard the authors of Ref. 184 proposed to describe the superplasticity of HTSC ceramics by an equation of the type (7) in which $A\propto d^{-3}$ (d is the grain size), $n=2$, and $U=U^{gb}$—the activation energy for grain-boundary diffusion of heavy cations.

It has been shown in a small number of experiments that at high values of the flow stress the exponent $n>2$. The authors of Ref. 176 believe that this disagrees with the concepts of grain-boundary diffusion and that in the description of the deformation here it is necessary to take into account the mechanisms of generation and motion of basal dislocations and the presence of microcracking, which arises because the perovskite-like structure lacks the five independent slip systems necessary for plasticity of a polycrystalline sample. It is proposed to describe the kinetics of plastic deformation at high stresses by the standard law of dislocation-diffusion creep, which has the form of Eq. (7) with parameters $n=3$ and $U=U^l$, the latter being the activation energy for lattice diffusion of heavy cations.

Of particular interest is the high-temperature deformation of metal oxide materials occupying an intermediate place between polycrystals and single crystals. In Ref. 185 the plasticity of a highly aligned sample (pseudo-single crystal) of $YBa_2Cu_3O_{7-x}$ was studied at temperatures of 875 and 925 K. A strong temperature dependence of the critical shear stress in the slip system [100/010](001) was found: it decreased from 83 to 23 MPa on heating to 50 °C. The limiting value of the plastic deformation was around 8% and was independent of temperature; after that deformation the samples suffered brittle fracture. A study of the rate dependence of the flow stress led the authors to conclude that the deformation is described by Eq. (7) with $n=4.7$ and that the main mechanism governing the deformation process is the climb of dislocations (this agrees with the analysis of that mechanism in Ref. 186). Microstructural studies have indicated that the grain-boundary sliding plays a negligible role, possibly because of the pinning of the boundaries by particles of the Y211 phase, which is the phase that forms, as a rule, in the growth of highly aligned samples from the melt.

A detailed study of the plastic deformation of Y123 ceramics with grain sizes $\geqslant5$ μm at temperatures $T\geqslant0.85T_m$ ($T_m=1275$ K is the melting temperature in air) was carried out in Ref. 187, with a careful analysis of the results, taking into account the whole body of accumulated data, including the previous results of the authors and the published results of others. It was found that at $T\geqslant800$ °C and for low stresses the deformation occurs by intergrain slip. The rate of deformation is described by Eq. (7) with the exponent $n=1$ and with $U=U^{gb}=6.8$ eV, where the latter is the activation energy for grain-boundary diffusion. At higher temperatures the deformation rate is controlled by bulk diffusion, and the activation energy increases to $U^l=11$ eV (usually $U^{gb}\simeq(0.6-0.8)U^l$). The bulk diffusion coefficient and the value of U^l agree with measured volume tracer diffusivities of yttrium. In the final analysis the authors of Ref. 187 came to the conclusion that the intergrain slip is governed by lattice diffusion in the case of large grains and/or high temperatures and by diffusion along grain boundaries for fine-grained ceramics and/or low temperatures, and that the kinetics of plastic deformation can be described by the equation

$$\dot{\varepsilon} = 98\Omega_{\text{mol}}\frac{\sigma}{kTd^2}\left(D^l + \frac{\pi\delta}{d}D^{gb}\right), \quad (8)$$

where $\Omega_{\text{mol}}=2\times10^{-28}$ m^3 is the molecular volume, d is the grain size, D^l and D^{gb} are the diffusion coefficients for lattice diffusion and grain-boundary, respectively, and $\delta=10^{-9}$ m is the width of a grain boundary.

In Ref. 188 the voluminous experimental data obtained in the study of high-temperature plasticity of $YBa_2Cu_3O_{7-\delta}$ ceramics was generalized in the form of the following defor-

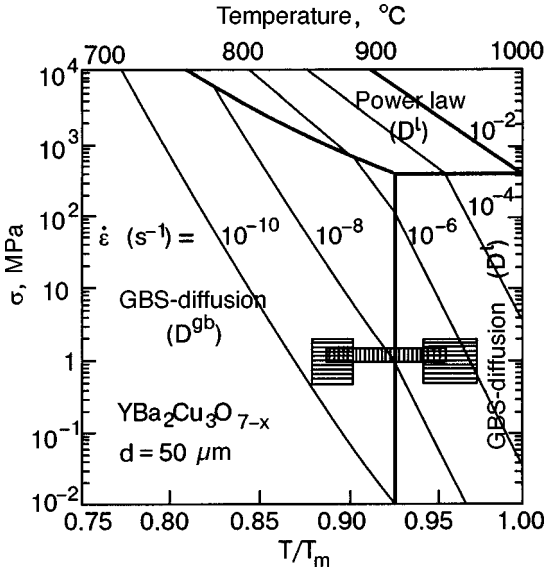

FIG. 22. Deformation map of stress versus homological temperature (T_m is the melting temperature) in air for polycrystalline YBCO with a grain size of 50 μm.[188] The experimentally investigated regions are shaded.

mation maps: $d-\sigma$, $d-T_m/T$, and $\sigma-T/T_m$ (Fig. 22). These maps reflect the main modes of deformation observed: superplastic flow, which occurs by intergrain slip, an important role being played in it by both grain-boundary and lattice diffusion; creep at high values of the flow stress, with the intragrain diffusion playing the predominant role. A map of the deformation mechanisms in the creep of Y123 ceramics was worked out in Ref. 184, where it was shown that the Nabarro-Herring creep with $n\simeq 1$ should dominate at high temperatures for practically realistic values of the stress and grain size, while power-law creep with $n>2$ dominates at high stresses (above 1 GPa) and in coarse-grained ceramics.

The high-temperature plasticity of another member of the family of ytterbium HTSCs—the compound $YBa_2Cu_4O_x$ (124), with $T_c=80$ K—was studied in Ref. 189. These crystals have an orthorhombic structure similar to that of Y123 but with two layers of Cu–O chains instead of one layer as in 123.[190] The experiments were done on compression at strain rates of $2\times10^{-6}-4\times10^{-5}$ s^{-1} in air and in oxygen at temperatures of 824–932 °C, in the stability region of the phase Y124. The samples were polycrystals with a density of $0.965\rho_R$ and with elongated grains 10–20 μm in size. At $T\geqslant 870$ °C the deformation kinetics was described by Eq. (7) with $n=1.54\pm0.25$, independently of the surrounding atmosphere. At a fixed deformation rate the flow stress was approximately 69% higher in oxygen than in air. The influence of oxygen was described by relation (7) with $A\propto(P_{O_2})^{1/m}$, where P_{O_2} is the oxygen pressure and $m\simeq-(4\pm1)$. In the region where n is independent of temperature the activation energy $U=4\pm0.6$ eV, which, in the opinion of the authors, corresponds to grain-boundary diffusion of Y or Ba cations. When the temperature was lowered at $T<870$ °C the value of n increased noticeably, attesting to a change in the deformation mechanism and to the accumulation of intergrain stresses.

At high temperatures Bi-HTSC ceramics are more plastic than YBCO. A study of BPSCCO samples[159] has shown that at temperatures above 800 °C and for a deformation rate of 1.3×10^{-5} s^{-1} the yield stress $\sigma_y\simeq10-30$ MPa, and the deformation of the samples reached 90% without fracture. The extremely high plasticity of the ceramic was attributed by the authors to the formation of a *c*-oriented texture, which is of undoubted technological interest in connection with the fabrication of items from HTSC powders.

A study of the temperature dependence of the mechanical properties of fused BSCCO 2212 ceramics in the temperature interval 20–800 °C in compressive tests[191] revealed three regions in which the mechanical properties behave differently: 1) from 20 to 350–400 °C the flow stress decreases linearly with increasing temperature, and the fracture is of a completely brittle character (no signs of macroscopic deformation are seen on the strain curve); 2) from 400 to 750 °C the strain curve exhibits characteristic discontinuities of the load due to the propagation of Lüders bands; 3) above 700 °C the strain curves have the typical form for plastic materials, but plastic flow is accompanied by partial microfracture. It may be that for $T>700$ °C the deformation is controlled by the diffusion mechanisms.

The high-temperature creep of $Bi_{1.65}Pb_{0.35}Sr_2Ca_2Cu_3O_{10+\delta}$ ceramics under compression at temperatures of 550–840 °C was investigated in Ref. 192. At 750 °C the ceramic deforms plastically to 25% without visible traces of fracture and to 55% with the formation of subsurface cracks to a depth of not more than 2 mm. The creep rate is described well by Eq. (7): n varied from 2.3 to 3.5, depending on temperature; the activation energy was $U=6.94\pm0.16$ eV at a stress of 5 MPa and $U=5.2\pm0.07$ eV at 30 MPa. In the opinion of the authors the deformation was controlled predominantly by the slip and climb of dislocations. At low stresses and in the initial stages of deformation the main contribution to the molding of the samples was from compacting due to a decrease in porosity, the role of which was reduced as the stress increased. Deformation at 750 °C decreased T_c and increased the width of the superconducting transition. An important conclusion is that the critical parameters of superconductivity in the deformed state are better in samples subjected to stress for a long time and being more highly compacted.

The plasticity of polycrystalline samples of the compound BSCCO 2212 of high density 6.6 g/cm^3, prepared by the method of hot isostatic pressing, was studied in Ref. 193. Compressive tests at a constant rate and in the creep regime were carried out in an oxygen atmosphere at a pressure of $(1-2.1)\times10^4$ Pa and temperatures of 780–835 °C. The intervals of temperature, stress, and oxygen pressure were were rather limited: at $T\leqslant785$ °C the deformation rates were too low to measure; at $T\simeq800$ °C and oxygen pressure of the order of 10^3 Pa a local melting occurred, and at overhigh stresses $\sigma>4.8$ MPa fracture of the samples occurred. At low stresses $\sigma\leqslant3$ MPa the plastic flow of the ceramic had a viscous character and was described by Eq. (7) with $n=1$ and activation energy $U=9.9\pm1.9$ eV, and in favorably oriented grains some dislocation activity was observed. At higher stresses the exponent $n\simeq5-6$ at the same value of the activation energy, and the dislocation activity was supplemented by microcracking, mainly along the (001) cleavage

planes. The measured activation energy may characterize the diffusion of Ca in the 2212 lattice.

High-temperature deformation and fracture of the superconducting phases BSCCO 2201, 2212, and 2223 have been studied in experiments on compression in air at temperatures of 730–835 °C.[194] The kinetics of the steady-state creep is described by Eq. (7) with $n \simeq 3.1-3.8$ and activation energies $U = 5.2 \pm 0.5$ eV (2201), 6.3 ± 2.1 eV (2212), and 9.6 ± 2.1 eV (2223). The value of n is typical of a dislocation-diffusion mechanism of creep. Transmission electron microscopy showed that the deformation of the samples occurred as a result of the simultaneous action of dislocation glide and microcracking. The fracture kinetics was apparently determined by bending of grains due to the motion of basal dislocations. The activation energy of the deformation process increases with increasing complexity of the crystal structure and has a typical value for HTSCs.

Samples of the ceramic $TlBa_2Ca_2Cu_3O_x$ (1223) with densities of $(0.73-0.86)\rho_R$ were tested under compression at a constant rate in the interval $2\times10^{-6}-4\times10^{-5}$ s^{-1} at temperatures of 750–850 °C.[195] The flow stress varied in the range 1–300 MPa. As in the case of the other HTSCs, deformation at the highest temperatures is probably controlled by diffusive viscous flow, while at lower temperatures a dislocation mechanism is dominant, as is evidenced by transmission microscopy of the deformed samples.

In concluding this Section let us mention one other important question for HTSC technology. High-temperature thermomechanical treatment of metal oxides is accompanied on the microscopic level not only by intragrain and grain-boundary dislocation and diffusion processes but also by parallel processes of sintering and growth of grains, recrystallization of the materials, etc. All of these processes are controlled by the diffusion of the least mobile structure components, which in YBCO and BSCCO compounds are the heavy cations Y, Ba, Sr, and Ca. Optimization of the chemical composition and preparation technology of HTSCs requires obtaining information about the diffusion parameters of those particles.[193] The study of high-temperature deformation of HTSCs, which, as a rule, is controlled by diffusion processes, yields valuable information about the cation kinetics.

7. INFLUENCE OF PHASE TRANSFORMATIONS ON THE MICROMECHANICAL PROPERTIES OF HTSCs

7.1. Influence of oxygen stoichiometry and oxygen ordering on the plasticity and fracture of $YBa_2Cu_3O_{7-\delta}$

$YBa_2Cu_3O_{7-\delta}$ crystals have a perovskite-like oxygen-deficient structure, and their physical/mechanical properties are largely determined by the behavior of the oxygen sublattice. In particular, the symmetry of the crystal lattice[196,197] and the elastic,[29] thermal,[198] and electromagnetic[199,200] properties are very sensitive to the oxygen stoichiometry. The oxygen concentration and the distribution of oxygen vacancies in the Cu–O chains influence both the value of the ionic charge of the lattice sites and the density of current carriers and are associated with metal-semiconductor transitions and a variety of transformations in the lattice structure and in the electronic and magnetic subsystems. Accordingly, the superconducting transition temperature T_c is lowered to complete vanishing of the superconductivity. The mechanical characteristics of YBCO (ultimate strength, yield stress, microhardness) are also sensitive to the oxygen content, as has been registered in numerous experiments on polycrystalline and single-crystal samples.[15,22,131,179,200] The resistance to plastic deformation of a crystalline solid at low and medium temperatures depends on the density of mobile dislocations and their velocity. The density of mobile dislocations is controlled by the dislocation nucleation and multiplication processes, and the velocity is determined by the interaction of the dislocations with the crystalline relief, lattice defects, and elementary excitations of the crystal. Since the properties of dislocations are determined by the type of crystal lattice and the values of the interatomic coupling forces, a generalized characteristic of which is provided by the elastic moduli, it is advisable to begin our discussion with the dependence of the structure and elastic moduli of $YBa_2Cu_3O_{7-\delta}$ crystals on the oxygen concentration.

With variation of the oxygen deficit δ in the $YBa_2Cu_3O_{7-\delta}$ system over the interval $1 \geqslant \delta \geqslant 0$ the crystal exhibits a nonsuperconducting tetragonal phase and several superconducting phases with orthorhombic lattices,[44,201–203] the most stable of which are the ortho I phase ($\delta = 0$), with oxygen ordering in the form of Cu–O chains, and the ortho II phase ($\delta = 0.5$), with Cu–O and Cu–Cu chains alternating along the a axis.

The nonsuperconducting tetragonal modification exists for $1 \geqslant \delta > (0.75-0.6)$: the lattice parameters $a = b < c/3$, basal-plane oxygen is either completely absent ($\delta = 1$) or occupies the (1/2,0,0) and (0,1/2,0) positions with equal probability. The ortho I phase, with $T_c \sim 90$ K, can contain a certain number of vacant oxygen sites in the Cu–O chains, and it is realized for $0.15 > \delta > 0$, with lattice parameters $a < b \simeq c/3$. For $0.35 \geqslant \delta \geqslant 0.15$ the ortho I phase is prevalent, but with inclusions of the ortho II phase. The ortho II phase arises for $0.6 > \delta > 0.35$ and can contain inclusions of the ortho I phase or be diluted with vacancies; the lattice parameters in this case obey the inequality $a < b < c/3$, and 40 K $< T_c <$ 60 K.

In the region of temperatures below the temperature of the brittle-plastic limit ($T \leqslant 960$ K) a decrease in oxygen concentration led to plastification of the ceramic and lowering of the ultimate strength.[179] According to the data of Ref. 22, the yield stress of samples of the tetragonal phase is 16% lower than for orthorhombic samples; the development of cracks was prevented by testing under compression at a constant strain rate of 2×10^{-5} s^{-1} at room temperature under a hydrostatic pressure of 0.4 GPa.

The authors of Ref. 15 obtained a lowering of the microhardness of the $YBa_2Cu_3O_{7-\delta}$ single crystals after heating to 500 K and explained this by the escape of oxygen from the sample. A study of the concentration dependence of the microhardness $H_V(\delta)$ of polycrystalline samples at room temperature[133] showed that an increase of δ is accompanied by a decrease in H_V, and the sharpest change of H_V occurs in the interval $0.3 \leqslant \delta \leqslant 0.4$. The data obtained on single crystals of the tetra ($\delta \simeq 0.9$) and ortho ($\delta \simeq 0.1$) phases indicate that the oxygen concentration determines not only the value of the hardness but also the character of its temperature dependence, which is sharper in the tetra phase.[133]

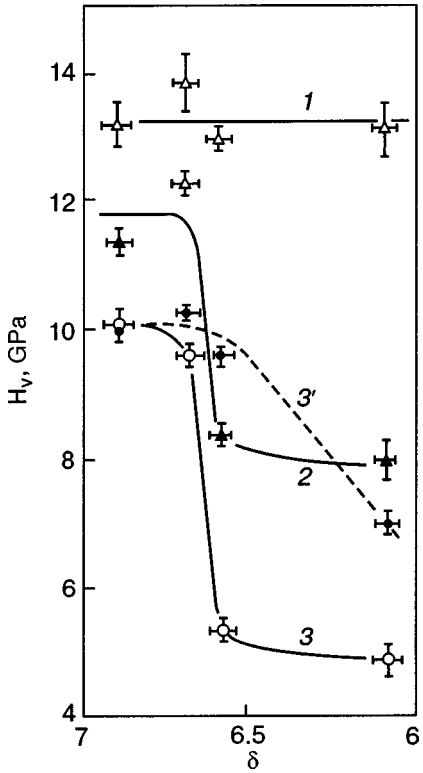

FIG. 23. Concentration dependence of the microhardness of YBCO single crystals at different temperatures [K]: 77 (*1*), 200 (*2*), 292 (*3*); *1,2,3*—crystals of the Y–Pt series; *3′*—crystals of the Y–Al series.[173]

The most detailed study of the dependence of the microhardness of YBCO compounds on the oxygen concentration (in the interval $0.1<\delta<0.9$) and on temperature (in the interval 77–300 K) was done in Ref. 173 on single crystals of two series: Y–Pt and Y–Al (the Al and Pt impurities were introduced into the melt and thence to the lattice from the crucible material). Unfortunately, these impurities had an appreciable influence on the micromechanical characteristics of the crystals (Figs. 15 and 23), which led to some distortions of the effects under discussion here. Figure 23 shows the $H_V(\delta)$ dependence for crystals of the Y–Pt series at three temperatures, 293, 200, and 77 K; it is seen in the figure that the removal of oxygen is accompanied by a decrease of H_V. The circumstance that the dependence $H_V(\delta)$ is strongest at room temperature is in agreement with the data obtained in Ref. 133 in the indentation of crystallites in ceramics: in both cases a sharp softening of the crystals occurred with increasing oxygen deficit in the interval $0.3<\delta<0.4$. In crystals of the Y–Al series the softening effect was also observed, but it was considerably weaker and the drop in $H_V(\delta)$ was shifted to larger δ. Because of the limited set of oxygen concentrations the threshold value of δ at which the drop begins was not established.

The jump in microhardness at an oxygen index $\delta=0.3-0.4$ (Fig. 23) is far removed from the boundary of the tetra phase and more likely corresponds to the region of the ortho I→ortho II transition. Observations of the structure of the samples with polarized optics confirm this conclusion: the ''soft'' crystals may contain twins, which are not characteristic of a tetragonal lattice. Thus the sharp change in H_V should apparently be attributed to a change in the properties of the lattice within the orthorhombic symmetry as a result of the simultaneous ordering of oxygen vacancies.

Ultrasonic measurements on YBCO samples have shown[29] that the elastic shear moduli increase monotonically by an average of 11% with increase of the oxygen concentration, i.e., for a variation $1>\delta>0$. The compressive moduli increase for $1>\delta>0.3$ and then decrease. The elastic constants of $YBa_2Cu_3O_6$ single crystals are on average 15% lower than those of $YBa_2Cu_3O_7$ (Ref. 29), and there are as yet no data at intermediate oxygen concentrations. These results permit the conclusion that the slight and linear variation of the elastic moduli with δ cannot be responsible for the measured dependence of the hardness on the oxygen concentration:[133,173] the effect apparently is of a dislocation nature.

Table II gives the thermal activation parameters of the plastic deformation process near an indenter impression in YBCO crystals with different oxygen concentration. It is seen that increasing δ in the interval $0.1<\delta<0.9$ leads to a decrease in the barrier height and activation volume by a factor of approximately 2.5. The aluminum impurity in Y–Al crystals alters the numerical values of these parameters somewhat but has practically no effect on the character of their dependence on the oxygen concentration.

There can be no doubt that the degree of filling of the oxygen positions in the Cu–O chains in impurity-free crystals has a sensitive influence on the properties of dislocations, including the parameters of the Peierls relief retarding their motion. It can be assumed that impurities of the aluminum type have a significant influence on the mobility of dislocations in the Peierls relief, since at low concentrations such ions substantially alter the oxygen environment of the (0,0,0) sites that are occupied by them and also on the degree of filling of the Cu1 positions and of the apical positions O4 [1204].

We note that the difference in the values of the barriers U_0 for crystals with $\delta=0.4$ and $\delta=0.1$ (Table II) is in qualitative agreement with the dependence of the activation energy of the detwinning process on the oxygen deficit.[16,17] In the latter case this is due to the fact that the motion of twinning dislocations in the YBCO lattice is associated with the diffusive motion of the chain oxygen in the twinning plane (110) in the direction counter to the direction of the twin shear; consequently, the activation energy for the motion of twin boundaries should correspond to the activation energy for oxygen diffusion and should vary in accordance with the change in concentration of the oxygen vacancies (or of the oxygen index).[16,17] The interrelation of twinning and slip can be examined only by analyzing the results of measurements on crystals of the ortho phase.

7.2. Influence of the tetra-ortho transition on the microhardness of $La_{1.85}Sr_{0.15}CuO_4$ crystals

The compound La_2CuO_4 is known to have two polymorphic modifications: high-temperature tetragonal $I4/mmm$, and low-temperature orthorhombic $Cmca$; the transition between them occurs at a temperature $T_{TO}\simeq 533$ K.[35] Substitution of La and Cu by some other cations leads to a lowering of the transition temperature and to a change in other physical properties of this compound: for example, partial

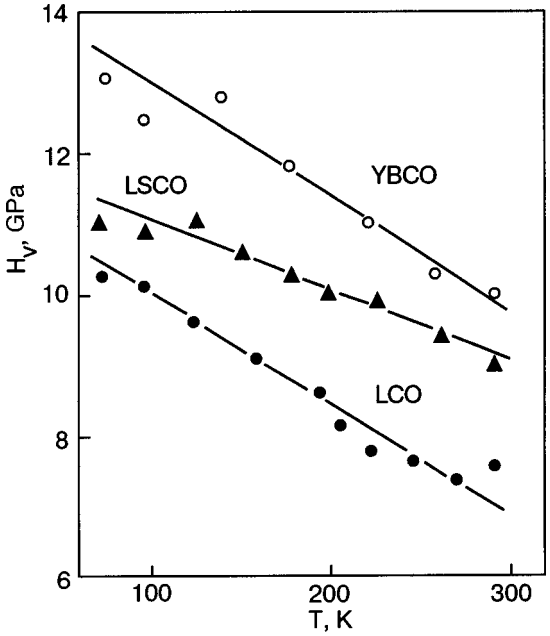

FIG. 24. Temperature dependence of the microhardness of single crystals of YBCO ($\delta \simeq 0.1$), La_2CuO_4, and $La_{1.85}Sr_{0.15}CuO_4$ (Ref. 18).

substitution of lanthanum by strontium ($La_{1.85}Sr_{0.15}O_4$) leads to values $T_{TO} \simeq 180$ and $T_c = 39.5$ K. It is of interest to ascertain the physical/mechanical properties of the tetra and ortho phases of this superconductor in the vicinity of the phase transition. The elastic moduli of the compound LSCO near the temperature T_{TO} has been studied in detail in a number of theoretical[205,206] and experimental[83,207] papers. Analysis of the $I4/mmm \rightarrow Cmca$ transition in Ref. 205 permitted calculation of the relative jumps of the elastic moduli starting from the values of the crystal lattice parameters. The absolute values of the moduli and their change at the phase transition have been measured experimentally for $x = 0.13$ (Ref. 83) and $x = 0.14$ (Ref. 207) on $La_{2-x}Sr_xCuO_4$ single crystals. Among the important conclusions that can be drawn is that the elastic constant C_{44} remains practically unchanged at the soft-mode tetra→ortho transition, while at the same time some other elastic constants decrease rather strongly, in particular the constant C_{66} decreases by more than 50% (Ref. 83).

As is seen in Fig. 24, the temperature dependence of the microhardness of $La_{2-x}Sr_xCuO_4$ ($x = 0.15$) crystals does not exhibit any features in the vicinity of the structural phase transition.[18] One can present several arguments as to the cause of this behavior of the microhardness, taking into account that the change in the plasticity and the elastic properties at the phase transition must be reconciled. For crystals of the LSCO family, like those of the YBCO family, there are typically two modes of deformation: twinning and slip. There is no information in the literature as to the twinning of the tetragonal modification of LSCO, but it can very easily take place in the ortho phase along two systems: $(110) \times [1\bar{1}0]$ and $(1\bar{1}0)[110]$. In view of the small value of the twin shear the deformation caused by it does not exceed 1.7% upon a complete twin reversal of the sample; consequently, the significant deformations ~7% near an indenter impression are mainly due to slip. The slip systems and the types and structure of the dislocations in LSCO are not yet known, but it was noted in Ref. 208 that an insignificant density of growth dislocations is observed in La_2CuO_4 crystals. By analogy with YBCO one can assume that the slip plane in LSCO crystals is the (001) basal plane, and the Burgers vector has the direction $\langle 100 \rangle$. This means that the elastic properties of dislocations and their mobility correlate with the elastic constant C_{44}, which, as was mentioned above, remains practically unchanged at the tetra→ortho structural transition.

7.3. Influence of the superconducting transition on the kinetics of microcreep of HTSCs

One of the most striking effects in the low-temperature physics of plasticity is the plastification (softening) of a metal at its transition to the superconducting state.[209,210] This effect has been registered in many conventional low-temperature superconductors. It is manifested in the stage of well-developed plastic deformation both in testing by the active deformation method and under conditions of creep. The change of state of the superconductor can also lead to a change in the kinetics of plastic flow—a transition from jumplike to smooth deformation.[211] It has been established that this effect is manifested most vividly in plastic fcc metals (lead, indium), for which the jump in the flow stress $\Delta\sigma_{NS}$ at the transition from the normal (N) to the superconducting (S) state reaches a relative value ~10%; in the case of the less plastic bcc metals (niobium) $\Delta\sigma_{NS}$ has a value ~1%. Taking a metal from the N to the S state in the process of creep can lead to an extremely significant increase in the creep rate: $\dot{\varepsilon}_S/\dot{\varepsilon}_N \sim 10-10^2$. In observations of this effect the superconducting transition is usually brought about by cooling to temperatures $T < T_c$ or, at a constant temperature $T < T_c$, by switching off and on a magnetic field $H > H_c$ (or, in individual cases, a current $j > j_c$).

At the present time it is thought that the main reason for the increase in plasticity at the transition of a metal from the normal to the superconducting state is a decrease in the electron drag force on dislocations as a result of the Cooper condensation of conduction electrons.[209,210]

Immediately after the discovery of high-temperature superconductivity, attempts were made to observe the softening effect at the $N-S$ transition in this new class of superconductors.[20,126,131,212–214] Various methods of mechanical testing were used: in Refs. 126, 131, and 212 the influence of temperature on the microhardness of single-crystal and polycrystalline HTSCs was studied in attempts to reveal features on the temperature dependence of the microhardness $H_V(T)$ near T_c; in Refs. 20, 21, and 213 the $N-S$ transition was brought about by turning a supercritical current on and off during microcreep of a $YBa_2Cu_3O_{7-\delta}$ ceramic, and a laser interferometer was used to register the deformation; in Ref. 214 the $N-S$ transition was also brought about by a current during testing by the creep method, but with the use of standard methods to register the deformation. The main results of the experiments listed have been summarized in Refs. 126 and 214.

Although attempts to detect this effect were undertaken in the study of the temperature dependence of the microhardness of HTSCs near T_c on single crystals, highly aligned

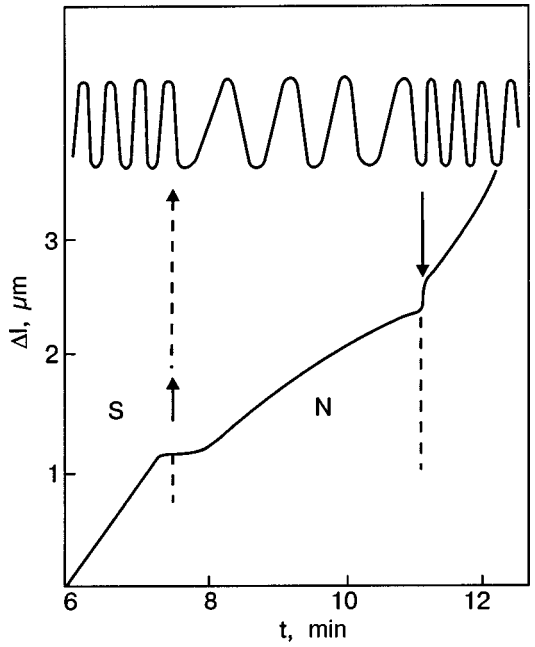

FIG. 25. Interferogram (upper) and a part of the creep curve of polycrystalline YBCO calculated from it for 77 K and $\sigma = 12$ MPa. Each oscillation on the interferogram corresponds to a change in the length of the sample by 0.3 μm. The arrows indicate the times at which a current $j = 25$ A/cm^2 was turned on and off.[19]

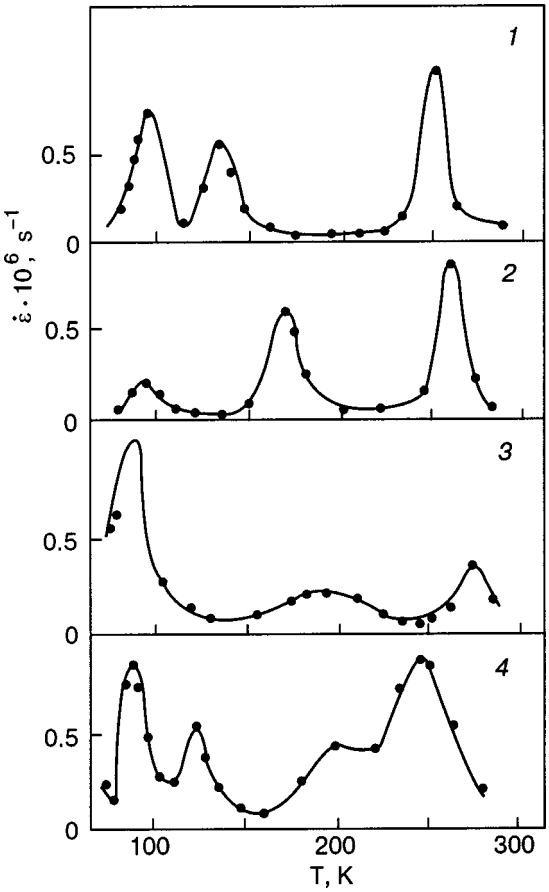

FIG. 26. Spectra of the rates of inelastic deformation in compression of a YBCO polycrystal. The applied stress $\sigma = 10$ MPa. Fine-grained sample with grain size $d = 1-3$ μm (*1*); single-phase large-grained samples with density $\rho = 5.5$ g/cm^3 (*2*) and $\rho = 5.8$ g/cm^3 (*3*); multiphase large-grained sample with grain size $d = 10-30$ μm (*4*, Ref. 20).

samples, and polycrystals of various density,[131,157,212] anomalies like those observed previously on conventional superconductors, i.e., an increase in the plastic compliance upon transition to the region $T < T_c$,[209,210] were not found for any of the Y-HTSCs (see, e.g., Figs. 14, 15, 18, and 19) or Bi-HTSCs (see Fig. 21). The authors attribute this to insufficient accuracy of the method used (the large scatter in the microhardness values) and to the small relative value of the effect in the case of the brittle, relatively aplastic metal oxide HTSCs.

In Refs. 19–21 and 213 the inelastic deformation of HTSC ceramics in the normal and superconducting states was studied by the microcreep method. The superconductivity was destroyed by passing a current $j > j_c$ (at 77 K the critical current density $j_c \simeq 15-25$ A/cm^2), and the deformation was recorded by a technique based on a laser interferometer, which permitted making precision measurements of the deformation rate. Upon passage of a current $j > j_c$ the interferogram always showed a slowing or stopping of the deformation (Fig. 25). A change in the microplastic deformation rate by a factor of 2–8 upon a change of state of a $YBa_2Cu_3O_{7-\delta}$ superconducting ceramic was also observed in Ref. 214. These observations can be regarded as weak manifestations of the plastification effect at an $N-S$ transition, and the authors of Ref. 19 believe that they are due to the easier motion of twin boundaries under conditions of decreased electron drag.

Figure 26 shows typical spectra of the inelastic deformation rates of the yttrium ceramics $YBa_2Cu_3O_{7-\delta}$ (Ref. 20): one for a fine-grained ceramic with a grain size of 1–3 μm (curve *1*); another for a multiphase coarse-grained ceramic with a grain size of 10–30 μm (curve *4*); two spectra (curves *2* and *3*) for single-phase coarse-grained samples from different batches. Curves *2* and *3* attest to the fact that for samples with the same value of T_c and somewhat different density (5.5 g/cm^3 for sample *2* and 5.8 g/cm^3 for sample *3*) there are large differences between the deformation rates at the maxima, whereas the temperatures of the maxima are practically identical. It is seen in Fig. 26 that of the three peaks present in all the spectra, the one with the highest stability in temperature is the peak at $T_{\max 1} \simeq 90$ K, which lies close to T_c. This peak was explained in Ref. 20 by an increase in the mobility of dislocations at the transition to the superconducting state, in analogy with the ideas developed for low-temperature superconductors.[209,210]

It is now known that the temperature dependence of different characteristics of high-temperature superconductors have anomalies near T_c (the Young's modulus, damping decrement, linear expansion coefficient). The authors of Ref. 20 believe that these effects are of the same nature as those observed in their study, viz., that the anomalies are caused by microplastic deformation occurring in places where high local shear stresses are acting.

Despite the encouraging results of Refs. 19–21, 213, and 214, an unambiguous answer as to the nature of the microplastic deformation of ceramics and to the influence of the superconducting transition on the plasticity of HTSCs has not been obtained. The main complications encountered by researchers are due primarily to the significant difference in both the electronic and mechanical properties of HTSCs

from those of ordinary low-temperature superconductors. In Refs. 19–21, 213, and 214 the superconductivity of HTSC ceramics was destroyed by passing a current of critical density through the sample. However, as was noted in Refs. 214 and 215 the state of the superconductor that arises in that case is not, strictly speaking, normal, and it would be more accurate to speak of a complex resistive state: at the current densities used, the superconductivity was destroyed only in the system of intergrain Josephson contacts,[215,216] while the grains themselves remained superconducting. The plasticity of metal oxide HTSCs and the observed value of the plastification effect at the $N-S$ transition in them turned out to be many times smaller than for ordinary metallic superconductors. A definitive answer to this question will require further studies, preferably on single crystals. Since the plastification effect at an $N-S$ transition increases with increasing density of mobile dislocations, it may be more promising in this regard to use the more plastic Bi-containing HTSCs.

8. MECHANICAL PROPERTIES OF HTSC COMPOSITES AND MIXTURES

To meet the demand for HTSC materials with suitable electrophysical, superconducting, and mechanical characteristics, attention has focused primarily on metal–ceramic composites. An enormous number of publications have been devoted to various topics in the problem of HTSC composites. It should be noted that modern technology is capable of producing bulk YBCO and Bi-2223 superconductors with high critical current density, up to 10^5 A/cm^2 at 77 K in a magnetic field of up to 1 T, and of manufacturing long multistrand cables with a critical current above 2 kA.[217–222] In this Section we discuss the mechanical properties of HTSC composites, as these are the decisive factor in their application, especially in the production of flexible cables and ribbons.

The main progress in improving the mechanical properties of HTSC materials (strength, plasticity, and fracture toughness) has been achieved through the use of heterophase structures and the introduction into the superconductor of particles of other compounds that do not degrade the electrical properties, e.g., particles of Ag, ZrO_2, or HfO_2. In the case of Y123 it has been shown that a substantial increase in strength and fracture toughness of a ceramic is obtained through the joint use of Ag and ZrO_2.

The introduction of particles of the oxide ZrO_2 into Y123 was done after the particles had first been coated with a protective layer of the Y211 phase, which has a higher melting temperature and prevents the undesirable reactions of ZrO_2 particles with the superconducting phase Y123 during sintering of the ceramic.[223] The introduction of 20 mol. % ZrO_2 made it possible to prepare a composite with fracture toughness $K_{1c}=4.5$ MPa$\cdot$m$^{1/2}$, which is almost 4 times higher than the value of K_{1c} for pure ceramic Y123. Here the strength remained at the previous level of 60 MPa, even though the density of the composite became smaller by 9%. The improvement of the mechanical characteristics for the YBCO$+x$$ZrO_2$ was attributed by the authors of Refs. 223 and 226 to the presence of a Zr-enriched phase on the surface of the YBCO granules and in the intergranular space.

Improvement of the elastic and strength properties of ceramic YBCO has also been achieved by the admixture of the oxide HfO_2 to the system.[224,225] The threefold increase in the microhardness of the YBCO$+x$$HfO_2$ system was explained by the presence of the $HfBaCuO_4$ phase.

The mechanical properties of HTSC/Ag composites extant in 1993 were partially reviewed in Ref. 227. Some of the information contained there and also more-recent results are discussed below.

Silver is present in composites both in the form of metal particles and as impurities of the Y123 lattice, which substitute for a small number of the copper ions.[228–230] The beneficial influence of silver particles is due to the high plasticity of silver and to the favorable distribution of internal stresses in a composite in which the Y123 phase is under compressive stresses and the plastic silver is in a state of tension.[231] The admixture of silver decreases the density of voids, increases the resistance to crack propagation, blunts the tips of the cracks, and suppresses their development. Silver increases the stability of a composite in a surrounding medium. We note that silver in composites predominantly occupies the space between grains and noticeably improves the intergrain contacts, leading to a sharp drop in the resistivity of samples even at extremely low Ag concentrations. These composites remain high-temperature superconductors even at large silver fractions of the order of 50–60%.

A detailed study of the mechanical properties of $YBa_2Cu_3Ag_xO_{7-y}$ composites upon variations of the silver content in the interval $x=0-1.5$ has shown[232] that the optimum value is $x=0.3$, at which an almost twofold increase in strength (to 230 MPa) is achieved, while the microhardness and fracture toughness are increased by almost 40%. Nonmonotonic dependence of the mechanical characteristics on the silver concentration is attributed by the authors of Refs. 232 and 233 to an appreciable influence of Ag on the sinterability of the ceramic; as x increases to 0.3 the porosity decreases, and the silver is uniformly distributed along the grain boundaries, filling the voids, which is accompanied by improvement of the strength characteristics of the ceramic; with further increase in x ($x=0.6$ and $x=1.5$) the silver balls come together more often and become larger. The admixture of silver cleaned the grain boundaries and increased the structural and chemical stability of the composite. Meanwhile, the difference in the coefficients of thermal expansion of Ag and YBCO can lead to the formation of voids around the silver balls and decrease the strength, hardness, and fracture toughness.[232]

A significant increase in the fracture toughness of a Y123/Ag composite with a silver fraction of 30 wt. % was registered in Ref. 234 (to 2.5 MPa$\cdot$m$^{1/2}$ at room temperature on notched samples). Better strength characteristics were obtained in Ref. 235 for a composite with a silver content of 20–25 wt. %.

In Ref. 236 the mechanical properties of a $YBa_2Cu_3O_{7-\delta}$–40 wt. % Ag composite were investigated over a very wide temperature interval 77–900 K. An increase of up to 50% in the compressive strength in comparison with a pure YBCO ceramic was found. The main difference of this composite, however, was its higher plasticity characteristics: the deformation to fracture amounted to 4–5% at tem-

peratures in the interval 300–900 K, whereas ordinary YBCO ceramics suffer brittle fracture under those conditions.

In grain-oriented YBCO/Ag the silver particles are located both between and inside grains, ensuring high mechanical properties of the composite in comparison with stoichiometric Y123 samples.[228] In particular, the presence of silver in the microstructure strongly decreased the macroscopic cracking, and such samples are difficult to cleave along the (001) cleavage planes.

In Ref. 237 special studies were made of the microstructure, strength, and deformability under compression of ceramics make from $YBa_2Cu_3O_{7-x}$ and Ag_2O powders by powder metallurgy technology, including extrusion. It was shown that the high strength (200 MPa) and plasticity (deformation to fracture greater than 5%) of samples containing 60 vol. % silver oxide, are due to metallization of Ag_2O particles as a result of the partial decomposition of the oxide, which led to the formation of a well-developed metallic layer at the YBCO–Ag_2O interphase boundaries. In the process of extrusion the plastic deformation occurs not only at the metallized grain boundaries but also in the grains of the ceramic. An appreciable fraction of the dislocations formed in the YBCO grains remained after a subsequent annealing of the composite in oxygen, which gave rise to efficient pinning centers in the volume of the superconducting grains. After annealing in oxygen, the extruded wire exhibited a sharp superconducting transition starting at 91 K and reaching zero resistance at 82 K.

The addition of small amounts (less than 5 vol. %) silver to a YBCO ceramic was found to have a detrimental effect on its mechanical properties,[238] which was believed to be due to the formation of large voids and dense domains during the sintering of the ceramic as a result of the localization of the liquid phase around the silver inclusions. With increasing volume fraction of silver the fracture toughness was observed to increase:[239] in a composite with 18 vol. % Ag the coefficient K_{1c}, measured from the length of the crack around an indenter impression, was 2.5 times higher than in pure YBCO. Microstructural studies showed that the main mechanism of increase in fracture toughness is the shunting of microcracks by the plastic silver particles. In both pure YBCO and YBCO/Ag composites, the dependence of H_V on the porosity is described by relation (4). However, the microhardness of the composite is significantly lower and less sensitive to internal defects.

In Refs. 240 and 241 the structure, acoustic, resistive, and magnetic properties of a Y123/Ag composite were studied over a wide interval of silver concentrations (0–100 vol. %). Analysis of the x-ray data and of the behavior of the structure-sensitive peak of the ultrasonic absorption showed that in the technologically important region of concentrations below 20 vol. % Ag the HTSC phase Y123 does not undergo any substantial changes. It was found that the formation of intergrain silver layers of various thickness largely determines the variation of the critical parameters and the elastic and relaxation properties of granular composites.

Composite ceramics Y123/Ag and Sm123/Ag with improved mechanical properties were prepared in Ref. 242. Grain-oriented Sm123/Ag containing an admixture of up to 20 wt. % Ag_2O have the high mechanical strength necessary for their use as permanent magnets.[243] As a result, the trapped field reached values of 2.1 T at 77 K and 9 T at 25 K; the maximum value of the trapped field was limited by fracture of the composite.

With the goal of improving the properties of HTSC ceramics the method of reinforcing them with filaments of another material, which was developed for ordinary ceramic construction materials. Silver was chosen as the metal for reinforcing the ceramic for the following reasons:[244] 1) the reserve of plasticity of silver is not less than 50%; 2) silver has a higher coefficient of thermal expansion, of the order of 2×10^{-5} deg^{-1} in the temperature interval 0–500 °C, which is important for prevention of cracking in the high-temperature processing of the composite; 3) silver has high thermal and electrical conductivity; 4) silver is paramagnetic.

In Ref. 244 the composite Y123/Ag was prepared with the use of a powder and silver filaments 0.5 mm in diameter and 35–55 mm long, uniformly distributed over the single crystal of the sample and oriented along its axis. The composite samples had high strength characteristics at 77 K in testing by the three-point bending method.

In Ref. 245 a comparative study of the physical/mechanical properties of Y123 samples reinforced with silver filaments (the filaments were 50 μm in diameter and 10 mm long, the volume fraction of silver was 0, 5, 8, 12, and 15%) and prepared by the usual sintering technology (first series of samples) and by the method of hot isostatic pressing—HIP (second series of samples). The second method gave substantially better results without degradation of the superconducting properties: the porosity of the samples of the first series increased linearly from 17% to 27% with increasing volume fraction of silver, whereas all the samples of the second series had a density of 92–96% of the x-ray value. The strength and fracture toughness of these conditions were determined in deformation by three-point bending of samples of rectangular cross section. The strength decreased linearly with increasing volume fraction of silver: from 34.3 ± 6 MPa to 21.7 ± 6.2 Mpa for the first series, and from 56.2 ± 7.3 MPa to 50.4 ± 4.2 MPa for the second series. However, the samples after HIP exhibited an increase of K_{1c} by almost a factor of four, from 1.2 ± 0.3 MPa$\cdot$m$^{1/2}$ to 4.5 ± 0.3 MPa$\cdot$m$^{1/2}$, whereas for the samples of the first series the increase was only by a factor of 1.5, from 0.8 ± 0.3 MPa$\cdot$m$^{1/2}$ to 1.23 ± 0.3 MPa$\cdot$m$^{1/2}$. The more complicated HIP technique in combination with laser annealing led to high mechanical properties of the Y123 composite reinforced with silver filaments, but the small grain size and large number of grain boundaries limit the possibility of increasing the critical current.

Substantial improvement in the physical/mechanical properties of HTSCs based on BSCCO has been achieved in BSCCO/Ag composites. Synthesis of $Bi_{1.5}Pb_{0.4}Sr_2Ca_2Cu_3O_x$/Ag composites by the admixture of Ag in the form of particles, whiskers, and wires has shown[146] that the addition of silver improves the growth of the grains of Bi-2223 and decreases the porosity of the samples; the composites have higher strength and compliance in testing by the three-point bending method. The fracture of the composites was of a brittle character. The dependence of the

strength σ_f on the porosity p of the composite containing 30 vol.% Ag (particles) was described by relation (4): $\sigma_f = 130\exp(-3.5p)$, with values varying from 55 MPa at $p = 0.25$ to 10 MPa at $p = 0.65$. The microhardness of this composite was lower than that of single-crystal BSCCO 2223: 460 ± 60 MPa as against 600 ± 70 MPa. Composites containing whiskers had greater strength and plasticity than those made with particles, but the best components turned out to be those made with long silver wires, owing to the high relative elongation of the wires.

BSCCO 2223/Ag composites were subjected to different modes of mechanical testing: bending, compression, tension, fatigue.[247,248] Cyclic deformation at 77 K between limits of -0.18% and 0.25% did not lead to noticeable degradation of the current-carrying properties of ribbons, which attests to the possible of their practical application.[248] It was found that a simple and reliable method of controlling the quality of ribbons and wires of BSCCO/Ag and for determining the optimal technical parameters of their fabrication was measurement of the microhardness,[249] as this quantity is sensitive to the density of the matrix, which has a strong influence on the critical current density.

By reinforcing the ceramic matrix of BPSCCO 2223 with fibers of Al_2O_3, which have high strength, one can obtain composites characterized by high toughness, strength, and fracture toughness at both room and nitrogen temperature.[250] Tests of samples with a notch in the three-point bending scheme gave the values $K_{1c} \simeq 6$ MPa$\cdot$m$^{1/2}$ at 77 K and $K_{1c} \simeq 3.5$ MPa$\cdot$m$^{1/2}$ at 293 K, whereas for the monolithic 2223 ceramic $K_{1c} < 1$ MPa$\cdot$m$^{1/2}$.

The preparation of BSCCO/Ag composites in the form of ribbons and wires involves various forms of thermomechanical treatment of silver tubes filled with a HTSC powder. This gives a high degree of grain orientation (texture), high density, good intergrain coupling, and a definite phase ratio 2223/2212, which in the final analysis makes for high critical current density.[219,251]

Thus a fortunate combination of coefficients of thermal expansion of structural elements, the structure and properties of the interfacial boundaries between granules and grains, the morphology and amount of fillers leads to stronger and tougher HTSC composite materials needed for making manufactured items and elements of devices of superconducting technology.

CONCLUSION

In fifteen years of intense study of the phyical/mechanical properties of metal oxide HTSCs, a vast and diverse body of information has been accumulated in this field, making it possible to develop new and more efficient technological methods of synthesis of materials of this type with the optimal combination of electrophysical, superconducting, and mechanical characteristics necessary for their practical application. In this review we have set forth a systematic and unified point of view on research results on the plasticity and strength of metal oxide crystals and ceramics under various modes of mechanical testing at low, room, and high temperatures.

The approach to the discussion of the mechanical properties of metal oxides in this and in our earlier review[29] is to view the problem with the eyes of specialists in the physics of plasticity and strength and attempt to discuss the main aspects of this problem in the framework of modern ideas of the structure, dynamics, and kinetics of various defects of the crystal structure as elementary ''carriers'' of inelastic deformation and fracture. Thus our reviews are aimed mainly toward workers in the field of the physics of plasticity and strength of solids. At the same time, we recognize that these reviews will also be useful for specialists in the fields of physical materials science and the technology of creating new materials, workers whose interests lie in the area where the basic science of materials and the engineering development work aimed at their practical application come together. Finally, as necessary they should help give specialists in the physics of superconductivity and electrophysical processes at least a rough idea of the crystal-physical, materials science, and technological sides of the problem of high-T_c superconductivity.

This review was submitted for publication on the eve of a significant date for the authors: November 27, 2003, the 90th anniversary of the birth of Prof. Valerian Ivanovich Startsev, a notable scientist and engineer of Ukraine, one of those researchers of the second half of the twentieth century whose works laid the foundation and fostered the development of the modern physics of plasticity and strength of solids at low temperatures. Part of his legacy is a large and efficiently operating scientific school to which the authors of this review belong. As a tribute to this outstanding scientist and human being, we dedicate this review to the glowing memory of Prof. V. I. Startsev.

*E-mail: lubenets@ilt.kharkov.ua

[1] J. G. Bednorz and K. A. Müller, Z. Phys. B **64**, 189 (1986).
[2] R. J. Cava, R. B. van Dover, B. Batlogg, and E. A. Rietman, Phys. Rev. Lett. **58**, 408 (1987).
[3] M. K. Wu, J. R. Ashburn, C. J. Torng, P. H. Hor, R. L. Meng, L. Gao, Z. J. Huang, Y. Q. Wang, and C. W. Chu, Phys. Rev. Lett. **58**, 908 (1987).
[4] H. Maeda, Y. Tanaka, M. Fukutomi, and T. Asano, Jpn. J. Appl. Phys. **27**, pt. 2 L209 (1988).
[5] S. S. Parkin, V. Y. Lee, E. M. Engler, A. I. Nazzal, T. C. Huang, G. Gorman, R. Savoy, and R. Beyers, Phys. Rev. Lett. **60**, 2539 (1988).
[6] A. Schilling, M. Cantoni, J. D. Guo, and H. R. Ott, Nature (London) **363**, 56 (1993); L. Gao, Y. Y. Xue, F. Chen, R. L. Meng, D. Ramirez, and C. W. Chu, Phys. Rev. B **50**, 4260 (1994).
[7] J. Nagamatsu, N. Nakagawa, T. Muranaka, Y. Zenitani, and J. Akimitsu, Nature (London) **410**, 63 (2001).
[8] A. F. Hebard, M. J. Rosseinsky, R. C. Haddon, D. W. Murphy, S. H. Glarum, T. T. M. Palstra, A. P. Ramirez, and A. R. Kortan, Nature (London) **350**, 600 (1991).
[9] J. H. Schon, Ch. Kloc, and B. Batlogg, Nature (London) **408**, 549 (2000).
[10] J. H. Schon, Ch. Kloc, and B. Batlogg, Science **293**, 2432 (2001).
[11] Z. K. Tang, L. Zhang, N. Wang, X. X. Zhang, G. H. Wen, G. D. Li, J. N. Wang, C. T. Chan, and P. Sheng, Science **292**, 2462 (2001).
[12] R. F. Cook, T. R. Dinger, and D. R. Clarke, Appl. Phys. Lett. **51**, 454 (1987).
[13] V. V. Demirskiĭ, H.-J. Kaufmann, S. V. Lubenets, V. D. Natsik, and L. S. Fomenko, Fiz. Tverd. Tela (Leningrad) **31**, 263 (1989) [Sov. Phys. Solid State **31**, 1065 (1989)].
[14] V. V. Demirskiĭ, S. V. Lubenets, V. D. Natsik, M. N. Sorin, L. S. Fomenko, and N. M. Chaĭkovskaya, Sverkhprovodimost' (KIAE) **3**(1), 84 (1990) [Superconductivity **3**, 80 (1990)].
[15] V. S. Bobrov, V. K. Vlasko-Vlasov, G. A. Emel'chenko, M. V. Indenbom, M. A. Lebedkin, Yu. A. Osip'yan, V. A. Tatarchenko, and B. Ya. Farber, Fiz. Tverd. Tela (Leningrad) **31**, 93 (1989) [Sov. Phys. Solid State **31**, 597 (1989)].

[16]L. A. Dorosinskiĭ, M. V. Indenbom, V. I. Nikitenko, and B. Ya. Farber, JETP Lett. **49**, 182 (1989).
[17]V. I. Nikitenko, L. A. Dorosinskii, A. A. Polyanskii, and V. K. Vlasko-Vlasov, in *Dislocations 93, Microstructures and Physical Properties*, Vols. 35–36 of Solid State Phenomena, edited by J. Rabier, A. George, Y. Brechet, and L. Kubin, Scitec Publications (1994), p. 587.
[18]L. S. Fomenko, S. V. Lubenets, V. S. Bobrov, and A. N. Izotov, Fiz. Tverd. Tela (St. Petersburg) **40**, 493 (1998) [Phys. Solid State **40**, 453 (1998)].
[19]N. N. Peschanskaya, B. I. Smirnov, V. V. Shpeĭzman, and P. N. Yakushev, Fiz. Tverd. Tela (Leningrad) **30**, 3503 (1988) [Sov. Phys. Solid State **30**, 2014 (1988)].
[20]N. N. Peschanskaya, B. I. Smirnov, Yu. P. Stepanov, V. V. Shpeĭzman, and P. N. Yakushev, Fiz. Tverd. Tela (Leningrad) **31**, 271 (1989) [Sov. Phys. Solid State **31**, 703 (1989)].
[21]V. P. Soldatov and N. M. Chaĭkovskaya, Fiz. Nizk. Temp. **19**, 1260 (1993) [Low Temp. Phys. **19**, 896 (1993)].
[22]J. Rabier and M. F. Denanot, Less Common Metals **164–165**, 223 (1990).
[23]O. A. Kaĭbyshev, R. M. Imaev, M. F. Imaev, and F. F. Musin, in *Proceedings of the First All-Union Conference on Physicochemistry and Technology of High-Temperature Superconducting Materials* [in Russian], Nauka, Moscow (1989), p. 248.
[24]O. A. Kaĭbyshev, R. M. Imaev, and M. F. Imaev, Dokl. Akad. Nauk SSSR **305**, 1120 (1992).
[25]M. F. Imaev, F. F. Musin, R. O. Kaĭbyshev, and M. R. Shagiev, Dokl. Ross. Akad. Nauk **338**, 184 (1994) [Phys. Dokl. **39**, 639 (1994)].
[26]V. N. Kuznetsov, V. I. Shalaev, V. V. Sagaradze, E. V. Dus'e, V. L. Arbuzov, A. E. Davletshin, V. R. Poskrebysheva, and S. M. Cheshnitskii, Sverkhprovodimost' (KIAE) **5**, 1939 (1992) [Superconductivity **5**, 1850 (1992)].
[27]K. C. Goretta, E. J. Zamirowski, J. M. Calderon-Moreno, D. J. Miller, Nan Chen, T. G. Holesinger, and J. L. Routbort, J. Mater. Res. **9**, 541 (1994).
[28]J. L. Routbort, D. J. Miller, E. J. Zamirowski, and K. C. Goretta, Supercond. Sci. Technol. **6**, 337 (1993).
[29]S. V. Lubenets, V. D. Natsik, and L. S. Fomenko, Fiz. Nizk. Temp. **21**, 475 (1995) [Low Temp. Phys. **21**, 367 (1995)].
[30]I. N. Khlyustikov and A. I. Buzdin, Usp. Fiz. Nauk **155**, 47 (1988) [Sov. Phys. Usp. **31**, 409 (1988)].
[31]V. L. Indenbom, JETP Lett. **46**, Suppl. S102 (1987).
[32]Yu. A. Osip'yan, N. S. Afonnikova, D. E. Batova, V. A. Goncharov, G. A. Emel'chenko, M. V. Indenbom, É. V. Suvorov, V. Sh. Shekhtman, and I. M. Shmyt'ko, Fiz. Tverd. Tela (Leningrad) **31**(3), 131 (1989) [Sov. Phys. Solid State **31**, 423 (1989)].
[33]K. Yvon and M. Francois, Z. Phys. B **76**, 413 (1989).
[34]O. V. Frank-Kamenetskaya, T. N. Kaminskaya, A. V. Nardov, and T. I. Ivanova, in *High-Temperature Superconductivity: Basic and Applied Research* [in Russian], edited by A. A. Kiselev, Mashinostroenie, Leningrad (1990), issue 1, p. 190.
[35]G. P. Shveĭkin, V. A. Gubanov, A. A. Fotiev, G. V. Bazuev, and A. A. Evdokimov, *Electronic Structure and Physico-Chemical Properties of High-Temperature Superconductors* [in Russian], Nauka, Moscow (1990).
[36]Yu.É. Kitaev, M. F. Limonov, A. P. Mirgorodskiĭ, A. G. Panfilov, and R. A. Évarestov, Fiz. Tverd. Tela (St. Petersburg) **36**, 865 (1994) [Phys. Solid State **36**, 475 (1994)].
[37]G. Yu. Bochkova and V. A. Voloshin, *Reviews of High-Temperature Superconductivity* [in Russian], issue 3 (1990), p. 36.
[38]V. A. Finkel', *High-Temperature Superconductivity: Materials Science, Technology, Application* [in Russian], ISDO, Kiev (1993).
[39]J. P. Zhou, C. C. Sorrell, S. X. Dou, and A. J. Bourdillon, Aust. J. Phys. **42**, 419 (1989).
[40]J. Rabier and M. F. Denanot, Philos. Mag. A **65**, 427 (1992).
[41]J. Rabier and M. F. Denanot, Rev. Phys. Appl. **25**, 55 (1990).
[42]M. J. Kramer, L. S. Chumbley, R. W. McCallum, W. J. Nellis, S. Weir, and E. P. Kvam, Physica C **166**, 115 (1990).
[43]F. Sandiumenge, V. Vilalta, J. Rabier, and X. Obradors, Physica C **372-376**, 1204 (2002).
[44]T. Joshida, K. Kuroda, and H. Saka, Philos. Mag. A **62**, 573 (1990).
[45]M. Verwerft, D. H. Dijken, Th. M. De Hosson, and A. C. Van Dersteen, Phys. Rev. B **50**, 3271 (1994); Ultramicroscopy **56**, 135 (1994).
[46]I. S. Smirnova, Phys. Status Solidi A **116**, 237 (1989).
[47]Z.-Q. Li, H. Shen, Y. Qin, J.-Y. Jiang, and J.-J. Du, Philos. Mag. Lett. **60**, 123 (1989).
[48]Yu. A. Osip'yan, N. S. Afonnikova, G. A. Emel'chenko, T. K. Parsamyan, I. M. Shmyt'ko, and V. Sh. Shekhtman, JETP Lett. **46**, 241 (1987).
[49]H. W. Zandbergen, G. van Tendeloo, T. Okabe, and S. Amelinckx, Phys. Status Solidi A **103**, 45 (1987).
[50]M. Hervieu, B. Domenges, C. Michel, G. Heger, J. Provost, and B. Raveau, Phys. Rev. B **36**, 3920 (1987).
[51]V. S. Boĭko, A. M. Kosevich, and Yu. A. Kosevich, Fiz. Nizk. Temp. **17**, 3 (1991) [Sov. J. Low Temp. Phys. **17**, 1 (1991)].
[52]V. S. Boĭko, R. I. Garber, and A. M. Kosevich, *Reversible Plasticity of Crystals* [in Russian], Nauka, Moscow (1991).
[53]H. M. Zandbergen, R. Gronsky, M. Y. Chu, L. C. DeJohnge, G. F. Holland, and A. Stacy, Physica C **166**, 255 (1990).
[54]C. Boulesteix and M. Ben Salem, J. Less-Common Met. **156**, 29 (1989).
[55]E. D. Specht, C. J. Sparks, A. G. Bhere, J. Brynestd, O. B. Cavin, and D. M. Kroeger, Phys. Rev. B **37**, 7426 (1988).
[56]V. I. Simonov, V. N. Molchanov, and B. K. Vaĭnshteĭn, JETP Lett. **46**, 253 (1987).
[57]D. Shi, Physica C **156**, 359 (1988).
[58]V. G. Pushin, V. V. Sagaradze, and É. N. Frizen, Sverkhprovodimost' (KIAE) **3**(10), 1 (1990) [Superconductivity **3**, S474 (1990)].
[59]V. K. Vlasko-Vlasov, M. V. Indenbom, and Yu. A. Ossipyan, Physica C **153-155**, 1677 (1988).
[60]Y. Zhu, M. Suenaga, and J. Tafto, Philos. Mag. A **67**, 1057 (1993).
[61]Y. Zhu, M. Suenaga, J. Tafto, and D. O. Welch, Phys. Rev. B **44**, 2871 (1991).
[62]Y. Zhu and M. Suenaga, Philos. Mag. A **66**, 457 (1992).
[63]Sh. Horinchi and A. Ono, Jpn. J. Appl. Phys. **33**, L304 (1994).
[64]C. S. Pande, A. K. Singh, L. Toth, D. H. Gubser, and S. Wolf, Phys. Rev. B **36**, 5669 (1987).
[65]P. Diko, K. Csach, J. Miskuf, and V. Kavecansky, J. Mater. Sci. **24**, 1995 (1989).
[66]V. S. Teodorescu, Leona C. Nistor, and S. V. Nistor, J. Appl. Phys. **67**, 2520 (1990).
[67]M. Rand, J. I. Lengford, A. Drake, and J. S. Abell, Cryogenics **33**, 291 (1993).
[68]Y. Zhu, M. Suenaga, Y. Xu, B. L. Sabatini, and A. R. Moodenbangh, Appl. Phys. Lett. **54**, 374 (1989).
[69]G. van Tendeloo and S. Amelincks, J. Less-Common Met. **164–165**, 92 (1990).
[70]N. S. Afonikova, I. K. Bdikin, Yu. A. Osip'yan, V. Sh. Shekhtman, and I. M. Shmyt'ko, Fiz. Tverd. Tela (Leningrad) **33**, 358 (1991) [Phys. Solid State **33**, 206 (1991)].
[71]S. Ikeda, T. Hatano, T. Matsumoto, A. Matsumoto, and K. Ogava, Jpn. J. Appl. Phys. **26**, L729 (1987).
[72]L. S. Chumbley, M. J. Kramer, M. R. Kim, and F. C. Laab, Mater. Sci. Eng., A **124**, L19 (1990).
[73]Y. Boiko, H. Jaeger, M. Aslan, K. Schulze, and G. Petzow, Mater. Lett. **11**, 207 (1991).
[74]T. Roy and T. E. Mitchell, Philos. Mag. A **63**, 225 (1991).
[75]Y. Zhu, J. Tafto, and M. Suenaga, MRS Bull. **16**, 54 (1991).
[76]J. R. LaGraff and D. A. Payne, Ferroelectrics **130**, 87 (1992).
[77]D. Müller and H. C. Freyhardt, Philos. Mag. Lett. **73**, 63 (1996).
[78]V. S. Boyko, Siu-Wai Chan, and M. Chopra, Phys. Rev. B **63**, 224521 (2001).
[79]A. M. Kosevich and V. S. Boĭko, Usp. Fiz. Nauk **104**, 201 (1971) [Sov. Phys. Usp. **14**, 286 (1971)].
[80]M. V. Klassen-Neklyudova, *Mechanical Twinning of Crystals*, Consultants Bureau, New York (1964), Izd-vo AN SSSR, Moscow (1960).
[81]E. H. Hewat, M. Dupuy, A. Bourret, J. J. Capponi, and M. Marezio, Solid State Commun. **64**, 517 (1987).
[82]O. Eibl, Solid State Commun. **67**, 1049 (1988).
[83]E. V. Bezuglyĭ, N. G. Burma, I. G. Kolobov, V. D. Fil', I. M. Vitebskiĭ, A. N. Knigavko, N. M. Lavrinenko, S. N. Barilo, D. I. Zhigunov, and L. E. Soshnikov, Fiz. Nizk. Temp. **21**, 86 (1995) [Low Temp. Phys. **21**, 65, Erratum 452 (1995)].
[84]D. L. Keiser, F. W. Gayle, R. S. Roth, and L. J. Swartzendruber, J. Mater. Res. **4**, 745 (1989).
[85]H. Schmid, E. Burkhardt, B. N. Sun, and J.-P. Rivera, Physica C **157**, 555 (1989).
[86]T. Hatanaka and A. Sawada, Jpn. J. Appl. Phys. **28**, L794 (1989).
[87]J. Giapinatzakis, D. M. Grinzberg, and P.-D. Han, J. Low Temp. Phys. **77**, 155 (1989).
[88]L. Dorosinskii, B. Farber, M. Indenbom, V. Nikitenko, A. Polyanskii, and V. Vlasko-Vlasov, Ferroelectrics **111**, 321 (1990).
[89]A. S. Raynes, S. W. Freiman, F. W. Gayle, and D. L. Keiser, J. Appl. Phys. **70**, 5254 (1991).
[90]A. V. Bondarenko, Doctoral Dissertation [in Russian], Kharkov (2003).

[91]S. J. Rothman, J. L. Routbort, V. Welp, and J. E. Baker, Phys. Rev. B **44**, 2326 (1991).
[92]J. R. Cost and J. T. Stanley, Scr. Metall. Mater. **28**, 773 (1993).
[93]A. Sawada, Y. Nishihata, K. Oka, and H. Unoki, Jpn. J. Appl. Phys. **28**, L1787 (1989).
[94]V. A. Goncharov, Yu. A. Osip'yan, É. V. Suvorov, and A. A. Sergeev, Izv. Ross. Akad. Nauk, Ser. Fiz. **59**, 133 (1995).
[95]V. V. Zoninashvili, V. I. Serdobintsev, I. A. Naskidashvili, L. M. Kolesnikova, and N. M. Yastrebova, Fiz. Tverd. Tela (Leningrad) **33**, 2806 (1991) [Phys. Solid State **33**, 1586 (1991)].
[96]L. A. Shuvalov, Izv. Akad. Nauk SSSR, Ser. Fiz. **43**, 1554 (1979).
[97]K. Aizu, J. Phys. Soc. Jpn. **27**, 387 (1969).
[98]K. Aizu, Phys. Rev. B **2**, 754 (1970).
[99]A. L. Roĭtburd, Usp. Fiz. Nauk **113**, 69 (1974) [sic].
[100]J. Sapriel, Phys. Rev. B **12**, 5128 (1975).
[101]L. N. Dem'yanets, Usp. Fiz. Nauk **161**, 71 (1991) [Sov. Phys. Usp. **33**, 36 (1991)].
[102]A. S. Povarennykh, *Hardness of Minerals* [in Russian], Izd.-vo AN UkrSSR, Kiev (1963).
[103]V. K. Grigorovich, *Hardness and Microhardness of Metals* [in Russian], Nauka, Moscow (1976).
[104]A. G. Evans and T. B. Wilshaw, Acta Metall. **24**, 939 (1976).
[105]A. G. Evans and E. A. Charles, J. Am. Ceram. Soc. **59**, 371 (1976).
[106]G. R. Anstis, P. Chantikul, B. R. Lawn, and D. B. Marshall, J. Am. Ceram. Soc. **64**, 533 (1981).
[107]D. Tabor, *The Hardness of Metals*, Clarendon Press, Oxford (1951).
[108]Yu. S. Boyarskaya, D. Z. Grabko, and M. S. Kats, *Physics of Microindentation Processes* [in Russian], Shtiintsa, Kishinev (1986).
[109]B. R. Lawn, A. G. Evans, and D. B. Marshall, J. Am. Ceram. Soc. **63**, 574 (1980).
[110]J. Dusza, Scripta Met. Mater. **26**, 337 (1992).
[111]A. G. Atkins, A. Silverio, and D. Tabor, J. Inst. Solids **94**, 369 (1966).
[112]D. Tabor, Rev. Phys. Tech. **1**, 195 (1970).
[113]A. P. Gerk, Philos. Mag. **32**, 355 (1975).
[114]V. M. Glazov and V. N. Vigdorovich, *Microhardness of Metals and Semiconductors* [in Russian], Metallurgiya, Moscow (1969).
[115]M. Kh. Shorshorov, V. P. Alekhin, and S. N. Bulychev, Fiz. Met. Metalloved. **43**, 374 (1977).
[116]C. Hays and E. G. Kendall, Metallography **6**, 275 (1973).
[117]J. Kumar, M. Thirumavalavan, F. D. Gnanam, and P. Ramasvamy, Phys. Status Solidi A **103**, 431 (1987).
[118]G. Berg and P. Grau, Cryst. Res. Technol. **28**, 647 (1993).
[119]S. V. Lubenets, V. D. Natsik, L. S. Fomenko, M. N. Sorin, N. M. Chaĭkovskaya, V. S. Bobrov, A. I. Izotov, and L. A. Zhokhov, Sverkprovodimost' (KIAE) **6**, 1406 (1993).
[120]Tong B. Tang and S. C. Fung, Solid State Commun. **87**, 325 (1993).
[121]J. H. Jia and Q. P. Kong, Phys. Status Solidi **145**, K51 (1994).
[122]V. N. Osipov, L. I. Derkachenko, Yu. G. Nosov, V. N. Gurin, W. Jung, and R. Muller, Solid State Commun. **57**, 377 (1996).
[123]E. Crucenau, J. Deutz, H. Klein, W. Schmitz, and H. Ullmaier, Mater. Sci. Eng., A **160**, L9 (1993).
[124]A. Goyal, P. O. Funkenbush, D. M. Kroeger, and S. J. Burns, J. Appl. Phys. **71**, 2363 (1992).
[125]L. S. Fomenko, S. V. Lubenets, V. D. Natsik, and H.-J. Kaufmann, in *High-Temperarture Superconductors*, Vol. 2, Proc. ICMC'90, edited by H. C. Freyhardt, R. Flukiger, and M. Peuckert, Informationsgesellschaft Verlag, Oberursel, FRG (1991), p. 841.
[126]L. S. Fomenko, H.-J. Kaufmann, S. V. Lubenets, V. D. Natsik, T. S. Orlova, N. N. Peschanskaya, V. V. Shpeizmann, and B. I. Smirnov, Acta Univ. Carol. Math. Phys. **32**, 131 (1991).
[127]H. C. Ling and M. F. Yan, J. Appl. Phys. **64**, 1307 (1988).
[128]L. P. Lyashenko, I. N. Ivleva, A. P. Pivovarov, A. S. Rogachev, V. I. Rubtsov, and G. A. Kazaryan, Sverkhprovodimost' (KIAE) **4**, 2184 (1991) [Superconductivity **4**, 2090 (1991)].
[129]S. X. Don, J. P. Zhou, N. Savvides, A. J. Bonrdillon, C. C. Sorrell, N. X. Tan, and K. E. Easterling, Philos. Mag. Lett. **57**, 149 (1988).
[130]M. Stubicar, M. Tuda, V. Zerjav, N. Stubicar, M. Prester, and N. Brnicevic, J. Cryst. Growth **91**, 423 (1988).
[131]S. V. Lubenets, V. D. Natsik, L. S. Fomenko, H.-J. Kaufmann, V. S. Bobrov, and A. N. Izotov, Fiz. Nizk. Temp. **23**, 902 (1997) [Low Temp. Phys. **23**, 678 (1997)].
[132]N. P. Kobelev, S. F. Kondakov, and Ya. M. Soĭfer, Fiz. Tverd. Tela (Leningrad) **31**, 57 (1989) [Sov. Phys. Solid State **31**, 1310 (1989)].
[133]B. Ya. Farber, N. S. Sidorov, V. I. Kulakov, Yu. A. Iunin, A. N. Izotov, G. A. Emel'chenko, V. S. Bobrov, L. S. Fomenko, V. D. Natsik, and S. V. Lubenets, Sverkhprovodimost' (KIAE) **4**, 2394 (1991) [Superconductivity **4**, 2296 (1991)].
[134]A. V. Stepanenko, V. A. Varavin, V. I. Lyubimov, A. S. Masakovskaya, N. V. Belyaeva, E. M. Gololobov, and N. M. Shimanskaya, Sverkhprovodimost' (KIAE) **3**, 1536 (1990) [Superconductivity **3**, 1222 (1990)].
[135]L. B. Harris and F. K. Nyang, J. Mater. Sci. Lett. **7**, 801 (1988).
[136]P. S. Kislyĭ, T. A. Prikhna, V. E. Moshchil', P. A. Nagornyĭ, M. G. Vasilenko-Sheremet'ev, and V. S. Mel'nikov. N. P. Pshentsova, in *Abstracts of the First All-Union Conference on High-Temperature Superconductivity* [in Russian], Kharkov (1988), Vol. 2, p. 124.
[137]V. N. Kovaleva, V. A. Moskalenko, V. D. Natsik, S. N. Smirnov, V. T. Zagoskin, and Yu. G. Litvinenko, Fiz. Nizk. Temp. **17**, 46 (1991) [Sov. J. Low Temp. Phys. **17**, 24 (1991)].
[138]W. D. Kingery, *Introduction to Ceramics*, Wiley, New York (1960), Stroĭizdat, Moscow (1967).
[139]V. I. Dotsenko, I. F. Kislyak, and V. D. Natsik, Fiz. Nizk. Temp. **15**, 83 (1989) [Sov. J. Low Temp. Phys. **15**, 46 (1989)].
[140]K. C. Goretta, M. L. Kullberg, D. Bar, G. A. Risch, and J. L. Routbort, Supercond. Sci. Technol. **4**, 544 (1991).
[141]P. Diko, M. Ye, M. Mehbod, and R. Deltour, Mater. Sci. Eng. **17**, 152 (1993).
[142]D. S. Ginley, B. Morozin, R. J. Baughman, E. I. Venturini, J. E. Schirber, and J. F. Kwak, J. Cryst. Growth **91**, 456 (1988).
[143]I. F. Kononyuk, V. V. Vashuk, L. V. Makhnach, and Yu. G. Zonov, Sverkhprovodimost' (KIAE) **2**(7), 77 (1989) [Superconductivity **2(7)**, 87 (1989)].
[144]T. G. Holesinger, D. J. Miller, L. S. Chumbley, M. J. Kramer, and K. W. Dennis, Physica C **202**, 109 (1992).
[145]S. V. Lubenets, V. D. Natsik, M. N. Sorin, L. S. Fomenko, N. M. Chaĭkovskaya, H.-J. Kaufmann, and K. Fischer, Sverkhprovodimost' (KIAE) **3**, 1857 (1990) [Superconductivity **3**, S258 (1990)].
[146]M. Muralidar, K. Narasimha Reddy, and V. Hari Babu, Phys. Status Solidi A **126**, 115 (1991).
[147]T. S. Orlova, B. I. Smirnov, and V. V. Shpeĭzman, Fiz. Tverd. Tela (Leningrad) **32**, 3163 (1990) [Sov. Phys. Solid State **32**, 1838 (1990)].
[148]C. Michel, M. Hervieu, M. M. Borel, A. Grandin, F. Deslandes, J. Provost, and B. Raveau, Z. Phys. B **68**, 421 (1987).
[149]B. Hebb, L. J. Gauckler, H. Heinrich, and G. Kostorz, J. Electron. Mater. **22**, 1279 (1993).
[150]S. X. Dou, H. K. Liu, A. J. Bourdillon, M. Kviz, N. X. Tan, and C. C. Sorrel, Phys. Rev. B **40**, 5266 (1989).
[151]C. Veerender, V. R. Dumke, and M. Nagabhooshanam, Phys. Status Solidi A **144**, 299 (1994).
[152]S. M. Khalil, Phys. Status Solidi A **178**, 731 (2000).
[153]M. M. Ibrahim, S. M. Khalil, and A. M. Ahmed, J. Phys. Chem. Solids **61**, 1553 (2000).
[154]S. M. Khalil, J. Phys. Chem. Solids **62**, 457 (2001).
[155]M. M. Ibrahim and S. M. Khalil, Eur. Phys. J. AP **14**, 79 (2001).
[156]A. I. Izotov, Candidate's Dissertation [in Rusian], Chernogolovka (1992).
[157]Y. Yoshino, A. Iwabuchi, K. Noto, N. Sakai, and M. Murakami, Physica C **357–360**, 796 (2001).
[158]L. S. Fomenko, S. V. Lubenets, and V. D. Natsik, in *Dislocations 93, Microstructures and Physical Properties*, Vols. 35–36 of Solid State Phenomena, edited by J. Rabier, A. George, Y. Brechet, and L. Kubin, Scitec Publications (1994), p. 513.
[159]H. Saka, J. Inagaki, T. Yoshida, T. Murase, and K. Kuroda, Jpn. J. Appl. Phys. Ser. 2, Lattice Defects in Ceram., **143**, 1989.
[160]A. Goyal, W. C. Oliver, P. D. Funkenbusch, D. M. Kroeger, and S. J. Burns, Physica C **183**, 221 (1991).
[161]H. Fujimoto, M. Murakami, and N. Koshizuka, Physica C **203**, 103 (1992).
[162]A. Leenders, M. Ullrich, and H. C. Freyhardt, Physica C **279**, 173 (1997).
[163]N. Sakai, S. J. Seo, K. Inone, T. Mijamoto, and M. Murakami, Physica C **335**, 107 (2000).
[164]A. Ya. Krasovskiĭ, *Brittleness of Metals at Low Tempreratures* [in Russian], Naukova Dumka, Kiev (1980).
[165]R. M. Tomson, in *Physical Metallurgy*, R. W. Cahn and P. Haasen (eds.), Elsevier, London (1983), Metallurgiya, Moscow (1987) (Russ. Vol. 3, p. 324).
[166]P. B. Hirsch, S. G. Roberts, and J. Samuels, Scr. Metall. **21**, 1523 (1987).
[167]R. Behrensmeier, M. Brede, and P. Haasen, Scr. Metall. **21**, 1581 (1987).
[168]A. George, J. Phys. III **1**, 909 (1991).
[169]J. J. Gilman, in *Atomic Mechanism of Fracture*, Materials of the International Conference on Questions of Fracture, April 1959 (USA), Russian transl. from English, M. A. Shtremel' (ed.), Metallurgizdat, Moscow (1963), p. 220.

[170]V. D. Kuznetsov, *Surface Energy of Solids* [in Russian], GITTL, Moscow (1954), p. 220.
[171]V. I. Trefilov, Yu. V. Mil'man, and S. A. Firstov, *Physical Principles of Strength of Refractory Metals* [in Russian], Naukova Dumka, Kiev (1975).
[172]M. Sh. Akchurin, E. N. Vasev, E. Yu. Mikhina, and V. R. Regel', Fiz. Tverd. Tela (Leningrad) **30**, 760 (1988) [Sov. Phys. Solid State **30**, 435 (1988)].
[173]S. V. Lubenets, V. D. Natsik, L. S. Fomenko, V. S. Bobrov, and A. N. Izotov, Fiz. Nizk. Temp. **21**, 324 (1995) [Low Temp. Phys. **21**, 274 (1995)].
[174]I. Matsubara, J. Hashimoto, K. Atago, H. Yamashita, M. Kinoshita, and T. Kawai, Jpn. J. Appl. Phys. **31**, Part **2**, no 1 A/B, **L14**, 1992 ().
[175]E. F. Talantsev, V. A. Ivchenko, and N. N. Syutkin, Sverkhprovodimost' (KIAE) **3**, 2017 (1990) [Superconductivity **3**, 1467 (1990)].
[176]I. M. Mikhaĭlovskiĭ, E. V. Sadanov, V. A. Ksenofontov, and O. V. Velikodnaya, Sverkhprovodimost' (KIAE) **5**, 1453 (1992) [Superconductivity **5**, 1422 (1992)].
[177]E. F. Talantsev, Supercond. Sci. Technol. **7**, 491 (1994).
[178]M. O. Eatough, D. S. Ginley, B. Morosin, and E. L. Venturini, Appl. Phys. Lett. **51**, 367 (1987).
[179]V. S. Bobrov, I. I. Zver'kova, A. P. Ivanov, A. N. Izotov, L. A. Novomlinskiĭ, R. K. Nikolaev, Yu. A. Osip'yan, N. S. Sidorov, and V. Sh. Shekhtman, Fiz. Tverd. Tela (Leningrad) **32**, 826 (1990) [Sov. Phys. Solid State **32**, 487 (1990)].
[180]V. V. Sagaradze, V. I. Zel'dovich, V. G. Pushin, S. V. Rushits, F. I. Filippov, D. A. Murzaev, O. S. Rinkevi ch, L. I. Yurchenko, V. A. Zavalishin, T. S. Boyarshinova, N. V. Nikolaeva, and V. P. Ketova, Sverkhprovodimost' (KIAE) **3**, No. 6, part 2, 1309 (1990) [Superconductivity **3**, S152 (1990)].
[181]G. Bussod, A. Pechenik, C.-T. Chu, and B. Dunn, J. Am. Ceram. Soc. **72**, 137 (1989).
[182]V. N. Kuznetsov, V. I. Shalaev, V. V. Sagaradze, V. L. Arbuzov, A.É. Davletshin, V. R. Poskrebysheva, and E. V. Dus'e, Sverkhprovodimost' (KIAE) **5**, 2041 (1992) [Superconductivity **5**, 1939 (1992)].
[183]J. Yun, M. P. Harmer, and Y. T. Chou, Scr. Metall. Mater. **29**, 267 (1993).
[184]J. Yun, M. P. Harmer, and Y. T. Chou, J. Mater. Sci. **30**, 4906 (1995).
[185]D. Rodgers, K. White, V. Selvamanickam, A. McGuire, and K. Salama, Supercond. Sci. Technol. **5**, 640 (1992).
[186]I. Chadek, *Creep of Metallic Materials* [in Russian], Mir, Moscow (1987).
[187]M. Jimenez-Melando, A. R. De Arellando-Lopez, A. Dominguez-Rodriguez, K. C. Goretta, and J. L. Routbort, Acta Metall. Mater. **43**, 2429 (1995).
[188]M. Jimenez-Melando, A. Dominguez-Rodriguez, and J. L. Routbort, Scr. Metall. Mater. **32**, 621 (1995).
[189]J. L. Routbort, D. J. Miller, M. A. Boling-Risser, J. A. Dunlap, and K. C. Goretta, Scr. Metall. Mater. **30**, 1241 (1994).
[190]P. Marsh, R. M. Fleming, M. L. Mandich, A. M. Degantolo, J. Kwo, M. Hong, and L. J. Martinez-Marinda, Nature (London) **334**, 141 (1988).
[191]I. I. Papirov, A. I. Pikalov, M. A. Tikhonovskiĭ, and A. M. Bovda, in *High-Temperature Superconductivity* [collected articles, in Russian], No. 3–4 (1991), p. 3.
[192]V. N. Kuznetsov, V. I. Shalaev, V. V. Sagaradze, E. V. Dus'e, V. L. Arbuzov, A.É. Davletshin, V. R. Poskrebysheva, and S. M. Cheshnitskiĭ, Sverkhprovodimost' (KIAE) **5**, 1939 (1992) [Superconductivity **5**, 1850 (1990)].
[193]J. L. Routbort, K. C. Goretta, D. J. Miller, D. B. Kazelas, C. Clauss, and A. Dominguez-Rodriguez, J. Mater. Sci. **7**, 2360 (1992).
[194]K. C. Goretta, E. J. Zamirowski, J. M. Calderon-Moreno, D. J. Miller, Nan Chen, T. G. Holesinger, and J. L. Routbort, J. Mater. Res. **9**, 541 (1994).
[195]L. R. Routbort, D. J. Miller, E. J. Zamirowski, and K. C. Goretta, Supercond. Sci. Technol. **6**, 337 (1993).
[196]J. D. Jorgensen, B. W. Veal, A. P. Paulikas, L. J. Nowicki, G. W. Grabtree, H. Claus, and W. K. Kwok, Phys. Rev. B **41**, 1863 (1990).
[197]S. Amelinckx, G. Van Tendeloo, and J. Van Landuyt, Solid State Ionics **39**, 37 (1990).
[198]Yu. A. Kirichenko, K. V. Rusanov, and E. G. Tyurina, Sverkhprovodimost' (KIAE) **3**, 1385 (1990) [Superconductivity **3**, 1075 (1990)].
[199]J. Cava, B. Batlogg, C. H. Chen, E. A. Rietman, S. M. Zahurak, and D. Werder, Phys. Rev. B **36**, 5719 (1987).
[200]T. Graf, G. Triscone, and J. Muller, J. Less-Common Met. **159**, 349 (1990).
[201]M. A. Alario-Franco, Sverkhprovodimost' (KIAE) **3**, 163 (1990) [Superconductivity **3**, 1362 (1990)].
[202]A. V. Vishnyakov, in *High-Temperature Superconductivity: Basic and Applied Research*, edited by A. A. Kiselev [in Russian], Mashinostroenie, Leningrad (1990), Vol. 1, p. 377.
[203]H. F. Poulsen, N. H. Andersen, J. V. Andersen, H. Bohr, and O. G. Mouristen, Nature (London) **349**, 594 (1991).
[204]V. F. Shamraĭ, S. A. Sibirtsev, G. M. Leĭtus, V. I. Nizhankovskiĭ, and S. F. Kim, Sverkhprovodimost' (KIAE) **6**, 1702 (1993).
[205]N. M. Plakida and V. S. Shakhmatov, Sverkhprovodimost' (KIAE) **6**, 669 (1993).
[206]Wu Ting and K. Fossheim, Phys. Rev. B **48**, 16751 (1993).
[207]A. Migliori, J. L. Sarrao, W. M. Visscher, T. Bell, M. Lei, S. Fisk, and R. G. Leisure, Physica B **183**, 1 (1993).
[208]V. A. Goncharov, Yu. A. Osip'yan, E. V. Suvorov, and A. A. Sergeev, Izv. Akad. Nauk SSSR Ser. Fiz. **59**, 133 (1995).
[209]V. I. Startsev, V. Ya. Il'ichev, and V. V. Pustovalov, *Plasticity and Strength of Metals and Alloys at Low Temperatures* [in Russian], Metallurgiya, Moscow (1975).
[210]M. I. Kaganov, V. Ya. Kravchenko, and V. D. Natsik, Usp. Fiz. Nauk **111**, 655 (1973) [Sov. Phys. Usp. **16**, 878 (1974)].
[211]N. I. Kuz'menko and V. V. Pustovalov, Fiz. Nizk. Temp. **5**, 1433 (1979) [Sov. J. Low Temp. Phys. **5**, 676 (1979)].
[212]D. Z. Grabko, Yu. S. Boyarskaya, R. P. Zhitaru, M. S. Kats, and V. V. Tsurkan, Sverkhprovodimost' (KIAE) **2**, 67 (1989) [Superconductivity **2**, 78 (1989)].
[213]N. N. Peschanskaya, B. I. Smirnov, and V. V. Shpeĭzman, Fiz. Tverd. Tela (Leningrad) **31**, 292 (1989) [Sov. Phys. Solid State **31**, 1446 (1989)].
[214]V. P. Soldatov, V. D. Natsik, and N. M. Chaĭkovskaya, Fiz. Tverd. Tela (Leningrad) **33**, 1777 (1991) [Phys. Solid State **33**, 999 (1991)].
[215]A. M. Dolgin, V. D. Natsik, and S. N. Smirnov, Fiz. Nizk. Temp. **16**, 1326 (1990) [J. Low Temp. Phys. **16**, 759 (1990)].
[216]E. E. Melikhov, Sverkhprovodimost' (KIAE) **2**, 5 (1989) [Superconductivity **2**, 7 (1989)].
[217]Q. Li, H. A. Hjuler, and T. Freltoft, Physica C **217**, 360 (1993).
[218]G. N. Riley, Jr., J. J. Gannon, Jr., P. K. Milles, and D. R. Parker, Appl. Supercond. **2**, 155 (1994).
[219]P. Kovac, I. Husek, W. Pachla, T. Melisek, and V. Kliment, Supercond. Sci. Technol. **8**, 341 (1995).
[220]T. Masuda, T. Kato, H. Yumura, M. Hirose, Sh. Isojima, Sh. Honjo, K. Matsuo, T. Miura, and Y. Takahashi, Physica C **372–376**, Part III, 1555 (2002).
[221]K. Ueda, Y. Ozawa, Y. Wachi, A. Kikuchi, T. Nakatsuka, and K. Iwadata, Physica C **378–381**, 1158 (2002).
[222]P. Corsaro, M. Bechis, P. Caracino, W. Castiglioni, G. Cavalleri, G. Coletta, G. Colombo, P. Ladie, A. Mansoldo, R. Mele, S. Montagner, C. Moro, M. Nassi, S. Spreafico, N. Kelley, and Ch. Wakefield, Physica C **378–381**, 1168 (2002).
[223]K. C. Goretta, M. L. Kullberg, D. Bär, B. A. Risch, and J. L. Routbort, Supercond. Sci. Technol. **4**, 544 (1991).
[224]R. Regnier, R. P. Gupta, and P. Truchot, J. Phys. C **21**, L463 (1988).
[225]V. N. Varyukhin, A. T. Kozakov, S. N. Loboda, and B. A. Panasyuk, JETP Lett. **16**, 434 (1990).
[226]V. N. Varyukhin, A. T. Kozakov, V. A. Dem'yanchenko, and S. I. Shevtsova, Sverkhprovodimost' (KIAE) **2**, 26 (1989) [Superconductivity **2**, 30 (1989)].
[227]K. V. Rusanov and Ye. G. Tyurina, Funct. Mater. **1**, 3 (1994).
[228]A. Goyal, P. D. Funkenbush, D. M. Kroeger, and S. J. Burns, Physica C **182**, 203 (1991).
[229]G. P. Meisner and C. A. Taylor, J. Appl. Phys. **69**, 5370 (1991).
[230]S. Yu. Sumarokov, N. I. Shevtsov, V. F. Tkachenko, R. F. Ramakaeva, L. A. Kotok, K. N. Belikov, and A. B. Blank, Sverkhprovodimost' (KIAE) **6**, 216 (1993).
[231]D. S. Kupperman, J. P. Singh, J. Faber, Jr., and R. L. Hitterman, J. Appl. Phys. **66**, 3396 (1989).
[232]A. P. Li, Q. H. Ni, and Q. P. Kong, Phys. Status Solidi A **127**, 187 (1991).
[233]A. B. Mosolov, Pis'ma Zh. Tekh. Fiz. **16**(6), 56 (1990) [Sov. Tech. Phys. Lett. **16(3)**, 228 (1990)].
[234]E. Yeh and K. W. White, J. Appl. Phys. **70**, 4989 (1991).
[235]R. V. Gol'dshteĭn, M. V. Elashkin, D. M. Klimov, A. V. Luzhkov, L. I. Mirkin, A. B. Mosolov, Yu. D. Tret'yakov, V. P. Shabatin, and S. A. Shesterikov, Dokl. Akad. Nauk SSSR **313**, 1121 (1990) [Sov. Phys. Dokl. **35**, 771 (1990).
[236]V. V. Sagaradze, Yu. A. Kotov, V. L. Arbuzov, V. E. Arkhipov, V. M. Alyab'ev, O. V. Antonova, A.É. Davletshin, V. A. Zavalishin, Yu. V. Mezentsev, V. G. Pushin, Yu. I. Filippov, V. I. Shalaev, and L. N. Yurchenko, SFTKh **4**, 1962 (1991) [Superconductivity **4**, 1874 (1991)].

[237]S. Samajdar and S. K. Samanto, J. Mater. Sci. **27**, 4709 (1992).
[238]W. H. Tuan and T. C. Tien, Mater. Chem. Phys. **39**, 72 (1994).
[239]W. H. Tuan and J. M. Wu, Mater. Sci. **28**, 1415 (1993).
[240]P. P. Pal'-Val', L. N. Pal'-Val', I. S. Braude, V. G. Khomenko, I. F. Kislyak, V. I. Dotsenko, and V. D. Natsik, Fiz. Nizk. Temp. **19**, 56 (1993) [Low Temp. Phys. **19**, 40 (1993)].
[241]V. I. Dotsenko, I. F. Kislyak, P. P. Pal'-Val', L. N. Pal'-Val', and V. D. Natsik, Fiz. Nizk. Temp. **19**, 49 (1993) [Low Temp. Phys. **19**, 35 (1993)].
[242]N. Sakai, S. J. Seo, K. Inine, T. Miyamoto, and M. Murakami, Physica C **335**, 107 (2000).
[243]U. Mizutani, A. Mase, K. Tazoe, H. Ikuta, T. Oka, Y. Itoh, Y. Yanagi, and M. Yoshikawa, Physica C **335**, 92 (2000).
[244]C. Vipulanandan and S. Salib, J. Mater. Sci. **30**, 763 (1995).
[245]G. E. Jang and K. Mukherjee, Supercond. Sci. Technol. **7**, 344 (1994).
[246]E. Brunnel, J. Degrieck, I. Van Driessche, and S. Hoste, Physica C **372–376**, 1063 (2002).
[247]J. K. F. Yau, N. Savvides, and C. C. Sorrell, Physica C **266**, 223 (1996).
[248]H. Kitaguchi, K. Itoh, H. Kumakura, T. Takeuchi, K. Togano, and H. Wada, Physica C **357–360**, 1193 (2001).
[249]I. Hušek, P. Kováč, and W. Pachla, Supercond. Sci. Technol. **8**, 617 (1995).
[250]A. Miyase, Y. S. Yuan, M. S. Wong, J. Schön, and S. S. Wang, Supercond. Sci. Technol. **8**, 626 (1995).
[251]Y. Hashinuma, R. Yamamoto, S. Hirano, S. Yoshizava, K. Matsunaga, A. Nishimura, A. Matsumoto, and H. Kumakura, Physica C **357–360**, 824 (2001).

Translated by Steve Torstveit

QUANTUM LIQUIDS AND QUANTUM CRYSTALS

Study of the spectra of electron–ripplon oscillations and dissipation processes in a two-dimensional electron crystal over liquid helium

V. E. Syvokon*

B. Verkin Institute for Low Temperature Physics and Engineering, National Academy of Sciences of Ukraine, pr. Lenina 47, Kharkov 61103, Ukraine

(Submitted November 20, 2003)
Fiz. Nizk. Temp. **30**, 509–522 (May 2004)

The resonance spectrum of coupled electron–ripplon oscillations in two-dimensional electron crystals over liquid helium are investigated in the range of surface electron densities $n_s = (3.2–10.8)\times 10^8$ cm^{-2} at holding electric fields $E_\perp = 300–1150$ V/cm, and in the temperature interval $T = 0.08–0.4$ K. As a result of an analysis of the spectra, the real χ_1 and imaginary χ_2 parts of the inverse conductivity σ^{-1} of the crystals are obtained as functions of T, n_s, and $E_\perp$. The value found for χ_2 is in good agreement with the theoretical estimates. Analysis of the dependences of χ_1 suggests that the energy losses in the electron crystal are due to defects of its crystal structure. © *2004 American Institute of Physics.* [DOI: 10.1063/1.1739132]

INTRODUCTION

In a two-dimensional (2D) electron layer on the surface of liquid helium for a certain relation between the kinetic and potential energies of the electrons a spatial ordering occurs, and an electron (Wigner) crystal forms. As a result of the crystallization the electrons are localized, which gives rise to the appearance of local depressions of the liquid (dimples).

The electron–electron scattering in the crystal and the degree of coupling of the electrons with the surface of the liquid can easily be varied over rather wide limits by changing the experimental parameters: the electron surface density n_s, the temperature T, the holding electric field $E_\perp$, directed normal to the surface, and the driving electric field $E_{\rm dr}$, which acts in the plane of the electron layer. An electron crystal on the surface of liquid helium is a promising system for studying the properties of both the 2D crystal itself and the surface of the liquid, as is shown, in particular, by the melting of the 2D crystal[1,2] and the change in surface tension of weak ^{3}He–^{4}He solid solutions.

Crystallization in the electron layer over liquid helium was first observed in the experiment by Grimes and Adams[4] from the appearance of coupled electron–ripplon oscillations (CEROs)—specific oscillations in which the phonon modes of the 2D crystal are coupled with capillary modes of the liquid surface.[5]

The resonance frequencies of the CEROs can be calculated without any adjustable parameters in the framework of a self-consistent theory,[6] and the results of the calculations are in good agreement with the experimental data.[7] The position and width of the CEROs depend on the value of the complex conductivity σ of the electron layer.

The conductivity of an electron crystal over liquid helium is a quantity that contains information about both the 2D electron layer and about the surface of the liquid, and also about the features of the coupling between these two subsystems.

Theoretically the conductivity of a Wigner crystal over liquid helium has been studied in the case of a uniform[8] and a nonuniform driving electric field in the layer[9] on the assumption that the main mechanism of energy loss from the crystal is the damping of capillary waves excited by the crystal during the motion. It has turned out, however, that this mechanism cannot explain the experimentally observed values of the width of the CERO resonances,[10] and the question of what processes govern the main contributions to the energy loss of the electron crystal in its motion remains open. The existing experimental information about the losses in an electron crystal over liquid helium is sparse and, apparently, insufficient for further, more detailed, theoretical analysis. Therefore, it is desirable to do additional and comprehensive experimental studies, and that was the goal of the present study. In it we measured the complex conductivity of the electron crystal as a function of the main quantities that govern its properties: temperature, electron surface density, and the holding electric field under conditions when the driving different is rather small and does not influence (or only weakly influences) the measured quantities. The studies were done in the frequency region corresponding to excitation of the CERO resonances in the experimental cell. It should be noted that, in addition to the conductivity measurements, investigations in the resonance region also yield additional information about the crystal, since, in particular, the frequency of the CERO resonances reflects the structure of the electron crystal. We note that the fact that the position and shape of the resonance curve are independent of the amplitude of the measuring signal and, thus, of the value of the driving field, are grounds for assuming that the measurement regime is linear, while the variation of the resonance spectrum with increasing signal amplitude attests to the nonlinear regime that can be brought about by structural changes in the crystal.

EXPERIMENT

In the present study we have used a cell with circular symmetry, having the form a flat capacitor formed by plates 2.7 mm in diameter with a 0.2 mm gap between them. The liquid helium surface was located approximately in the middle of the gap, the thickness of the helium layer amounting to 0.9–1.3 mm in different experiments. The surface of the liquid was charged at a temperature $T\sim 1.3-1.5$ K by the brief heating of a tungsten filament located outside the capacitor gap. Electrons escaping from the filament were thermalized on atoms of the vapor and were held to the helium surface by a positive potential of 60–230 V applied to the lower electrode. The lower electrode was made in three equal sectors connected independently to the voltage source. Such a construction permitted adjustment of the apparatus to obtain an identical height of the liquid helium relative to the lower electrode and thereby uniformity of the holding electric field. The horizontal adjustment of the cell was monitored by measuring the punch-through voltage on each of the sectors. As a result of the adjustment the thickness of the liquid layer was identical along the lower electrode to within an error of 20 μm, making for high uniformity of the holding electric field and the electron surface density. For forming the profile of the electron spot a guard ring on which a negative potential was applied was used. To determine the electron surface density n_s the crystallization temperature, which is proportional to n_s, was measured. In the majority of experiments the electron density was also registered at the end of a series of measurements to check that there had been no uncontrolled losses of electrons during the measurements.

The upper capacitor plate consisted of a system of ring-shaped measuring electrodes. The input signal—an ac voltage with the required frequency—was applied to the outer electrode, and the response signal, proportional to the current induced in it, was taken from the inner electrode.

The relation between the output current J and the input voltage with amplitude V_0 and frequency ω,

$$J=(G_1+i\omega G_2)V_0\exp(i\omega t), \tag{1}$$

for a known geometry of the cell depends on the conductivity σ of the electron layer, the coefficients G_1 and G_2 being functions of it. These functions, determined by solution of Maxwell's equations, have the form[11]

$$G_1=n_se^2\sum_{n=1}^{\infty}A_n\frac{n_se^2\omega^2\chi_1}{(m\omega^2_{\beta_n}-n_se^2\omega\chi_2)^2+(n_se^2\omega\chi_1)^2}, \tag{2}$$

$$G_2=n_se^2\sum_{n=1}^{\infty}A_n\frac{m\omega^2_{\beta_n}-n_se^2\omega\chi_2}{(m\omega^2_{\beta_n}-n_se^2\omega\chi_2)^2+(n_se^2\omega\chi_1)^2}+g_0. \tag{3}$$

Here m is the mass of the electron, χ_1 and χ_2 are the real and imaginary parts of the inverse conductivity of the two-dimensional electron system: $\chi_1=\mathrm{Re}\,\sigma^{-1}$; $\chi_2=\mathrm{Im}\,\sigma^{-1}$, $\omega^2_{\beta_n}=4\pi n_se^2F_n/m$, and the coefficients A_n, g_0, and F_n depend on the shape and dimensions of the experimental cell.

In the experiment two linearly independent components of the output current, the amplitude and phase, were measured in a certain frequency interval, and G_1 and G_2 were thereby determined. The real and imaginary parts of the conductivity of the electron layer were the solutions of the system of equations (2), (3). In principle, for determining the conductivity it is sufficient to measure the real and imaginary parts of the response at a single frequency. The choice of this frequency is largely determined by the experimental conditions and capabilities. In order to ensure a linear regime of measurements it is necessary to use an input signal with a minimal amplitude, but then the measurements are substantially affected by the signal-to-noise ratio and a greater influence of systematic errors due to the model description of the measuring line and the input circuits of the measuring devices.

A characteristic feature of the present study is that the conductivity measurements were made in a frequency region in which resonances of coupled electron–ripplon oscillations were excited in the experimental cell. In that case the conductivity of the electron crystal can be determined in two ways: either as a result of measurement of the phase and amplitude of the output current at any fixed frequency, or as a result of measurement of the frequency dependence of the amplitude of the output current in the region of the resonance and a determination of the position and width of the resonance curve. In the determination of the conductivity from the amplitude and phase of the output current at a fixed frequency it is desirable to use measurements at a resonance frequency, since then the signal-to-noise ratio is maximal and the influence of the measurement errors, including systematic errors, is minimal. In that case, however, it must be borne in mind that the effective electric field in the plane of the electron layer under consider conditions can be higher than under nonresonance conditions at the same value of the amplitude of the input signal; this can give rise to nonlinear effects.

In studies in the resonance region it is necessary first of all the establish which resonance oscillations are possible in the system under study. The change in the charge density in the electron layer can be determined as a result of solution of Laplace's equation for a two-dimensional conducting layer with allowance for the geometry of the cell and the corresponding boundary conditions. In the case of a circular geometry the density perturbation due to plasma resonance in a layer of uniform density located between electrodes of infinite extent has the form[12]

$$\delta\rho\sim J_m(kr)\exp(im\varphi), \tag{4}$$

where r and φ are polar coordinates, and $J_m(x)$ is the Bessel function of order m. The possible resonance modes can be described by numbers m and n, where n enumerates the ascending sequence $k_1,\ldots,k_n$ from the admissible boundary conditions.

The equation for k has the form

$$mJ_m(kR)-kRJ_{m+1}(kR)=0, \tag{5}$$

where R is the radius of the electron layer. In the case of axisymmetric oscillations ($m=0$) this equation reduces to $J_1(kR)=0$, and the number n in that case simply enumerates the zeroes of the first-order Bessel function.

In this paper for determining the conductivity we measured the amplitude and phase near the fundamental mode (0,1) of coupled electron–ripplon oscillations. The amplitude

of the input signal in all the measurements was 1 mV. The (0,1) resonances for a crystal with a density corresponding to the condition of complete screening of the holding field has also been studied at a fixed low temperature 83 mK at amplitudes V_0 equal to 0.3, 0.5, and 2 mV. It is found that the position and relative amplitude of the (0,1) resonance remain constant within the error limits of the experiment at these amplitudes of the input signal, but for $V_0=2$ mV there is a noticeable frequency shift and a change in the relative amplitude of the resonance. Therefore, the amplitude of the input voltage $V_0=1$ mV at which the measurements were made in the present study apparently corresponds to the boundary of the region of linearity (the regions in which the conductivity is independent of the amplitude of the excited signal or, in other words, independent of the value of the holding field).

The real and imaginary parts of the conductivity of the electron crystal were determined as a result of solution of the system of equations (2), (3) with respect to χ_1 and χ_2. In the calculation we used 40 terms in each of the series on the right-hand sides of the equations, which is significantly greater than the number of terms that have a substantial influence on the solution. The rather rapid convergence of the series at parameter values corresponding to the experimental conditions makes it possible to greatly simplify the system of equations in the case when the measurements are done at the resonance frequency. Equations (2) and (3) were obtained under conditions of circular symmetry in the system and take only the resonance feature $(0,n)$ into account. It is seen from Eq. (2) that the first term in the sum $(n=1)$ is resonantly large at

$$m\omega_{\beta 1}^2 - n_s e^2 \omega \chi_2 = 0, \tag{6}$$

which corresponds to excitation of the (0,1) resonance. Therefore, in making measurements directly near the maximum of the amplitude of the output current one can drop all but the first term of the sum. The values of G_1 and G_2 are determined in an experiment from the measured values of the amplitude and phase of the output current with allowance for the characteristics of the measuring line. When only the first term of the sum is taken into account, it quickly follows from Eq. (1) that $\chi_1 = A_1/G_1$, and χ_2 is easily determined from condition (6).

The calculations were done both with the use of these approximate formulas and with a rather large number of terms (40 of them) taken into account in Eqs. (2) and (3). The values of the parts of the conductivity of the electron crystal calculated in the two different ways run parallel on the graphs and, as we shall see below, are in good agreement with each other.

As was noted above, the conductivity of an electron crystal over liquid helium was considered theoretically in Ref. 8 under the assumption that the main mechanism of loss is due to the damping of the capillary waves excited by the crystal during motion. The response function Z_1 of the electron crystal to an ac driving field with frequency ω was calculated. The real and imaginary parts of Z_1 have the form

$$\mathrm{Re}\, Z_1 = \sum_{l=1}^{\infty} C_l \frac{\omega_l^2(\omega^2-\omega_l^2+4\gamma_l^2)}{(\omega^2-\omega_l^2)^2+4\omega^2\gamma_l^2} - 1, \tag{7}$$

$$\mathrm{Im}\, Z_1 = \sum_{l=1}^{\infty} C_l \frac{2\gamma_l}{\omega} \frac{\omega_l^4}{(\omega^2-\omega_l^2)^2+4\omega^2\gamma_l^2}, \tag{8}$$

where C_l is a coefficient characterizing the intensity of the electron–ripplon coupling, ω_l and γ_l are, respectively, the frequencies and damping coefficients of the capillary waves whose wave vectors coincide with the reciprocal lattice vectors of the electron crystal. The coefficient C_l can be expressed as[6]

$$C_l = \frac{3n_s V_l^2}{\alpha m \omega_l^2} \exp(-k_l \langle u_l^2 \rangle/2), \tag{9}$$

where the value of V_l in the limit of high holding fields $E_\perp$ is proportional to the field: $V_l \propto eE_\perp$, α is the coefficient surface surface tension, k_l is the wave vector corresponding to the frequency ω_l, and $\langle u_l^2 \rangle$ is the mean-square displacement of the electrons at the sites of the crystal lattice. The effective mobility of the electrons is expressed in terms of the response function Z_1 as

$$\mu = \frac{e}{m\omega} \frac{\mathrm{Im}\, Z_1}{|Z_1|^2}. \tag{10}$$

It was noted in Ref. 8 that other mechanisms of slowing the crystal besides capillary wave damping are possible, involving collisions with pre-existing surface excitations or vapor atoms. Taking those mechanisms into account leads to the addition of a term ν/ω on the right-hand side of the expression for Z_1, where ν is a certain characteristic frequency corresponding to this mechanism of dissipation, and the expression for the density (10) remains the same in form.

The calculated in Ref. 8 components function Z_1 are related to the experimentally determined real and imaginary parts χ_1 and χ_2 of the inverse conductivity of the electron crystal by the relations

$$\chi_1 = \frac{m\omega}{ne^2} \mathrm{Im}\, Z_1, \quad \chi_2 = -\frac{m\omega}{ne^2} \mathrm{Re}\, Z_1. \tag{11}$$

Thus the experimental results can be compared with the predictions of the theory without the use of adjustable parameters. The experiments were done under conditions such that the resonances of the CEROs corresponding to coupling of the phonon modes of the crystal with the low-frequency capillary mode ω_1 are observed.

RESULTS AND DISCUSSION

Figure 1 shows the smoothed frequency dependence of the amplitude of the response to excitation in the existence region of the coupled electron–ripplon resonance (0,1) at different temperatures; the curves are shifted with respect to each other along the vertical by an amount 0.001, except for the lowest curves (corresponding to the lowest temperatures), the position of which was not changed and corresponds to the scales along the vertical axes. Figure 1a pertains to the so-called saturated case, when the electron layer is completely screened by the holding electric field, while Fig. 1b corresponds to the case of incomplete screening. In both cases the electron surface density n_s was 6.4×10^8 cm^{-2}. The temperature of Wigner crystallization of the electron layer at such a surface density is 0.58 K.

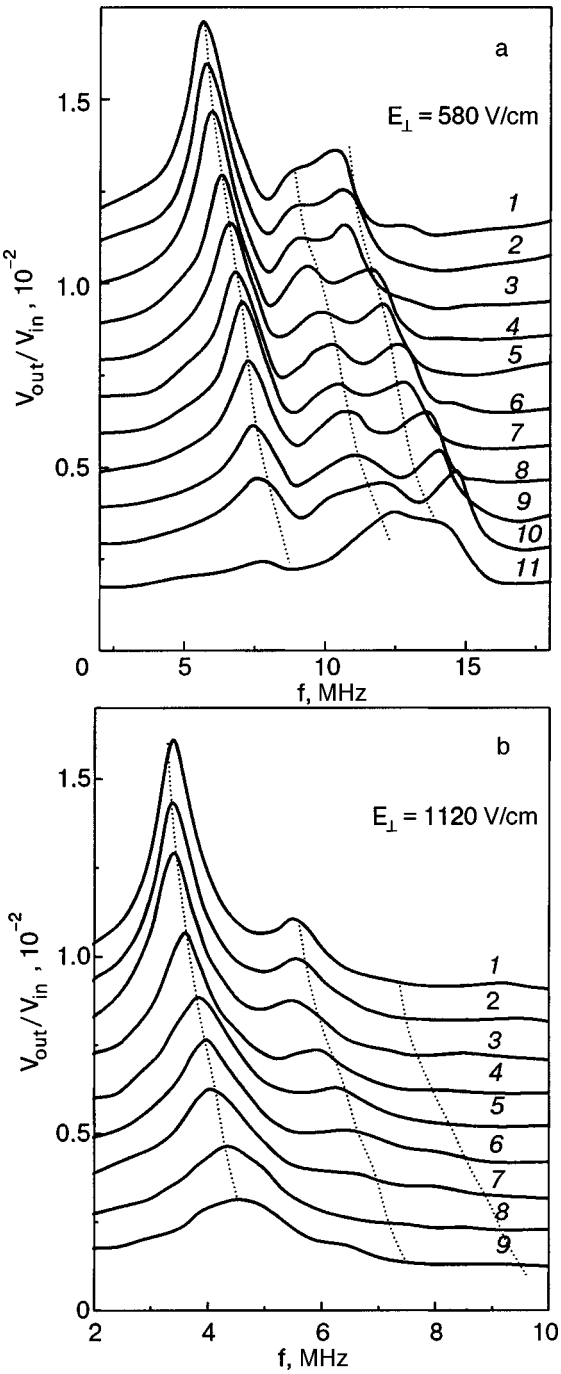

FIG. 1. Resonance spectra of the CEROs of a 2D electron crystal with a surface density $n_s = 6.4\times10^8$ cm^{-2} at different values of the holding field $E_\perp$ and temperature T [mK]: 81 (*1*), 90 (*2*), 101 (*3*), 131 (*4*), 163 (*5*), 194 (*6*), 221 (*7*), 254 (*8*), 299 (*9*), 356 (*10*), 400 (*11*) (a); 82 (*1*), 92 (*2*), 102 (*3*), 130 (*4*), 163 (*5*), 194 (*6*), 256 (*7*), 293 (*8*), 359 (*9*) (b). The curves except for the lowest have been shifted relative to each other along the vertical by 0.001. The dotted lines are the result of a calculation of the frequencies of the resonance modes (0,1), (0,2), and (0,3) in the theory of Ref. 6.

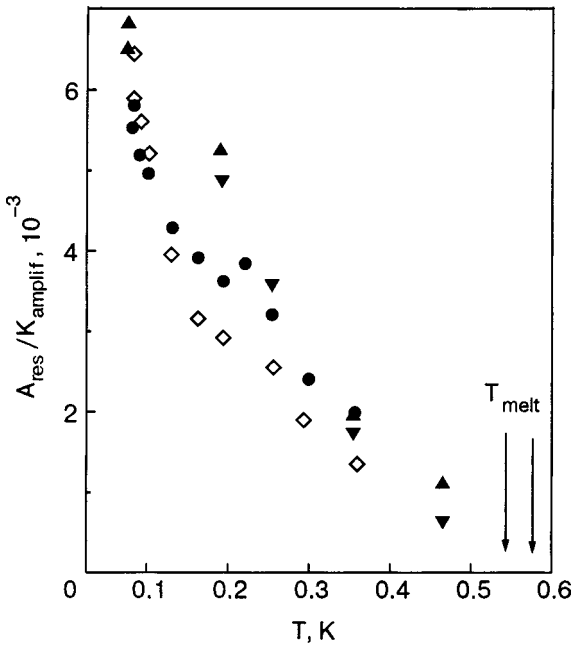

FIG. 2. Temperature dependence of the amplitude of the (0,1) resonance of the CEROs for a crystal with $n_s = 6.4\times10^8$ cm^{-2} at $E_\perp = 580$ V/cm (●) and 1120 V/cm (◇) and crystals with $n_s = 5.8\times10^8$ cm^{-2} (▲) and $n_s = 5.7\times10^8$ cm^{-2} (▼) at $E_\perp = 510$ V/cm. The arrows indicate the melting temperature of the crystals; the left one corresponds to $n_s = 5.8\times10^8$ cm^{-2}, and the right one to $n_s = 6.4\times10^8$ cm^{-2}.

The resonance features are clearly visible in both series of curves in Fig. 1. On all of the curves the resonance peaks are most clearly pronounced at relatively low frequencies. These peaks can be interpreted as resulting from the excitation of the (0,1) mode of coupled electron–ripplon oscillations. It is well seen that as the temperature increases, the frequencies of these resonances increases and their relative amplitudes decrease. Other resonance features besides (0,1) are also observed, and their frequencies also increase with increasing temperature. The amplitudes of the (0,1) resonances, which, as was shown above, directly reflect the energy losses from the electron crystal, decrease as the temperature approaches the melting temperature of the crystal, as is well seen in Fig. 2. Figure 2 reflects the results of different experiments in which the measuring lines were somewhat different, and so for comparison the measured amplitudes A_{res} have been divided by the gain of the corresponding preamplifiers K_{amplif}. Figure 2 shows the data for electron crystals whose surface densities n_s are a little different, equal to 5.8×10^8 and 6.4×10^8 cm^{-2}. The arrows indicate the melting temperatures T_{melt} of these crystals; the higher density corresponds to the higher melting temperature. As can be seen in the figure, as the temperature approaches T_{melt} the amplitude of the (0,1) modes tends toward zero by an approximately linear law, and this characteristic of the dependence begins to be manifested already at temperatures $\sim$0.2 K, i.e., considerably below the melting temperature.

The presence of a single dependence of the amplitude of the resonance over a wide range of temperatures and the fact that the temperature obtained by extrapolation of that dependence to zero amplitude coincides with T_{melt} may indicate that the mechanisms responsible for the energy loss from the crystal and for its melting have a common nature. Since, as was shown in Ref. 1, the melting of an electron crystal occurs by the Kosterlitz–Thouless mechanism,[13] i.e., is of a dislocation nature, it is natural to expect that dislocations in the Wigner crystal can play an important role in its energy losses as well.

The resonance curves of the amplitude (Fig. 1) with the corresponding curves of the phase shift of the measuring signal have been used to determine the real and imaginary

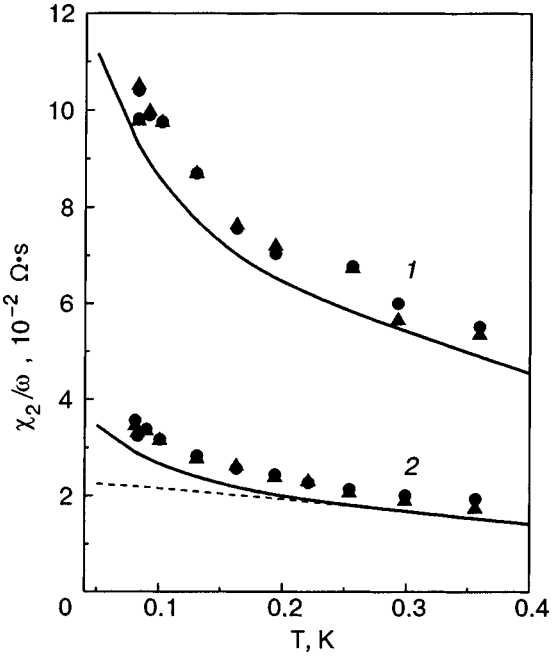

FIG. 3. Temperature dependence of the imaginary part of the inverse conductivity of an electron crystal with $n_s = 6.4\times10^8$ cm^{-2} at holding fields of $E_\perp = 1120$ V/cm (*1*) and $E_\perp = 580$ V/cm (*2*). (●)—The result of a solution of the system of equations (2), (3); (▲)—the result of a simplified calculation. The solid curves show estimates in the framework of the theory of Ref. 8 with the ^{3}He impurity taken into account at a concentration of 5.5×10^{-7}, and the dashed line shows the calculation for pure ^{4}He.

parts χ_1 and χ_2 of the inverse conductivity of the electron layer. The processing of the experimental data was done by two methods: from the amplitude and shift of the phase at the point of the (0,1) resonance, and from the amplitude $A \sim 1/\chi_1$ in a simplified calculation. The values obtained for χ_1 and χ_2 at different temperatures generalize pertain to different frequencies, and, if the absence of frequency dependence of the conductivity is not assumed, then the construction of the temperature dependences of χ_1 and χ_2 is not completely correct, since the different experimental conditions correspond to different temperatures. However, an analysis of the response function Z_1 in the theory of Ref. 8 shows that at low frequencies $\omega \ll \omega_1$ (this condition holds in the present experiment) the approximation $\chi_2/\omega \sim \mathrm{Re}\, Z_1 \sim C_1$ and $\chi_1 \sim \gamma + \nu$ is rather good, i.e., the frequency dependence of χ_1 and χ_2/ω can be neglected, then the procedure used to process the data is completely applicable.

In Fig. 3 the experimentally obtained temperature dependence of χ_2/ω for an electron crystal with a density $n_s = 6.4\times10^8$ cm^{-2} at values of the holding field $E_\perp = 1120$ V/cm and $E_\perp = 580$ V/cm (this latter field is completely screened by the electron layer) is compared with the results of a calculation in the framework of the theory of Ref. 8. The experimental data are pairs of points denoted by different symbols, corresponding to different ways of processing (complete and simplified) the same data, and the solid curves are the theoretical estimates. The dashed curve shows a calculation under the condition that the coefficient of surface tension of the liquid corresponds to that of pure ^{4}He. The theoretical values of χ_2/ω at $T > 0.2$ K are approximately 10% lower than the experimental values. This is very good agreement, especially if it is taken into account that no adjustable parameters were used in the calculation. The reason for the small differences between theory and experiment may be due to both experimental errors and the approximations of the theory.

At temperatures $T < 0.2$ K the difference between theory and experiment increases because of the influence of the natural ^{3}He impurity, which at sufficiently low temperatures leads to a noticeable decrease in the surface tension of the liquid. The solid curves in Fig. 3 are the result of theoretical estimates in which the surface of surface tension corresponding to a solution ^{3}He–^{4}He with an atomic concentration of ^{3}He equal to 5.5×10^{-7} was used. In a certain sense the concentration 5.5×10^{-7} can be considered to be an adjustable parameter, since the concentration of ^{3}He in the ^{4}He was not independently measured. It should be noted, however, that such a concentration of ^{3}He in natural ^{4}He lies in the range of typical abundances. When the ^{3}He impurity is taken into account, the discrepancy between theory and experiment at low temperatures ($\sim$0.1 K), where the influence of the impurity is substantial, becomes the same as at $T > 0.2$ K, where the presence of ^{3}He has practically no effect on the results of the measurements.

The good agreement of the experimental and theoretical values of χ_2/ω attest to the fact that the self-consistent theory[6] is extremely successful for calculating the electron–ripplon coupling coefficient, at least in the region of parameters corresponding to the present experiment. Using the results of Ref. 6, one can determine the frequency of the coupled electron–ripplon resonances. When only the coupling with the lowest-lying capillary mode ω_1 is taken into account, the frequencies of the coupled oscillations have the form

$$\omega_{\mathrm{res},p}^2 = \frac{\omega_1^2 \omega_p^2(k)}{C_1 \omega_1^2 + \omega_p^2(k)}, \tag{12}$$

where $\omega_p(k)$ is the vibrational spectrum of the Wigner crystal above an ideally flat surface. Calculation of the resonance frequencies that follow from the theory allows one to understand which modes correspond to the features in Fig. 1. The results of the calculation are shown by the dotted lines in that figure. In the calculations we used correlation factors for taking into account the existing discrepancy between theory and experiment. These factors equal 1.09 for the data in Fig. 1a and 1.05 for the data in Fig. 1b. It is well seen that the resonance features in Fig. 1a can be interpreted as the (0,1), (0,2), and (0,3) modes, while those in Fig. 1b can be interpreted as (0,1) and (0,2). The (0,3) mode is practically unnoticeable in Fig. 1b. In addition, the amplitude of the (0,1) mode in Fig. 1b is considerably larger than the amplitude of the (0,2) mode in the entire temperature interval, whereas in Fig. 1a the amplitudes of the (0,2) mode and even of the (0,3) mode, which is not seen at all in Fig. 1b, are comparable to the amplitude of the fundamental mode (0,1) and even exceed it. Such behavior can be a consequence of nonlinear effects, which are more easily manifested the closer the temperature of the electron crystal is to its melting point.

The real part χ_1 of the inverse conductivity, which contains the energy loss of the crystal, is shown in Fig. 4 for the same (Fig. 1) experimental conditions. The value of χ_1 is higher for the larger value of $E_\perp$ and grows with increasing

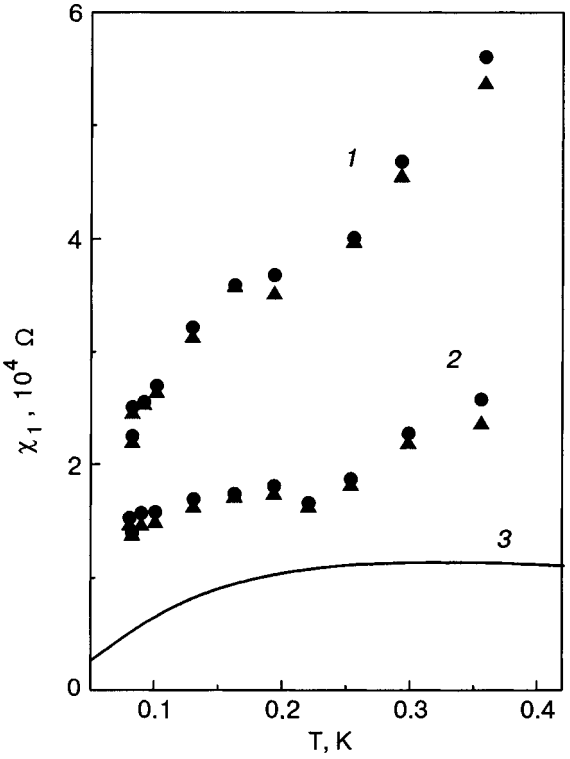

FIG. 4. Temperature dependence of the real part of the inverse conductivity of an electron crystal with $n_s=6.4\times10^8$ cm^{-2} at holding fields of 1120 V/cm (*1*) and 580 V/cm (*2*). The curve (*3*) shows the result of a rescaling of the experimental data[14] for a crystal with $n_s=5.5\times10^8$ cm^{-2} at $E_\perp=540$ V/cm.

temperature. Line *3* in Fig. 4 shows the dependence $\chi_1(T)$ rescaled according to the formula $\chi_1=(ne\mu)^{-1}$ from the experimental data of Ref. 14 for a crystal with nearly the same parameters ($n_s=5.5\times10^8$ cm^{-2}, $E_\perp=540$ V/cm). It is seen that the values of χ_1 obtained from the data of Ref. 14 turn out to be smaller by approximately a factor of two than the values measured in the present study. Apparently this is partially due to the noncoincidence of the experimental conditions, but there is a notable qualitative difference as well. While at temperatures $T<0.2$ the $\chi_1(T)$ curves in the two studies are similar, at $T>0.2$ K the value of χ_1 obtained by us increases with increasing temperature, in contrast to the results of Ref. 14, where no dependence of χ_1 on temperature was observed. This difference is apparently due to the influence of the measuring signal. In Ref. 14 the measurements were made at frequencies of 0.75 and 1 MHz at an amplitude of the measuring signal of 1.25 mV, while in the present study the analogous measurements were made at frequencies of 3–4 MHz at a signal amplitude of 1 mV. A rough estimate shows that the driving field in the measurements of Ref. 14 was lower by a factor of 2.5–4 than that in the present study, and the observed growth of χ_1 at $T>0.2$ may be due to nonlinear effects.

The curves presented above reflect not only the temperature dependence of the conductivity but also its dependence on the holding field. The holding field has a substantial influence on the electron–ripplon coupling ($C_1\sim E_\perp^2$) and thereby on all the properties of the crystal.

Figure 5a shows the resonance spectra of the electron–ripplon vibrations of a 2D Wigner crystal with a surface density of 6.4×10^8 cm^{-2}, determined at a temperature 83 mK at different values of the holding fields. Plotted along the vertical axis is the amplitude of the voltage created by the current J across the input resistance of the preamplifier of the measuring line. The value of the measuring signal was 1 mV and, as was noted above, was a compromise devised to ensure an acceptable signal-to-nose ratio at the lowest possible influence on the results of the measurements.

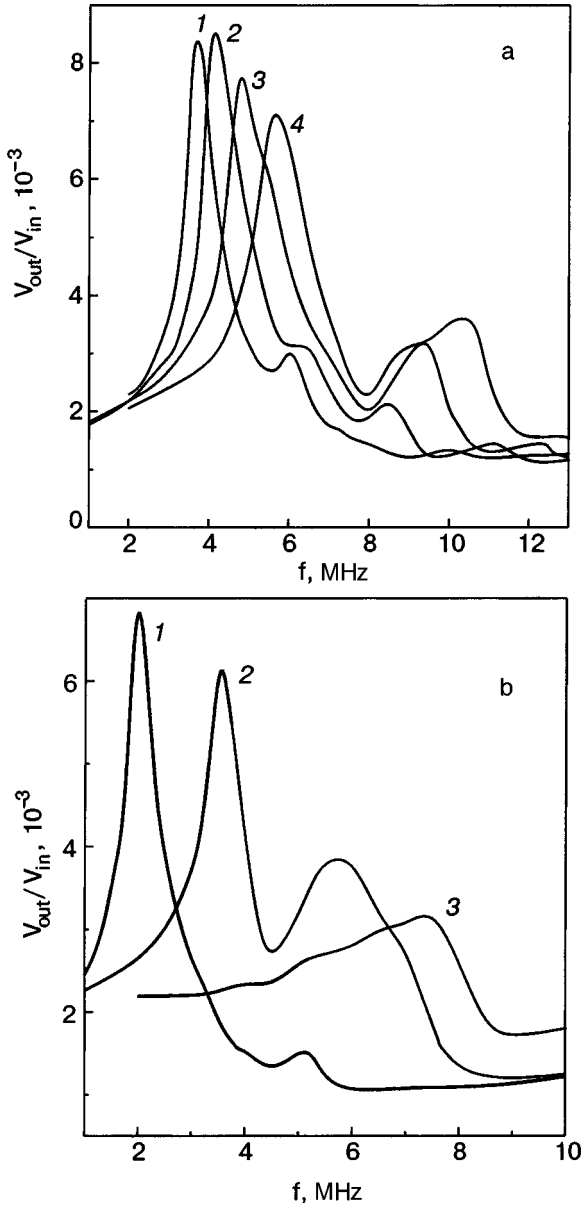

FIG. 5. Resonance spectra of the CEROs for crystals with $n_s=6.4\times10^8$ cm^{-2} (a) and $n_s=3.2\times10^8$ cm^{-2} (b) at $T=83$ mK for different values of the holding field $E_\perp$ [V/cm]: 1000 (*1*), 850 (*2*), 705 (*3*), 590 (*4*) (a); 1150 (*1*), 570 (*2*), 300 (*3*) (b).

In Fig. 5a the resonance features are pronounced maxima of the amplitude at low frequencies and less pronounced maxima at higher frequencies. The most pronounced maxima of the amplitude in the low-frequency region correspond to the resonance mode (0,1). Their position is in good agreement with the theoretical estimates Eq. (1). The other features can be interpreted as the excitation of the (0,2) and (0,3) modes. They are less pronounced the higher the holding field (on curve *1*, corresponding to the highest

holding field, the (0,3) mode is not seen at all). With decreasing holding field the resonances (0,2) and (0,3) are shifted to the region of lower frequencies in comparison with the theoretical estimates, and their amplitudes increase. The observed qualitative changes of the CERO spectrum with changes in the holding field are similar to those observed upon changes in temperature (Fig. 1a). The changes of the spectrum are less noticeable the lower the holding field.

This is seen particularly clearly in Fig. 5b, which shows the resonance spectra of coupled electron–ripplon oscillations for the crystal with $n_s = 3.2\times10^8$ cm^{-2}. At a low holding field $E_\perp = 300$ V/cm (curve *3*), when there is complete screening of the holding field, the resonance features are indistinct, and it is practically impossible to make out the individual resonances. However, even in the case of a holding field $E_\perp = 570$ V/cm (curve 2) the frequencies of the obtained resonances (0,1) and (0,2) are in good agreement with the theoretical estimates, and the same is observed at $E_\perp = 1150$ V/cm (curve *1*), and in the latter case the amplitude of the (0,2) mode is substantially lower than the that of the (0,1) mode. It is quite likely that such an indistinct resonance picture for $E_\perp = 300$ V/cm may be due to the nonlinear influence of the measuring signal, which leads to disruptions of the structure of the electron crystal; owing to the capacitive coupling of the electron layer with the measuring electrodes, the electric field excited by the measuring signal in the plane of the electron layer is proportional to the frequency, so that the probability of nonlinear effects increases with increasing frequency. However, it cannot be ruled out that the cause of the observed features of the spectrum may be due to features of the frequency dependence of the conductivity.

The real and imaginary parts χ_1 and χ_2 of the conductivity of the 2D crystal, calculated from measurements of the amplitude and phase at the resonance resistivity, are presented in Fig. 6.

In Fig. 6a the experimentally determined values of χ_2/ω for 2D electron crystals with $n_s = 6.4\times10^8$ and 3.2×10^8 cm^{-2} (points) are compared with the values calculated in the framework of Ref. 8 (solid curves). The agreement of the theory and experiment is seen to be good. It should be mentioned once again that helium of technical purity was used in the experiment, and in the calculation the coefficient of surface tension was assumed to to be that corresponding to a solution ^{3}He–^{4}He with an atomic concentration of ^{3}He equal to 5.5×10^{-7}. As is seen in Fig. 3, the difference between the experimental and theoretical data for χ_2/ω in the temperature region $T > 0.2$ K, where the coefficient of surface tension of ^{4}He of natural purity is practically no different from the coefficient of surface tension of isotropically pure ^{4}He, is around 10%. Therefore, one can say that the agreement between theory and experiment for the data in Fig. 6a is good to approximately that accuracy.

In the region of rather low frequencies the values of χ_2/ω turn out to be proportional to the electron–ripplon coupling coefficient C_1, and at low frequencies the effective mass of the electrons in the crystal, m_{eff}, is also proportional to this coefficient, i.e., m_{eff} in this case characterizes the imaginary part of the conductivity of the crystal. The effective mass of the electron crystal with a surface density of 6.3×10^8 cm^{-2} was measured in Ref. 15, but the values obtained turned out to be markedly higher than those calculated in the self-consistent theory,[8] which, as we have said, gives good quantitative agreement with the experimental data of the present study.

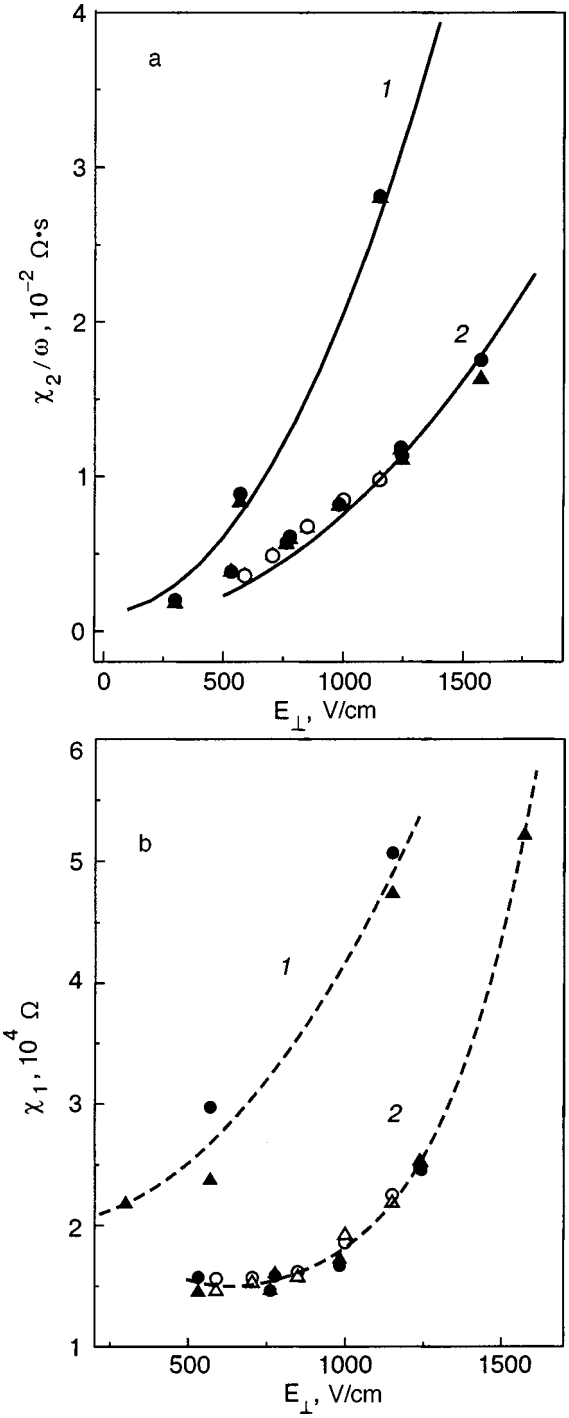

FIG. 6. Dependence of the imaginary (a) and real (b) parts of the inverse conductivity of electron crystals with $n_s = 3.2\times10^8$ cm^{-2} (*1*) and $n_s = 6.4\times10^8$ cm^{-2} (*2*) on the holding field at $T = 83$ mK. The filled and unfilled symbols correspond to different series of measurements. The solid curves show the theoretical estimates in the framework of Ref. 8. The dashed curves are of an auxiliary character.

Figure 6b shows the real part χ_1 of the inverse conductivity as a function of the holding field for crystals with a surface density of 3.2×10^8 and 6.4×10^8 cm^{-2}. The dashed curves are of a provisional nature and have been drawn for convenience. The figure illustrates the increase of the real

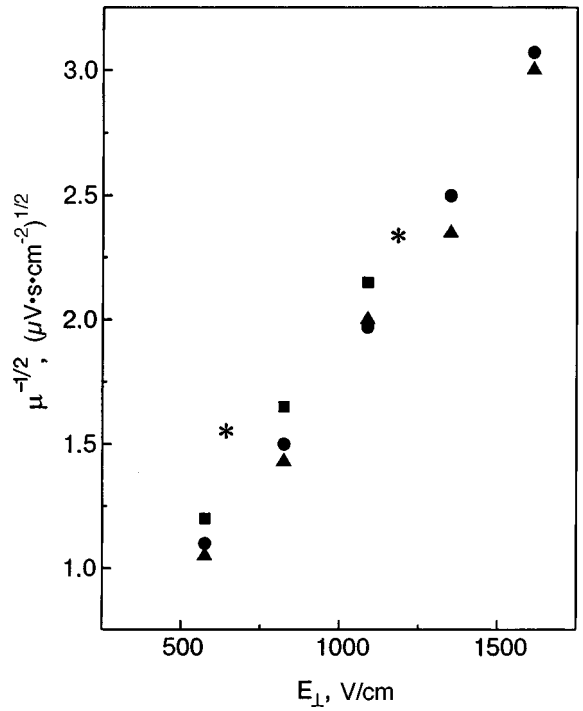

FIG. 7. Comparison of the mobility of electrons in a crystal with $n_s = 6.4 \times 10^8$ cm^{-2} at $T = 0.36$ (*) with the results of Ref. 15 obtained under nearly similar conditions: $n_s = 6.3 \times 10^8$ cm^{-2} and $T = 0.42$ K, for various frequencies.

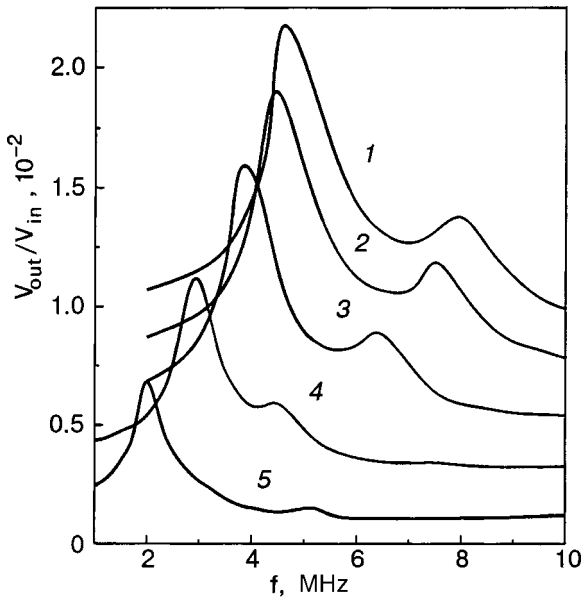

FIG. 8. Resonance spectra of the CEROs for crystals with different n_s [10^8 cm^{-2}]: 3.2 (*1*), 5.2 (*2*), 7.6 (*3*), 9.2 (*4*), 10.8 (*5*) at $T = 83$ mK with a holding field $E_\perp = 1150$ V/cm.

part of the inverse conductivity of an electron crystal with increasing holding field, and the dependence is different for crystals with different surface densities.

The values obtained in this study for the energy loss from the electron crystal are in good agreement with the results of Ref. 15, as is illustrated in Fig. 7, where the dependence of $\mu^{-1/2}$ is plotted as a function of the holding field (μ is the mobility, $\mu = (ne\chi_1)^{-1}$). Despite some difference in the temperatures at which the measurements were made, it is seen that rather good quantitative agreement is observed between the experimental data obtained in the present study (asterisks) and the data of Ref. 15.

Yet another important parameter that affects the properties of a 2D Wigner crystal is the surface density of electrons. Figure 8 shows the spectrum of coupled electron–ripplon oscillations, measured at a low fixed temperature $T = 83$ mK and a fixed holding field $E_\perp = 1150$ V/cm for 2D electron crystals with various surface densities $3.2 \times 10^8 - 10.8 \times 10^8$ cm^{-2}. In the spectra the (0,1) mode is pronounced and the (0,2) mode is clearly visible, its amplitude being much smaller than that of (0,1) on all the curves. The (0,3) mode, unlike the case in Fig. 1a, is not seen at all. The spectra corresponding to the crystals with different n_s are qualitatively similar, but the shift of the position of the (0,1) amplitude maximum with changing n_s is described well in the framework of the self-consistent theory.[6]

Good agreement with the theory of Ref. 8 is demonstrated in Fig. 9a, which shows the dependence of χ_2/ω on n_s, where the points are experimental data calculated from measurements at frequencies corresponding to the maxima of the amplitude, and the curve is the result of a theoretical estimation.

The dependence of the real part of the inverse conductivity on n_s is given in Fig. 9b. With increasing n_s at fixed T and $E_\perp$ the value of χ_1 decreases sharply. Thus the energy loss in the Wigner crystal, which is determined by the quantity χ_1, depends in a marked way on the holding field, the temperature, and the electron surface density. The absolute values of the losses can be compared with the values that follow from the assumption that the main loss mechanism is damping of capillary waves. Experimentally the damping of capillary waves with wavelengths $\lambda \sim 3.3-20$ μm was studied in Ref. 16. The results were presented in the form of the temperature dependence of the damping factor k''/k', which can be linked with the coefficient γ by the relation $k''/k' = (2/3)\gamma/\omega$. The value of the damping factor decreases with increasing frequency, and for the highest frequency at $T < 0.2$ K it is approximately 10^{-5}. Since in the present study the electron crystal is investigated at frequencies $\omega \sim 10^7$, approximately an order of magnitude higher than those at which the damping of capillary waves was investigated, the value of the damping factor $\sim 10^{-5}$ can be regarded as an estimated upper bound. This implies an estimated upper bound for the quantity $\gamma \sim 10^{-5} \times 10^7 = 10^2$. Analysis of the experimental values of χ_1 with the use of relations (11) shows that if it is assumed that the main mechanism of energy loss in the crystal is the damping of capillary waves,[8] then the value of γ should be of the order of 10^5. Thus the experimental values of the loss are at least three orders of magnitude greater than the estimates that follow from considering the damping of capillary waves to be the main loss mechanism.

In an analysis of the $\chi_1(T, E_\perp, n_s)$ dependences obtained, interesting results were obtained if the energy loss data are presented in the form $G_{\chi_1} = (n_s e^2/2m)(\chi_1/C_1)$, where the functional dependence on n_s, $E_\perp$, and T is taken into account in the forms which are characteristic for electron–ripplon coupling (the coefficient C_1 and the dependence on n_s). The relation between G_{χ_1} and χ_1 is analogous

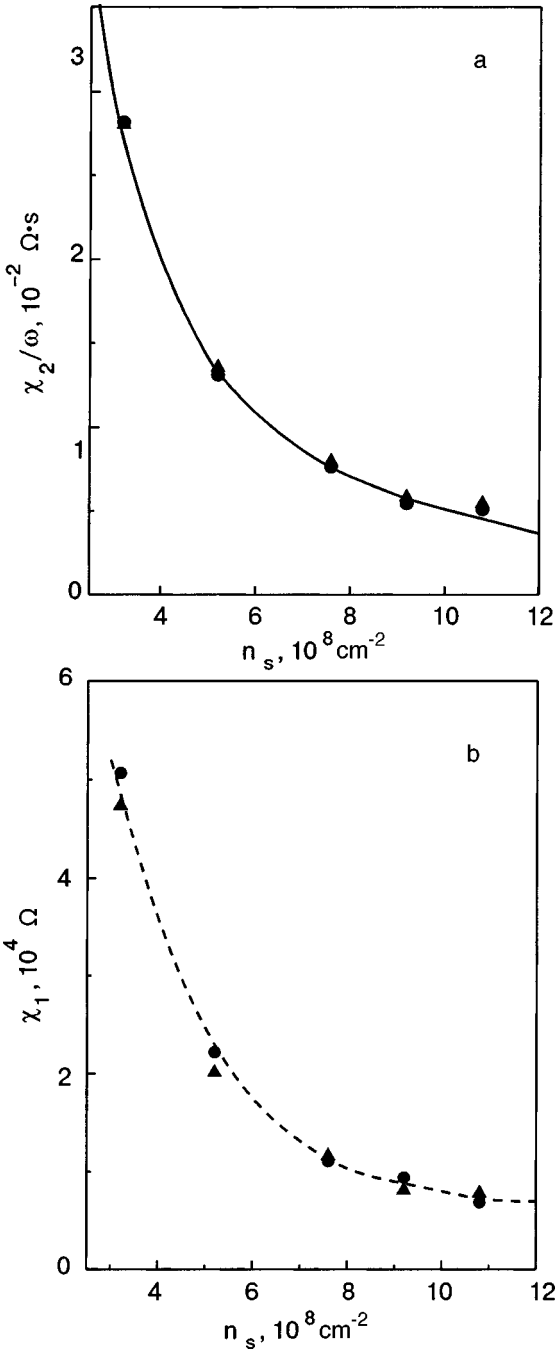

FIG. 9. Density dependence of the imaginary (a) and real (b) parts of the inverse conductivity of electron crystals at $T=83$ mK and $E_\perp=1150$ V/cm. The solid curve is a theoretical estimate in the framework of Ref. 8. The dashed curve is of an auxiliary character.

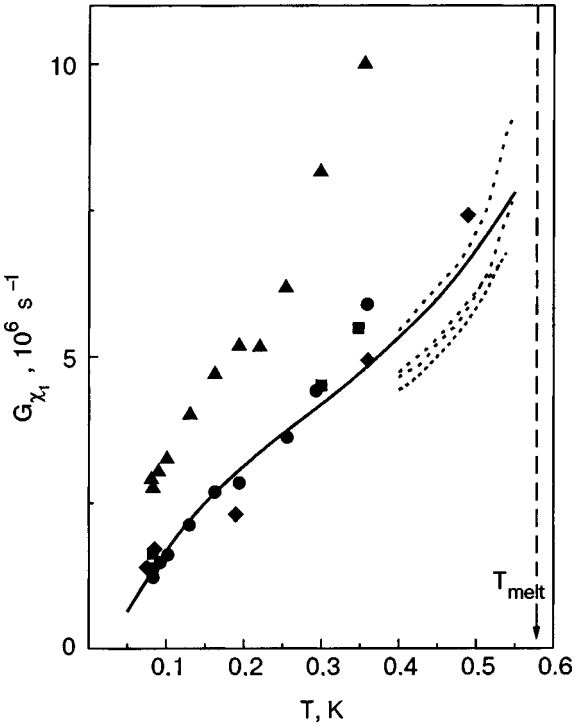

FIG. 10. Temperature dependence of the quantity $G_{\chi_1}=(e^2/2m)(n_s\chi/C_1)$ for a crystal with $n_s=6.4\times10^8$ cm^{-2} at $E_\perp=580$ V/cm (▲) and $E_\perp=1120$ V/cm (●) and for crystals with $n_s=9.1\times10^8$ cm^{-2} at $E_\perp=830$ V/cm (■) and $n_s=12\times10^8$ cm^{-2} at $E_\perp=1120$ V/cm (♦). The solid line shows a calculation according to the experimental data of Ref. 14 for a crystal with $n_s=5.5\times10^8$ cm^{-2} at $E_\perp=540$ V/cm; the dotted curves (from top to bottom) are calculations according to the experimental data of Ref. 15 for a crystal with $n_s=6.3\times10^8$ cm^{-2} for $E_\perp=570$, 845, 1121, and 1672 V/cm. The vertical dashed line corresponds to the melting temperature of the crystal with $n_s=6.4\times10^8$ cm^{-2}.

to the relation between γ and χ_1 in (11), but the definite physical meaning in G_{χ_1} is not made explicit, unlike the case of γ; this is simply a useful way of representing the experimental data on the energy loss of the crystal. Figure 10 shows the temperature dependence of G_{χ_1} for a crystal with $n_s=6.4\times10^8$ cm^{-2} at $E_\perp=580$ (▲) and 1120 V/cm (●) and for crystals with $n_s=9.1\times10^8$ cm^{-2} at $E_\perp=830$ V/cm (■) and $n_s=12\times10^8$ cm^{-2} at $E_\perp=1120$ V/cm (♦). It is seen that a unified dependence of G_{χ_1} is observed at large holding fields ($E_\perp>830$ V/cm) and for crystals with different surface densities, while for $E_\perp=580$ V/cm the values of G_{χ_1} turn out to be higher. The solid line is the result of a calculation according to the data of Ref. 14 for a crystal with $n_s=5.5\times10^8$ cm^{-2} at $E_\perp=540$ V/cm. One notices that this dependence agrees with the data obtained in the present study at high holding fields but differs markedly from G_{χ_1} for close value of the holding field $E_\perp=580$ V/cm. The dotted curves in Fig. 10 show the result of a calculation of $G_{\chi_1}(T)$ from the experimental data of Ref. 15, obtained in a study of an electron crystal with a density $n_s=6.3\times10^8$ cm^{-2} for different holding fields. The upper curve corresponds to the lowest value of the holding field $E_\perp=580$ V/cm, and the third curve from the top of these curves is for the field $E_\perp=1120$ V/cm, i.e., the experimental conditions in Ref. 15 are almost the same as those for the data of the present study, which are shown in Fig. 10. It is seen that G_{χ_1} decreases with increasing value of the holding field, and the data of Ref. 15 show that this decrease has a tendency toward saturation at high holding fields. The values of G_{χ_1} calculated according to the data of Ref. 15 correlate well with the results of the present study, which were obtained at higher holding fields but are noticeably smaller than the values of G_{χ_1} corresponding to the lowest field.

Such a pattern is evidence that G_{χ_1} is influenced by factors that are manifested differently in different experiments; its influence is suppressed as the holding field is increased. One such factor can be nonlinearity of the measurements, i.e., dependence of the results of measurements on the value

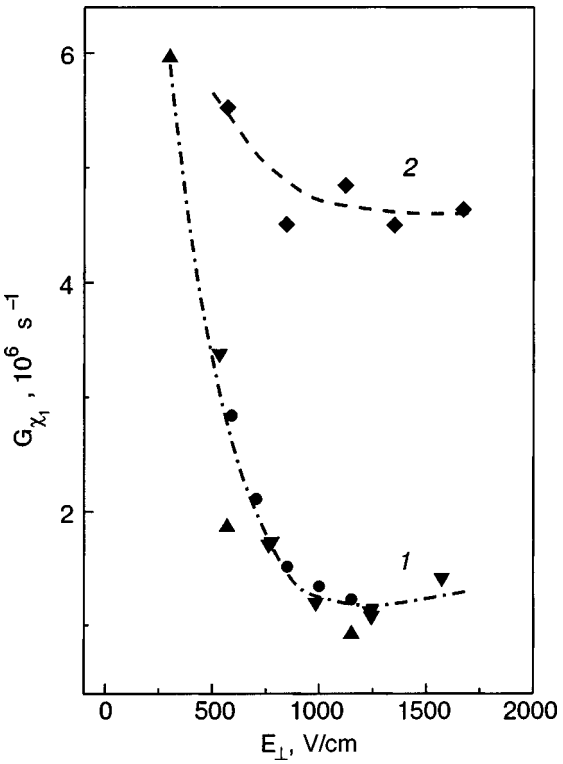

FIG. 11. Dependence of the quantity $G_{\chi_1}=(e^2/2m)(n_s\chi/C_1)$ on the holding field for $T=83$ mK for crystals with $n_s=6.4\times10^8$ cm^{-2} (▲, ▼) and $n_s=3.2\times10^8$ cm^{-2} (●) (*1*) and at $T=0.42$ K for a crystal with $n_s=6.3\times10^8$ cm^{-2} (◆), calculated according to the experimental data of Ref. 15 (*2*). The curves are of an auxiliary character.

of the driving field. As was noted above, the effective driving fields in the measurements of Refs. 14 and 15 were apparently smaller than in the present study, i.e., the measurement regime was closer to linear on account of the comparatively weak dependence of G_{χ_1} on the holding field. In the present study the measurement regime becomes close to linear at higher values of the holding fields than in Refs. 14 and 15.

Above, in an analysis of the resonance spectra (Fig. 1), it was assumed that the behavior of the (0,2) and (0,3) modes at small holding fields is a consequence of nonlinear effects which are suppressed as the holding field is increased. If that is the case, and the holding field indeed stabilizes the electron crystal, then it is clear that the value of G_{χ_1} is due to nonlinear processes. The higher the degree of nonlinearity, the more pronounced the dependence of G_{χ_1} on $E_\perp$.

The value of G_{χ_1} increases with increasing temperature (see Fig. 10) and has a tendency to increase sharply as the temperature approaches the melting point of the Wigner crystal, denoted in the figure by the vertical dashed line.

The dependence of G_{χ_1} on $E_\perp$ is seen more clearly in an analysis of the data obtained in measurements of $\chi_2(E_\perp)$ at fixed T and n_s.

Figure 11 shows the dependence of G_{χ_1} on the holding electric field $E_\perp$ for crystals with a surface density of 6.4×10^8 and 3.2×10^8 cm^{-2}, determined at a temperature of 83 mK, and also the dependence $G_{\chi_1}(E_\perp)$ at a temperature of 0.42 K, rescaled according to the data of Ref. 15 for an electron crystal with $n_s=6.3\times10^8$ cm^{-2}. It is seen that the points corresponding to different crystals at $T=83$ mK conform to a single curve. An appreciable dependence of G_{χ_1} on $E_\perp$ is observed at low fields, and for $E_\perp>1000$ V/cm the dependence goes out to a plateau. Roughly the same behavior is also observed at higher temperatures, as is illustrated by curve *2*, calculated according to the data of Ref. 15.

Thus at $E_\perp>1000$ V/cm the value of G_{χ_1} is independent of the holding field and the electron surface density. At lower holding fields ($E_\perp<1000$ V/cm) a sharp growth of G_{χ_1} is observed with decreasing field. The reason for this may be nonlinear effects due to the influence of the driving electric field on the conductivity of the crystal, this influence being suppressed as the holding electric field is increased. The nonlinearity can culminate in destruction of the 2D crystal structure, as is indirectly confirmed by the qualitative changes in the spectrum of the coupled electron–ripplon oscillations in Fig. 1. At large $E_\perp$ the stability of the crystal against the measuring signal increases, the measurement regime at that same signal level becomes closer to linear, and the parameter G_{χ_1} ceases to depend on the field, its value in this case being determined by mechanisms that are not related to the structural changes in the crystal.

The $G_{\chi_1}(E_\perp)$ curves for crystals with $n_s=3.2\times10^8$ and 6.4×10^8 cm^{-2} coincide (Fig. 11), indicating that G_{χ_1} is independent of n_s. This is also confirmed by the results of the conductivity measurements made at different n_s but fixed $E_\perp$ and T. At the same time as an appreciable dependence $\chi_1(n_s)$ is observed in these experiments (Fig. 9b), there is practically no $G_{\chi_1}(n_s)$ dependence. Under certain conditions ($E_\perp>1000$ V/cm, $\omega<\omega_1$) the real part of the inverse conductivity of the electron crystal can be written in the form $\chi_1\sim(C_1/n_s)\tilde{\chi}_1(T)$, where the function $\tilde{\chi}_1(T)$ depends on temperature but remains the same for crystals with different $E_\perp$ and n_s. This curious circumstance can prove useful in the theory analysis of the possible damping mechanisms in an electron crystal. From an experimental standpoint it is necessary to measure the conductivity of the electron crystal in different driving fields for investigation of the influence of nonlinear effects.

CONCLUSION

Thus in the present study we have investigated experimentally the conductivity of a 2D electron crystal over a liquid helium surface as a function of the main parameters that govern the electron–ripplon coupling and the properties of the crystal: the electron surface density, the holding electric field, and the temperature. Different series of measurements were made in which only one of these parameters was varied while the other two were held fixed. The studies covered the range of frequencies at which resonances of the coupled electron–ripplon oscillations were excited in the experimental cell. The conductivity of the crystal was determined from measurements of the amplitude and phase shift of the measuring signal at the frequency of the (0,1) resonance mode in its passage through the experimental cell. It was found that the behavior of the imaginary part of the inverse conductivity, which reflects the inertial properties of the crystal, is in good quantitative agreement with the existing theoretical ideas. At the same time, the mechanisms governing the energy loss from the crystal, i.e., the real part of

the conductivity, remain unclear. The dependence of the real part of the conductivity on the holding field, together with the changes in the spectrum of coupled oscillations, suggests that under certain conditions a substantial contribution to the energy loss from the crystal is made by processes due to the presence or the formation of defects of the 2D crystal structure of the electron crystal.

The author is grateful to V. V. Dotsenko for assistance in the experiments and to Yu. Z. Kovdra, Yu. P. Monarkha, and S. S. Sokolov for fruitful discussions.

*E-mail: syvokon@ilt.kharkov.ua

[1] G. Deville, E. Y. Andrei, and F. I. B. Williams, Phys. Rev. Lett. **53**, 588 (1984).
[2] D. C. Glattli, E. Y. Andrei, and F. I. B. Williams, Surf. Sci. **196**, 17 (1988).
[3] G. Deville, J. Low Temp. Phys. **72**, 135 (1988).
[4] C. C. Grimes and G. Adams, Phys. Rev. Lett. **42**, 795 (1979).
[5] D. S. Fisher, B. I. Halperin, and P. M. Platzman, Phys. Rev. Lett. **42**, 798 (1979).
[6] Yu. P. Monarka and V. B. Shikin, Fiz. Nizk. Temp. **9**, 913 (1983) [Sov. J. Low Temp. Phys. **9**, 471 (1983)].
[7] V. E. Syvokon', V. V. Dotsenko, Yu. Z. Kovdrya, and V. N. Grigor'ev, Fiz. Nizk. Temp. **22**, 1107 (1996) [Low Temp. Phys. **22**, 845 (1996)].
[8] Yu. P. Monarkha, Fiz. Nizk. Temp. **6**, 685 (1980) [Sov. J. Low Temp. Phys. **6**, (1980)].
[9] Yu. P. Monarkha, Fiz. Nizk. Temp. **7**, 692 (1981) [Sov. J. Low Temp. Phys. **7**, 338 (1981)].
[10] V. V. Dotsenko, V. E. Syvokon', Yu. Z. Kovdrya, and V. N. Grigor'ev, Fiz. Nizk. Temp. **23**, 1028 (1997) [Low Temp. Phys. **23**, 772 (1997)].
[11] V. E. Syvokon', V. V. Dotsenko, S. S. Sokolov, Yu. Z. Kovdrya, and V. N. Grigor'ev, Fiz. Nizk. Temp. **22**, 715 (1996) [Low Temp. Phys. **22**, 549 (1996)].
[12] C. F. Barenghi, C. J. Mellor, J. Meredith, C. M. Muirhead, P. K. H. Sommerfeld, and W. F. Vinen, Philos. Trans. R. Soc. London, Ser. A **334**, 139 (1991).
[13] J. M. Kosterlitz and D. J. Thouless, J. Phys. C **6**, 1181 (1973).
[14] R. Mehrotra, B. M. Guenin, and A. J. Dahm, Phys. Rev. Lett. **48**, 641 (1982).
[15] M. A. Stan and A. J. Dahm, Phys. Rev. B **40**, 8995 (1989).
[16] P. Roche, G. Deville, K. O. Keshishev, N. J. Appleyard, and F. I. B. Williams, Phys. Rev. Lett. **75**, 3316 (1995).

Translated by Steve Torstveit

SUPERCONDUCTIVITY, INCLUDING HIGH-TEMPERATURE SUPERCONDUCTIVITY

Electronic topological transition in $Re_{1-x}Mo_x$ alloys and its influence on the temperature of the superconducting transition

T. A. Ignatyeva and A. N. Velikodny

*National Science Center "Kharkov Institute of Physics and Technology," ul. Akademicheskaya 1, Kharkov 61108, Ukraine**

(Submitted May 21, 2003; revised December 5, 2003)
Fiz. Nizk. Temp. **30**, 523–534 (May 2004)

The features of the variation in the superconducting transition temperature T_c of $Re_{1-x}Mo_x$ alloys in the interval of Mo concentrations C up to 5 at.% (within the solid solution region) are investigated at pressures P of up to 10 kbar. A nonlinear increase of T_c to ≈ 5 K is observed when an impurity of $C \approx 4.7$ at.% Mo is added, and an inflection point is observed at $C \approx 2.35$ at.% Mo. The dependence $(\partial T_c/\partial P)(C)$ has a minimum at the same Mo concentration. This attests to the presence of a critical energy $E_c < E_F^0$ in the electron spectrum of Re. An Mo impurity, which is electronegative relative to Re, lowers the Fermi energy E_F^0 of Re, and when it crosses the level E_c of the top of the filled d band, which lies below the Fermi energy, an electronic topological transition (ETT) occurs under the influence of the Mo impurity at a concentration $C \approx 2.35$ at.%. The minimum and asymmetry of $(1/T_c)(\partial T_c/\partial P)(C)$ correspond to the appearance of a new hole pocket of the Fermi surface. The d electrons, with a high electronic density of states, emerge on the Fermi level; this gives a substantial contribution to the increase of T_c. In a quantitative comparison of the theory with experiment the difference $E_F^0 - E_c \approx 0.017$ eV and other parameters of the ETT are determined. © *2004 American Institute of Physics.* [DOI: 10.1063/1.1739133]

1. INTRODUCTION

The interest of researchers in studying the features of the electron spectrum of Re is not accidental. Rhenium is a transition metal having a complex electronic structure[1] that influences its physical properties. The increase in the superconducting transition temperature T_c of rhenium under the influence of impurities of negative valence (Mo, W) in the region of the solid solution was treated in Ref. 2 as being the result of the possible existence of a critical energy E_c (Refs. 3 and 4) in the electron spectrum of Re below the Fermi level E_F^0. There was no experimental proof. This brings us to the problem addressed in the present study: to investigate the features of the electron spectrum of rhenium in an energy interval below E_F^0, to determine the existence of E_c from the presence of an electronic topological transition (ETT), to find the critical values of the ETT parameters, including the distance $E_F^0 - E_c$, from a quantitative comparison of the theory[4,5] with experiment, and to correlated the ETT in Re under the influence of impurities of different valences with the changes in T_c.

The alloy $Re_{1-x}Mo_x$ in the solid solution region was chosen as the object of study, and the method chosen for determining the critical energy in the electron spectrum at the ETT was that of investigating the extremum of the derivative $(\partial T_c/\partial P)(P,C)$ (see Refs. 4 and 6), where P is the pressure and C is the impurity concentration. This method is based on studying the singularities $\delta\nu \approx (E_F^0 - E_c)^{1/2}$ predicted by Lifshits[3] in the electronic density of states, which arise in the electron spectrum of a metal in the presence of a critical energy E_c close to the Fermi level. Such features appear under the condition $E_F^0 \approx E_c$ as one of four possible types of electronic topological transitions, which alter the topology of the Fermi surface (FS).[3,4] This condition can be realized by varying E_F^0 under the influence of pressure in pure metals[3] or, as follows from Refs. 4–6, pressure plus impurities in alloys. ETTs were first observed from the features of the superconducting characteristics in Tl and its solid solutions containing small admixtures of impurities[6] and were given a theoretical grounding in Ref. 4. Those papers established a link between $\delta\nu \approx (E_F^0 - E_c)^{1/2}$ and the nonlinearity of $T_c(P,C)$ and $\partial\delta\nu/\partial E$ with the extremum of the derivative $(\partial T_c/\partial P)(P,C)$ at ETTs. In Ref. 4 the types of ETTs were defined in accordance with the asymmetry of the dependence $(\partial T_c/\partial P)(P,C)$ and the signs of the parameters of the ETT. In Refs. 7–9 and 12 it was shown that by simultaneous variation of the two parameters affecting E_F^0, one can bring E_F^0 maximally close to the singularity of the electron spectrum by the admixture of an impurity, which acts comparatively sharply, and then, using pressure to vary E_F^0 smoothly, pass through the singularity E_c in a narrow energy interval or determine the derivative of the measured characteristic with respect to pressure for the given impurity concentration. The energy region studied, $E > E_F^0$ or $E < E_F^0$, is determined by the the valence of the impurity used.

The results obtained by studying the ETTs from the superconducting characteristics for Tl, In, Mo, Re, α-U, Cd and their alloys have been compared quantitatively with the theory of Makarov and Bar'yakhtar[4,5] in Refs. 7–10 and 12.

For those metals the values of the ETT parameters $\pm(E_F^0 - E_c)$, the critical values of the impurity concentration or pressure at which the ETT occurs, and other parameters. Later it was show theoretically[17,18] and experimentally[13,19] that for normal metals the extremum corresponding to $\partial\delta\nu/\partial E$ at the ETT is manifested in the thermopower $(\alpha/T)(P,C)$. Alloys of thallium, indium,[7,8,19] Mo–Re, and Mo–Re–Nb[12,13] have been studied both in the superconducting and normal states, and a relation between the extrema of $(1/T_c)(\partial T_c/\partial P)(P,C)$ and $(\alpha/T)(P,C)$ at the ETT in the two cases was established. The results of those studies showed that investigation of the character of the behavior of $(1/T_c)(\partial T_c/\partial P)(P,C)$ and of the thermopower $(\alpha/T)\times(P,C)$ can be an efficient method for finding the critical points of the electron spectrum near the Fermi energy and can provide an unambiguous criterion of ETT. The extrema of $(1/T_c)(\partial T_c/\partial P)(P,C)$ and of the thermopower $(\alpha/T)\times(P,C)$ are always determined against a background of smooth variations of the quantities themselves and do in fact coincide with E_c or with a critical value of the parameter under whose influence the ETT occurs. As to the singularity $\delta\nu \approx (E_F^0 - E_c)^{1/2}$, which is manifested as nonlinearity in $T_c(C)$, the heat capacity, etc., it is difficult to identify against the background of the smooth variation of the quantity itself. At the same time, in combination with $(1/T_c)(\partial T_c/\partial P)\times(P,C)$ these data help determine the type of transition, and in a quantitative comparison with theory they increase the number of experimental points processed, which raises the confidence level for the parameter values obtained. One of the important parameters determined from the results of studies of the ETT in a comparison of theory with experiment[7–10,12,13] is the distance from the Fermi energy to the critical point $\pm(E_F^0 - E_c)$. The value of this quantity for different metals is 10^{-2}–10^{-3} eV and lies within the error limits of the theoretical calculations of the band structure of the electron spectrum. Therefore a comparison of these results with theoretical calculations of the band structure can only be qualitative. In addition, it is necessary to be mindful of the fact that the thermodynamic and kinetic characteristics contain the integrated electronic density of states, and it is impossible to identify the direction in which the change in the FS occurs in studies of the ETTs in accordance with the singularity of $\delta\nu(E_F)$. Therefore a comparison of the results of this study with the calculations of Ref. 1 can be regarded as qualitative, and the numerical values of $\pm(E_F^0 - E_c)$ obtained from the ETT data should be thought of as supplementary information.

Let us return to the discussion of the electronic structure of rhenium. Theoretical calculations of the electron spectrum of Re and comparison of these with the results of experimental studies of the Fermi surface are carried out in detail in Ref. 1. The topology of large parts of the Fermi surface of Re has been studied rather well, and the calculation of Ref. 1 agree with experiment, the topology of small parts of the FS along the AL and ΓM line, in accordance with calculations,[1] is very sensitive to the value of E_F^0 and has not been determined to sufficient accuracy. These calculations showed that a slight increase of E_F^0 by approximately 0.05 eV leads to a substantial change in the FS of rhenium in the 8th or 9th (10th) Brillouin zone. These theoretical findings point to possible changes in the topology of the FS of rhenium upon small changes in the Fermi energy in pure rhenium under external influences. In Refs. 2 and 15, where the dependences $T_c(P,C)$ and $(\partial T_c/\partial P)(P,C)$ for Re and its alloys in the energy region above E_F^0, a nonlinear dependence of $T_c(P)$ for Re and a high sensitivity of this derivative to small admixtures of impurities were observed, and an extremum of the dependence $(\partial T_c/\partial P)(P,C)$ was also observed in Re–Os alloys. These results were explained as being a manifestation of an ETT in Re at $E_F^0 \approx E_{c1}$. In Ref. 9, as a result of a comparison of the experimental data[15] with the theory,[4] the values of the ETT parameters in Re, including the distance from E_F^0 to the new pocket (E_{c1}) of the FS, which equaled ≈ 0.001 eV, were determined.

In the energy interval $E < E_F^0$ the $T_c(P)$ dependence was obtained only for several concentrations of rhenium alloys containing small admixtures of the impurities Mo and W,[2,15] indicating nontrivial behavior of T_c under the influence of impurities of lower valence, but giving no information about the ETTs in that energy region.

This energy region was investigated in the presence study. The features of the superconducting characteristics $T_c(C)$ and $(\partial T_c/\partial P)(P,C)$ of $Re_{1-x}Mo_x$ alloys was studied in the concentration interval 0–5 at. % Mo (the solid-solution region) and pressures of 0–10 kbar. The values of the thermopower were measured for several concentrations. A minimum of $(\partial T_c/\partial P)(P,C)$ was observed which is correlated with the nonlinear increase of $T_c(C)$ and the results on the thermopower. Using the concepts previously developed for ETTs, one can regard the results to be a consequence of an ETT in the energy region below E_F^0. The quantitative characteristics of ETTs are determined by comparison of the experimental data with the theory[4,5,9] The influence of the ETTs on the variation of T_c in rhenium under the influence of impurities is examined.

2. SAMPLE PREPARATION AND MEASUREMENT TECHNIQUES

$Re_{1-x}Mo_x$ alloys were prepared by electron-beam melting in a vacuum of 10^{-6} torr. The initial preforms, 6×8 mm in cross section and 60 mm long, were formed by pressing a mixture of high-purity Re and Mo powders in a certain weight relation and then melting. The number of passes through the melting zone (6–8) in two opposite directions was sufficient to give good uniformity of the impurity distribution in the sample. Stresses were eliminated by annealing the preforms at a temperature of $\approx 800\,^\circ$C. The samples for the measurements were cut out along the direction of motion of the melting zone, with dimensions of $1\times 0.5\times 7$ mm. The uniformity of the impurity distribution over the volume was monitored by the width of the superconducting transition, which was equal to 0.05–0.1 K. The impurity concentration was determined from the spectrum of the characteristic radiation to an accuracy as good as 3%. Measurements of the superconducting characteristics were carried out by the usual potentiometric method in an intermediate-temperature cryostat. The pressure was created in a high-pressure multiplier[20] and was determined from a manganin pressure gauge using the values of the coefficients known from the literature: $\partial \ln R/\partial P = 2.48\times 10^{-6}$ bar^{-1} at a

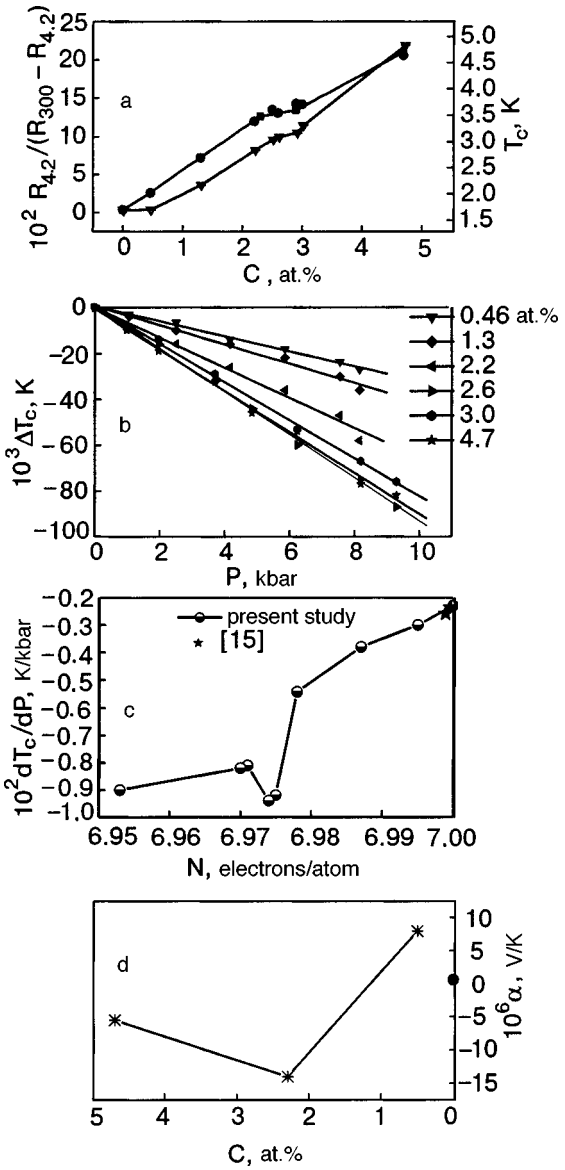

FIG. 1. a—Concentration dependence of the superconducting transition temperature T_c (▽) and the residual resistivity $\rho = R_{4.2\,\mathrm{K}}/(R_{300\,\mathrm{K}} - R_{4.2\,\mathrm{K}})$ (■,●) for the Re–Mo system; b—the dependence of the change in T_c on pressure for Re–Mo with different concentrations of the Mo impurity (the concentrations are indicated at the side of the panel); c—concentration dependence of dT_c/dP; d—thermopower of Re–Mo with concentrations of 0.5, 2.3, and 4.7 at. % Mo at $T \approx 6$ K.

temperature of 300 K and $\partial \ln R/\partial P = 2.6\times 10^{-6}$ bar^{-1} at 4.2 K. The uniformity of the pressure was judged from the parallel displacement of the transition of the samples to the superconducting state under the influence of pressure relative to the $P=0$ case. The experimental technique is described in detail in Ref. 21.

3. RESULTS OF THE MEASUREMENTS

Figure 1 shows the results of measurements of $T_c(C)$, $T_c(P)$, $(\partial T_c/\partial P)(C)$, and residual resistivity ρ of $Re_{1-x}Mo_x$ samples with different impurity concentrations (0–5 at. %) and the thermopower for several Mo concentrations (0.5, 2.3, and 4.7 at. %). As is seen in Fig. 1a, the admixture of Mo impurity to Re leads to nonlinear growth of $\rho(C)$ and of $T_c(C)$ from 1.7 K for pure Re to ≈ 5 K for $Re_{0.953}Mo_{0.047}$ with an inflection point of the $T_c(C)$ and $\rho(C)$ curves at ≈ 2.3 at. % Mo. Figure 1b shows the $\Delta T_c(P)$ dependence for $Re_{1-x}Mo_x$ alloys of various composition in the pressure interval 0–10 kbar; they are linear, and the derivative with respect to pressure is negative for all impurity concentrations. The $(\partial T_c/\partial P)(C)$ dependence is constructed from the data on $T_c(P)_{P\to 0}$ for the alloys studied and is plotted on the scale of electron concentration N in Fig. 1c. Here a minimum is observed at $N \approx 6.977$ electrons/atom, which corresponds to 2.3 at. % Mo. Figure 1d shows the values of the thermopower at 6.2 K for Re–Mo samples of three Mo concentrations (0.5, 2.3, and 4.7 at. %), measured simultaneously. The given values are negative, with the minimum corresponding to $C \approx 2.3$ at. % Mo. The value of the thermopower for pure rhenium, according to published data, fluctuates strongly, and the value shown in the graph was taken from the table in Ref. 22. The nonlinear growth of T_c, with an inflection point at $C \approx 2.3$ at. % Mo on the $T_c(C)$ curves, and of the residual resistivity $\rho = R_{4.2\,\mathrm{K}}/(R_{300\,\mathrm{K}} - R_{4.2\,\mathrm{K}})$ as a function of the impurity concentration, correlates with the fact that the minimum of $(\partial T_c/\partial P)(C)$ and the lowest value of $(\alpha/T)(C)$ are found at this same concentration; this attests to the commonality of their nature. According to notions about the connection between features of the superconducting and normal characteristics with ETTs under the influence of an impurity and pressure,[4,17] they can be attributed to changes in the topology of the Fermi surface under the influence of the impurity. The minimum and asymmetry in the $(\partial T_c/\partial P)(C)$ dependence, according to the theory,[4] corresponds to the formation of a hole pocket of the Fermi surface as E_F^0 decreases under the influence of the impurity. The sign and the minimum value of the thermopower for the alloys with 2.3 at. % Mo relative to the other two alloys (Fig. 1d) correlates with the results for $(\partial T_c/\partial P)(C)$ and confirms that the change in topology of the Fermi surface as being one in which a hole pocket appears on the Fermi surface.

4. COMPARISON OF THEORY WITH EXPERIMENT

For comparison of the theory with experiment we consider the $(1/T_c)(\partial T_c/\partial P)(C)$ and $T_c(C)$ curves for the systems Re–Mo (the results of the present study) and Re–Os (Refs. 2 and 15), which are shown in Fig. 2.

According to existing notions about ETTs in metals and alloys,[4,5,9] the features on these curves correspond to electronic topological transitions in rhenium under the influence of impurities. These features appear against the background of smooth components of T_c and its derivative, which are determined by the smooth variations of the electronic and phonon spectra.

In considering the results of this study, it is necessary to be mindful of the fact that the rather high concentrations of impurities in the alloys studied can affect the phonon spectrum. Experimentally, according to neutron diffraction data, a softening of the phonon spectrum is observed[23] which, according to theoretical estimates of T_c for Re, Re–Mo, and deformed Re,[23] introduces slight changes to $T_c(C)$ in comparison with the changes due to the electron spectrum. In this paper $T_c(C)$ is considered to be the result of changes of a smooth component $T_c^0(C)$ and a topological component

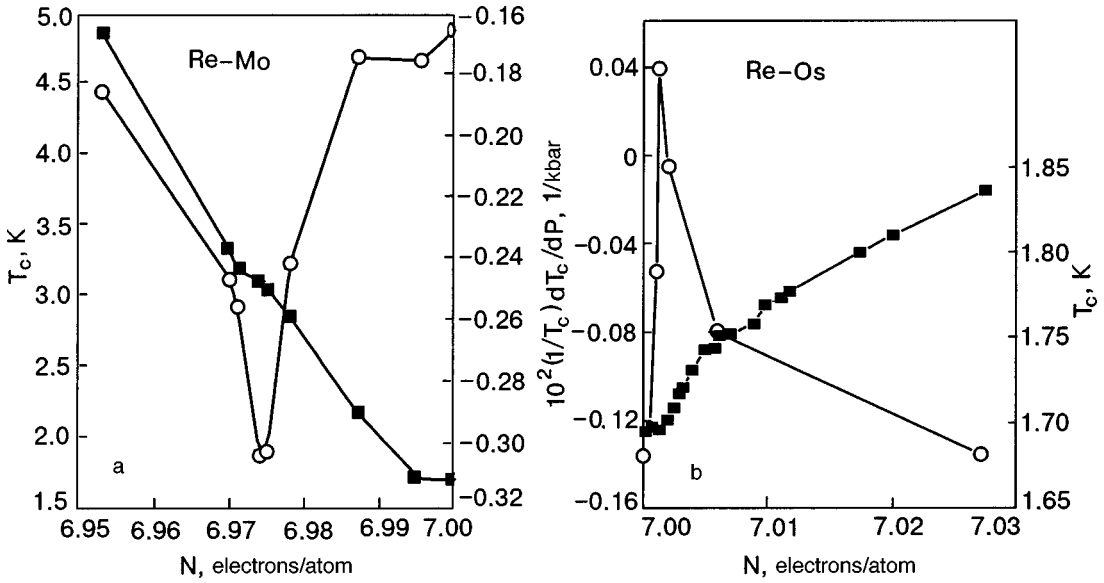

FIG. 2. Experimental concentration dependence of $T_c(N)$ (■) and $(1/T_c(\partial T_c/\partial P)(N)$ (○) for the systems Re–Mo (a, present study) and Re–Os (b, Refs. 2 and 15).

δT_c, which is due to the singularity $\delta\nu \approx (E_F^0 - E_c)^{1/2}$ in the electronic density of states. The changes of the phonon spectrum are reflected in the smooth background T_c^0, but the changes in the electronic density of states are assumed to be the determining factor. The influence of impurities on T_c due to their action as scattering centers is taken into account through a damping parameter Γ according to the theory of Ref. 16.

The comparison of the theory with experiment is done by the least squares method. The values of the parameters governing the electronic topological transition in rhenium under the influence of a Mo impurity are found. In the fitting of the parameters the experimental data for $T_c(C)$ and $(1/T_c)(\partial T_c/\partial P)(C)$ were used simultaneously, since they are described by the same parameters. This increased the number of data processed and improved the confidence level of the parameter values obtained.

In the present paper we use expression (2.15) from Ref. 9 with the approach proposed in Refs. 5 and 10, taking into consideration that the impurity concentrations are rather high. In this case the substantial variation of the smooth component $T_c^0(C)$ under the influence of the impurity must be taken into account as $\ln T_c^0(C) = \ln[T_c^* + (\partial T_c^0/\partial C)\Delta C]$, leaving $T_c^0(C)$ under the ln sign. Here T_c^* is the superconducting transition temperature of the pure metal. When these remarks are taken into account, the expression for comparison of the theory with experiment has the form of formula (1) below. In the limiting case of low concentrations this formula takes the form of expression (7) from Ref. 10, where the problem considered was the change of T_c under pressure and the $\ln T_c^0(P)$ dependence was written in the form

$$\ln T_c^* + \ln\left(1 + \frac{1}{T_c^*}\frac{\partial T_c^0}{\partial P}\Delta P\right) = \ln T_c^* + KP,$$

where the coefficient $K = (1/T_c^*)(\partial T_c^0/\partial P) \ll 1$, and $\ln[1 + (1/T_c^*)(\partial T_c^0/\partial P)\Delta P]$ can be written as KP. In the present paper we take into account that T_c is considerably more sensitive to the impurity than to pressure.[9,12] In this case $(1/T_c^*)(\partial T_c^0/\partial C)\Delta C$ can be close to 1 at comparatively high impurity concentrations, in which case it is more correct to write $\ln T_c^0(C)$ in the form

$$\ln T_c^* + \ln\left(1 + \frac{1}{T_c^*}\frac{\partial T_c^0}{\partial C}\Delta C\right).$$

The expression for comparison of theory with experiment in this approximation has the form

$$\ln\frac{T_c}{T_c^0}(C) = \frac{V}{2}I(\beta), \quad \text{where } T_c^0(C) = T_c^* + \frac{\partial T_c^0}{\partial C}\Delta C;$$

$$V = \frac{\delta\nu(E_F^0 + 2T_C^*)}{\nu_0^*(E_F^0)} = \frac{a\sqrt{2T_c^*}}{\nu_0^*(E_F^0)} \quad \text{(see Ref. 9)}$$

$$\beta = E_F^0 - E_c, \quad \ln\frac{T_c}{T_c^*}(C) = \ln\left(1 + \frac{1}{T_c^*}\frac{\partial T_c^0}{\partial C}\Delta C\right) + \frac{1}{2}\frac{\delta\nu(E_F^0 + 2T_c^*)}{\nu_0^*(E_F^0)}I(\beta);$$

$$I(\beta) = \int_{-\beta}^{\infty}\left|F\left(\frac{y}{SK_F}\right)\right|^2 \times \sqrt{\beta + y + \sqrt{(\beta+y)^2 + (\Gamma/2)^2}}\frac{\tanh(y/T_c)}{y}dy,$$

or, with the integrand normalized to $2T_c^*$, $I(\beta)$ takes the form

$$I(\beta,\lambda)=\sqrt{2T_c^*}\int_{-\beta}^{\infty}\left|F\left(\frac{2T_c^*}{SK_F}y\right)\right|^2\sqrt{\frac{1}{2T_c^*}\frac{\partial\beta}{\partial C}\Delta C+y+\sqrt{\left(\frac{1}{2T_c^*}\frac{\partial\beta}{\partial C}\Delta C+y\right)^2+\left(\frac{\Gamma}{4T_c^*}\right)^2}}\frac{\tanh\dfrac{y}{\lambda}}{y}dy,$$

where

$$\pm\frac{\partial\beta}{\partial C}\Delta C=\pm\frac{\partial(E_F^0-E_c)}{\partial C}\Delta C,\quad \frac{\Gamma}{4T_c^*}=B_6\rho,\quad \lambda=\frac{T_c}{2T_c^*}.$$

Then

$$\ln\frac{T_c}{T_c^*}(C)=\ln\left(1+\frac{1}{T_c^*}\frac{\partial T_c^0}{\partial C}\Delta C\right)+\frac{1}{2}\frac{\delta\nu(E_F^0+2T_c^*)}{\nu_0^*(E_F^0)}I(\beta,\lambda).\qquad(1)$$

Here T_c^0 is the smooth component of the variation of T_c under the influence of the impurity without the ETT taken into account; T_c^* is the superconducting transition temperature of the pure metal in the absence of external influences; $\beta=(E_F^0-E_c)$ is the distance from the Fermi level to the critical energy in the electron spectrum; Γ is the damping parameter, which takes into account process of scattering on impurities: $\Gamma\approx\rho$, where $\rho=R_{4.2\ \mathrm{K}}/(R_{300\ \mathrm{K}}-R_{4.2\ \mathrm{K}})$ is the residual resistivity. The $\rho(C)$ dependence is determined experimentally (see Fig. 1a) and is used in the quantitative calculations; $|F(T_c^*y/SK_F)|$ is the kernel of the effective electron–electron attraction. In this paper we compare the results for the Frohlich–Debye kernel[9] and the real kernel.[10]

We note that formula (1) of this paper generalizes the cases of pressure- and impurity-induced variations of T_c but is limited to the linear approximation for the change of T_c^0.

We introduce the following notation for the parameters:

$$B_1=V\sqrt{2T_c^*}=\frac{\delta\nu(E_F^0+2T_c^*)}{\nu_0^*(E_F^0)}\sqrt{2T_c^*},$$

where V is the relative change in the electronic density of states when $E_F^0=E_c+2T_c^*$; $B_3=(1/T_c^*)(\partial T_c^0/\partial C)$ is the change in the smooth component T_c^0 under the influence of the impurity; $B_4=(1/2T_c^*)\partial(E_F^0-E_c)/\partial C$ is the rate of change of $(E_F^0-E_c)$ under the influence of the impurity at the ETT; $B_5=C_{\mathrm{cr}}$ is the critical impurity concentration at which the ETT occurs; $B_6=\Gamma/4T_c^*\rho$ is the coefficient of proportionality between $\Gamma\approx1/\tau$ and $\rho=R_{4.2\ \mathrm{K}}/(R_{300\ \mathrm{K}}-R_{4.2\ \mathrm{K}})$. Then formula (1) is written in the form

$$\ln\frac{T_c}{T_c^*}(C)=\ln(1+B_3\Delta C)+\frac{B_1}{2}\int_{-\beta}^{\infty}\left|F\left(\frac{2T_c^*}{SK_E}y\right)\right|^2\times\sqrt{B_4\Delta C+y+\sqrt{(B_4\Delta C+y)^2+(B_6\rho)^2}}\frac{\tanh\dfrac{y}{\lambda}}{y}dy.\qquad(2)$$

The expression for $(1/T_c)(\partial T_c/\partial P)(C)$ obtained by differentiating formula (1) with allowance for the fact that T_c and the other parameters are functions of P and C is

$$\frac{1}{T_c}\frac{\partial T_c}{\partial P}=\frac{\dfrac{1}{T_c^0}\dfrac{\partial T_c^0}{\partial P}+\dfrac{B_1}{2}\dfrac{\partial\beta}{\partial C}\dfrac{\partial C}{\partial P}I'_\beta(\beta,\lambda)}{1+\dfrac{V}{2\lambda}J(\beta,\lambda)},\qquad(3)$$

where

$$J(\beta,\lambda)=\int_{-\beta}^{\infty}\left|F\left(\frac{2T_c^*}{SK_F}y\right)\right|^2\sqrt{\frac{1}{2T_c^*}\frac{\partial\beta}{\partial C}+y+\sqrt{\left(\frac{1}{2T_c^*}\frac{\partial\beta}{\partial C}+y\right)^2+\left(\frac{\Gamma}{4T_c^*}\right)^2}}\cosh^{-2}\frac{y}{\lambda}dy.$$

Using the tabulated values of $J(\beta,\lambda)$ within the specified range of integration, one can estimate the denominator of formula (3), which is approximately equal to unity for the system Re–Mo. Then the simplified expression for the derivative is

$$\frac{1}{T_c}\frac{\partial T_c}{\partial P}=\frac{\dfrac{1}{T_c^*}\dfrac{\partial T_c^0}{\partial P}+\dfrac{1}{T_c^*}\dfrac{\partial^2T_c^0}{\partial C\partial P}\Delta C}{1+\dfrac{1}{T_c^*}\dfrac{\partial T_c^0}{\partial C}\Delta C}+\left(\frac{1}{2}\frac{\delta\nu(E_F^0+2T_c^*)}{\nu_0^*(E_F^0)}\sqrt{2T_c^*}\right)\times\frac{1}{2T_c^*}\frac{\partial(E_F^0-E_c)}{\partial C}\frac{\partial C}{\partial P}I'_\beta(\beta,\lambda).$$

All of the symbols with an asterisk* pertain to pure rhenium without allowance for the the topology.

Using the parameters B_1, B_3, B_4, B_5, and B_6 introduced above and also $B_2=(1/T_c^*)(\partial^2T_c^0/\partial C\partial P)$, $B_7=\partial C/\partial P$ (the relative effectiveness of the influence of the impurity and pressure on the Fermi energy), and $B_8=(1/T_c^*)\partial T_c^0/\partial P$ (the change in the smooth component T_c^0 under the influence of pressure), we can rewrite formula (3) as

$$\frac{1}{T_c}\frac{\partial T_c}{\partial P}=\frac{B_8+B_2\Delta C}{1+B_3\Delta C}+\frac{1}{2}B_1B_4B_7I'_\beta(\beta,\lambda).\qquad(4)$$

As a result of a comparison of the theory according to formulas (2) and (4) with the experiment (Fig. 2), we obtained the values of the ETT parameters for the Re–Mo ($E<E_F^0$) and Re–Os ($E>E_F^0$) systems; these are given in Table

TABLE I. Parameters of the electronic topological transition for the Re-Mo and Re-Os systems.

Parameters	Dimensions	Re–Mo		Re–Os	
		Frohlich kernel	Real kernel	Frohlich kernel	Frohlich kernel (Ref. 9)
$B_1=\frac{\delta\nu(E_F^0+2T_c^*)}{\nu_0^*(E_F^0)}\sqrt{2T_c^*}$	$K^{1/2}$	$B_1=(19.6\pm0.6)\cdot10^{-3}$ $V=10.8\cdot10^{-3}$	$23.3\cdot10^{-3}$	$V=B_1/\sqrt{2T_c^*}=$ $=(5.6\pm0.6)\cdot10^{-3}$	$V=B_1/\sqrt{2T_c^*}=$ $=(6.0\pm0.6)\cdot10^{-3}$
$B_2=\frac{1}{T_c^*}\frac{\partial^2T_c^0}{\partial C\,\partial P}$	1/(at.%·kbar)	$(-1.2\pm0.3)\cdot10^{-4}$		$(4.9\pm1.7)\cdot10^{-5}$	
$B_3=\frac{1}{T_c^*}\frac{\partial T_c^0}{\partial C}$	1/at.%	$(22.5\pm0.3)\cdot10^{-2}$	$18.8\cdot10^{-2}$	$-(8.68\pm2.0)\cdot10^{-2}$	
$B_4=\frac{1}{2T_c^*}\frac{\partial(E_F-E_c)}{\partial C}$	1/at.%	18.9 ± 4.0	20.5 ± 6.0	-25 ± 3 or $\frac{\partial(E_F-E_c)}{\partial C}=$ $=-9.3\cdot10^{-3}$eV/at.%	$\frac{\partial(E_F-E_c)}{\partial C}=$ $=-9\cdot10^{-3}$eV/at.%
$B_5=C_{cr}$	at.%	2.35 ± 0.03		0.125	
$B_6=\frac{\Gamma}{4T_c^*\rho}$	K^{-1}	6	5		
$B_7=\frac{\partial C}{\partial P}$	at.%/kbar	$-(8.5\pm2.0)\cdot10^{-3}$	$-(7.5\pm1.2)\cdot10^{-3}$	$(16.5\pm2.0)\cdot10^{-3}$	$16.9\cdot10^{-3}$
$B_8=\frac{1}{T_c^*}\frac{\partial T_c^0}{\partial P}$	1/kbar	$-(1.58\pm0.8)\cdot10^{-3}$	$-1.7\cdot10^{-3}$	$-(2.1\pm0.5)\cdot10^{-3}$	$-2.35\cdot10^{-3}$
T_c^*	K	1.57	1.66	1.67	

I. Also given there are the parameters for the Re–Os system which were obtained in Ref. 9 by comparison of the theory of Ref. 4 with the experiment of Ref. 15. According to the data in Table I we can make a quantitative comparison of the features of the electron spectrum of rhenium on the two sides of the Fermi energy.

A parameter common to the whole set of experimental data for Re and its alloys (from different studies) is $B_8=(1/T_c^*)(\partial T_c^0/\partial P)$, the value of which, as is seen from Table I, agrees to within 15–20% for the different data. For Re–Os good quantitative agreement of the results of the calculations of the present study and those of Ref. 9 is also seen, although different experimental results were used in the calculations. This shows that the chosen theoretical approximation of the concentration dependences $\ln[T_c/T_c^*(C)]$ and $(1/T_c)(\partial T_c/\partial P)(C)$ (formulas (2) and (4)) is a fair approximation of the experimental results.

With the values of the parameters B_4 and B_5 (see Table I) taken into account, the distance of E_F^0 to the critical points E_{c1} and E_{c2} were determined: $E_F^0-E_{c2}=0.017$ eV for Re–Mo and $E_{c1}-E_F^0=0.001$ eV for Re–Os.

Thus it is seen that E_{c2} is found below the Fermi energy E_F^0, and E_{c1} is above E_F^0. The parameter $B_7=\partial C/\partial P\approx10^{-2}$ shows that the presence of an impurity is considerably more effective than pressure in changing the Fermi energy. The sign of the parameter B_7 shows that variation of the pressure shifts the Fermi energy of rhenium in the same direction as does the admixture of an Os impurity (higher valence) and in the opposite direction to the admixture of an Mo impurity (lower valence). The fact that in both cases the parameter $B_1=\delta\nu(E_F^0+2T_c^*)\sqrt{2T_c^*}/\nu_0^*(E_F)$ is positive implies that the electronic density of states on both sides of E_F^0 increases at the ETT when impurities of any valence are added, and the topological contributions $\delta T_c(C)$ are positive. When the sign and magnitude of the smooth component T_c^0 are taken into account, this corresponds to the situation that E_F^0 of pure Re is found at a minimum of the electronic density of states (see Sec. 5).

The results of a quantitative comparison of the experimental data and the theoretical dependences $T_c(C)$ and $(1/T_c)\partial T_c/\partial P)(C)$ with different kernels of the electron–phonon interaction for the Re–Mo system are presented in Figs. 3 and 4, respectively.

It is clear from the table and figures that the type of kernel of the electron–phonon interaction does not have a substantial influence on the agreement of experiment and

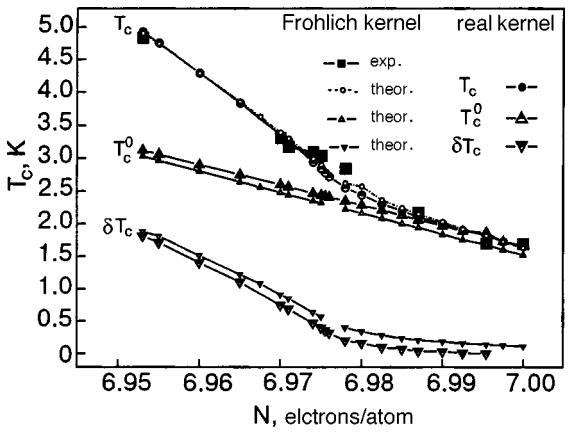

FIG. 3. Results of a comparison of theory and experiment (■) for the dependence $T_c(N)$ in the Re–Mo system with different kernels of the electron–phonon interaction.

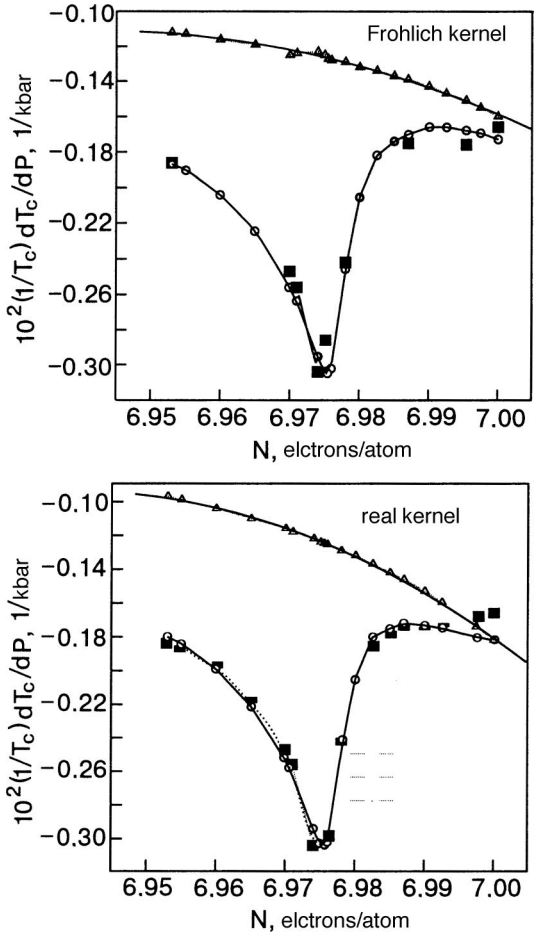

FIG. 4. Results of a comparison of the theory (○) with experiment (■) for the dependence of $(1/T_c(\partial T_c/\partial P)(N)$ in the Re–Mo system for different kernels of the electron–phonon interaction (△ is the theoretical calculation for T_c^0).

theory: the difference of the quantitative characteristics lies within the error limits for the determination of the parameters. The quantitative agreement of the theory and experiment for $T_c(C)$ and $(1/T_c)(\partial T_c/\partial P)(C)$ of $Re_{1-x}Mo_x$ alloys with allowance for the ETT at the same values of the parameters attests to the commonality of the nature of the features of those characteristics.

In the next Section we consider the influence of ETTs on the variation of T_c for rhenium under the influence of impurities of different valence.

5. DISCUSSION OF THE RESULTS

One of the main results of this study is the detection of an ETT in the system $Re_{1-x}Mo_x$ from the position of the minimum of $(1/T_c)(\partial T_c/\partial P)(C)$. According to the theory of Ref. 4, the minimum and the asymmetry of the $(1/T_c)\times(\partial T_c/\partial P)(C)$ curve and the sign of the parameters B_1 and B_4 (see Table I) are due to the appearance of a new hole pocket of the Fermi surface as the E_F^0 level of rhenium decreases under the influence of Mo. The negative sign and the change in the thermopower as functions of composition for the given concentrations (Fig. 1d) also corresponds to changes in the topology of the hole pockets of the Fermi surface.

Let us discuss these results in combination with earlier experimental data and their theoretical processing for pure rhenium and its weak solutions. It follows from the experimental results[15] that E_F^0 in pure rhenium does in fact fall in the region of energies where such a topological singularity is already partially mainfested in pure Re, as nonlinearity of $T_c(P)$ at comparatively low pressures. The extremum of $(1/T_c)(\partial T_c/\partial P)(C)$ (see Fig. 2) at small admixtures ($\sim$0.125 at. %) of osmium corresponds to the appearance of an electron group as E_F^0 rises under the influence of the Os impurity.[2,9,15] As in the case of thallium,[7] such a feature is manifested in rhenium as an anomaly in two parts: nonlinearity of $T_c(P)$ in the pure metal at energies above E_F^0, including an energy interval containing E_{c1}, and the continuation of the anomaly as a ''shoulder'' or ''wing'' of the feature in the energy region below E_F^0. Because of this, the $T_c(P)$ dependence of pure rhenium is sensitive to small admixtures of impurities of different valence,[15] when, by shifting E_F^0 through a change in the impurity concentration, one can arrive at different parts of the nonlinear $T_c(P)$ dependence. The appearance of a ''wing'' of the feature, due to the small electron group above the Fermi level at energies below E_F^0, may be one of the mechanisms that lead to a kink in the $T_c(C)$ and $(1/T_c)(\partial T_c/\partial P)(C)$ curves for the $Re_{1-x}Mo_x$ system at low Mo concentrations, as is seen from the results of the present study (Fig. 2a). In Refs. 2,9, and 15 it was concluded that there is a critical energy $E_{c1}>E_F^0$ corresponding to the bottom of the new pocket of the Fermi surface, at a distance of $\approx$0.001 eV from E_F^0 (Ref. 9). The value $E_{c1}-E_F^0\approx 0.001$ eV is less than the error of the theoretical calculations.[1] This brings clarity to the discussion in Ref. 1 as to the presence or absence of an electron pocket in the 8th, 9th, and 10th Brillouin zones in pure rhenium. The results of the present study suggest that there is another critical energy E_{c2} that lies a distance $\approx$0.017 eV below the Fermi level E_F^0. It corresponds to the top of the band whose crossing with the Fermi level leads to the new hole pocket of the Fermi surface under the influence of a Mo impurity. This is qualitatively comparable with the theoretical calculations, according to which there are several d bands[1] below the Fermi level with a high partial density of states.[24] It can be supposed that the energy E_{c2} observed experimentally from the ETT corresponds to the top of one of those bands. Quantitative estimates of the distance $E_F^0-E_{c2}$ obtained in the study of Re–Mo alloys in the present study supplement the information about the fine structure of the electron spectrum of rhenium below the Fermi level.

We have made estimates of the influence of the ETT on the temperature of the superconducting transition of rhenium, according to Ref. 9. We call attention to the fact that an impurity of lower valence (Mo) increases T_c from 1.7 K for pure rhenium to $\approx$5 K for $C\approx$4.7 at. % Mo, while an impurity of higher valence (Os) increases it only to $\approx$1.9 K at $C\approx$5 at. % Os.[2] To establish how the changes in T_c are related to the valence of an impurity (with both the sign and the concentration taken into account) it is necessary to determine the signs and magnitudes of the contributions of the changes of the smooth component $\Delta T_c^0=T_c^0-T_c^*$ and the topological contribution δT_c to the resultant change $\Delta T_c(C)=\Delta T_c^0+\delta T_c$. Figure 5 shows the experimental

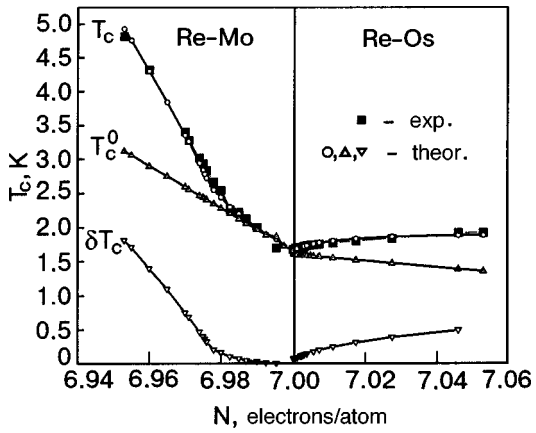

FIG. 5. Concentration dependence of T_c, T_c, δT_c (theory) for the systems Re–Mo and Re–Os: experimental points $T_c(N)$ (■) for Re–Mo (the results of the present study) and for Re–Os (the data of Ref. 2).

curves of $T_c(N)$ and the results of a theoretical processing for the systems $Re_{1-x}Mo_x$ and $Re_{1-y}Os_y$ on the electron concentration scale. The $T_c(N)$ curves are separated into the smooth T_c^0 and topological δT_c components for alloys with impurities of different valence in accordance with the values of the parameters (see Table I) and formula (2). It follows from Fig. 5 that the topological contributions $\delta T_c(C)$ are positive on both sides of E_F^0 and that the change in the smooth component $\Delta T_c^0 > 0$ when $E < E_F^0$ and $\Delta T_c^0 < 0$ when $E > E_F^0$. The relative size of the two components determines the sign and magnitude of the resultant change ΔT_c: for an Mo impurity both components $\delta T_c(C)$ and ΔT_c^0 have the same sign and reinforce each other, while for an Os impurity they have different signs and partially compensate each other. This corresponds to a substantial quantitative difference in the changes of T_c in rhenium under the influence of Mo and Os impurities.

Let us discuss in more detail the determination of the sign of the changes in the smooth component ΔT_c^0 under the external influences of an impurity and pressure. We recall that ΔT_c^0 is treated under the assumption that the change of the phonon spectrum is insignificant and that the predominant role in the influence on T_c is played by the electronic density of states. The change T_c^0 under the influence of an impurity can be written as

$$T_c^0(C) = \frac{\partial T_c^0}{\partial C}\Delta C = \frac{\partial T_c^0}{\partial E}\frac{\partial E}{\partial C}\Delta C,$$

and in the case of pressure as

$$T_c^0(P) = \frac{\partial T_c^0}{\partial P}\Delta P = \frac{\partial T_c^0}{\partial E}\frac{\partial E}{\partial P}\Delta P.$$

In both cases it is assumed that $\partial T_c^0/\partial E \approx \partial \nu_0/\partial E$ and that the sign of $\partial T_c^0/\partial E$ is determined by the sign of $\partial \nu_0/\partial E$ independently of the form of the influence on the Fermi energy of pure Re ($\partial \nu_0/\partial E$ corresponds to the electronic structure of the pure metal). Upon a change in E_F^0 under conditions of hydrostatic pressure one always has $(\partial E/\partial P)\Delta P > 0$. Consequently, the sign of $\partial T_c^0/\partial P$ is determined by the sign of $\partial T_c^0/\partial E$ or, equivalently, of $\partial \nu_0/\partial E$. This conclusion is of interest in itself, since $\partial T_c/\partial P$ is an experimentally measured quantity, and, by comparing the signs of $\partial T_c/\partial P|_{P\to 0}$ and $\partial \nu_0/\partial E$ one can judge the character of the conductivity of the pure material (electron or hole). The sign of $\partial T_c/\partial P|_{P\to 0}$ for pure rhenium is negative; it was determined experimentally in Ref. 15 and in the present study as the parameter $B_8 = (1/T_c^*)(\partial T_c^0/\partial P)$ (see Table I). Then the changes in δT_c due to the nonlinear contributions on both sides of the Fermi energy of Re must be considered against the background of the negative trend of $\partial \nu_0/\partial E$ of pure Re, i.e., against the background of the hole pockets. Such an interpretation agrees with Ref. 1, where the theoretical dependence $\nu(E)$, obtained in accordance with the band structure of Re, has a negative derivative at energies $E \approx E_F^0$.

Taking into account what we have above, let us consider the sign of the change in the smooth component ΔT_c^0 under the influence of impurities, which is determined by the product $(\partial T_c^0/\partial E)(\partial E/\partial C)\Delta C$. The sign of $\partial T_c^0/\partial E$ for rhenium has already been found to be negative for any change of the Fermi energy E_F^0. The sign of $(\partial E/\partial C)\Delta C$ corresponds to the valence of the impurity. If we let energies be measured from E_F^0, then $\Delta E > 0$ for an Os impurity and $\Delta E < 0$ for a Mo impurity. Then for Re the sign of the change in the smooth component ΔT_c^0 (the sign of the product) is negative in the case of an impurity of higher valence (Os) and positive for an impurity of lower valence (Mo); see Fig. 5. When the signs of the topological and smooth contributions to the resultant change in T_c for impurities of different valence are taken into account, there is agreement in terms of their quantitative difference. In the Re–Mo system the change ΔT_c is substantially larger than in Re–Os. It follows from the results of this study that in rhenium the small pockets of the Fermi surface arising at the ETT turn out to have a substantial effect on the change in T_c, comparable to that of the main groups. Furthermore, the positive sign of the resultant change of T_c in Re under the influence of impurities of different valence corresponds to the fact that in pure rhenium E_F^0 is found at the minimum of the electronic density of states.

Topological features of the electronic density of states of rhenium $(\delta\nu/\nu_0)(E_F)$ and their agreement with the topological component $\delta T_c/T_c^0$ for the $Re_{1-x}Mo_x$ and $Re_{1-y}Os_y$ systems can be estimated using formulas (2.7) and (2.8) of Ref. 9 and the parameter B_1 from Table I. The curves of $(\delta\nu/\nu_0)(E_F)$ as a function of $E - E_F^0$ in the energy intervals $E \leqslant E_F^0$ and $E \geqslant E_F^0$ were calculated for the Re–Os and Re–Mo systems and are presented in Fig. 6a, where the critical energies E_{c1} and E_{c2} are indicated. The reference point for the energy $(E - E_F^0)$ is the value of E_F^0 for pure rhenium. These results show that the features of the changes in $(\delta\nu/\nu_0)(E_F)$ for any changes of E_F^0 are positive and agree quantitatively with the changes $\delta T_c/T_c^0$ (Fig. 6b). According to the results of Ref. 24, below the Fermi level the *d* electrons have a high partial density of states. Consequently, it can be assumed that as E_F^0 is lowered, when a new hole pocket of the Fermi surface forms under the influence of the Mo impurity, the *d* electrons, with a high electronic density states, emerge on the Fermi level and make a substantial contribution to the increase of T_c. The sign of the change in T_c, as we have seen, corresponds to the valence of the impurities if the electronic topological transitions are taken into account.

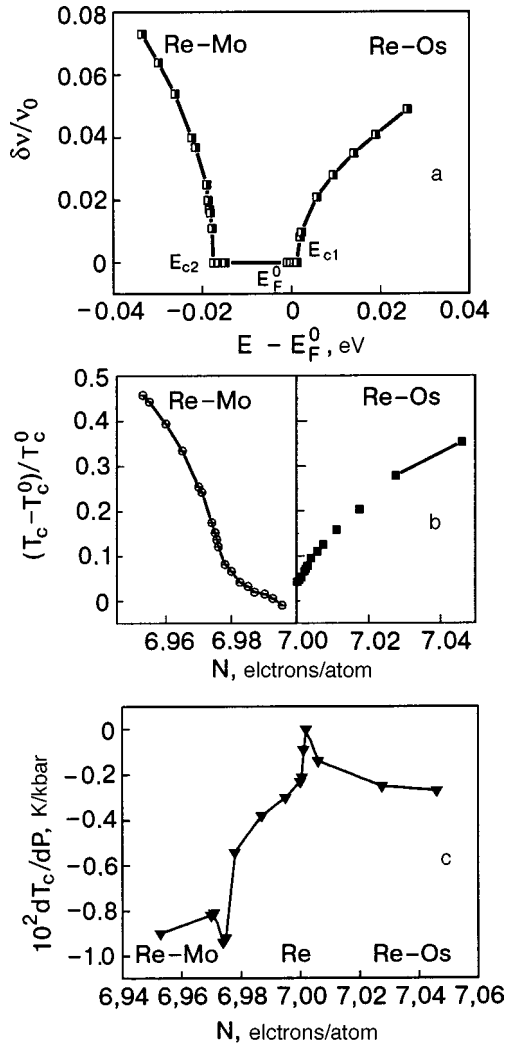

FIG. 6. a—Relative variation of the topological contribution to the electronic density of states as a function of $E-E_F^0$ for the systems Re–Mo and Re–Os with an indication of the critical energies (calculation according to Eqs. (2.7) and (2.8) of Ref. 9 with the parameters B_1); b—relative variation of the topological contribution $(\delta T_c(N)/T_c^0)$ (theory); c—experimental dependence of $(dT_c/dP)(N)$ for the systems Re–Mo (present study) and Re–Os (Ref. 2).

The question of the reasons for the increase of T_c has been discussed previously in a study of the spectra of the electron–phonon interaction by the method of point-contact (PC) spectroscopy. In those experiments the appearance of a new peak in the PC spectra of Re–Mo alloys was observed, starting with the concentration $C \approx 3$ at. % Mo and above.[23] Analogous features have been obtained in the PC spectra of the Re–W system and were first interpreted as a manifestation of quasilocal oscillations in the phonon spectrum. However, neutron diffraction studies have revealed only a smooth variation of the phonon density of states $g(\omega)$ in the low-frequency region of the spectrum, and therefore quantitative estimates of the change in T_c taking into account only the change in the phonon spectrum have failed to explain the increase of T_c in rhenium. If the electron–phonon coupling parameter $\lambda_{\text{eff}} \sim g(\omega)\nu(E)$ (where $\nu(E)$ is the electronic density of states) determined experimentally from the PC spectra is used for estimating T_c, then one observes quantitative agreement with the experimental data on T_c (Ref. 23). The authors of Ref. 23 came to the conclusion that the features of the PC spectra and the increase in T_c are due to features of the electron spectrum. The results of our study—the observation of an ETT at $C \approx 2.35$ at. % Mo in Re—can be regarded as experimental confirmation of that conjecture.

6. CONCLUSIONS

1. In the $Re_{1-x}Mo_x$ system a minimum of the derivative $(1/T_c)(\partial T_c/\partial P)(C)$ is found at a concentration $C \approx 2.35$ at. % Mo. In accordance with the exchange of electronic topological transitions (ETTs),[4] the minimum and asymmetry of the derivative and sign of the parameters B_1 and B_4 correspond to an ETT—the formation of a hole pocket of the Fermi surface.

2. The parameters of the ETT for the $Re_{1-x}Mo_x$ system have been determined by a quantitative comparison of the theory[4] with experiment: the distance from the Fermi level to the critical point is $E_F^0 - E_{c2} \approx 0.017$ eV, and the critical concentration at which the change in topology of the Fermi surface occurs is $C_{\text{cr}} \approx 2.35$ at. % Mo.

3. We have established a correlation between the nonlinear changes in the superconducting transition temperature of Re under the influence of impurities, with an extremum of $(1/T_c)(\partial T_c/\partial P)(C)$ in $Re_{1-x}Mo_x$ and $Re_{1-y}Os_y$ alloys. The variations of T_c in these systems was considered with allowance for the ETTs at E_{c2} in the energy interval $E < E_F^0$ for $Re_{1-x}Mo_x$ and at E_{c1} in the energy interval $E > E_F^0$ for $Re_{1-y}Os_y$. It is shown that these transitions have a substantial influence on T_c in rhenium.

4. In the framework of the ETT theory we have separated the contributions of the smooth and topological components of the change in T_c for the systems $Re_{1-x}Mo_x$ and $Re_{1-y}Os_y$ in accordance with the ETT parameters given in Table I. We have shown that they are quantitatively comparable. Estimates were made for $(\delta\nu/\nu_0)(E_F)$ according to the theory[4,9] with allowance for the values of the parameters V for Re–Os and Re–Mo alloys (see Table I). We showed that the changes $(\delta\nu/\nu_0)(E_F) > 0$ when impurities of any valence are added, and they agree with the variations of $\delta T_c/T_c^0$ in both cases.

5. We have shown that the resultant change in T_c is positive on both side of the Fermi energy. This accords with the fact that E_F^0 lies close to the minimum of the electronic density of states. From the whole set of experimental data on the study of ETTs it follows that E_F^0 is almost coincident with E_{c1}. This is in qualitative agreement with the theoretical calculations of the electronic density of states[24] and is quantitatively consistent with the changes in the superconducting transition temperature.

6. We have shown that taking into account the sign and magnitude of the contributions to the change in T_c in rhenium alloys from the smooth and topological components leads to a correspondence between the variation of $T_c(C)$ and the valence of the particular impurity.

*E-mail: tikhonovsky@kipt.kharkov.ua

[1] L. F. Mattheiss, Phys. Rev. **151**, 464 (1966).
[2] C. W. Chu, W. L. McMillan, and H. L. Luo, Phys. Rev. B **3**, 3757 (1971).

[3] I. M. Lifshits, Zh. Éksp. Teor. Fiz. **38**, 1569 (1960) [Sov. Phys. JETP **11**, 1130 (1960)]; L. Van Hove, Phys. Rev. **89**, 1189 (1953).
[4] V. I. Makarov and V. G. Bar'yakhtar, Zh. Éksp. Teor. Fiz. **48**, 1717 (1965) [Sov. Phys. JETP **21**, 1151 (1965)].
[5] V. I. Makarov, Fiz. Nizk. Temp. **3**, 1 (1977) [Sov. J. Low Temp. Phys. **3**, 9 (1977)].
[6] B. G. Lazarev, L. S. Lazareva, V. I. Makarov, and T. A. Ignat'eva, Zh. Éksp. Teor. Fiz. **48**, 1065 (1965) [Sov. Phys. JETP **21**, 711 (1965)]; N. B. Brandt, N. I. Ginzburg, B. G. Lazarev, L. S. Lazareva, V. I. Makarov, and T. A. Ignat'eva, Zh. Éksp. Teor. Fiz. **49**, 85 (1965) [Sov. Phys. JETP **22**, 61 (1965)].
[7] T. A. Ignat'eva, Yu. A. Cherevan', and V. I. Makarov, Zh. Éksp. Teor. Fiz. **67**, 94 (1974) [Sov. Phys. JETP **40**, 492 (1975)].
[8] I. Ya. Volynskiĭ, V. I. Makarov, and V. V. Gann, Zh. Éksp. Teor. Fiz. **69**, 1019 (1975) [Sov. Phys. JETP **42**, 518 (1975)].
[9] V. G. Bar'yakhtar, V. V. Gann, V. I. Makarov, and T. A. Ignat'eva, Zh. Éksp. Teor. Fiz. **62**, 1118 (1972) [Sov. Phys. JETP **35**, 591 (1972)].
[10] V. I. Makarov, V. Z. Kleĭner, and T. A. Ignat'eva, Fiz. Nizk. Temp. **5**, 1022 (1979) [Sov. J. Low Temp. Phys. **5**, 482 (1979)].
[11] C. L. Watlington, J. W. Cook, and M. J. Skove, Phys. Rev. B **15**, 1370 (1977).
[12] T. A. Ignat'eva, V. V. Gann, and A. N. Velikodnyĭ, Fiz. Nizk. Temp. **20**, 1133 (1994) [Low Temp. Phys. **20**, 890 (1994)].
[13] T. A. Ignat'eva and A. N. Velikodnyĭ, Fiz. Nizk. Temp. **28**, 569 (2002) [Low Temp. Phys. **28**, 403 (2002)].
[14] M. A. Krivoglaz and Tyu-Khao, Fiz. Met. Metalloved. **21**, 817 (1966).
[15] C. W. Chu, T. F. Smith, and W. B. Gardner, Phys. Rev. Lett. **20**, 198 (1968); C. W. Chu, T. F. Smith, and W. B. Gardner, Phys. Rev. B **1**, 214 (1970).
[16] V. I. Makarov, V. G. Bar'yakhtar, and V. V. Gann, Zh. Éksp. Teor. Fiz. **67**, 168 (1974) [Sov. Phys. JETP **40**, 85 (1975)].
[17] V. G. Vaks, A. V. Trefilov, and S. V. Fomichev, Zh. Éksp. Teor. Fiz. **80**, 1613 (1981) [Sov. Phys. JETP **53**, 830 (1981)].
[18] A. A. Varlamov and A. V. Pantsulaya, Zh. Éksp. Teor. Fiz. **89**, 2188 (1985) [Sov. Phys. JETP **62**, 1263 (1985)]; A. A. Abrikosov and A. V. Pantsulaya, Fiz. Tverd. Tela (Leningrad) **28**, 2140 (1986) [Sov. Phys. Solid State **28**, 1195 (1986)].
[19] V. S. Egorov and A. N. Fedorov, Zh. Éksp. Teor. Fiz. **85**, 1647 (1983) [Sov. Phys. JETP **58**, 517 (1983)]; N. V. Zavaritskiĭ, V. I. Makarov, and A. A. Yurgens, JETP Lett. **42**, 182 (1985).
[20] E. S. Itskevich, Prib. Tekh. Éksper., No. **4**, 148 (1963); N. B. Brandt and Ya. G. Ponomarev, Zh. Éksp. Teor. Fiz. **55**, 1215 (1968) [Sov. Phys. JETP **28**, 635 (1969)].
[21] T. A. Ignat'eva and A. N. Velikodnyĭ, Vopr. At. Nauk Tekh. Ser. Vak. Chist. Met. Sverkhprovodniki **5**, 78 (2003).
[22] F. J. Blatt, P. A. Schroeder, C. L. Foiles, and D. Greig, *Thermoelectric Power of Metals*, Plenum Press, New York (1976), Metallurgiya, Moscow (1980) (Russ. p. 247).
[23] N. A. Tulina, Fiz. Nizk. Temp. **5**, 499 (1983) [Sov. J. Low Temp. Phys. **9**, 252 (1983)]; A. V. Belushkin, M. G. Zemlyanov, I. Natkanets, N. A. Tulina, S. Khabrylo, and Yu. L. Shitikov, Preprint R14-87-644, Dubna [in Russian], Kurchatov Institute of Atomic Energy, FTT Akad. Nauk SSSR, Moscow (1987).
[24] V. V. Nemoshkalenko and V. N. Antonov, Vl. N. Antonov, Dokl. Akad. Nauk SSSR **260**, 72 (1981) [Sov. Phys. Dokl. **26**, 851 (1981)].

Translated by Steve Torstveit

Chiral symmetry breaking and the Josephson current in a ballistic superconductor–quantum wire–superconductor junction

I. V. Krive*

Department of Applied Physics, Chalmers University of Technology and Göteborg University, SE-412 96 Göteborg, Sweden; B. Verkin Institute for Low Temperature Physics and Engineering of the National Academy of Sciences of Ukraine, 47 Lenin Ave., Kharkov 61103, Ukraine

L. Y. Gorelik, R. I. Shekhter, and M. Jonson

Department of Applied Physics, Chalmers University of Technology and Göteborg University, SE-412 96 Göteborg, Sweden

(Submitted November 7, 2003; revised December 15, 2003)
Fiz. Nizk. Temp. **30**, 535–543 (April 2004)

We evaluate the Josephson current through a quasi-1D quantum wire coupled to bulk superconductors. It is shown that the interplay of Rashba spin–orbit interaction and Zeeman splitting results in the appearance of a Josephson current even in the absence of any phase difference between the superconductors. In a transparent junction ($D \simeq 1$) at low temperatures this anomalous supercurrent J_{an} appears abruptly for a Zeeman splitting of the order of the Andreev level spacing as the magnetic field is varied. In a low-transparency ($D \ll 1$) junction one has $J_{an} \propto \sqrt{D}$ under special (resonance) conditions. In the absence of Zeeman splitting the anomalous supercurrent disappears. We have investigated the influence of dispersion asymmetry induced by the Rashba interaction in quasi-1D quantum wires on the critical Josephson current and have shown that the breakdown of chiral symmetry enhances the supercurrent. © *2004 American Institute of Physics.* [DOI: 10.1063/1.1739160]

1. INTRODUCTION

Quantum wires (QWs) have the potential of being the basic elements in future nanometer-scale electronic devices. Electron transport in QWs is coherent and ballistic. It results in a number of spectacular phenomena such as conductance quantization, persistent current oscillations in ring-shaped wires (quantum rings), etc. At present, QWs are realized experimentally in the form of long and narrow channels ($L \gg d \sim \lambda_F$, where λ_F is the electron Fermi wavelength) in a two-dimensional electron gas (2DEG) (see Ref. 1) and as conducting 1D and quasi-1D molecular systems. The most successful and promising realization of 1D conductors is single-wall carbon nanotubes.[2] It has been shown both theoretically[3] and experimentally[4] that in carbon nanotubes the effects of Coulomb interaction are significant and that they transform the conduction electron system into a Luttinger liquid. In quantum wires formed in a 2DEG the electron–electron interaction is less pronounced (presumably due the screening effects of the nearby bulk metallic electrodes), and the electron transport in these systems can in many cases be successfully described by Fermi liquid theory.

It has long been known[5] that electrons confined to a plane (e.g., in MOSFET structures or in heterostructures) experience a strong spin–orbit interaction originating from interface electric field (Rashba spin–orbit interaction). Recently it was shown experimentally that the strength of the Rashba coupling can be controlled by a gate voltage.[6] The Rashba effect leads to various interesting suggestions in spintronics, and it has been a subject of active theoretical and experimental studies in recent years (see, e.g., Ref. 7 and references therein).

For quasi-1D electron systems the influence of the Rashba interaction on thermodynamic and transport properties of quantum wires was considered in Refs. 8 and 9. There it was shown that in the presence of an in-plane confinement potential and spin–orbit interactions the electron spectrum is qualitatively modified. Chiral symmetry, which is usually assumed to be present in QWs, is violated, resulting in the appearance of a dispersion asymmetry. To be more precise, the right-moving spin-up[1)] (left-moving spin-down) and left-moving spin-up (right-moving spin-down) electrons have different Fermi velocities.[8] This implies that electrons in quantum wires with Rashba interaction are ''chiral particles,'' and their spin projections are correlated with the direction of motion. Being interested in low-energy ($E \ll \varepsilon_F$) properties of quantum wires, we can classify these particles as belonging to two subbands (''1'' and ''2'') characterized by their Fermi velocities (see Fig. 1). Notice that this electron spectrum pertains to a weak or moderate spin–orbit interaction. As was demonstrated in Ref. 10 for a strong Rashba interaction, the projection of electron spin is strongly correlated with the direction of motion, and left- and right-moving electrons with the Fermi energy always have opposite spin projections.

The unusual spectral properties of electrons in QWs have to show up in situations when spin degrees of freedom are nontrivially involved in the electron dynamics. Here we consider the Josephson current in a long S–QW–S junction for an electron spectrum with dispersion asymmetry and large Zeeman splitting. Recently the combined effect of Zeeman and spin–orbit interactions on the Josephson current in a short ballistic junction formed in a 2DEG was studied

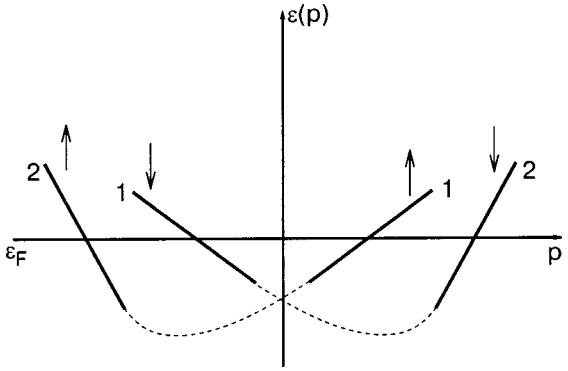

FIG. 1. Schematic energy spectrum of 1D electrons with dispersion asymmetry. The particles with energies close to the Fermi energy ε_F have an almost linear dependence on momentum and are classified by their Fermi volocities (v_{1F}—subband 1, v_{2F}—subband 2).

theoretically.[11] Notice that interaction-induced dispersion asymmetry in the electron spectrum is a specific property of quasi-one-dimensional geometry.[8] For a pure 2D geometry spin–orbit interaction does not lead to chiral symmetry breaking, and the peculiar effects produced by chiral particles do not manifest themselves in the short and wide SNS junction considered in Ref. 11. In particular, we show that the combined effect of Rashba and Zeeman interactions results in the appearance of an anomalous Josephson current $J_{an}=J(\varphi=0)$ in a long S–QW–S junction. For a transparent junction the supercurrent induced by the Rashba and Zeeman interactions at low temperatures is a step-like periodic or quasiperiodic function of magnetic field (see Fig. 2). The periodicity depends on the ratio of the Fermi velocities and is controlled by the strength of the spin–orbit interaction. The amplitude of the anomalous current at $T=0$ is of the order of the critical Josephson current in a long S–N–S junction and it appears abruptly at finite values of the Zeeman splitting of the order of the Andreev level spacing (Fig. 2). For a low-transparency junction ($D\ll 1$), realized by introducing a scattering barrier (impurity) into the normal region, the

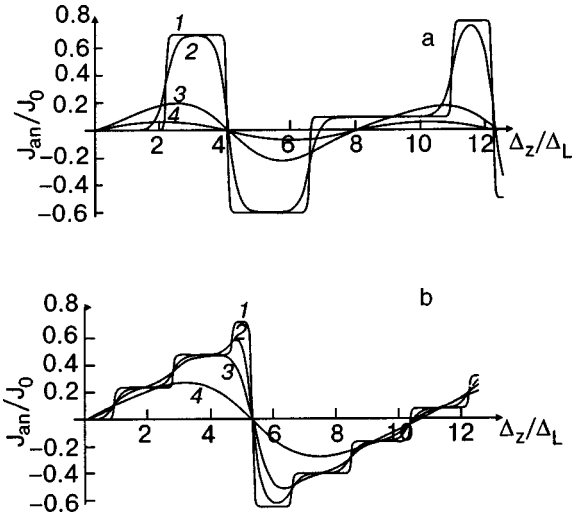

FIG. 2. The dependence of the normalized anomalous Josephson current J_{an}/J_0 ($J_0=ev_F/L$) on the dimensionless Zeeman splitting Δ_Z/Δ_L ($\Delta_L=\hbar v_F/L$). (a) Asymmetry parameter $\lambda_a=0.3$. The different plots (*1–4*) correspond to different temperatures $T=(0.1,0.5,3,5)T^*$, where $T^*=\Delta_L/2\pi$. (b) $\lambda_a=0.7$; $T=(0.1,0.5,1,3)T^*$.

maximum amplitude of J_{an} at special (resonance) conditions is of the order of $\sqrt{D}$. Notice that this unusual dependence on transparency, which corresponds to tunneling of a single electron through a barrier (its entangled partner passes resonantly through the structure) also holds for the critical Josephson current even in the absence of dispersion asymmetry. This effect can be interpreted as a tunnel splitting of the de Gennes—Saint-James bound state[12] shifted by magnetic field to the vicinity of the Fermi level. Analogous effects of giant critical supercurrents in tunnel SIS (''I'' stands for insulator) and SINIS structures were discussed in Ref. 13 (see also Ref. 14, where resonance effects are considered for a persistent current in a normal metal ring).

When the Zeeman splitting vanishes, the anomalous supercurrent and all the above described resonance effects disappear. Then the Josephson current in a low-D junction is small ($\sim D$). What is the influence of dispersion asymmetry on the critical current? There is a general statement[15] that spin–orbit interaction in systems with the Aharonov—Bohm geometry suppresses persistent currents. Although the theorem directly concerns normal ring-shaped conductors, it also holds for linear hybrid systems with Andreev mirrors by virtue of the analogy between persistent currents in a normal 1D ring and Josephson currents in a long SNS junction. We show here that the cited statement is not valid when the spin–orbit interaction is accompanied by chiral symmetry breaking. Rashba spin–orbit interaction in quantum wires always enhances the critical current.

2. ANOMALOUS JOSEPHSON CURRENT

The Josephson current, being an equilibrium supercurrent between two superconductors, can be calculated from the general thermodynamic relation

$$J=\frac{e}{\hbar}\frac{\partial\Omega}{\partial\varphi}, \tag{1}$$

where Ω is the thermodynamic potential of the junction considered and φ is the phase difference between the two superconductors. We have included a factor of 2, which usually appears in Eq. (1) in combination with the electric charge, into the definition of Ω. This factor originates from spin degeneracy, and in the presence of Zeeman splitting $\Omega=\Omega_\uparrow+\Omega_\downarrow$ and $\Omega_\uparrow\neq\Omega_\downarrow$.

In general both the Andreev bound states ($E<|\Delta|$, where Δ is the superconducting order parameter) and the continuum scattering states ($E\geqslant|\Delta|$) contribute to the supercurrent. In two limiting cases—short ($L\ll\xi_0=\hbar v_F/|\Delta|$, where L is the junction length) and long ($L\gg\xi_0$) junctions — only bound states are relevant. This statement is well known for the case of short junctions (see, e.g., Ref. 16 and references therein). For a long junction it has been shown that the Josephson current through a long SNS junction does not depend on $|\Delta|$ at all.[17] Then, one can formally put $|\Delta|\to\infty$ and sum over all Andreev bound states E_n ($n=0,\pm1,\pm2,\ldots$) with the natural assumption that the supercurrent vanishes in the limit $L\to\infty$. This procedure (analogous to Casimir energy evaluation in quantum field theory; see, e.g., Ref. 18) reproduces all known results for a long ballistic SNS junction. In what follows we will consider only long junctions.

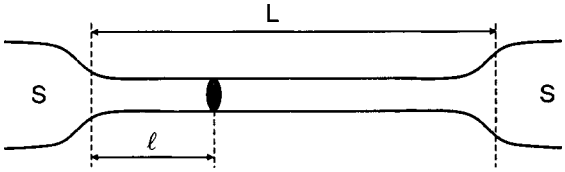

FIG. 3. A long ($L \gg \xi_0$) ballistic S–N–S junction with a scattering barrier (shaded region).

To get analytical results we consider a single barrier junction of length L, where the barrier is located at the point $x=l \leqslant L$; the distance l is measured from the left bank of the junction (see Fig. 3). We start with the general equation for Andreev bound state energies expressed in terms of scattering matrices of electrons ($\hat{S}_E$) and holes ($\hat{S}^*_{-E}$) in the normal region[19]

$$\det(1-\alpha_A \hat{S}_E \hat{r}_A \hat{S}^*_{-E} \hat{r}^*_A)=0, \tag{2}$$

where $\alpha_A=\exp[-2i \arccos(E/|\Delta|)] \simeq -1$ in our case ($E \ll \Delta$), and $\hat{r}_A$ is a diagonal matrix that only depends on the superconducting phases (see Appendix). Since the presence of a magnetic field violates T-symmetry, the two-channel scattering of spin-1/2 electrons is described by a 4×4 nonsymmetric unitary matrix $\hat{S}_E$. The normal backscattering in our approach (we neglect spin flips induced by a weak Rashba interaction) is always accompanied by a change of "channel index" $1 \Leftrightarrow 2$ (see Fig. 1). This allows us to parametrize the scattering matrix by 7 independent real parameters (see Appendix).

After straightforward (although rather lengthy) transformations, Eq. (2) results in a transcendental equation for Andreev level energies of the form

$$\cos\left[\left(E+\frac{\eta}{2}\Delta_Z\right)\delta_L^{(+)}\right]+R\cos\left[\left(E+\frac{\eta}{2}\Delta_Z\right)\delta_{L-2l}^{(+)}\right] + D\cos\left[\left(E+\frac{\eta}{2}\Delta_Z\right)\delta_L^{(-)}+\eta\varphi\right]=0. \tag{3}$$

Here $\Delta_Z=g\mu_B H$ is the Zeeman energy splitting ($g=2$ for bare electrons, and we assume that the magnetic field H is applied locally on the quantum wire only), $\eta=\pm 1$, D is the transparency of the junction, $D+R=1$, and

$$\delta_x^{(\pm)}=\frac{x}{\hbar}\left(\frac{1}{v_{1F}}\pm\frac{1}{v_{2F}}\right). \tag{4}$$

In the limit $H=0$ and $v_{1F}=v_{2F}$ (absence of spin–orbit interaction) Eq. (3) reduces to a well-known spectral equation for Andreev levels in a long SNS junction with a single barrier.[16,20]

For a transparent junction ($D=1$) the Andreev bound states are described by two independent sets of energy levels

$$E^{(1)}_{n,\eta}=\pi\Delta_L^{(1)}\left(n+\frac{1}{2}+\eta\frac{\varphi+\chi_1}{2\pi}\right), \tag{5}$$

$$E^{(2)}_{m,\eta}=\pi\Delta_L^{(2)}\left(m+\frac{1}{2}+\eta\frac{\varphi-\chi_2}{2\pi}\right),$$

where the integers $n,m=0,\pm 1,\pm 2,\ldots$ and $\eta=\pm 1$ are the standard quantum numbers of the Andreev–Kulik spectrum in a perfectly transmitting SNS junction;[21] $\Delta_L^{(j)}=\hbar v_{jF}/L$ and $\chi_j=\Delta_Z/\Delta_L^{(j)}$ is the phase acquired due to the Zeeman interaction. Notice that for a given band index ("1" or "2") the relative sign between the superconducting phase difference φ and the magnetic phase χ_j is fixed and is different for channels "1" and "2." This is a direct consequence of the chiral properties of the electrons in our model. In the absence of spectral asymmetry the two energy spectra in Eq. (5) correspond to Zeeman-split Andreev levels.

Knowing explicitly the energy spectrum (5), it is straightforward to evaluate the Josephson current. It takes the form

$$J(\varphi,T,H)=\frac{2eT}{\hbar}\sum_{k=1}^{\infty}(-1)^{k+1}\left\{+\frac{\sin k(\varphi+\chi_1)}{\sinh(2\pi kT/\Delta_L^{(1)})} + \frac{\sin k(\varphi-\chi_2)}{\sinh(2\pi kT/\Delta_L^{(2)})}\right\}. \tag{6}$$

It is readily seen from Eq. (6) that an anomalous Josephson current $J_{an}\equiv J(\varphi=0)$ appears only if both the Zeeman splitting (Δ_Z) and dispersion asymmetry ($v_{1F}\neq v_{2F}$) are nonzero. Here we use the term "anomalous" just to define the supercurrent at $\varphi=0$. Actually this current is induced by Zeeman splitting in a 1D electron system with dispersion asymmetry. The direction (sign) of J_{an} is completely determined by the sign of the asymmetry parameter [see Eq. (8)]. At high temperatures $T \geqslant \Delta_L^{(j)}$ the anomalous supercurrent is exponentially small. In the low-temperature region ($T \ll \Delta_L^{(j)}$) it is a piecewise constant function of magnetic field represented by the series

$$J_{an}(H)=\frac{e}{\pi L}\sum_{k=1}^{\infty}\frac{(-1)^{k+1}}{k}(v_{1F}\sin k\chi_1 - v_{2F}\sin k\chi_2). \tag{7}$$

For rational values $v_{1F}/v_{2F}=p/q$ ($p \leqslant q$ are integers) J_{an} is a periodic function of magnetic field with period $\delta H = 2\pi q\Delta_L^{(1)}/g\mu_B$; otherwise it is a quasiperiodic function.

It is convenient to introduce the mean Fermi velocity $v_F=(v_{1F}+v_{2F})/2$ and the asymmetry parameter λ_a,

$$\lambda_a=\frac{v_{1F}-v_{2F}}{v_{1F}+v_{2F}}, \tag{8}$$

which determines the strength of Rashba spin–orbit interaction in a 1D quantum wire. The dependence of the normalized anomalous supercurrent J_{an}/J_0 ($J_0=ev_F/L$) on the dimensionless Zeeman splitting $\chi=\Delta_Z/\Delta_L$ ($\Delta_L=\hbar v_F/L$) for $\lambda_a=0.3$ and for different temperatures is shown in Fig. 2a. In the limit of strong asymmetry (this range of parameters, however, seems to be unrealistic),[8] when only one of the two channels ("1" or "2") contributes to Eq. (6), the dependence of the anomalous current on the magnetic field becomes analogous to the well-known phase dependence of the Josephson current.[21] The approach to this simple behavior takes place via stages of staircase-like dependences (see Fig. 2b). Notice that we plotted the figures assuming that $v_{1F} \geqslant v_{2F}$. The interchange $v_{1F} \leftrightarrow v_{2F}$ makes the supercurrent Eq. (7) change sign.

3. GIANT CRITICAL CURRENT IN A MAGNETICALLY CONTROLLED LOW-TRANSPARENCY JUNCTION

Now we consider the limit $D \ll 1$, which pertains to low-transparency SNS junctions. As is well known (see, e.g., Refs. 16, 20), the supercurrent in this limit for a single barrier junction in the absence of Zeeman and spin–orbit interactions is described by the simple formula $J(\varphi)=J_c \sin\varphi$, where the critical current at low temperatures $T \ll \Delta_L$ is of the order of D ($J_c \sim De v_F/L$). Interesting physics for low-D junctions appears when resonant electron tunneling occurs. This is, for instance, the case for the symmetric double-barrier ballistic junction considered in Refs. 13 and 16. There it was shown that for resonance conditions (realized for a special set of junction lengths) a giant critical supercurrent appears, $J_c \propto D_b$, where D_b is the transparency of a *single* barrier. Analogous results were obtained for the persistent current in a ballistic ring with a double barrier.[14] Notice that for the symmetric structure considered in Ref. 13 the normal current (transmission coefficient, which determines the current through a double-barrier structure with normal leads) at resonance conditions does not depend on barrier transparency at all. This means that for the hybrid structure considered in Ref. 13, the superconductivity actually suppresses electron transport.

We show below that in a magnetically controlled single-barrier junction there are conditions when superconductivity in the leads strongly enhances electron transport, and a mesoscopic hybrid structure is characterized by a giant critical current $J_c \propto \sqrt{D}$.

We start with the case of a symmetric single-barrier junction, when the scattering barrier is situated in the middle of the normal region, i.e., $l=L/2$ in Eq. (3). Then $\delta^{\pm}_{(x=0)}=0$, and the second cosine term in the spectral equation (3) is equal to one:

$$\cos\left[\left(E+\frac{\eta}{2}\Delta_Z\right)\delta^{(+)}_{L-2l}\right]=1. \tag{9}$$

When the condition (9) is fulfilled, the spectral equation is reduced to the much simpler expression

$$\cos^2\left[\frac{1}{2}\left(E+\frac{\eta}{2}\Delta_Z\right)\delta^{(+)}_L\right] = D\sin^2\left[\frac{1}{2}\left(E+\frac{\eta}{2}\Delta_Z\right)\delta^{(-)}_L+\eta\varphi\right]. \tag{10}$$

By using Eq. (10), one can readily evaluate the partial supercurrent $j_{\{\alpha\}}$ characterized by 3 quantum numbers $\{\alpha\}=(n,\eta,\sigma)$, where $n=0,\pm1,\pm2,\ldots$; $\eta,\sigma=\pm1$:

$$j_{\{\alpha\}}=\frac{e}{\hbar}\frac{\partial E_{\{\alpha\}}}{\partial\varphi}=-\frac{e\eta\sigma}{\hbar}\frac{\sqrt{D}\cos\frac{1}{2}\left[E_{\{\alpha\}}\delta^{(-)}_L+\eta\left(\frac{1}{2}\Delta_Z\delta^{(-)}_L+\varphi\right)\right]}{\delta^{(+)}_L\sin\frac{1}{2}\left[\frac{\delta^{(+)}_L}{2}\left(E_{\{\alpha\}}+\frac{\eta}{2}\Delta_Z\right)\right]+\sigma\delta^{(-)}_L\sqrt{D}\cos\frac{1}{2}\left[E_{\{\alpha\}}\delta^{(-)}_L+\eta\left(\frac{1}{2}\Delta_Z\delta^{(-)}_L+\varphi\right)\right]}, \tag{11}$$

where $E_{\{\alpha\}}\equiv E_{n,\eta,\sigma}$ is a solution of Eq. (10). The Josephson current at $T=0$ is a sum of partial currents over all occupied states.

The resonance current (of order $\sqrt{D}$) is formed by non-compensated partial currents carried by the Andreev levels in the vicinity of the Fermi energy, i.e., for $E_{\{\alpha\}}=0^-$ when $D\to0$. Such levels exist only for a discrete set of Zeeman splittings

$$\Delta^{(k)}_Z=\frac{2\pi(2k+1)}{\delta^{(+)}_L}, \quad k=0,1,2,\ldots \tag{12}$$

At a given $\Delta^{(k)}_Z$ (controlled, e.g., by an external local magnetic field) two ($\eta=\pm1$) Andreev levels contribute to the resonance Josephson current J_r, which can be represented in the form

$$J_r(\varphi)=J_0\sqrt{D}\frac{1-\lambda_a^2}{2}\frac{\sin\left(\frac{1}{2}\Delta^{(k)}_Z\delta^{(+)}_L\lambda_a+\varphi\right)}{\left|\sin\frac{1}{2}\left(\frac{1}{2}\Delta^{(k)}_Z\delta^{(+)}_L\lambda_a+\varphi\right)\right|}, \tag{13}$$

where $J_0=ev_F/L$, and the asymmetry parameter λ_a is defined in Eq. (8).

In the absence of spin–orbit interaction ($\lambda_a=0$) Eq. (13) has the typical form of a resonance Josephson current (see, e.g., Ref. 16) associated with the contribution of a single Andreev level. One can interpret this result as follows. Let us assume for a moment that the potential barrier is infinite. Then, a symmetric SNINS junction (''I'' stands for the insulator ''layer'') breaks into two identical INS-hybrid structures. In each of the two systems de Gennes–Saint-James energy levels[12] with spacing $2\pi\hbar v_F/L$ are formed. For a finite barrier these levels are split with the characteristic splitting energy $\delta\sim\sqrt{D}\Delta_L\ll\Delta_L$. The tunnel-split levels, being localized already on the whole length L between the two superconductors, are nothing but the Andreev energy levels, i.e., they depend on the superconducting phase difference. Although the partial current of a single level is large (of the order of $\sqrt{D}$, see Refs. 13, 16), the current carried by a pair of split levels is small ($\sim D$) due to a partial cancellation. A Zeeman splitting of order Δ_L shifts the set of Andreev levels so that the Fermi energy lies in between the split levels. Now only the lower state is occupied, and this results in an uncompensated, large Josephson current. In other words only one of the two electrons of the Cooper pairs that form the supercurrent *tunnels* through the barrier. Its entangled partner at resonance conditions passes through the hybrid SFIFS structure (''F'' denotes the region with nonzero Zeeman splitting) without backscattering. Since the quantized electron–hole spectrum is formed by Andreev scattering, the

resonance structure for a single barrier junction disappears when the leads are in the normal state. Hence, electron transport through a normal region in our case is enhanced by superconductivity.

The effect of chiral symmetry breaking on the physical picture described above is to additionally split the degenerate Andreev levels. A dispersion asymmetry $\lambda_a \neq 0$ lifts the left–right symmetry of electron transport through the junction and splits the doubly degenerate Andreev levels at $\varphi = 0$. This results in the appearance of a giant anomalous Josephson current [see Eq. (13)] at $\varphi = 0$.

We saw that it is indispensable that Eq. (9) holds in order for resonant transport through the single barrier hybrid structure to occur. This equation can be satisfied not only for the symmetric junction considered above. One can easily check that for a fixed value of the Zeeman splitting $\Delta_Z^{(k)}$ given by Eq. (12) there is a set of points where a barrier still supports resonant transport. These points, determined by their coordinates $x_m^{(k)}$ measured from the middle of the junction, are (m is an integer)

$$x_m^{(k)} = \pm \frac{m}{2k+1} L, \quad 0 \leqslant m \leqslant k + 1/2. \tag{14}$$

The temperature dependence of the $\sqrt{D}$-currents is determined by the energy scale $\delta \sim \sqrt{D}\Delta_L$, and at temperatures $T \geqslant \delta$, which are much less than Δ_L, all resonance effects are washed out.

4. INFLUENCE OF CHIRAL SYMMETRY BREAKING ON THE CRITICAL CURRENT

There is a general statement[15] that spin–orbit interaction in 1D systems with the Aharonov–Bohm geometry produces additional reduction factors in the Fourier expansion of thermodynamic or transport quantities. This statement holds for spin–orbit Hamiltonians for which the transfer matrix is factorized into spin–orbit and spatial parts. In a pure 1D case the spin–orbit interaction is represented by the Hamiltonian $\mathcal{H}_{1D}^{(so)} = \alpha_{(so)} \hat{p}_x \sigma_z$, which is the product of spin-dependent and spatial operators, and thus it satisfies the above-described requirements. However, as was shown by direct calculation in Ref. 8, the spin–orbit interaction of electrons in 1D quantum wires formed in a 2DEG by an in-plane confinement potential cannot be reduced to the Hamiltonian $\mathcal{H}_{1D}^{so}$. Instead, a violation of left–right symmetry of 1D electron transport, characterized by a dispersion asymmetry parameter λ_a, appears. We show now that in quantum wires with broken chiral symmetry the spin–orbit interaction enhances a persistent current.

There is a close analogy between the Josephson current in a long SNS junction and the persistent current in a normal metal ring. For a long ($L \gg \hbar v_F/|\Delta|$) SNS junction the Andreev boundary conditions can be recast[22] in the form of twisted boundary conditions for chiral (right- or left-moving) fermions on a ring with circumference $2L$ pierced by the magnetic flux $\Phi/\Phi_0 = 1/2 \pm \varphi/2\pi$, where $\Phi_0 = hc/e$ is the normal flux quantum. Due to this mapping the corresponding formulas for the persistent current in a normal diamagnetic (with odd number of spinless fermions) 1D ring and the formulas for the Josephson current coincide up to numerical factors. Here we consider the influence of dispersion asymmetry in the electron spectrum on the off-resonance supercurrent through a single barrier SNS junction (notice that resonace effects disappear in zero magnetic field).

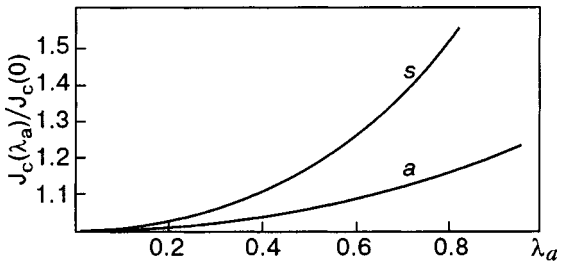

FIG. 4. The dependence of the normalized critical current $J_c(\lambda_a)/J_c(\lambda_a = 0)$ in a low-transparency ($D \ll 1$) S–N–S junction on the parameter of dispersion asymmetry λ_a. The curve labeled by "s" corresponds to the case of symmetric junction ($l = L/2$), while the curve "a" describes a strongly asymmetric junction ($l = 0$).

In a low-transparency 1D SNS junction the critical current in the presence of dispersion asymmetry is of the form $J_c = f(\lambda_a) D e v_F / L$. To evaluate the function $f(\lambda_a)$ analytically we consider two limiting cases: (i) an asymmetric junction $l = 0$, and (ii) a symmetric junction $l = L/2$.

The first case models a junction with strong normal backscattering at one of the two interfaces. In zero magnetic field the spectral equation Eq. (3), in the limit considered is reduced to

$$\cos(E\delta_L^{(+)}) \simeq -\frac{D}{2}\cos(E\delta_L^{(-)} + \eta\varphi). \tag{15}$$

The energy spectrum and the partial supercurrents in the limit $D \ll 1$ are

$$E_n^{(0)} = \frac{\pi}{2\delta_L^{(+)}}\left(n + \frac{1}{2}\right),$$

$$j_{n,\eta}^{(a)} = \eta(-1)^{n+1}\frac{e}{\hbar}\frac{D}{2\delta_L^{(+)}}\sin\left[\pi\left(n + \frac{1}{2}\right)\lambda_a + \eta\varphi\right]. \tag{16}$$

By summing partial currents over quantum numbers of occupied states ($E_n^{(0)} \leqslant 0$) at $T = 0$ one gets

$$J^{(a)} = \sum_{n=-1;\,\eta=\pm 1}^{\infty} j_{n,\eta}^{(a)} = J_c^{(a)}(\lambda_a)\sin\varphi,$$

$$J_c^{(a)}(\lambda_a) = \frac{e v_F}{4L} D \frac{1-\lambda_a^2}{\cos(\pi\lambda_a/2)}. \tag{17}$$

The critical current in the absence of spin–orbit interaction $J_c^{(a)}(0) = D e v_F/4L$ coincides with the known results (see, e.g., Ref. 16). The normalized current $J_c^{(a)}(\varphi)/J_c^{(a)}(0)$ is shown in Fig. 4 (curve "a").

For a symmetric junction the analogous calculation leads to the expression

$$J_c^{(s)}(\lambda_a) = \frac{e v_F}{\pi L} D \frac{\pi\lambda_a(1-\lambda_a^2)}{\sin(\pi\lambda_a)}; \quad J_c^{(s)}(0) = \frac{e v_F}{\pi L} D. \tag{18}$$

The curve labeled by "s" in Fig. 4 demonstrates the dependence of the critical current in a symmetric junction on the spin–orbit parameter λ_a. We see that the spin–orbit Rashba interaction in quasi-1D quantum wires always enhances the critical current. The qualitative explanation of the

unusual impact of chiral symmetry breaking on the critical Josephson current is as follows. The Josephson current (as any other thermodynamic persistent current) is a sum of partial currents of all occupied energy levels. The partial currents of adjacent energy levels are opposite in sign, and for chiral invariant systems (i.e., without dispersion asymmetry) they almost perfectly cancel each other to produce a net current of the order of a single-level current. When chiral invariance is broken the absolute values of the partial currents of adjacent energy levels are different, and the cancellation of currents for distant levels is less perfect. This results in enhancement of the critical Josephson current. However, the effect is numerically not large.

5. CONCLUSION

In quantum wires formed in a two-dimensional electron gas (2DEG) by lateral confinement the Rashba spin–orbit interaction is not reduced to a pure 1D Hamiltonian $\mathcal{H}_{1D}^{(so)} = \alpha_{(so)}\hat{p}_x\sigma_z$. As was shown in Ref. 8, the presence of an in-plane confinement potential qualitatively modifies the energy spectrum of the 1D electrons so that a dispersion asymmetry appears. As a result, the chiral symmetry is broken in quantum wires with Rashba coupling. Although the effect was shown[8] not to be numerically large, the breakdown of symmetry leads to qualitatively novel predictions.

We have considered here the influence of dispersion asymmetry and Zeeman splitting on the Josephson current through a superconductor/quantum wire/superconductor junction. We showed that the violation of chiral symmetry in a quantum wire results in qualitatively new effects in weak superconductivity. In particular, the interplay of the Zeeman and Rashba interactions induces a Josephson current through the hybrid 1D structure even in the absence of any phase difference between the superconductors. At low temperatures ($T \ll \hbar v_F/L$) the anomalous supercurrent can be of the order of the critical Josephson current. For a transparent junction with small or moderate dispersion asymmetry [characterized by the dimensionless parameter $\lambda_a = (v_{1F} - v_{2F})/(v_{1F} + v_{2F})$] it appears, as a function of the Zeeman splitting Δ_Z, abruptly at $\Delta_Z \sim \hbar v_F/L$. In a low-transparency ($D \ll 1$) junction, the anomalous Josephson current under special (resonance) conditions is of the order of $\sqrt{D}$. In zero magnetic field the anomalous supercurrent disappears (as it should), since the spin–orbit interaction itself respects T-symmetry. However, the influence of the spin–orbit interaction on the critical Josephson current through a quasi-1D structure is still anomalous. Contrary to what holds for chiral invariant systems with the Aharonov–Bohm geometry, where spin–orbit effects suppress persistent currents,[15] the breakdown of chiral symmetry results in an enhancement of the supercurrent.

All the phenomena described above are absent in a 2D-junction when the effects of transverse mode quantization are neglected.[11] We have considered the limiting case of a single (transverse) channel because this is the case for which the effects induced by a dispersion asymmetry in the electron spectrum are most pronounced. The anomalous supercurrent (7) is a sign-alternating function of the transverse channel index, since for neighboring channels the spin projections of the chiral states are opposite.[8] Besides, the absolute value of the dispersion asymmetry parameter $\lambda_a^{(j)}$ decreases with transverse-channel number j. So, for a multichannel junction the effects related to a dispersion asymmetry phenomenon will be strongly suppressed, and they completely disappear in the pure 2D case.

We have evaluated the Josephson current through a S–QW–S junction in a model of noninteracting electrons. In QWs the effects of electron–electron interaction can be significant, and here we comment on how interaction effects could modify the results obtained. Electronic properties of 1D QWs are usually described by a Luttinger liquid (LL) model (see, e.g., Ref. 23). The supercurrent in a S–LL–S junction with repulsive electron–electron interaction depends strongly on the quality of electrical contact of the nanowire with the bulk superconductors. For adiabatic contacts, when only Andreev scattering takes place at the interfaces, the Josephson current through a perfect wire is not renormalized by interaction.[22,24] For tunnel contacts electron–electron interaction in a wire renormalizes the barrier transparencies (Kane–Fisher effect[25]), and for repulsive interaction the critical current is strongly suppressed.[26]

We are interested in spin–orbit effects in a S–QW–S junction. It is reasonable to expect that Eqs. (6) and (7) derived for a perfect junction (without normal backscattering) will be valid even for interacting electrons. One could expect also that in a tunneling regime ($D \ll 1$) the interaction effects in Eqs. (13), (17), and (18) can be estimated by replacing the bare transparency D by the interaction-renormalized one[22] $D_g \sim D(d/L)^{K_\rho^{-1}-1}$ (here $d \ll L$ is the width of the wire and K_ρ is the LL correlation parameter). In quantum wires formed in a 2DEG the Coulomb interaction is not strong[1] and it can be controlled by the gate electrodes. For weakly interacting electrons (a conceivable case for ''semiconducting'' QWs), when the electron picture of charge transport through a 1D wire is still valid,[27] the interaction effects can actually be accounted for by replacing the bare transmission coefficient by the renormalized one.

The authors thank E. Bezuglyi, A. Kadigrobov, and V. Shumeiko for fruitful discussions. This research is supported by the Royal Swedish Academy of Sciences (KVA) and by the Swedish Research Council (LYG, RIS). IVK acknowledges the hospitality of the Department of Applied Physics, Chalmers University of Technology and Göteborg University.

6. APPENDIX

We consider electron transport through a normal region of length L with a local scatterer placed a distance l from the left bank, at point $x = l$. In our two-channel chiral model (the term ''chiral'' here means that left- and right-moving particles with a given Fermi velocity have opposite spin polarizations; see Fig. 1) backscattering by a nonmagnetic impurity corresponds to a backward interchannel scattering (''1'' $\Leftrightarrow$ ''2''). In the presence of a magnetic field and interchannel scattering the general 4×4 nonsymmetric S-matrix can be parametrized as follows:

$$\hat{S}_E = \begin{pmatrix} |r|\sigma_1 \exp i(\rho_R + \sigma_3\mu_R) & |t|\sigma_3 \exp i(\alpha_R + \sigma_3\eta_R) \\ |t|\sigma_3 \exp i(\alpha_L + \sigma_3\eta_L) & |r|\sigma_1 \exp i(\rho_L + \sigma_3\mu_L) \end{pmatrix}.$$

Here $\sigma_{1,3}$ are the Pauli matrices, $t_{R,L}=|t|\exp(i\eta_{R,L})$, $r_{R,L}=|r|\exp(i\rho_{R,L})$, and $|t|^2+|r|^2=1$. Unitarity of the S-matrix ($SS^{\dagger}=I$) implies the relations

$$\mu_R+\eta_R=\mu_L+\eta_L\,,\quad \rho_R+\rho_L=\alpha_R+\alpha_L\,. \tag{19}$$

Thus, the scattering matrix in our problem is described by 7 independent real parameters. For a point scatterer with energy-independent scattering amplitudes (t_0,r_0) one readily gets that $|t|^2=|t_0|^2\equiv D$ (D is the junction transparency). The phases are

$$\mu_R=-(L-1)k_-\,,\quad \rho_R=(L-l)k_+\,,\quad \eta_R=Lk_-^{\uparrow\downarrow}$$
$$\alpha_R=Lk_+^{\uparrow\downarrow}\,,\quad \mu_L=lk_-\,,\quad \rho_L=lk_+\,,\quad \eta_L=Lk_-^{\downarrow\uparrow}\,,$$
$$\alpha_L=Lk_+^{\downarrow\uparrow}\,, \tag{20}$$

where

$$k_\pm=k_+^{\uparrow\uparrow}\pm k_+^{\downarrow\downarrow}\,,\quad k_\pm^{\sigma\sigma'}=\frac{1}{2}(k_1^{\sigma'}\pm k_2^{\sigma'}),$$
$$k_j^{\sigma}(\pm E)=k_{jF}+\frac{\pm E+\sigma g\mu_B H/2}{\hbar v_{jF}} \tag{21}$$

and k_j, v_{jF} ($j=1,2$) are the Fermi momentum and the Fermi velocity in the jth channel.

The diagonal matrix $\hat{r}_A$ in Eq. (2) takes the form

$$\hat{r}_A=\begin{pmatrix}\exp(i\varphi/2i)\hat{I} & 0\\ 0 & \exp(-i\varphi/2i)\hat{I}\end{pmatrix}, \tag{22}$$

where φ is the superconducting phase difference and $\hat{I}$ is the 2×2 unit matrix.

*E-mail: krive@ilt.kharkov.ua

[1)]Under conditions of the Rashba effect the electron spin lies in the plane of the heterostructure transition layer and is always perpendicular to the electron momentum. The terms spin-"up" and spin-"down" determine two opposite spin projections orthogonal to the line of the quantum wire at the 2D interface.

[1] S. Tarucha, T. Honda, and T. Saku, Solid State Commun. **94**, 413 (1995); A. Yakoby, H. L. Stormer, N. S. Wigreen, L. N. Pfeiffer, R. W. Baldwin, and K. W. West, Phys. Rev. Lett. **77**, 4612 (1996).
[2] S. J. Tans, M. H. Devoret, H. Dai, A. Thess, R. E. Smalley, L. J. Geerlings, and C. Dekker, Nature (London) **386**, 474 (1997).
[3] R. Egger and A. O. Gogolin, Phys. Rev. Lett. **79**, 5082 (1997); C. L. Kane, L. Balents, and M. P. A. Fisher, Phys. Rev. Lett. **79**, 5086 (1997).
[4] M. Bockrath, D. H. Cobden, J. Lu, A. G. Rinzler, G. Andrew, R. E. Smalley, L. Balents, and P. L. McEuen, Nature (London) **397**, 598 (1999); Z. Yao, H. W. J. Postma, L. Balents, and C. Dekker, *ibid.* **402**, 273 (1999).
[5] E. I. Rashba, Fiz. Tverd. Tela (Leningrad) **2**, 1224 (1960) [Sov. Phys. Solid State **2**, 1109 (1960)]; Y. A. Bychkov and E. I. Rashba, J. Phys. C **17**, 6039 (1984).
[6] J. Nitta, T. Akasaki, H. Takayanagi, and T. Enoki, Phys. Rev. Lett. **78**, 1335 (1997); D. Grundler, *ibid.* **84**, 6074 (2000).
[7] F. Mireles and G. Kirczenow, Phys. Rev. B **64**, 024426 (2001).
[8] A. V. Moroz and C. H. Barnes, Phys. Rev. B **60**, 14272 (1999).
[9] A. V. Moroz, K. V. Samokhin, and C. H. Barnes, Phys. Rev. B **62**, 16900 (2000).
[10] M. Governale and U. Zulicke, Phys. Rev. B **66**, 073311 (2002).
[11] E. V. Bezuglyi, A. S. Rozhavsky, I. D. Vagner, and P. Wyder, Phys. Rev. B **66**, 052508 (2002).
[12] P. G. de Gennes and D. Saint-James, Phys. Lett. **4**, 151 (1963).
[13] G. Wendin and V. S. Shumeiko, Phys. Rev. B **53**, R6006 (1996); Superlattices Microstruct. **4**, 569 (1996).
[14] P. Sandström and I. V. Krive, Phys. Rev. B **56**, 9255 (1997).
[15] Y. Meir, Y. Gefen, and O. Entin-Wohlman, Phys. Rev. Lett. **63**, 798 (1989).
[16] P. Samuelsson, J. Lantz, V. S. Shumeiko, and G. Wendin, Phys. Rev. B **62**, 1319 (2000).
[17] A. Svidzinsky, T. N. Antsygina, and E. N. Bratus, Zh. éksp. Teor. Fiz. **61**, 1612 (1971) [Sov. Phys. JETP **34**, 860 (1972)].
[18] V. M. Mostepanenko and N. N. Trunov, *The Casimir Effect and its Application*, Claredon Press, Oxford (1997).
[19] C. W. J. Beenakker, Phys. Rev. Lett. **67**, 3836 (1991).
[20] P. F. Bagwell, Phys. Rev. B **46**, 12573 (1992).
[21] I. O. Kulik, Zh. Eksp. Teor. Fiz. **57**, 1745 (1969) [Sov. Phys. JETP **30**, 944 (1970)].
[22] D. L. Maslov, M. Stone, P. M. Goldbart, and D. Loss, Phys. Rev. B **53**, 1548 (1996).
[23] A. O. Gogolin, A. A. Nersesyan, and A. M. Tsvelik, *Bosonization and Strongly Correlated Systems*, Cambridge University Press (1998).
[24] Affleck, J.-S. Caux, and A. Zagoskin, Phys. Rev. B **62**, 1433 (2000).
[25] C. L. Kane and M. P. A. Fisher, Phys. Rev. Lett. **68**, 1220 (1992); Phys. Rev. B **46**, 15233 (1992).
[26] R. Fazio, F. W. J. Hekking, and A. A. Odintsov, Phys. Rev. Lett. **74**, 1843 (1995).
[27] K. A. Matveev, D. Yue, and L. I. Glazman, Phys. Rev. Lett. **71**, 3351 (1993).

This article was published in English in the original Russian journal. Reproduced here with stylistic changes by AIP.

LOW-TEMPERATURE MAGNETISM

Oscillations and change of sign in indirect exchange coupling of Fe/Au/Tb trilayer structures

E. Shypil,* A. Pogorily, and D. Podyalovsky

Institute of Magnetism, National Academy of Sciences of Ukraine 36-b Vernadsky Ave., Kiev 03142, Ukraine
(Submitted August 20, 2003)
Fiz. Nizk. Temp. **30**, 544–550 (April 2004)

The indirect exchange coupling between Fe and Tb layers through an Au layer exhibits oscillatory behavior with respect to the thickness of the nonmagnetic metal. Different experimental tools such as the polar magnetooptical Kerr effect, ferromagnetic resonance, and magnetotransport were used to investigate Fe/Au/Tb trilayers with Au thickness varying from 0 to 3.5 nm, prepared in an MBE system. From the experimental data we reconstruct the dynamics of the Fe and Tb magnetic moments with increasing thickness of the Au interlayer and show for the first time that there is a change of sign in the interaction between Fe and Tb, which is observed experimentally. © *2004 American Institute of Physics.*
[DOI: 10.1063/1.1739161]

INTRODUCTION

Rare earth–transition metal (RE–TM) alloys and compounds have been of fundamental and practical interest for many years.[1] The presence of various exchange interactions (RE–RE, TM–TM, RE–TM) makes understanding of physical processes complicated, though on the other hand they show the way to create new magnetic materials with novel properties. There are well known examples of high-energy permanent magnets created on the basis of $RECo_5$ and magnetooptical media for rewriteable memory storage based on RE–CoFe amorphous films. The main feature of these artificial materials is the ferrimagnetic ordering, meaning that the RE and TM magnetic sublattices are oriented antiparallel with perpendicular anisotropy and have a compensation point at a definite composition. The major source of the perpendicular magnetic anisotropy is known to be single-ion anisotropy of the RE ion, which possesses an orbital angular momentum.[1] This is also valid for RE/TM multilayer films, where an interface region gives the main contribution to the perpendicular anisotropy.[2,3] The exchange interaction in this system is fairly complex: the magnetic moments of the $3d$ shells of the TM atoms are thought to participate in the direct interaction exchange, whereas the orbital moments of the deep $4f$ shells of the RE atoms need mediation of the conduction electrons for their indirect exchange.[4] The polarization of conduction electrons as a result of spin interaction with the TM sublattice also has a significant influence on the exchange interaction in the RE sublattice, which is manifested, for example, in a steep rise of the Curie temperature T_C for the Tb–Fe alloy[5] compared with the T_C for pure terbium.[6] According to the RKKY (Ruderman–Kittel–Kasuda–Yosida) model the polarization oscillates in strength and sign with increasing distance from the magnetic ion.

Oscillatory interlayer coupling between ferromagnetic metal layers separated by a nonmagnetic metal spacer has been observed in many systems: Fe/Cr, Fe/Cu, Fe/Al, Fe/Ag, Fe/Au, Fe/Pd.[7] Nonmagnetic layers adjacent to the ferromagnetic layers become spin polarized, and these atoms develop magnetic moments.[8,9] As the interlayer thickness is varied, the exchange coupling of the magnetic layers is found to vary in sign, oscillating between antiferromagnetic and ferromagnetic coupling. This is manifested, for example, as an oscillation in the magnitude of the GMR effect with increasing separation of the magnetic layers.[10,11]

The authors of Refs. 12 and 13 investigated Co/X/Gd multilayers with X = Pt, Cu, and Y, hoping to see oscillatory behavior of the coupling. However, in contrast with the results for Gd/Y/Gd[14] and Co/Cu/Co,[15] where the oscillatory behavior of the coupling is well known, no oscillation of the coupling was found.

Hoffmann and Scherschlichtis reported their study of Tb and Fe multilayers separated by different nonmagnetic metal interlayers (Au, Ta, Pt).[16] It was shown that the net magnetic moment of this system oscillates weakly with interlayer thickness, although *the indirect coupling did not show a change in sign*.

In this article we describe measurements of Fe/xAu/Tb, $x = 0-35$ Å, bi- and trilayers carefully grown under clean conditions in an MBE system, to investigate the effect of interlayer thickness. We show that oscillations of the net magnetic moment are seen in magnetooptical, magnetotransport, and magnetic resonance measurements. Moreover, we demonstrate for the first time experimentally that *the indirect coupling changes sign* with interlayer thickness.

EXPERIMENTAL DETAILS

Two sets of Fe/Au/Tb trilayers were prepared on quartz and silicon substrates by electron-beam evaporation in an MBE system having a background pressure of 1×10^{-10} Torr and a pressure of better than 1×10^{-9} Torr during the film growth. To minimize interdiffusion of the layers the substrate temperature during evaporation was kept near

0°C. The rate of evaporation did not exceed 0.4 Å/s and was controlled with a calibrated quartz crystal monitor. Samples on quartz substrates were protected with a 30 Å thick layer of Al_2O_3, whereas samples on Si substrates were capped with a 30 Å Au layer. Polar magnetooptical Kerr effect (PMOKE), ferromagnetic resonance (FMR), and magnetotransport methods were used to characterize the films magnetically. PMOKE was measured at room temperature using a 630 nm laser in an applied field up to 1.8 T perpendicular to the film plane. The FMR was measured at room temperature by means of conventional modulation rf spectrometer at 9.41 GHz with an applied magnetic field (up to 0.7 T) in the film plane. The extraordinary Hall effect (EHE) and magnetoresistance (MR) of the trilayers were measured using standard techniques. The required five electrical contacts were made on the film samples using Ag paint, and the offset voltage in the Hall configuration was compensated in zero magnetic field. Hall voltages (in the range of millivolts for the film on the quartz substrate and a few tenths of a millivolt for those on the silicon substrate) were measured, using a 1 mA current with an applied field of 9 kOe perpendicular to the film plane, whereas the MR measurements were done with field both in plane and perpendicular to it. The thickness of the individual layers, 3 monolayers for Fe ($d_{Fe}=3$ ML) and 3 monolayers for Tb ($d_{Tb}=3$ ML), were chosen on the basis of the previous experiments in which the ferrimagnetic ordering of Fe/Tb multilayers has been shown.[17] Also it was shown for the control films that the 3 ML=8 Å Fe film is ferromagnetic at room temperature, whereas the 3 ML =12 Å Tb film is paramagnetic down to 5 K.[18]

RESULTS AND DISCUSSION

Two periods of oscillation

Understanding of the magnetic coupling via different spacers between TM and RE layers (in ferromagnetic or paramagnetic state) is lacking. However, the phenomenon of magnetic coupling for two TM ferromagnetic layers separated by a nonmagnetic spacer is better understood.[7,10,19,20] Information about the properties of this latter system can be useful in understanding the nature of the coupling that is being investigated here. It was shown that the amplitude of the coupling strength (exchange constant) and the period of oscillations depend on the material and thickness of interlayer, whereas the phase of the exchange coupling oscillations depend upon the properties of the ferromagnetic layers.

For noble-metal spacers theoretical works based on the RKKY model have predicted two oscillations of the interlayer coupling with the spacer thickness, reflecting the topological properties of the Fermi surface:[21]

$$J_{\text{inter}}(d)=1/d^2[A_1\sin(2\pi d/\Lambda_1+\Phi_1)+A_2\sin(2\pi d/\Lambda_2+\Phi_2)] \quad (1)$$

where $J_{\text{inter}}(d)$ is the interlayer exchange energy as a function of the spacer thickness d; A_1, A_2 are the amplitudes and Λ_1, Λ_2 are the periods of the energy oscillations.

The phases and the amplitude ratio A_1/A_2 have been found to depend critically on sample quality and ferromagnetic layer thickness. It is only for a few trilayers that two periods of oscillations and antiferromagnetic coupling have been observed for spacers thinner than 3–4 ML, e.g., for Fe/Au/Fe.[22]

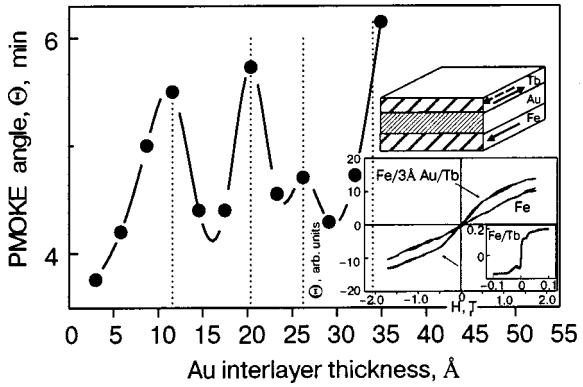

FIG. 1. Oscillation of PMOKE angle for Fe/xAu/Tb trilayers as a function of d_{Au} (quartz substrate). Top inset: Schematic diagram of trilayer. Bottom inset: PMOKE loop for the trilayers compared with the control 8 Å Fe film. Arrows show the kink at a critical field H_{cr} where the susceptibility changes. Bottom right quadrant: Fe/Tb bilayer shows rectangular loop with perpendicular anisotropy.[18]

In Fig. 1 the PMOKE signal measured at room temperature is plotted as a function of Au film thickness for Fe/Au/Tb trilayers (top inset), prepared on a quartz substrate. For a free Fe layer we observed an unsaturated signal (bottom inset), while the Fe/Tb bilayer showed a rectangular loop with perpendicular anisotropy[18] (right bottom quadrant). With the introduction of a 1 ML spacer layer ($d_{\text{Au}}=3$ Å), the PMOKE loop showed that the magnetic moments of the Fe and Tb layers are no longer perpendicular to the film plane. For trilayers with different d_{Au} we observed very narrow loops with no remanence and with a kink, clearly showing two regions with different magnetic susceptibilities. We suppose that the low-field susceptibility is a measure of indirect exchange between Fe and Tb via Au. The difference of the loops for the control Fe film with $d_{\text{Fe}}=8$ Å and for trilayers shows that interaction between Fe and Tb layers still exists. Fragments of the loop at magnetic fields above the kink show that the Fe magnetization is affected by the Au. The PMOKE angle was taken at the kink point. The loop indicates the rotation of the magnetic moments of the layers from the film plane (at $H=0$) with increasing perpendicular magnetic field: the position of the kink (values of the PMOKE angle and magnetic field) oscillates as d_{Au} increased. Oscillations of the Kerr angle with Au thickness having one clear period of about 8 Å and some feature of the second period of 26 Å are observed.

Oscillation of the magnetic moment as a function of Au for thickness greater than 20 Å was seen in sputtered multilayers of $[\text{Fe/Au/Tb}]_{12}$ by Hoffman and Scherschlicht.[16] The first period (8 Å, i.e., 2.8 ML) observed by us on trilayers correlates well with that seen on multilayers. Interestingly, in general we observed both periods for the Fe/Au/Tb system, that is 2.8 ML and 8.9 ML. These correlate well with the oscillation periods 2.5 and 8.6 ML, which were measured for the Fe/Au/Fe system[23] and also with the values of 2.5 and 8.6 ML extracted[24] from measurements of the Au Fermi surface. The facts that the feature of the second oscillation period appears and also the high amplitude ratio, $A_{1\,\max}/A_{1\,\min}$,

show that the growth conditions for the trilayers were good and the interface is sharp. The amplitude ratio of the PMOKE angle, $A'_{1\,\max}/A'_{1\,\min}$, seen in our work, which is proportional to the net magnetic moment, is evaluated as 1.26–1.33 for trilayers on the quartz substrate and 1.64 for the silicon substrate.

The sign change of the coupling

Furthermore, we present direct evidence for the change in the sign of the coupling, alternating between ferromagnetic and antiferromagnetic interaction. From studies of RE–TM amorphous alloy films it is known that the sign of the Hall resistivity changes at the compensation composition due to the change in spin direction,[25–28] meaning that either the Fe or Tb magnetic moment dominates in the perpendicular anisotropy. For Tb/Fe multilayers with different layer thickness it was also shown that the Hall voltage dependence is determined by the interface.[29,30] For Fe/Au/Tb trilayers the indirect exchange between Fe and Tb goes by means of polarized conduction electrons of Au. Since the magnetic moments of Fe and Tb separated by a thin Au spacer come into the film plane gradually as the thickness of the spacer layer increases, at a small spacer thickness they make some angle with the film plane, and hence some perpendicular exchange of indirectly coupled Fe and Tb still exists. Namely, polarized conduction electrons of Au become the main carriers of this exchange. On the other hand, the Au layer has the lowest electrical resistivity in the trilayer studied ($2.2\times10^{8}\ \Omega\cdot$m at $T=293$ K against $10\times$ and $120\times10^{8}\ \Omega\cdot$m for Fe and Tb, respectively[31]). This means that magnetotransport methods, particularly the extraordinary Hall effect, can be very informative for these samples.

Magnetotransport data plotted in Fig. 2 for two sets of trilayers, prepared on quartz and silicon substrates (to increase the range of investigated spacer thickness), show oscillations of the Hall resistivity and magnetoresistance (MR) with Au thickness. The thickness of the Fe and Tb layers was kept the same at 8 Å and 12 Å, respectively, while the thickness of the Au layer was increased. We observed alternate (''right'' and ''left'') loops for the extraordinary Hall effect for different interlayer thickness, showing a sign change of the interaction (Fig. 2). The Hall resistivity in Figs. 2a,c, where an Au layer is interposed between Fe and Tb films, also shows that the magnetic moments of Fe and Tb perpendicular to the film plane are no longer strong. This further shows that the Au film presents an indirect interaction between Fe and Tb with some perpendicular component of magnetization still remaining.

Also shown (Fig. 2c) is the Hall resistivity for a bilayer Fe(8 Å)/Tb(12 Å) without Au in between. It is apparent that the positive (''right'') EHE loops correspond to the parallel coupling, while the negative (''left'') EHE loops are displayed for the antiparallel arrangement (Figs. 2a,c). The MR variation as a function of Au interlayer thickness in transverse and perpendicular geometries is plotted in Figs. 2b,d. Increase in the MR is observed at the periods of the EHE-resistivity modulations, where the antiparallel coupling of Fe and Tb magnetic moments occurs. This is apparent for the samples with low Au thickness (the set of samples prepared on the Si substrates). As the MR signal was very low, the MR

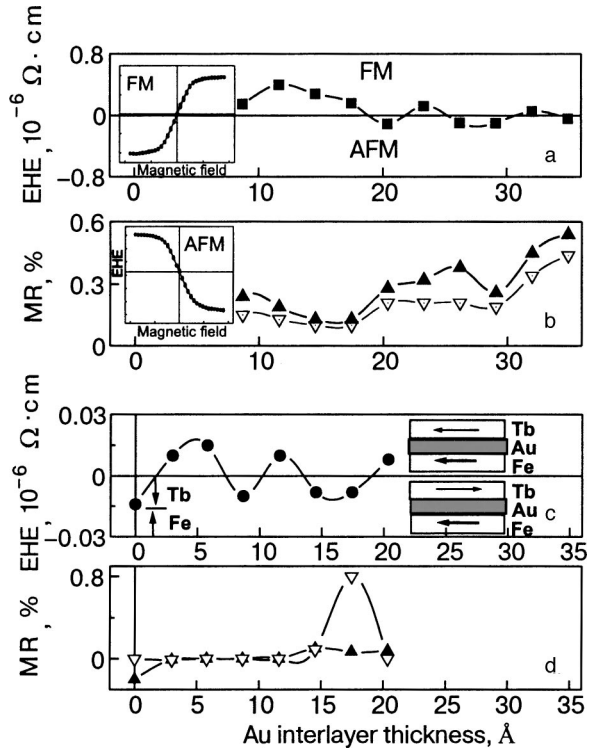

FIG. 2. Extraordinary Hall effect resistivity (a,c) and magnetoresistance (b,d) (perpendicular—white triangles; transverse—black triangles) as a function of Au interlayer thickness. Samples on quartz substrate (a,b); silicon substrate (c,d). The change of sign in the extraordinary Hall effect loops is shown at the left of panels a and b; the top ''right'' loop corresponds to positive values of EHE resistivity in panel a, the lower, ''left'' loop corresponds to the negative values in panel a. Inset in panel c: Schematic of the Fe and Tb magnetization orientations as a result of coupling via the Au spacer.

maximum could be checked only for the second AFM state ($d_{\mathrm{Au}}=15$–20 Å). The same trend of MR increase for the antiparallel coupling is seen at higher Au thickness (the set of samples prepared on the quartz substrates).

Also the influence of substrate on the phase of oscillations can be seen in a comparison of the two sets. One observes that Hall resistivity oscillations having the same periods for the two sets of samples demonstrate some shift of phases (Figs. 2a,c). It is quite plausible that the Fe layers (being only 3 ML thick) prepared on quartz and silicon substrates (with different surface energies) are not the same and, having some structural differences, may affect the phase of the exchange coupling oscillations.

Ferromagnetic resonance

FMR is known to be one of the most powerful experimental techniques in the study of the magnetic properties of ultrathin films. The main advance for our case is the high sensitivity, providing detailed information about the magnetic and structural quality of thin films to monolayer thicknesses; moreover, that resonance can spread to the paramagnetic region.[32]

FMR data shown in Fig. 3 display oscillations of the resonance field with Au interlayer thickness for two sets of trilayers, prepared on quartz and silicon substrates. Quartz

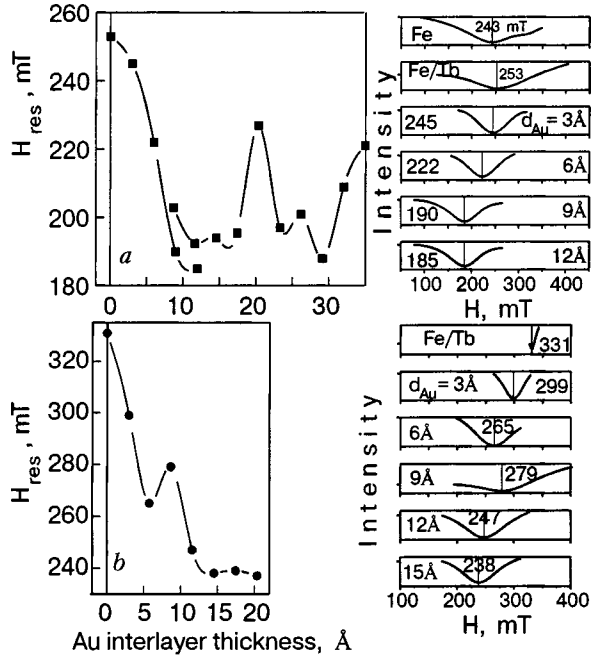

FIG. 3. Resonance fields (H_{res}), obtained (with magnetic field up to 0.7 T, applied in the film plane, and an rf frequency of 9.41 GHz) from FMR data, plotted as a function of Au interlayer thickness for two sets of samples on quartz (a) and on silicon (b) substrates. FMR signals as a function of magnetic field are also shown at the right, where the resonant fields are also indicated in these figures.

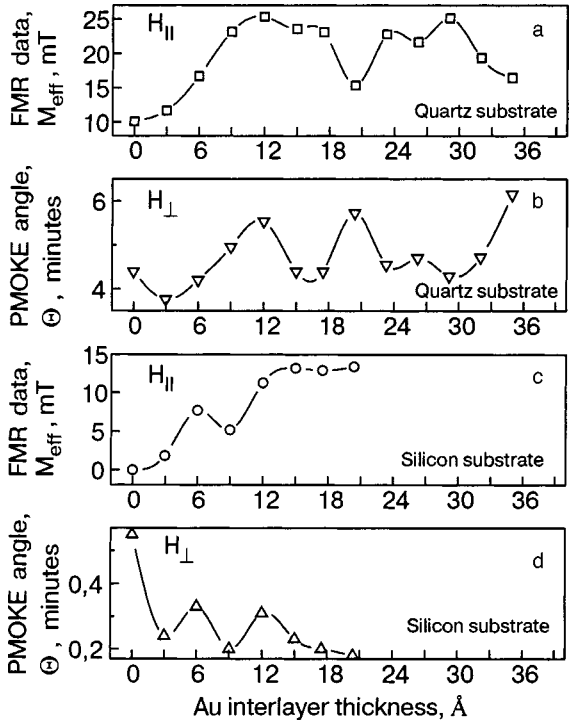

FIG. 4. M_{eff} (a and c) from FMR measurements and Θ (b and d) measured by PMOKE for trilayers with different Au thickness, prepared on quartz (a and b) and silicon (c and d) substrates.

and silicon were chosen from among the other insulating materials to be used as substrates because their FMR signals do not overlap those from the trilayers.

The H_{res} oscillations also correlate well with magnetooptical and magnetotransport measurements. For the sets of trilayers prepared on the quartz substrate one can see the similar dependences for the PMOKE and FMR signals for $d_{Au}>15$ Å, where the maxima of the Kerr angle and H_{res} are found at the same Au thickness, $d_{Au}=20$, 26, and 35 Å (Figs. 1 and 3,a). They correspond to AFM coupling for the magnetotransport data (Fig. 2,a). Samples prepared on the silicon substrate demonstrate AFM coupling at $d_{Au}=9$ Å (Figs. 2c and 3b).

The FMR signals as a function of magnetic field present the dynamics of magnetic moments in Fe/Au/Tb trilayers. The first FMR signal shown is for the control 8 Å thick Fe film (at the right in Fig. 3a). For the 8 Å Fe/12 Å Tb bilayer H_{res} is shifted to higher fields, indicating the appearance of PMA in bilayers due to the Fe–Tb interaction.[18] Introduction of 1 ML of Au at the interface causes a significant decrease of the resonance field compared to that of the 8Fe/12Tb bilayer. Now H_{res} is almost the same as for the control Fe film. With further increase of Au thickness the resonance field decays, followed by its oscillation between ferromagnetic and antiferromagnetic coupling. For the antiparallel coupling the shape of the FMR line is much wider than for the parallel ordering. The resonance fields are higher for samples prepared on the silicon substrate, again showing the influence of the substrate on the Fe layer.[33]

The experimental values of H_{res} for the parallel orientation, substituted into the known Kittel equation[34]

$$\frac{\omega}{\gamma}=\sqrt{H_{res}(H_{res}+4\pi M_{eff})} \tag{2}$$

(where $\omega=2\pi f$ is the microwave frequency, $f=9.38$ GHz, $\gamma=g\mu_B/\hbar$ is the gyromagnetic ratio, g is the spectroscopic splitting factor, and $\hbar$ is Planck's constant), give the effective magnetization $4\pi M_{eff}$, which includes the input of perpendicular anisotropy due to the change of form factor and to the growth anisotropy, as well. M_{eff} and Θ measured by FMR and PMOKE for the trilayers with different Au thickness, prepared on the quartz and silicon substrates, are shown in Fig. 4. Analysis of these data shows that for both sets of samples up to the Au thickness $d_{Au}<15$ Å the FMR and PMOKE data dependences correlate, whereas at $d_{Au}>15$ Å the dependences are found to be in antiphase, i.e., the maximum of the one correlates with the minimum of the other. This means that $d_{Au}=15$ Å is some critical distance for strong coupling between Fe and Tb. Earlier in a Mössbauer study of Fe/Tb multilayers with different layer thickness it was shown that the radius of coupling between Fe and Tb is about 7–15 Å.[35] Hence at interlayer thickness less than 15 Å both direct (hybridization of the Fe and Tb bands) and indirect (RKKY) interactions via the spacer exist, while at higher thickness only the indirect interaction occurs. The main feature of the direct interaction between Fe and Tb layers is the perpendicular anisotropy. When a spacer appears between them and grows in thickness the input of the direct interaction gradually decreases while the input of indirect interaction grows. Our data show that at $d_{Au}>15$ Å the long-range indirect interaction between Fe and Tb layers has the advantage. Under this condition the magnetic moment of the Fe and the induced magnetic moment of the Tb are in the film

plane, and measurements by experimental methods with different geometry (FMR and PMOKE) give opposite results.

Substrate effect

Note that in the PMOKE dependence for the samples on the Si substrate (Fig. 4d), the sample with $d_{Au}=9$ Å, showing AFM coupling in FMR and EHE, demonstrated a minimum in PMOKE, contrary to samples on the quartz substrate. This can be explained by the substrate effect.

We did not use any seed layer (e.g., Ta, Ag, Cu, etc.) while preparing trilayers on Si substrates, as the latter might affect the trilayer interactions. In general, by using two kinds of substrates and different experimental methods we got information about the main features of the interactions and also about the substrate effect.

Always the signal for samples on the Si substrate was about one order of magnitude less than on the quartz. This shows that some amount of Fe did not participate in the coupling (because of the appearance of silicides at the Si/Fe interface)[33] and the interaction did not give a significant perpendicular anisotropy input. In other words, the Fe and Tb moments were in-plane (or nearly so) for the Si substrate and out-of-plane for the quartz. As a result, the PMOKE method, which is sensitive to the perpendicular input, showed a maximum for the samples on the quartz substrate and a minimum for those on Si.

DYNAMICS OF THE Fe AND Tb MAGNETIC MOMENTS

Now we can construct the dynamics of the Fe and Tb magnetic moments with an Au interlayer, starting with an Fe/Tb bilayer. Without an Au layer, perpendicular magnetic anisotropy is observed at the Fe/Tb interface, similar to that which is observed in amorphous Fe–Tb films with composition close to the compensation point: the Fe and Tb magnetic moment vectors are antiparallel to one another and perpendicular to the film plane. This is seen from the PMOKE and from the large FMR resonance field data. Only one ML of Au interposed between Fe and Tb layers is enough to decrease sharply this short-range magnetic interaction. This is supported by the change of the loop shape in PMOKE[18] as well as by the sharp decrease of the FMR resonance field. With further increase of the Au spacer thickness the magnetic moment vectors change their mutual orientations, coming closer and closer to the film plane, as is seen from the EHE and FMR data. Comparison of the PMOKE, FMR, and EHE data show that when $d_{Au}>15$ Å presumably the main character of the Fe–Tb interaction is the indirect exchange. This interaction is observed up to 12 ML of Au, with an oscillation period of 2.8 ML. At the minima of the oscillations sharp increases in the MR are seen, showing a change of sign for the long-range exchange interaction. It is known that the MR is a measure of the type and strength of antiparallel coupling.[36]

The most significant feature of the oscillating mode for the indirect exchange interaction is the weak decay of the modulation amplitude.[16] The presence of oscillations up to 15–17 MLs of Au cannot be expected from RKKY theory (r^{-3} or r^{-2} decay is expected for a ferromagnetic layer). This coupling feature is unique and needs further investigation.

CONCLUSIONS

In summary, carefully prepared Fe(3 ML)/xAu/Tb(3 ML) trilayers under clean conditions display oscillations in the exchange interaction, which can be seen with different methods of characterization. The experimental results correlate well with existing experimental and theoretical data. For the first time it is shown experimentally that:

(i) Fe and Tb layers separated by a thin Au layer couple their magnetic moments parallel or antiparallel for different Au thickness, i.e., *the sign of the exchange interaction oscillates*;
(ii) EHE is a powerful tool for studying indirect exchange coupling;
(iii) at a spacer thickness within the radius of Fe–Tb coupling (7–15 Å) both short-and long-range exchange interactions coexist, while at higher spacer thickness the indirect interaction has the advantage;
(iv) the substrate can affect the features and sign of the coupling.

We are grateful to Jagadeesh S. Moodera, Francis Bitter Magnet Lab, MIT, Cambridge, Massachusetts, USA, for stimulating this work, to Tae Hee Kim for sample preparations, and to Geetha Berera for experimental assistance.

This work was supported by STCU Grant No. 1086.

*E-mail: elena@imag.kiev.ua

[1] P. Chaudhari, J. J. Cuomo, and R. J. Gambino, Appl. Phys. Lett. **22**, 337 (1973); Z. S. Shan, D. J. Sellmyer, S. S. Jaswal, Y. J. Wang, and J. X. Shen, *ibid.* **42**, 10446 (1990); B. Scholz, R. A. Brand, and W. Keune, Phys. Rev. B **50**, 2537 (1994).
[2] K. Yamauchi, K. Habu, and N. Sato, J. Appl. Phys. **64**, 5748 (1988).
[3] A. E. Freitag and A. R. Chowdhury, J. Appl. Phys. **82**, 5039 (1997).
[4] R. Ballou, J. Magn. Magn. Mater. **129**, 1 (1994); B. Dieny, R. Ribas, and B. Barbara, *ibid.* **130**, 189 (1994).
[5] N. Sato, J. Appl. Phys. **59**, 2514 (1986); N. Sato and K. Habu, *ibid.* **61**, 4287 (1986).
[6] W. C. Thoburn, S. Legvold, and F. H. Spedding, Phys. Rev. **112**, 56 (1958).
[7] B. Heinrich and J. F. Cochran, Adv. Phys. **42**, 523 (1993).
[8] M. Bohm and U. Krey, J. Magn. Magn. Mater. **192**, 27 (1999).
[9] T. Emoto, N. Hosoito, and T. Shinjo, J. Magn. Magn. Mater. **189**, 136 (1998).
[10] S. S. P. Parkin, Annu. Rev. Mater. Sci. **25**, 357 (1995).
[11] P. Bruno, *Magnetische Schichtsysteme*, edited by P. H. Dederichs and P. Grünberg, Forschungszentrum Jülich (1999).
[12] K. Takanashi, H. Fujimori, and H. Kurokawa, J. Magn. Magn. Mater. **126**, 242 (1993).
[13] K. Takanashi, H. Fujimori, and H. Kurokawa, Appl. Phys. Lett. **63**, 11 (1993).
[14] C. F. Majkrzak, J. W. Cable, J. Kwo, M. Hong, D. B. McWhan, Y. Yafet, V. Waszczak, and C. Vettier, Phys. Rev. Lett. **56**, 2700 (1986).
[15] D. H. Mosca, F. Petroff, A. Fert, P. A. Schroeder, W. P. Pratt, and Jr. R. Laloee, J. Magn. Magn. Mater. **94**, L1 (1991).
[16] H. Hoffmann and R. Scherschlicht, *Festkörperprobleme*, edited by R. Helbig, Vieweg, Braunschweig/Wiesbaden (1998).
[17] E. Shypil and A. Pogorily, J. Magn. Magn. Mater. **157/158**, 293 (1996).
[18] E. V. Shypil, A. M. Pogorily, D. I. Podyalovski, and Y. A. Pogoryelov, Fiz. Nizk. Temp. **27**, 879 (2001) [Low Temp. Phys. **27**, 650 (2001)].
[19] S. M. Rezende, C. Chesman, M. A. Lucena, A. Azevedo, F. M. de Aguiar, and S. S. P. Parkin, J. Appl. Phys. **84**, 958 (1998).
[20] M. D. Stiles, J. Magn. Magn. Mater. **200**, 322 (1999).

[21] A. Ney, F. Wilhelm, M. Farle, P. Poulopoulos, P. Srivastava, and K. Baberschke, Phys. Rev. B **59**, R3938 (1999).
[22] J. Unguris, R. J. Celotta, and D. T. Pierce, Phys. Rev. Lett. **79**, 2734 (1997).
[23] J. Unguris, R. J. Celotta, and D. T. Pierce, J. Appl. Phys. **75**, 6437 (1994).
[24] P. Bruno and L. Chappert, Phys. Rev. Lett. **67**, 1602 (1991).
[25] A. Ogawa, T. Katayama, M. Hirano, and T. Tsusina, Jpn. J. Appl. Phys. **15**, 87 (1976).
[26] M. Hartman and T. R. McGuire, Phys. Rev. Lett. **51**, 1194 (1983).
[27] R. J. Gambino and T. R. McGuire, J. Magn. Magn. Mater. **54–57**, 1365 (1986).
[28] T. R. McGuire, R. J. Gambino, A. E. Bell, and G. J. Sprokel, J. Magn. Magn. Mater. **54–57**, 1387 (1986).
[29] S. Kim, S. R. Lee, and J. D. Chung, J. Appl. Phys. **73**, 6344 (1993).
[30] E. Shypil, A. Pogorily, L. Uba, and S. Uba, Functional Materials **2**, 208 (1995).
[31] D. R. Lide (ed.) *Chemical Rubber Company Handbook of Chemistry and Physics*, CRC Press, Boca Raton, Florida, USA, 79th edition (1998).
[32] M. Farle, Rep. Prog. Phys. **61**, 755 (1998).
[33] F. Zavaliche, W. Wulfhekel, Hai Xu, and J. Kirchner, J. Appl. Phys. **88**, 5289 (2000).
[34] R. F. Soohoo, *Magnetic Thin Films*, Harper and Row, New York (1965).
[35] O. Kuzmak, E. Shypil, V. Shevchenko, and S. Kharitonsky, Ukr. J. Phys. **36**, 584 (1991).
[36] K. Inomato and Y. Saito, J. Magn. Magn. Mater. **126**, 425 (1993).

This article was published in English in the original Russian journal. Reproduced here with stylistic changes by AIP.

Magnetoresistive study of the antiferromagnetic–weak ferromagnetic transition in single-crystal $La_2CuO_{4+\delta}$

B. I. Belevtsev,* N. V. Dalakova, V. N. Savitsky, A. S. Panfilov, and I. S. Braude

B. Verkin Institute for Low Temperature Physics and Engineering of the National Academy of Sciences, 47 Lenin Ave., Kharkov 61103, Ukraine

A. V. Bondarenko

V. N. Karazin Kharkov National University, pl. Svobodi 4, Kharkov 61077, Ukraine

(Submitted December 4, 2003)
Fiz. Nizk. Temp. **30**, 551–557 (April 2004)

Resistive measurements were made to study the magnetic field-induced antiferromagnetic (AF)—weak ferromagnetic (WF) transition in the La_2CuO_4 single crystal. The magnetic field (dc or pulsed) was applied normally to the CuO_2 layers. The transition manifested itself in a drastic decrease of the resistance in critical fields of 5–7 T. The study is the first to display the effect of the AF–WF transition on the conductivity of the La_2CuO_4 single crystal in the direction parallel to the CuO_2 layers. The results provide support for the three-dimensional nature of the hopping conduction of this layered oxide. © *2004 American Institute of Physics.*
[DOI: 10.1063/1.1739162]

1. INTRODUCTION

The transport and magnetic properties of cuprate $La_2CuO_{4+\delta}$ have attracted considerable attention in the area of superconducting research. This is a parent compound for one of the family of high-temperature superconductors, and study of its properties is considered to be important for elucidation of still unclear nature of superconductivity in cuprates. Stoichiometric La_2CuO_4 ($\delta=0$) is an antiferromagnetic (AF) insulator with a Néel temperature T_N of about 320 K, but doping it with bivalent metals (such as Sr) or with excess oxygen ($\delta\neq 0$) leads to destruction of the long-range AF order and a decrease in T_N (Ref. 1–3). A fairly high doping results in a transition to a metallic state.

The perovskite crystal lattice of La_2CuO_4 is orthorhombic (below about 530 K) and consists of CuO_2 layers separated by La_2O_2 layers (the latter consisting of two buckled La–O layers).[2,3] In the $Bmab$ space group the CuO_2 layers are perpendicular to the **c** axis and parallel to the ab plane.[3] The CuO_6 octahedra are tilted in a staggered way; the tilting is uniform in a given cb plane. The AF state is strongly connected with crystal lattice features.[4] The magnetic state is determined by d^9Cu^{2+} ions with spin $S=0.5$. In the CuO_2 planes, the magnetic structure is characterized by a simple two-dimensional (2D) AF array with nearest neighbors having antiparallel moments.[4] Due to the above-mentioned tilting of the CuO_6 octahedra, the spins are canted 0.17° in the cb plane away from the **b** axis.[4,5] As a result, a weak ferromagnetic (FM) moment perpendicular to the CuO_2 plane appears in each layer. Below T_N, the directions of the FM moments in neighboring CuO_2 planes are opposite, so that the system as a whole is a three-dimensional (3D) AF.[5]

Application of high enough magnetic field along the **c** axis causes a magnetic transition to a weak-ferromagnetic (WF) state, in which all canted moments are aligned along the field direction.[5] The transition is accompanied by a jump-like change in the resistivity.[5] The critical field H_c of the transition is temperature dependent. It goes to zero for T approaching T_N, but increases with decreasing temperature and amounts to 5–6 T below 100 K. Hole doping of La_2CuO_4, leading to lower T_N, causes smaller H_c values as well (down to about 3 T at low temperature for samples with T_N about 100 K).[6] Some magnetic transitions have also been found for field applied parallel to the ab plane.[7] In this case, for field parallel to the **b** axis, a spin-flop transition was found at a field H_1 of about 10 T, and a transition to the FM state at a field H_2 of about 20 T. These transitions manifest themselves as weak knees (no jumps) in the MR curves.[7] It is believed that no magnetic transition should take place when field is applied parallel to the **a** axis, which is perpendicular to the staggered moments.[7,8]

Doping with excess oxygen introduces charge carriers (holes) in the CuO_2 planes. At small enough δ (<0.01), $La_2CuO_{4+\delta}$ remains insulating, although T_N is lowered considerably.[9,10] The excess oxygen atoms reside at interstitial sites between La–O planes.[11] Each such excess atom is surrounded by a tetrahedron of apical oxygen atoms. For layered cuprates, in which the CuO_2 planes are the main conducting units, a quasi-2D behavior is expected for the in-plane transport. This has actually been found in many cuprates[12] but not in $La_2CuO_{4+\delta}$. In this compound, the Mott's variable-range hopping (VRH), with temperature dependence of the resistance described by the expression

$$R \approx R_0 \exp\left(\frac{T_0}{T}\right)^{1/4}, \tag{1}$$

is found[13,14] at low T for both the in-plane (current **J** parallel to the CuO_2 planes) and out-of-plane (**J**$\|$**c**) transport. The fractional exponent of 1/4 in Eq. (1) corresponds to 3D system (for 2D systems, it should be equal to 1/3).[15] At the same time, the hopping conduction in $La_2CuO_{4+\delta}$ samples with fairly high crystal perfection shows considerable anisotropy,

so that the values of R_0 and T_0 in Eq. (1) are different for the in-plane and out-of-plane transport. The in-plane conductivity σ_{ab} is found to be considerably higher than the out-of-plane conductivity σ_c. The ratio σ_{ab}/σ_c is strongly temperature dependent. It is minimal (about 10) in the liquid-helium temperature range but increases dramatically with temperature and saturates above 200 K to maximal values of the order of 100.[16–18]

The 3D character of the VRH in $La_2CuO_{4+\delta}$ testifies that a hole transfer between CuO_2 is likely not only at **J**‖**c**, but at **J**‖**a**, **b**, as well. In considering this question it is important to know the exact nature of the holes in $La_2CuO_{4+\delta}$. Although about 17 years have passed since the discovery of superconductivity in doped $La_2CuO_{4+\delta}$, the nature of the holes in it still cannot be considered completely clear. This in turn makes it hard to gain insight into the nature of the cuprate's superconductivity. In the undoped state, the CuO_2 planes present a lattice of d^9Cu^{2+} ($S=0.5$) and p^6O^{2-} ($S=0$) ions. Doping with excess oxygen causes (to ensure neutrality) the appearance of additional holes in the planes. This can be achieved in two ways: 1) some of the d^9Cu^{2+} ions change into the d^8Cu^{3+} ($S=0$) state, or 2) some of the in-plane oxygen ions p^6O^{2-} change into the p^5O^{1-} ($S=0.5$) state. In either case, the holes induce strong local perturbations of the AF order. In the known literature[19–25] both kinds of holes have been taken into account in theoretical models of fundamental properties of the cuprates. There is much speculation, however, that holes in $La_2CuO_{4+\delta}$ have a strong oxygen character,[19–24] and this view has strong experimental support.[20,22,26] At the same time, due to the overlapping of the *d* and *p* orbitals and hybridization of the *d* and *p* bands, the *d* orbitals exert a significant influence on the hole motion.

According to Ref. 21, owing to the special the character of the excess oxygen as interstitial atoms[11] with weak oxygen—oxygen bonding, the holes can be delocalized from the CuO_2 planes onto the apical O atoms, i.e., into the $La_2O_{2+\delta}$ region between adjacent CuO_2 planes. This assures the 3D nature of the VRH in $La_2CuO_{4+\delta}$. In this way the $La_2CuO_{4+\delta}$ system differs drastically from the Sr-doped system, where the holes remain quasi-two-dimensional. In fact, the ratio σ_{ab}/σ_c in lightly doped $La_{1-x}Sr_xCuO_4$ crystals of good quality can be as high as several thousand.[27]

In this communication we report the results of a study of the AF–WF transition by magnetoresistance (MR) measurements in a $La_2CuO_{4+\delta}$ single crystal. In the known previous studies[5,28–31] the MR investigations of the AF–WF transition in $La_2CuO_{4+\delta}$ were done for the case when both the magnetic field and transport current are perpendicular to the CuO_2 planes (i.e., **H**‖**c** and **J**‖**c**). Under these conditions a rather sharp decrease in the resistance has been found as the critical field H_c was approached from below. The amplitude of the relative change in resistance ($\Delta R/R_n$, where R_n is the resistance in the AF state) due to the AF–WF transition depends on temperature. It is maximal in the range 20–30 K, where it can amount to 0.30–0.50 in fairly perfect crystals.[5,7,29–31]

It is known that the enhancement of spin order usually leads to a decrease in resistivity of metallic systems. For example, a considerable decrease in resistivity can occur at transitions from the paramagnetic to the FM or AF state in some metals, alloys, or even in some FM perovskite oxides, such as mixed-valence manganites.[32–34] This is usually attributed to a decrease in the scattering rate of quasi-free charge carriers on disordered local spins as a result of the above-mentioned magnetic transitions. The situation is rather different in the case of insulating $La_2CuO_{4+\delta}$. Here the transition to the 3D AF state produces hardly any noticeable change in the hopping conductivity at T_N (apparently for the reason that 2D AF correlations in the CuO_2 planes persist up to temperatures far above T_N; Refs. 1–3), while the transition to the 3D WF state increases the conductivity enormously. Since the VRH in $La_2CuO_{4+\delta}$ has a pronounced 3D character, it can be expected that the AF–WF transition would manifest itself in resistivity in field **H**‖**c** not only for the transport current perpendicular to the CuO_2 planes, as was found in Refs. 5, 29–31, but for the in-plane hole transport as well. In the present study this effect has been actually revealed, as described below.

2. EXPERIMENTAL

A single-crystal $La_2CuO_{4+\delta}$ sample with dimensions of $1.3\times0.3\times0.39$ mm is investigated. This sample was studied previously in Ref. 18, where it was indicated as sample No. 1 with $T_N=188$ K. After that study, the sample was annealed additionally in an oxygen atmosphere (700 °C, 5.5 days) in the hope that oxygen content (that is, δ) would be increased. It turned out, however, that the thermal treatment caused only a slight decrease in T_N (down to 182 K) and in the resistivity. The T_N value was determined from magnetic susceptibility measurements.

The crystallographic orientation of the sample was determined from an x-ray diffraction study. This reveals that the sample has a quantity of twins, which inevitably appear in $La_2CuO_{4+\delta}$ crystals when cooled through tetragonal-to-orthorhombic structural transition at $T\approx530$ K.[3] As a result, a peculiar domain structure is developed. The orientation of the **c** axis is the same in each domain, but the orientations of the **a** and **b** axes are switched (or reversed) in a fixed way between two possible orientations upon crossing the domain (twin) boundaries. In this connection, although in what follows we will speak conventionally about **a** or **b** directions of transport current in the sample studied, they should, first of all, be taken as two mutually perpendicular in-plane current directions in the twinned crystal. In a heavily twinned crystal no significant anisotropy in the in-plane conductivity can be expected, even assuming that some intrinsic conductivity anisotropy within the CuO_2 planes is present. In the present study, however, pronounced anisotropy in the conductivity (and rather significant anisotropy in the MR) is found for these two in-plane directions. This matter will be touched upon in the next Section of this paper. In contrast, we can speak about the **c** directions in the sample studied without any reservation or possible misunderstanding.

In this study, the dc resistance in the directions parallel to CuO_2 planes was measured by the Montgomery method,[35] which is appropriate for systems with a pronounced anisotropy of the conductivity. Contacts between the measuring wires and the sample were made using a conducting silver paste. The measurements were done in field **H**‖**c** in a helium

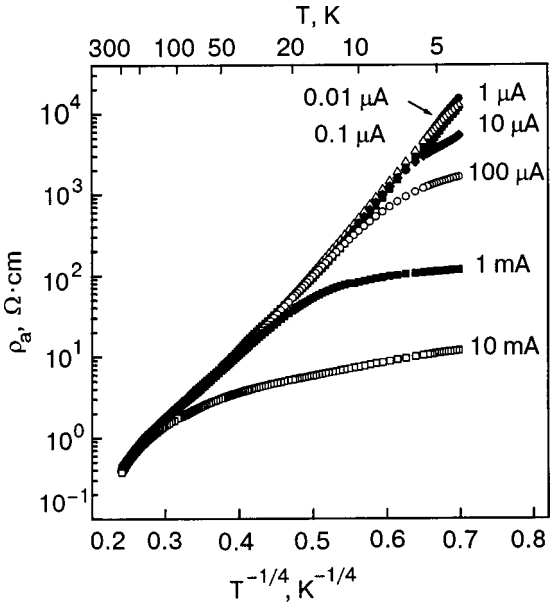

FIG. 1. The temperature dependence of the resistivity ρ_a of single-crystal $La_2CuO_{4+\delta}$ measured at different values of transport current. In all cases the current was directed parallel to the crystallographic axis **a**. The dependences are presented as $\log \rho_a$ versus $T^{-1/4}$.

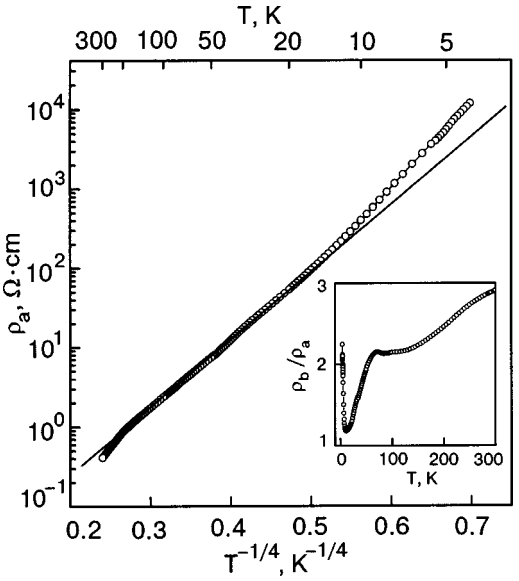

FIG. 2. The temperature dependence of the resistivity ρ_a of single-crystal $La_2CuO_{4+\delta}$ measured for transport current equal to 1 μA. The current was directed parallel to the crystallographic axis **a**. The inset shows temperature behavior of the ratio of the resistivities ρ_b and ρ_a for measuring currents directed along the crystallographic axes **b** and **a**.

cryostat with a superconducting solenoid. Although the maximum field in the cryostat (about 6 T) has appeared to be quite sufficient in most cases to reveal manifestations of the AF–WF transition in the MR of the sample studied, a somewhat higher field is needed to study the transition more thoroughly, especially for the study of hysteretic phenomena in the $R(H)$ curves in the vicinity of the critical field H_c.[5,29–31] This hysteretic behavior is considered as an indication of a first-order transition. For this reason, a part of the dc resistance measurements in this study were done in pulsed magnetic field with amplitude up to 15 T. The nearly sinusoidal pulse has a duration about 33 ms, during which the field is swept from zero to a maximum amplitude and back to zero. For these measurements a field **H**‖**c** and transport currents **J**‖**c** and **J**‖**a** were used. The rate of variations in magnetic field was up to 10^3 T/s. Other essential details of the pulse measuring technique employed can be found in Ref. 36.

3. RESULTS AND DISCUSSION

The temperature dependences of the resistivity ρ_a measured along the **a** axis (**J**‖**a**) is shown in Fig. 1 for different magnitudes of the measuring current. It is seen that the $\rho(T)$ behavior is essentially independent of the current in the whole measuring temperature range, 4.2 K$\leqslant T \leqslant$300 K, for current magnitude less than about 1 μA; that is, Ohm's law holds in this case. For better consideration, one of these Ohmic $\rho(T)$ curves (at $J=1$ μA) is presented separately in Fig. 2. It can be seen that Mott's law [Eq. (1)] is obeyed fairly well in the range 20 K$\leqslant T \leqslant$200 K. In the range $T<20$ K, a steeper [as compared to Eq. (1)] increase in R with decreasing temperature is found. This deviation from Mott's law at low temperature is rather typical for $La_2CuO_{4+\delta}$ and was observed earlier in Refs. 14 and 31. In Ref. 14, a possible reason for this behavior is suggested: the presence of superconducting inclusions in the insulating sample due to phase separation in $La_2CuO_{4+\delta}$.

The magnetic structure of $La_2CuO_{4+\delta}$, according to neutron diffraction data,[2,4] is anisotropic for all three orthorhombic axes. The same can be expected, therefore, for transport and magnetic properties. In the presence of twins, however, the measured transport and magnetic properties

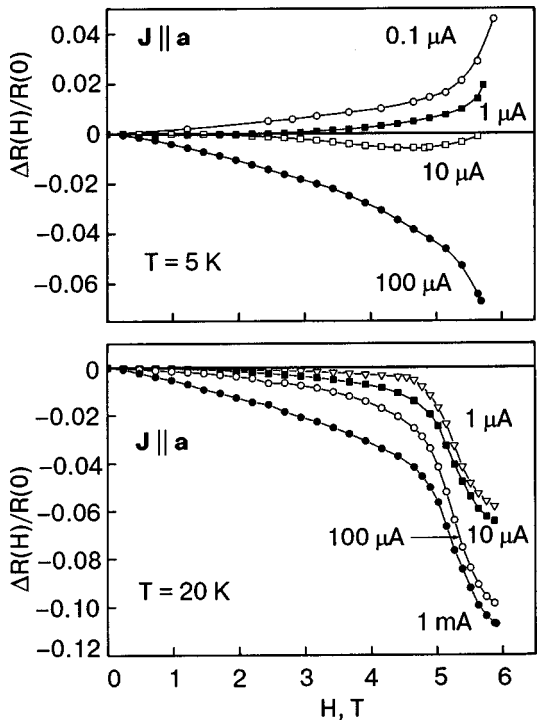

FIG. 3. Magnetoresistance curves at $T=5$ and 20 K measured for single-crystal $La_2CuO_{4+\delta}$ in an out-of-plane dc magnetic field (**H**‖**c**) for different amplitudes of the measuring current, directed along the crystallographic axis **a**.

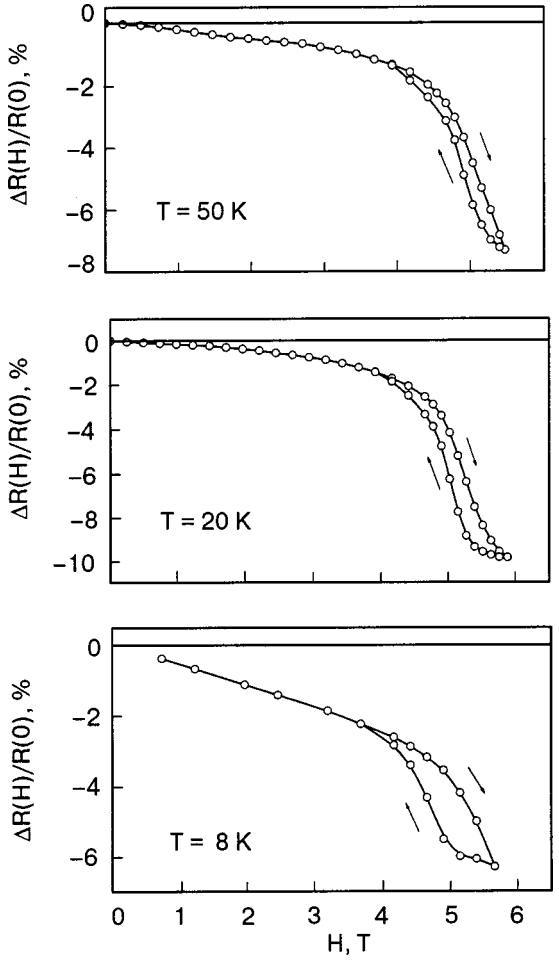

FIG. 4. Magnetoresistance curves at various fixed temperatures measured for single-crystal $La_2CuO_{4+\delta}$ in an out-of-plane dc magnetic field (**H**‖**c**) for measuring current (100 μA) directed along the crystallographic axis **a**.

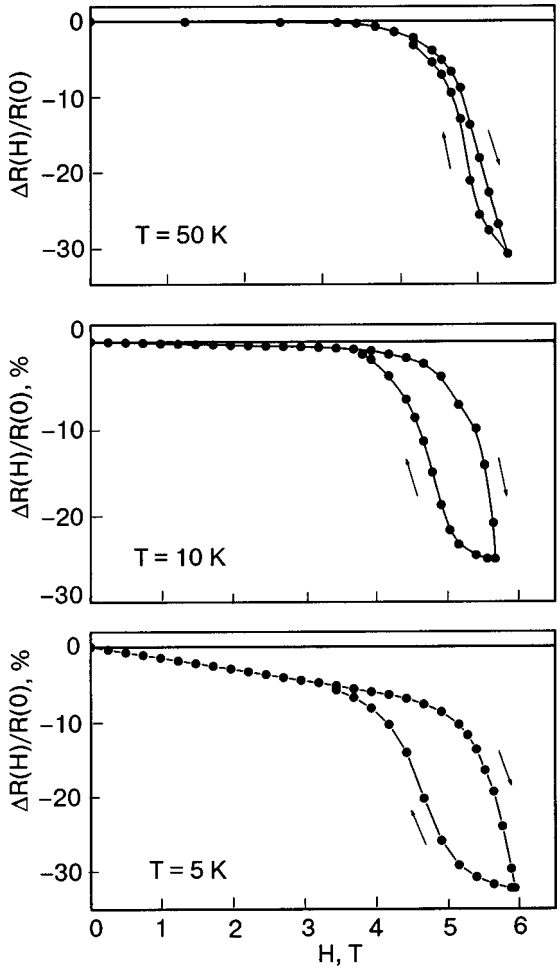

FIG. 5. Magnetoresistance curves at various fixed temperatures measured for single-crystal $La_2CuO_{4+\delta}$ in an out-of-plane dc magnetic field (**H**‖**c**) for measuring current (100 μA) directed along the crystallographic axis **b**.

usually show quite definite anisotropy solely for directions parallel and perpendicular to the CuO_2 planes. Recently, in untwinned $La_2CuO_{4+\delta}$ crystals, a clear in-plane anisotropy of the magnetic susceptibility χ was found.[37] A similar phenomenon may be expected in the transport properties of $La_2CuO_{4+\delta}$ samples without twins.

In a sample with multiple twins, no considerable in-plane anisotropy could be expected. However, the measured ratio ρ_b/ρ_a in the sample studied (see inset in Fig. 2) reveals a rather distinct anisotropy. The ratio is close to unity at $T \approx 11-12$ K, but it increases with temperature and approaches value of about 3 at room temperature. A similar behavior was found in a previously studied sample with a somewhat higher $T_N \approx 188$ K.[18] The $a-b$ anisotropic behavior of the conductivity in a twinned sample (in the case that the conductivities σ_a and σ_b are inherently different) can be observed only when, *first*, the existing twins are few in number (so that the measured resistivity is not properly averaged between the two possible crystal orientations), and, *second*, a given current direction is really parallel to the **a** (or **b**) axis in most of the crystal. The results of this study therefore give evidence that the intrinsic conductivity anisotropy in the CuO_2 planes of $La_2CuO_{4+\delta}$ is quite credible.

We found that the MR behavior of the sample studied depends significantly on the magnitude of the measuring current, especially at low temperature. The upper panel of Fig. 3 presents the MR curves recorded at $T=5$ K for the case **J**‖**a**. It can be seen that for low currents (that is in the Ohmic regime) the MR is positive, but for high enough currents ($J \geqslant 1$ μA) the MR becomes negative and increases strongly above $H \simeq 5$ T. Positive MR was observed only at low temperature ($T<20$ K) for both the in-plane current directions used, **J**‖**a** and **J**‖**b**. At fairly high temperature, $T \geqslant 20$ K, only negative MR is observed, which increases profoundly above $H \simeq 5$ T, as well (lower panel of Fig. 3). We have attributed this rather sharp increase to an influence of the AF–WF transition, as will be discussed in more detail below. As to the positive MR at low temperature ($T<20$ K), this could be attributed to the presence of superconducting inclusions due to phase separation, as was mentioned above. For example, in Ref. 38, positive MR attributed to superconducting inclusions has been found in the low-temperature range ($T<10$ K) in even more resistive $La_2CuO_{4+\delta}$ with higher T_N.

For all of the temperature range in which the MR was measured in this study (4.2 K$\leqslant T \leqslant$90 K), the MR magnitude is strongly dependent on the measuring current (as illustrated by Fig. 3). For this reason, to compare MR curves with an evident effect of AF–WF transition at different temperatures we have used only data for rather high currents,

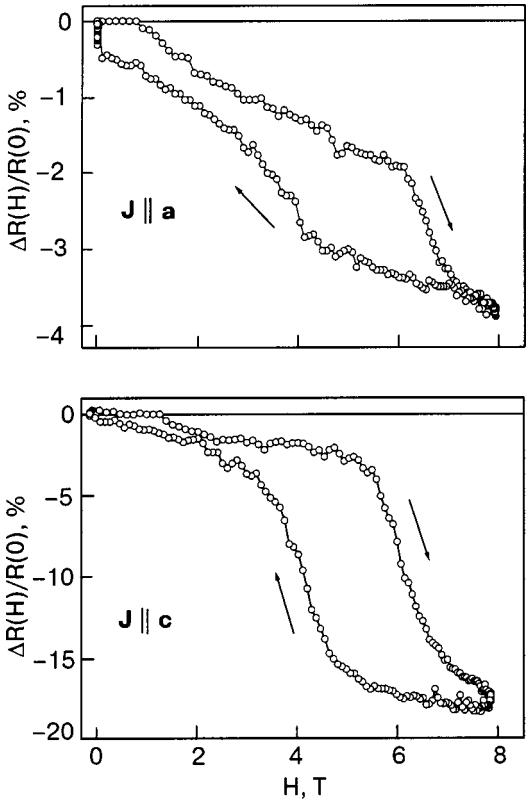

FIG. 6. Magnetoresistance curves registered for single-crystal $La_2CuO_{4+\delta}$ in an out-of-plane pulsed magnetic field (**H**‖**c**) at $T=4.2$ K for the in-plane and out-of-plane current directions (**J**‖**a** and **J**‖**c**) with current magnitudes of 6 μA and 7.4 μA, respectively.

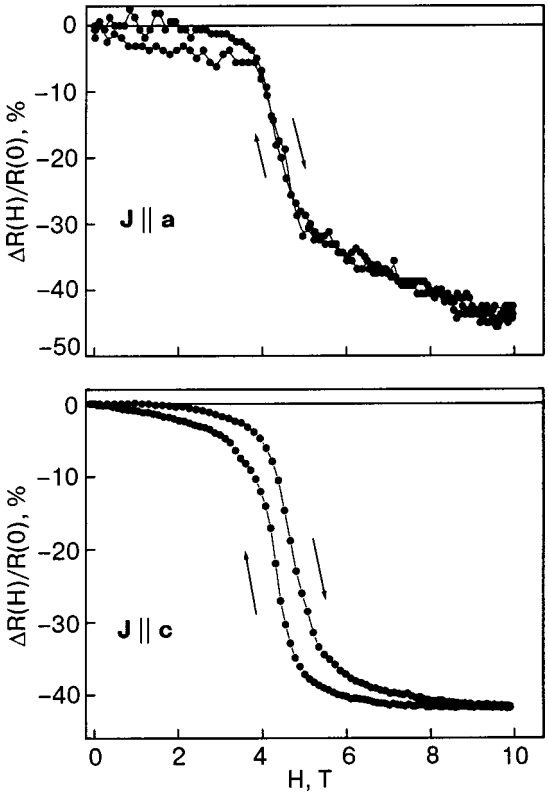

FIG. 7. Magnetoresistance curves registered for single-crystal $La_2CuO_{4+\delta}$ in the out-of-plane pulsed magnetic field (**H**‖**c**) at $T=77$ K for the in-plane and out-of-plane current directions (**J**‖**a** and **J**‖**c**) with current magnitudes 5.93 mA and 178 μA, respectively.

that is, for the non-Ohmic conduction regime. Some examples of the MR curves at **H**‖**c** for the cases **J**‖**a** and **J**‖**b** and current $J=100$ μA are shown in Figs. 4 and 5 for certain selected temperatures. It is obvious from the curves that a rather sharp decrease in resistance occurs when H exceeds some critical magnitude (in the range 5–6 T). All main features of this resistive transition are quite identical to those found in the MR behavior of $La_2CuO_{4+\delta}$ at the AF–WF transition for the case **H**‖**c**, and the out-of-plane current direction (**J**‖**c**), when mainly interplane hopping is affected by the transition.[5,28–30] The results obtained show that the AF–WF transition influences hopping conduction in the directions parallel to CuO_2 planes as well. This effect, although anticipated (as is indicated above), had never been seen previously in $La_2CuO_{4+\delta}$, to our knowledge.

The following features of the resistive transition can be pointed out. First, the transition is sharper and the relative changes in resistance, $\Delta R/R_n$, are larger for the **b** direction of the transport current than for the **a** direction (compare Figs. 4 and 5). Second, the MR curves are hysteretic in the field range of the transition, as expected. The hysteresis becomes more pronounced for decreasing temperature. The latter feature of the MR curves is quite consistent with that found previously at the AF–WF transition for **J**‖**c**.[5,29–31] Third, a considerable negative MR in the low-field range below the magnetic transition can be observed (Figs. 4 and 5). This contribution to the total MR is not hysteretic and, maybe, has little if any relationship to the magnetic transition. For a given current (for example, for $J=100$ μA, as in Figs. 4 and 5) the contribution of this type of MR increases with decreasing temperature and is more pronounced for the **a** direction of the measuring current. It is found as well that the negative MR at low field increases with current magnitude (Fig. 3) and, therefore, with an applied voltage, so it is much more pronounced in the non-Ohmic regime of hopping conductivity (compare Figs. 1 and 3). In previous studies, negative MR in the AF $La_2CuO_{4+\delta}$ for the case of both the current and field parallel to CuO_2 was found and discussed to a certain degree.[14,18] The nature of the negative MR in rather low field **H**‖**c** and **J**‖**a**, **b** revealed in this work remains unclear and is worthy of additional study.

It is evident from Figs. 4 and 5 that the maximal dc field of about 6 T used for these measurements is not high enough to accomplish the magnetic transition in full measure. To overcome this disadvantage, measurements were done in pulsed magnetic field with magnitude up to 15 T. The MR curves were recorded at temperatures $T=4.2$, 20.4, and 77 K for both the in-plane and out-of-plane directions of the transport current. Examples of MR curves for pulsed field at $T=4.2$ and 77 K are shown in Figs. 6 and 7.

The pulsed MR measurements enabled us to see the magnetic transitions in full measure. The MR curves for the low-temperature region were found to be quite similar for both methods (compare Figs. 4 and 6). It is also seen that the resistive transition for the out-of-plane current direction is sharper, and the relative changes in resistance, $\Delta R/R_n$, are generally larger than those for the in-plane direction. The MR curves in pulsed magnetic field at $T=77$ K are less hysteretic than those at $T=4.2$ K, as expected (Fig. 7). The maximum values of $\Delta R/R_n \approx 50\%$ found in this study for

pulsed magnetic field agree well with those found in previous studies in dc magnetic field.[7]

In conclusion, we have found that the AF–WF transition in $La_2CuO_{4+\delta}$ is clearly manifested in the in-plane hopping conductivity. This supports the 3D nature of hopping conduction in this compound.

*E-mail: belevtsev@ilt.kharkov.ua

[1] A. Aharony, R. J. Birgeneau, A. Coniglio, M. A. Kastner, and H. E. Stanley, Phys. Rev. Lett. **60**, 1330 (1988).
[2] Y. Endoh, K. Yamada, R. J. Birgeneau, D. R. Gabbe, H. P. Jenssen, M. A. Kastner, C. J. Peters, P. J. Picone, T. R. Thurston, J. M. Tranquada, G. Shirane, Y. Hidaka, M. Oda, Y. Enomoto, M. Suzuki, and T. Murakami, Phys. Rev. B **37**, 7443 (1988).
[3] M. A. Kastner, R. G. Birgeneau, G. Shirane, and Y. Endoh, Rev. Mod. Phys. **70**, 897 (1998).
[4] D. Vaknin, S. K. Sinha, D. E. Moncton, D. C. Johnston, J. M. Newsam, C. R. Safinya, and H. E. King, Jr., Phys. Rev. Lett. **58**, 2802 (1987).
[5] T. Thio, T. R. Thurston, N. W. Preyer, P. J. Picone, M. A. Kastner, H. P. Jenssen, D. R. Gabbe, C. Y. Chen, R. J. Birgeneau, and A. Aharony, Phys. Rev. B **38**, 905 (1988).
[6] N. Bazhan and V. N. Bevz, Sverkhprovodimost' (KIAE) **4**, 116 (1991) [Superconductivity **4**, 100 (1991)].
[7] T. Thio, C. Y. Chen, B. S. Freer, D. R. Gabbe, H. P. Jenssen, M. A. Kastner, P. J. Picone, N. W. Preyer, and R. J. Birgeneau, Phys. Rev. B **41**, 231 (1990).
[8] O. Gogolin and A. S. Ioselevich, Zh. Éksp. Teor. Fiz. **98**, 682 (1990) [Sov. Phys. JETP **71**, 380 (1990)].
[9] A. A. Zakharov and A. A. Nikonov, JETP Lett. **60**, 348 (1994).
[10] B. W. Statt, P. C. Hammel, Z. Fisk, S. W. Cheong, F. C. Chou, D. C. Johnson, and J. E. Schirber, Phys. Rev. B **52**, 15575 (1995).
[11] C. Chaillout, J. Chenavas, S. W. Cheong, Z. Fisk, M. Marezio, B. Morozin, and J. E. Schirber, Physica C **170**, 87 (1990).
[12] Y. Iye, in *Physical Properties of High Temperature Superconductors III*, edited by D. M. Ginsberg, World Scientific, Singapore (1992), Ch. 4, p. 285.
[13] M. A. Kastner, R. J. Birgeneau, C. Y. Chen, Y. M. Chiang, D. R. Gabbe, H. P. Jenssen, T. Junk, C. J. Peters, P. J. Picine, T. Thio, T. R. Thurston, and H. L. Tuller, Phys. Rev. B **37**, 111 (1988).
[14] B. I. Belevtsev, N. V. Dalakova, and A. S. Panfilov, Fiz. Nizk. Temp. **23**, 375 (1997) [Low Temp. Phys. **23**, 274 (1997)].
[15] B. I. Shklovskii and A. L. Efros, *Electronic Properties of Doped Semiconductors*, Springer, New York (1984).
[16] N. W. Preyer, R. J. Birgeneau, C. Y. Chen, D. R. Gabbe, H. P. Jenssen, M. A. Kastner, P. J. Picone, and Tineke Thio, Phys. Rev. B **39**, 11563 (1989).
[17] M. F. Hundley, R. S. Kwok, S. W. Cheong, J. D. Thompson, and Z. Fisk, Physica C **172**, 455 (1991).
[18] B. I. Belevtsev, N. V. Dalakova, A. V. Bondarenko, A. S. Panfilov, and I. S. Braude, Fiz. Nizk. Temp. **29**, 400 (2003) [Low Temp. Phys. **29**, 300 (2003)].
[19] V. J. Emery, Phys. Rev. Lett. **58**, 2794 (1987).
[20] W. E. Pickett, Rev. Mod. Phys. **61**, 433 (1989).
[21] R. K. Kremer, A. Simon, E. Sigmund, and V. Hizhnyakov, in *Phase Separation in Cuprate Superconductors*, edited by E. Sigmund and K. A. Müller, Springer, Heidelberg (1994), p. 66.
[22] W. Brenig, Phys. Rep. **251**, 1 (1995).
[23] V. M. Loktev, Fiz. Nizk. Temp. **22**, 3 (1996) [Low Temp. Phys. **22**, 1 (1996)].
[24] N. C. Yeh, Bulletin of Associations of Asia Pacific Physical Societies (AAPPS), Vol. 12, No. 2, pp. 2–20 (2002); preprint cond-mat/0210656.
[25] E. W. Carlson, V. J. Emery, S. A. Kivelson, and D. Orgad, preprint cond-mat/0206217.
[26] J. M. Tranquada, S. M. Heald, and A. R. Moodenbaugh, Phys. Rev. B **36**, 5263 (1987).
[27] S. Komiya, Y. Ando, X. F. Sun, and A. N. Lavrov, Phys. Rev. B **65**, 214535 (2002).
[28] S. W. Cheong, Z. Fisk, J. O. Willis, S. E. Brown, J. D. Thompson, J. P. Remeika, A. S. Cooper, R. M. Aikin, D. Schiferl, and G. Gruner, Solid State Commun. **65**, 111 (1988).
[29] A. D. Balaev, A. B. Bykov, L. N. Dem'yanets, N. B. Ivanova, S. G. Ovchinnikova, B. P. Khrustalev, and V. K. Chernov, Zh. Éksp. Teor. Fiz. **100**, 1365 (1991) [Sov. Phys. JETP **73**, 756 (1991)].
[30] A. A. Zakharov, A. A. Teplov, E. P. Krasnoperov, M. B. Tsetlin, A. K. Tsigankov, S. N. Barilo, and P. V. Gritskov, JETP Lett. **54**, 30 (1991).
[31] A. A. Zakharov, E. P. Krasnoperov, B. I. Savel'ev, A. A. Teplov, M. B. Tsetlin, and A. A. Shikov, Sverkhprovodimost' (KIAE) **4**, 1906 (1991) [Superconductivity **4**, 1815 (1991)].
[32] S. V. Vonsovsky, *Magnetism*, Wiley, New York (1974).
[33] E. Gratz and M. J. Zuckermann, in *Handbook of the Physics and Chemistry of Rare Earths*, edited by K. A. Geshneider Jr. and L. Eyring, North-Holland, Amsterdam (1982), p. 117.
[34] J. M. D. Coey, M. Viret, and S. von Molnar, Adv. Phys. **48**, 167 (1999).
[35] H. C. Montgomery, J. Appl. Phys. **42**, 2971 (1971).
[36] K. L. Dudko, N. V. Gapon, V. N. Savitsky, and V. V. Solov'ev, Fiz. Nizk. Temp. **21**, 270 (1995) [Low Temp. Phys. **21**, 205 (1995)].
[37] A. N. Lavrov, Y. Ando, S. Komiya, and I. Tsukada, Phys. Rev. Lett. **87**, 017001 (2001).
[38] B. I. Belevtsev, N. V. Dalakova, and A. S. Panfilov, Fiz. Nizk. Temp. **24**, 1086 (1998) [Low Temp. Phys. **24**, 815 (1998)].

This article was published in English in the original Russian journal. Reproduced here with stylistic changes by AIP.

Magnetic susceptibility of resonance donor impurities of transition elements in semiconductors

V. I. Okulov,* G. A. Alshanskii, V. L. Konstantinov, A. V. Korolyov, É. A. Neifeld, and L. D. Sabirzyanova

Institute of Metal Physics of the Urals Branch of the Russian Academy of Sciences, ul. S. Kovalevskoi 18, Ekaterinburg 620219, Russia

E. A. Pamyatnykh

Urals State University, pr. Lenina 51, Ekaterinburg 620083, Russia

S. U. Paranchich

Chernovtsy National University, ul. Kotsyubinskogo 2, Chernovtsy 58012, Ukraine
(Submitted December 16, 2003)
Fiz. Nizk. Temp. **30**, 558–562 (May 2004)

It is shown that in the resonance scattering of electrons on donor impurities of transition elements in semiconductors there is a contribution to the spin susceptibility from the electron density localized at the impurities. The Curie constant due to this has an unusual dependence on the impurity concentration. An expression for the spin susceptibility of resonantly scattered electrons is obtained in the Friedel approach. The experimental data obtained on mercury selenide containing iron impurities confirm the theoretical results and permit determination of the effective spin of the resonance state. © *2004 American Institute of Physics.*
[DOI: 10.1063/1.1739163]

Impurities of transition elements in semiconductors at low concentrations can possess donor energy levels that fall in the conduction band. In such a case the behavior of the electron mobility manifests certain features that are typical of gapless semiconductors. Mercury selenide containing iron impurities has attracted much attention in connection with the observation of such effects, and the results of that research are reflected in several review articles.[1,2] The features that arise have their origin in the fact that the interaction of conduction electrons with impurity ions at energies close to the donor level energy ε_d has a resonance character. Resonance phenomena at low temperatures become noticeable when, with increasing impurity concentration, the Fermi energy reaches the energy ε_d. Upon further increase of the impurity concentration the Fermi energy and the electron density stabilize, i.e., remain nearly unchanged as the number of impurities is increased. It is in this region of stabilization of the electron density that one observes the anomalies of the electron mobility considered here: a maximum in the concentration dependence and a characteristic dependence on temperature.[1,2] To explain the rise of the mobility with growth of the impurity concentration given the known presence of resonance scattering, which suppresses the mobility, a model based on the assumption that ordering of the impurity ions occurs is widely used.[3] However, it has been shown[4] that the concentration maximum of the mobility can be explained in the framework of the known theory of mobility in the presence of scattering on ions if it is taken into account that under conditions of stabilization of the electron density the effective charge of each of the ions decreases as they increase in number. The use of a general approach based on the theory of resonance scattering and the Friedel sum rule[5] permits a simple explanation of the observed concentration and temperature anomalies of the mobility.[6]

In the development of models permitting a consistent description of the evidence of the interaction of electrons with transition-element impurities, the study of the magnetic susceptibility of the system of impurity ions is of considerable importance. For mercury selenide containing iron impurities there is a vast amount of experimental data on the susceptibility, but a number of the observed regularities have not been given adequate theoretical analysis. In particular, a quantitative description of the unusual concentration dependence of the Curie constant[4,7] has not been given. Thus it remains a topical problem to treat theoretically the susceptibility of localized spins of resonance donor impurities. In this report we propose a simple solution of this problem in the framework of the resonance scattering theory and the Friedel approach. The experimental data we have obtained on the temperature dependence of the susceptibility of localized moments in mercury selenide containing iron impurities are presented, and their agreement with the proposed theoretical predictions is demonstrated for certain parameter values which are consistent with the existing ideas. The available data on the field dependence and quantum oscillations of the susceptibility are also discussed in relationship to the behavior of the amplitudes of the de Haas–van Alphen and Shubnikov–de Haas oscillations.

Let us start by considering the influence on the density of states of the resonance scattering of electrons with a given value of the energy ε. If singly ionized donor impurities with concentration n_i have a resonance energy ε_d, then, corre-

sponding to the resonance is a certain contribution to the density of states in the form of the function

$$n_i g(\varepsilon)=\frac{n_i\Delta}{\pi}[(\varepsilon-\varepsilon_d)^2+\Delta^2]^{-1}, \tag{1}$$

where Δ is the width of the resonance, which is small compared to ε_d. This resonance function appears in the expression for the spin susceptibility of the electron density localized at impurities via an integral that we introduce as follows:

$$\eta=-2n_i\int d\varepsilon\, g(\varepsilon)\frac{df(\varepsilon)}{d\varepsilon}$$
$$=2n_i\int\frac{d\varepsilon\, g(\varepsilon)}{4kT\cosh^2[(\varepsilon-\varepsilon_F)/2kT]}, \tag{2}$$

where $f(\varepsilon)$ is the Fermi function, ε_F is the Fermi energy, T is the temperature, and k is Boltzmann's constant. The integral in formula (2) should be extended to an interval with a width of the order of Δ in the vicinity of the energy ε_d within which formula (1) remains valid. The character of the dependence of η on temperature and impurity concentration is determined by the value of the energy kT in relation to Δ and of ε_F in relation to ε_d. We shall assume that all the electrons originate from the donors in question and that their density is such that the Fermi energy is higher than ε_d. Then the Fermi energy changes little as the donor concentration is increased further, and the conduction electron density $n_e(\varepsilon_F)$ remains close to the value $n_0=n_e(\varepsilon_d)$. It is at such concentrations that the electron density, in addition to the conducting electron fraction, contains the part under discussion, consisting of electrons localized at resonance donor impurities, which gives a contribution to the electron density equal to

$$n_i z=n_i-n_0, \tag{3}$$

where z is the occupation number of the localized states:

$$z=\int d\varepsilon\, g(\varepsilon)f(\varepsilon). \tag{4}$$

In the ground state one can write z in the form

$$z=\frac{1}{2}+\frac{1}{\pi}\arctan\left(\frac{\varepsilon_F-\varepsilon_d}{\Delta}\right),\quad T=0. \tag{5}$$

Relation (3) is then an equation for determining the Fermi energy in the resonance interval $|\varepsilon_F-\varepsilon_d|\leqslant\Delta$. Here it is easy to find the density of states with the Fermi energy, and η is then equal to

$$\eta=2n_i g(\varepsilon_F)=\frac{2n_i}{\pi\Delta}\sin^2\left(\frac{\pi n_0}{n_i}\right),\quad T=0. \tag{6}$$

If the temperature is substantially higher than Δ/k, then we can take the limit of the exponential functions appearing in the Fermi function in expressions (2) and (4), and we then get

$$\eta=zn_i/kT=(n_i-n_0)/kT,\quad T\gg\Delta/k. \tag{7}$$

Formulas (6) and (7) provide a basis for a simple analysis of the spin susceptibility of donor impurities.

Let us take as the initial form of the expression for the spin susceptibility of the electrons the well-known equation obtained by simplifying the result of the electron liquid theory, retaining the description of the role of the electron–electron interaction on a qualitative level. Considering only the susceptibility of the localized electrons, in accordance with what we have said, we write it in the form

$$\chi_d=\mu^2\eta/(1+\psi\eta), \tag{8}$$

where the parameter ψ describes the exchange interaction of the electrons in the states localized on impurities, and μ^2 contains factors reflecting the role of the interaction between electrons in localized and conducting states and also the difference of the effective spin of a localized state from the spin of a free electron. If the ionized donor does not have spin ($S=0$), then the following simple formula is valid for μ^2:

$$\mu^2=\mu_0^2(1+\psi_{ed})=4\mu_0^2(\langle s^2\rangle/3)(1+\psi_{ed}),\quad S=0, \tag{9}$$

where μ_0 is the Bohr magneton, ψ_{ed} is the coupling constant, and $\langle s^2\rangle=s(s+1)=3/4$. For a more realistic case, when the ion spin S is nonzero, we generalize the second expression in equation (9) by introducing the spin s_d of the localized state:

$$\mu^2=4\mu_0^2(\langle s_d^2\rangle/3)(1+\psi_{ed}),\quad S>0. \tag{10}$$

The value of $\langle s_d^2\rangle$ is a parameter of the completely filled localized state, which for the impurity as a whole is close to the state of the un-ionized donor. Here, if in addition to the spin S of the ionized impurity the spin s_a of the un-ionized impurity is also known, then one can determine s_d by using a sum rule. For example, for $S_a<S$ we set

$$\langle s_d^2\rangle=\langle S^2\rangle-\langle S_a^2\rangle=S(S+1)-S_a(S_a+1). \tag{11}$$

Then at small ψ_{ed} the value of μ^2 will be known rather exactly. In the more complicated situations, when the proposed method of determining the effective moment is inapplicable, it remains, on the whole, a phenomenological parameter.

The expressions (6) and (7) given above enable one to write the following formula for the susceptibility at low and high temperatures:

$$\chi_d=\frac{\mu^2 n_i\sin^2(\pi n_0/n_i)}{\Delta_1+\psi n_i\sin^2(\pi n_0/n_i)},\quad T\ll\Delta/k, \tag{12}$$

$$\chi_d=\frac{\mu^2(n_i-n_0)}{kT+\psi(n_i-n_0)},\quad T\gg\Delta/k, \tag{13}$$

where $\Delta_1=\pi\Delta/2$. The main qualitative feature of the susceptibility described by these formulas consists in the characteristic unusual concentration dependences which reflect the stabilization of the electron density in the presence of resonance scattering on donor impurities. It is manifested in terms containing the limiting density n_0 both in the susceptibility without the interaction taken into account and in the parameters that characterize the exchange coupling in the localized states. It is also important that the theory confirms that the susceptibility of resonance donor states at high temperatures obeys the Curie–Weiss law. The susceptibility χ_d under discussion appears in the total magnetic susceptibility of the crystal, which contains a contribution from the local-

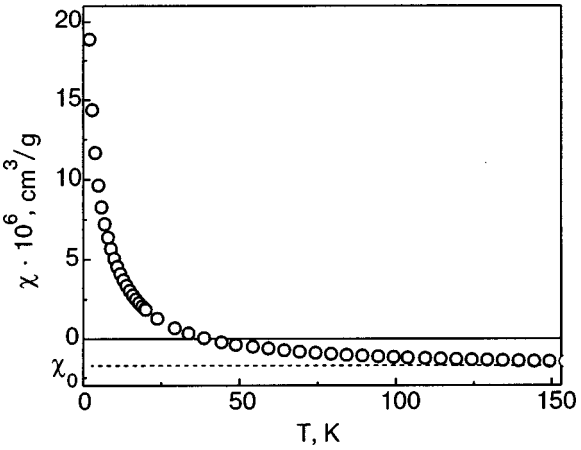

FIG. 1. Temperature dependence of the magnetic susceptibility of mercury selenide containing iron impurities. The impurity concentration is 1×10^{19} cm^{-3}.

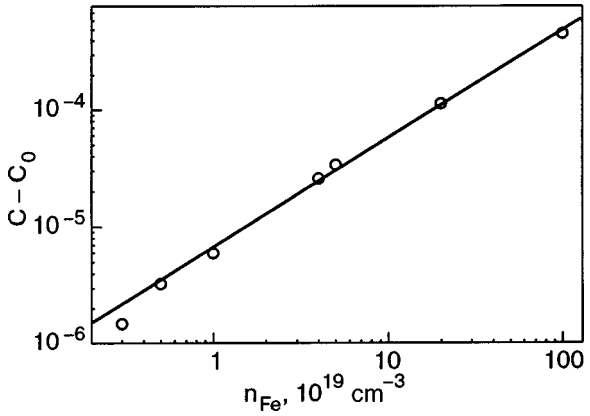

FIG. 2. Dependence of the Curie constant in the magnetic susceptibility of the localized moments on iron impurities in mercury selenide versus the concentration of the iron impurities. C_0 is the value of the Curie constant for $n_{\mathrm{Fe}}=n_0$.

ized moments of the ionized impurities, χ_d^0, which also obeys the Curie law, and the weakly temperature-dependent susceptibility χ^0 of the matrix.

The experimental data discussed below in connection with the proposed theoretical results were obtained by us on crystals of mercury selenide containing iron impurities. Some of the data were reported previously in conference proceedings[6,8] and in a journal article,[4] and information about the experimental techniques can be found in those places. The measurements were made on a set of samples with iron concentrations in the interval from 10^{18} to 10^{21} cm^{-3}. On that same set of samples we studied the concentration and temperature dependences of the electron mobility and showed that the anomalies observed in them are in good agreement with the theoretical results obtained on the basis of resonance scattering theory and the Friedel approach. In the present paper we have also focused our attention on the analysis of those experimental data which permit verification of the conclusions of the theory mentioned. Moreover, the results pertaining to the temperature dependence of the susceptibility of the localized moments are also of interest in this regard. In all the samples studied the contributions to the susceptibility from the iron impurities are distinct, and their temperature dependence obeys the Curie law (Fig. 1). A detailed processing of the data on the concentration dependence of the Curie constant (Fig. 2) in the susceptibility $\chi_d^0+\chi_d$ showed that it conforms well to a dependence of the form

$$Cn_{\mathrm{Fe}}=C_0n_{\mathrm{Fe}}+\delta C(n_{\mathrm{Fe}}-n_0), \tag{14}$$

where n_{Fe} is the concentration of iron impurities, n_0 is the limiting density of conduction electrons introduced above, which is determined in experiments on the mobility, $C_0=4\mu_0^2S(S+1)n_{\mathrm{Fe}}/3k$ is the Curie constant corresponding to spin $S=5/2$, and $C_0+\delta C$ is the Curie constant for spin 2.1. It is easy to see that relation (14) corresponds to formula (13) with allowance for relations (10) and (11) for spin values $S=5/2$ and $S_a=2$ and a value of the constant $\psi_{ed}=0.1$. It is known that an iron donor ion has spin 5/2 and an iron impurity can have spin 2. The value found for the effective magnetic moment is also reasonable. One can therefore conclude that one of the main inferences of the proposed theory is in complete agreement with the experimental data. As to the temperature dependence of the form $(T+\theta)^{-1}$ predicted by the theory, the results of a processing of the available data show that noticeable values of θ can be revealed only for high impurity concentrations exceeding the resonance value by one or two orders of magnitude; this result agrees with the data of Ref. 7. At such concentrations the application of the theory proposed here can hardly be justified.

Data from experiments on quantum oscillations of the susceptibility and conductivity in a magnetic field can also be of substantial importance for the development of the ideas of the effects of resonance scattering of electrons. Our studies of the de Haas–van Alphen effect, the first results of which were reported previously,[8] were devoted to establishing the correlation between the concentration dependence of the amplitudes of the magnetoresistance and susceptibility oscillations. It was found that the Dingle temperature of the quantum oscillations has a minimum in the same region of concentrations in which the electron mobility has a maximum. In this case the values of the Dingle temperature in the susceptibility oscillations are significantly lower. However, for obtaining more complete quantitative results in this circle of problems a detailed study of the shape of the oscillations with allowance for the spin splitting and other factors is required.

This study was supported by the Russian Foundation for Basic Research, Grant No. 03-02-16246 and the Russian–American Program BRHE, Grant EK-005-00 (REC-005).

*E-mail: okulov@imp.uran.ru

[1] Z. Wilamowski, Acta Phys. Pol. A **77**, 133 (1990).
[2] I. M. Tsidil'kovskiĭ, Usp. Fiz. Nauk **35**, 85 (1992) [Sov. Phys. Usp. **35**, 85 (1992)].
[3] J. Mycielski, Solid State Commun. **60**, 165 (1986).
[4] G. A. Alshanskii, V. L. Konstantinov, A. V. Korolyov, E. A. Neifeld, V. I. Okulov, S. U. Paranchich, and L. D. Sabirzyanova, Phys. Met. Metallogr. **93**, Suppl. 1, 142 (2002).
[5] J. Friedel, Nuovo Cimento, Suppl. **2**, 287 (1958).
[6] V. I. Okulov, A. V. Korolev, E. A. Neĭfel'd, L. D. Sabirzyanova, S. Yu. Paranchich, and K. S. Redkina, *E-MRS Fall Meeting 2002, Symposium G:*

Solid Solution of the II-VI Compound-Growth, Characterization and Applications, Zakopane, Poland (2002), Abstr. 50.
[7] A. Lewicki, Z. Tarnawski, and A. Mycielski, Acta Phys. Pol. A **67**, 357 (1985).
[8] V. L. Konstantinov, A. V. Korolev, É. A. Neĭfel'd, V. I. Okulov, S. Yu. Paranchich, L. D. Sabirzyanova, and G. A. Al'shanskiĭ, *Abstracts of the XXXI Conference on Low Temperature Physics* [in Russian], Moscow (1998), p. 56.

Translated by Steve Torstveit

Intrinsic and extrinsic inhomogeneities in mixed-valence manganites*

B. I. Belevtsev[a)]

B. Verkin Institute for Low Temperature Physics and Engineering of the National Academy of Sciences of Ukraine, 47 Lenin Ave., Kharkov 61103, Ukraine

(Submitted October 14, 2003)
Fiz. Nizk. Temp. **30**, 563–567 (April 2004)

It is suggested that extrinsic inhomogeneities in mixed-valence manganites deserve more attention and that they should be taken into account on equal footing with the hypothetical phase separation when examinating experimental data and developing theoretical models for the influence of stoichiometric and other types of inhomogeneities on the properties of these and other transition-metal oxides. © *2004 American Institute of Physics.* [DOI: 10.1063/1.1739164]

The structural, magnetic, and electron transport properties of mixed-valence manganites of the type $R_{1-x}A_xMnO_3$ (where R is a rare-earth element and A is a divalent alkaline-earth element) have attracted much attention in the scientific community in the last decade (see reviews[1–6]). That interest has been stimulated by the observation of huge negative magnetoresistance (MR) near the Curie temperature T_C of the paramagnetic–ferromagnetic transition for manganites with $0.2 \leqslant x \leqslant 0.5$. This phenomenon has been called ''colossal'' magnetoresistance (CMR) and is expected to be used in advanced technology. The unique properties of mixed-valence manganites are determined by complex spin, charge, and orbital ordered phases, and are therefore of great fundamental interest for the physics of strongly correlated electrons. At the present time it is believed that one of the key feature of manganites is their intrinsic inhomogeneities in the form of coexisting competing ferromagnetic and antiferromagnetic/ paramagnetic phases.[3,4,6] This phenomenon is generally called ''phase separation.'' In Refs. 3 and 6, theoretical computational models were developed for two cases: 1) electronic phase separation, which implies nanocluster coexistence; 2) disorder-driven phase separation, which leads to rather large (micrometer size) coexisting clusters. Existence of the nanoscale as well as micrometer-size inhomogeneities in manganites has been corroborated experimentally (see Refs. 3, 4, and 6 and references therein). Some other examples of the phase-separation models can be found in Refs. 4 and 7–10 (actually, there is a vast literature on the subject, but it cannot be cited more fully in this brief communication). On this basis it is hoped that the transport and magnetoresistive properties (including CMR) of manganites can be explained with the phase separation effects taken into account.

In spite of enormous theoretical and experimental activity in the area of phase separation in manganites, many questions (sometimes rather simple and naive) remain open. Intrinsic inhomogeneities are believed to arise for thermodynamic reasons, so that relative fraction of competing phases should depend on temperature, pressure, and magnetic field. The known experimental studies give numerous (though predominantly indirect) indications of structural and magnetic inhomogeneities in manganites, but are they in all cases intrinsic? The point is that extrinsic inhomogeneities are inevitably present in all manganites (even in single-crystal samples). Extrinsic inhomogeneities arise due to various technological factors in the sample preparation. They can cause inhomogeneity in the chemical composition (first of all in the oxygen content), structural inhomogeneities (polycrystalline or even granular structure), strain inhomogeneities, and so on. It is easy to find in the literature numerous experimental studies in which the finding of phase separation effects is proclaimed, but the interpretations are often doubtful. In such cases the effects of technological inhomogeneities are quite obvious or, at least, can not be ruled out. In some cases the magnetic inhomogeneities, induced by extrinsic causes, can depend significantly on temperature, pressure, and magnetic field as well, and their apparent influence on the magnetic and transport properties of mixed-valence manganites may agree generally with that predicted by some of the numerous phase-separation theoretical models. It should be noted, however, that a quantitative comparison of the known models with experiment is practically impossible (or is too ambiguous).

Consider briefly the main sources of extrinsic inhomogeneities. Mixed-valence manganites are complex perovskite-like oxides consisting of at least four elements. Their properties are very sensitive to crystal imperfections, especially to the structural, composition and other types of inhomogeneity in the crystal lattice. The crystal perfection (and corresponding level of inhomogeneity) depends strongly on the method of preparation, and on preparation conditions for the given method. In rough outline, the following methods of manganite growth are used: 1) thin film growth (mostly with the pulsed-laser deposition method); 2) solid-state reaction method; 3) floating zone method.

Thin manganite films can be prepared in highly oriented or even single-crystal epitaxial form with a fairly perfect crystal lattice. The highest values of the magnetoresistance have been observed in thin films. But it should be taken into account that films are always in an inhomogeneous strained state due to inevitable substrate-film lattice interaction, which, as a rule, induces considerable magnetic and magnetoresistance anisotropy.[11] Due to the strained state, some other film properties (among other things, the value of T_C) can be quite different from those of bulk materials.

Consider some examples of extrinsic inhomogeneities in

films. A comprehensive and thorough study (by high-resolution electron microscopy)[12] of epitaxial $La_{1-x}Ca_xMnO_3$ ($x \approx 0.3-0.35$) films grown on $SrTiO_3$ substrates has revealed that close to the substrate a perfectly coherent strained layer is formed, above which crystal blocks with columnar structure grow; these blocks and the boundary regions between them accomodate the lattice mismatch between substrate and film. The boundary regions between blocks (domains) are nonstoichiometric, having deficiencies of oxygen and lanthanum. Similar results are reported in Ref. 13, where secondary-phase nonstoichiometric rods were found in $La_{0.7}Ca_{0.3}MnO_3$ films grown on $LaAlO_3$ and $SrTiO_3$ substrates. The films have a domain structure, in which the rods are believed to be responsible for relieving stress during film growth. Magnetic force microscopy study of pulsed-laser-deposited $La_{1-x}Sr_xMnO_3$ ($x=0.23$ and 0.3) films[14] have revealed local FM regions at temperatures above the T_C of the film. These regions with higher T_C were found around the grain boundaries and attributed to local variation of the strain in the film. The above examples show that even epitaxial films prepared under optimal conditions have inhomogeneous strains and a local nonstoichiometry that can play a significant role in the transport and magnetoresistive properties of thin films.

The solid-state reaction (SSR) technique enables preparing ceramic or polycrystalline samples. The crystal quality (and, therefore, the resistive, magnetoresistive, and magnetic properties) of the SSR samples depends in a crucial way on the preparation conditions, especially on sintering and annealing temperature. In samples prepared with optimal sintering temperature, fairly sharp resistive and magnetic transitions near T_C are observed, whereas quite different resistive and magnetization behavior is seen for samples with the same nominal composition but prepared at low temperature.[15] This is to be attributed to compositional and structural inhomogeneity of samples sintered at low temperatures. For all preparation conditions, however, SSR samples are always polycrystalline and inevitably contain at least one source of inhomogeneity: grain-boundary regions. These are regions of structural, magnetic, and stoichiometric disorder, and they therefore have different conducting and magnetic properties as compared with these inside the grains. Beside this, rather appreciable compositional inhomogeneities (not associated with grain boundaries) cannot be eliminated in SSR samples even when they are prepared under optimal conditions. The common methods of checking of stoichiometric inhomogeneity and mixed-phase state (x-ray powder diffraction or electron microprobe analysis) have too low accuracy to come to an unambiguous conclusion about composition homogeneity. For example, if a sample is a mixture of two phases of $R_{1-x}A_xMnO_3$, composed from the same elements but with appreciably different values of x or oxygen concentration, it is hard or even impossible to see clearly enough the two-phase state in a diffraction pattern, even if the volume fractions of the phases are comparable, whereas the magnetic and other properties of these phases can be significantly different. Only nonperovskite-type impurities can be detected quite clearly down to 2%. Electronic microprobe elemental analysis has an accuracy about $\pm 5\%$ in most cases, leaving room for stoichiometic disorder within these limits. More powerful, but much more expensive methods, like neutron diffraction or small-angle neutron scattering, are not in common use, but even those methods have their limits of accuracy. Since the properties of manganites are very sensitive to chemical composition and, therefore, to stoichiometric disorder, it is not surprising to find in the literature quite different properties of manganites of the same nominal composition, prepared by the SSR method. In spite of the unavoidable technological inhomogeneity, the SSR method is in common use for preparation of mixed-valence manganites of various composition. The reason is that the SSR method appears to be not very sophisticated (at least, at first glance) and does not require expensive equipment. With proper experience and rather hard work it is possible to obtain polycrystalline samples of rather good quality, with sharp resistive and magnetic transitions. For example, a generally recognized phase diagram for the system $La_{1-x}Ca_xMnO_3$ has been obtained for SSR polycrystalline specimens.[5]

It is easy to find in the literature hundreds of papers devoted to film or bulk ceramic manganites, but far fewer studies concern single-crystal samples. The obvious reason is that it is not so easy to prepare manganite single crystals. But even single crystals prepared by the floating zone method are not free from defects and extrinsic inhomogeneities. In reality, they have mosaic blocks, twins, inhomogeneous strains, and stoichiometric disorder.[16–18]

The experimental data therefore show that technological inhomogeneities are unavoidable for any preparation method, and they can actually be called ''intrinsic'' as well. For this reason, (i) in many cases it is better to speak about multiphase coexistence instead of phase separation; (ii) the technological inhomogeneities should be directly taken into account in new theoretical models. The latter demand derives from the circumstance that manganite materials which can be used in advanced technology will surely have some crystal imperfections or inhomogeneities. Moreover, in some cases specific types of inhomogeneities should even be specially induced to provide necessary properties. For example, grain boundaries or specially prepared percolation structures can ensure high MR in low fields in the temperature range far below T_C, which may be necessary for some applications.

As to phase separation, this concept has, on the one hand, now become a commonplace, while, on the other hand, the term is too general to imply anything specific. In interpreting their results, experimentalists often speak quite generally about phase separation or just mention it, meaning not much by it. And how could they, since at least a dozen diverse models (suggesting quite different mechanisms of phase separation) have been developed, which in practice, however, cannot be numerically compared with experiment? In spite of this, the phase-separation concept appears to be very attractive, since it can give a quite natural qualitative explanation for both the huge drop in resistance and the CMR in the vicinity of magnetic transitions in manganites, taking into account a percolational character of these transitions.[4,8] Consider, for example, the $La_{1-x}Ca_xMnO_3$ system. According to Refs. 19–24, the paramagnetic-ferromagnetic (PM-FM) transition in this compound is of first order for the range $0.25 < x < 0.4$. It is found in these

compounds that FM metallic clusters are present well above T_C, while some PM insulating clusters can persist down to a range far below T_C.[25–27] That seems natural for a first-order transition, where nucleation of the FM clusters above T_C is quite expected, as well as the presence of some amount of PM clusters below T_C. After all, a transition of this type is hysteretic and depends on the rate of heating or cooling. In this case real phase separation and percolation processes can be expected around T_C. Since the PM phase is insulating and the FM one is metallic, some kind of insulator-metal transition takes place near T_C. The technological inhomogeneities broaden the temperature range of the PM-FM transition, so that it may appear smoother and more continuous, like a second-order transition.

For Ca concentration outside of the above-indicated range, $0.25 \leqslant x \leqslant 0.4$, the PM-FM transition is found to be of second order in $La_{1-x}Ca_xMnO_3$ samples with $x = 0.20$, 0.40, and 0.45 (Refs. 22, 29, 30). According to the phase diagram for this system,[1,3,5,6] these concentrations are close to the critical ones: $x \approx 0.2$ (which is a border between the FM metallic and insulating states) and $x = 0.5$ (which is a border between FM metallic and insulating charge-ordered states). It is clear that unavoidable technological stoichiometric disorder will have a greater impact on the magnetic transition for samples having nominal Ca concentrations near the above-mentioned critical values. The T_C value depends rather strongly on x near these threshold concentrations, whereas the concentration dependence of T_C near the optimal doping ($x \approx 0.35$) is rather weak (see the phase diagram in Refs. 1, 3, 5, and 6). In this case, the magnetic transition for a sample with nonoptimal concentration should be broader than that for the optimally doped samples, even if the level of compositional inhomogeneity is equal in both cases. It cannot be ruled out, therefore, that a second-order transition found for these $La_{1-x}Ca_xMnO_3$ samples is just a rather broadened (smeared) first-order transition.

It should be noted that the PM-FM transition is found to be of second order in Sr-doped $La_{1-x}Sr_xMnO_3$ samples ($x = 0.3$ and 0.33) as well.[19,31] The Sr manganites are more conductive than Ca manganites and have much higher T_C (maximum T_C are about 260 K and 370 K for Ca and Sr manganites, respectively). It seems that manganites with higher conductivity and T_C are more prone to a second-order transition than those with low conductivity and T_C. In homogeneous samples with a perfect crystal lattice the second-order transition from the PM to the FM state should proceed at once in the whole sample volume as soon as the temperature crosses T_C from above. No nuclei of the FM phase above T_C and no supercooling or hysteresis phenomena should occur at this transition. Only thermodynamic fluctuations of the order parameter (the magnetization) are expected, which, however, should be confined to a narrow critical region around T_C (Refs. 32, 33). These fluctuations of the magnetic order have usually a rather noticeable effect on ''nonmagnetic'' properties such as the temperature coefficient of the resistivity, heat capacity, magnetoresistance, and thermal expansion in the vicinity of T_C (Refs. 32, 33).

Stoichiometric disorder and inhomogeneous strains of the crystal lattice, which are unavoidable in real manganites due to the above-indicated technological reasons, can undoubtedly have a pronounced effect on the second-order PM-FM transitions. This effect has long been known and considered for simple FM metals.[33] Take, for example, as in Ref. 33, a system consisting of multiple phases with different T_C. There is some volume distribution of regions with different T_C within the sample. The presence of interphase transition regions between different phases should be taken into account as well. The temperature dependence of the magnetization for this sample will show a somewhat broadened PM-FM transition[33] (the temperature width of the transition depends on how wide is the distribution of T_C in the sample). From that an averaged T_C value can be determined. But some parts of the sample have T_C greater or less than this averaged value. Therefore, it can be found by some experimental methods that some FM clusters exist above T_C, their volume increasing as T_C is approached from above, while PM clusters can be found below T_C, their volume fraction decreasing as the temperature decreases away from T_C. The reason for this behavior is quite obvious when the sample inhomogeneity is taken into account. Now, even if every single phase of this multiphase system undergoes a second-order transition, the total character of the transition will not be that for the homogeneous system. It will be of a percolational nature. If the PM and FM phase states differ drastically in their conductivity, CMR can be found. Imagine that the size of the inhomogeneities is rather small, say, a few nanometers (which is quite possible for technological inhomogeneities). Is it possible in this case to attribute with any certainty the magnetotransport behavior of this system near the PM-FM transition to the phase separation effect? The negative answer is obvious, since technological inhomogeneities can by themselves provide this behavior.

Due to enormous theoretical activity in this area, it is rather appropriate to believe that phase separation really takes place in manganites and in other transition-metal oxides (although it is difficult to make the right choice among the numerous proposals for the phase separation mechanisms). But how can one reliably enough distinguish these thermodynamic effects from those of extrinsic inhomogeneities? That is a really difficult problem. I think that theoreticians should not disregard the influence of extrinsic inhomogeneities, but, on the contrary, they should take them into account in their models quite directly along with intrinsic inhomogeneities. This necessity was indicated quite clearly in the paper by Yukalov.[10] One of the principal ideas of that paper is that real systems are never free from external perturbations, and that makes the system stochastically unstable even if the external perturbations are infinitesimally small. After all, extrinsic inhomogeneities can even stimulate the appearance of thermodynamic phase separation, so that some kind of interaction between them is possible.

In conclusion, when considering the experimental data for mixed-valence manganites and developing theoretical models for them, the unavoidable influence of extrinsic disorder and inhomogeneities should always be taken into account. These inhomogeneities can act separately as well as together with the suggested intrinsic inhomogeneities (phase separation) and determine to a great extent the magnetic and magnetotransport properties of these compounds. Although, for the most part, the known properties of the

$La_{1-x}Ca_xMnO_3$ system near the PM-FM transition have been used here in support of the above-mentioned point of view, the general conclusion of this paper is applicable (in the author's opinion) to other magnetic transitions in manganites (for example, for transitions to charge-ordered states) and to related magnetic transition-metal oxides, such as the cobaltites $La_{1-x}Sr_xCoO_3$.

The author sincerely acknowledges a very useful discussion of some questions touched upon in this note with Dr. P. A. Joy from the National Chemical Laboratory, Pune, India.

*This paper does not fit in with any of the permanent rubrics of this journal. It is actually better suited to a category such as "Critical reviews" or "Viewpoint" that some journals offer. In his paper, B. I. Belevtsev (on the strength of the analysis of published experimental and theoretical works) considers the important and topical question of the influence of intrinsic and extrinsic inhomogeneities on the properties of mixed-valence manganites with colossal magnetoresistance. The editors have decided to publish Belevtsev's paper in the hope that it will be of interest to our readers.

a)E-mail: belevtsev@ilt.kharkov.ua

[1] A. P. Ramírez, J. Phys.: Condens. Matter **9**, 8171 (1997).
[2] J. M. D. Coey, M. Viret, and S. von Molnar, Adv. Phys. **48**, 167 (1999).
[3] E. Dagotto, T. Hotta, and A. Moreo, Phys. Rep. **344**, 1 (2001).
[4] E. L. Nagaev, Phys. Usp. **39**, 781 (1996); Phys. Rep. **346**, 387 (2001).
[5] K. H. Kim, M. Uehara, V. Kiryukhin, and S.-W. Cheong, in *Colossal Magnetoresistive Manganites*, edited by T. Chatterji, Kluwer Academic Publ., Dordrecht, Netherlands (2003); preprint cond-mat/0212113.
[6] E. Dagotto, J. Burgy, and A. Moreo, Solid State Commun. **126**, 9 (2003); E. Dagotto, preprint cond-mat/0302550.
[7] N. D. Mathur and P. B. Littlewood, Solid State Commun. **119**, 271 (2001).
[8] A. O. Sboychakov, A. L. Rakhmanov, K. I. Kugel, M. Yu. Kagan, and I. V. Brodsky, JETP **95**, 753 (2002).
[9] G. Iadonisi, V. Cataudella, G. De Fillipis, V. Marigliano Ramaglia, C. A. Perroni, and F. Ventriglia, Phys. Status Solidi B **237**, 215 (2003).
[10] V. I. Yukalov, preprint cond-mat/0308127.
[11] B. I. Belevtsev, V. B. Krasovitsky, D. G. Naugle, K. D. D. Rathnayaka, A. Parasiris, S. R. Surthi, R. K. Pandey, and M. A. Rom, Phys. Status Solidi A **188**, 1187 (2001).
[12] O. I. Lebedev, G. Van Tendeloo, A. M. Abakumov, S. Amelinckx, B. Leibold, and H.-U. Habermeier, Philos. Mag. **79**, 1461 (1999); G. Van Tendeloo, O. I. Lebedev, and S. Amelinckx, J. Magn. Magn. Mater. **211**, 73 (2000).
[13] C. J. Lu, Z. L. Wang, C. Kwon, and Q. X. Jia, J. Appl. Phys. **88**, 4032 (2000).
[14] Yeong-Ah Soh, G. Aeppli, N. D. Mathur, and M. G. Blamire, J. Appl. Phys. **87**, 6743 (2000).
[15] P. A. Joy, P. S. Anil Kumar, and S. K. Date, Mater. Res. Bull. **14/15**, 2143 (1999).
[16] D. Shulyatev, S. Karabashev, A. Arsenov, Ya. Mukovskii, and S. Zverkov, in *Defects and Surface-Induced Effects in Advanced Perovskites*, edited by G. Borstel *et al.*, Kluwer Academic Publishers, Netherlands (2000), p. 455.
[17] D. Shulyatev, S. Karabashev, A. Arsenov, Ya. Mukovskii, and S. Zverkov, J. Cryst. Growth **237–239**, 810 (2002).
[18] Bas B. Van Aken, A. Meetsma, Y. Tomioka, Y. Tokura, and Thomas T. M. Palstra, Phys. Rev. B **66**, 224414 (2002); B. B. Van Aken, Ph. D. Thesis, University of Groningen (2001), www.ub.rug.nl/eldoc/dis/science.
[19] J. Mira and J. Rivas, Phys. Rev. B **60**, 2998 (1999).
[20] H. S. Shin, J. E. Lee, Y. S. Nam, H. L. Ju, and C. W. Park, Solid State Commun. **118**, 377 (2001).
[21] Y. B. Zhang, S. Li, P. Hing, C. Q. Sun, W. Gao, and S. X. Dou, Solid State Commun. **120**, 107 (2001).
[22] Chang Seop Hong, Wan Seop Kim, and Nam Hwi Hur, Phys. Rev. B **63**, 092504 (2001).
[23] J. E. Gordon, C. Marcenat, J. P. Franck, I. Isaac, Guanwen Zhang, R. Lortz, C. Meingast, F. Bouquet, R. A. Fisher, and N. E. Phillips, Phys. Rev. B **65**, 024441 (2002).
[24] C. P. Adams, J. W. Lynn, V. N. Smolyaninova, A. Biswas, R. L. Greene, W. Ratcliff II, S.-W. Cheong, Y. M. Mukovskii, and D. A. Shulyatev, preprint cond-mat/0304031.
[25] J. M. De Teresa, M. R. Ibarra, P. A. Algarabel, C. Ritter, C. Marquina, J. Blasco, J. Garcia, A. del Moral, and Z. Arnold, Nature (London) **386**, 256 (1997).
[26] Joonghoe Dho, Ilryong Kim, Soonchil Lee, K. H. Kim, H. J. Lee, J. H. Jung, and T. W. Noh, Phys. Rev. B **59**, 492 (1999).
[27] G. Papavassiliou, M. Fardis, M. Belesi, T. G. Maris, G. Kallias, M. Pissas, D. Niarchos, C. Dimitropoulos, and J. Dolinsek, Phys. Rev. Lett. **84**, 761 (2000).
[28] X. Bohigas, J. Tejada, M. L. Marínez-Sarrión, S. Trirr, and R. Black, J. Magn. Magn. Mater. **208**, 85 (2000).
[29] J. J. Rhyne, H. Kaiser, L. Stumpe, J. F. Mitchell, T. McCloskey, and A. R. Chourasia, J. Magn. Magn. Mater. **226**, 775 (2001).
[30] D. Kim, B. Revaz, B. L. Zink, F. Hellman, J. J. Rhyne, and J. F. Mitchell, Phys. Rev. Lett. **89**, 227202 (2002).
[31] P. Novák, M. Maryŝko, M. M. Savosta, and A. N. Ulyanov, Phys. Rev. B **60**, 6655 (1999).
[32] S. V. Vonsovsky, *Magnetism*, Wiley, New York (1974), Nauka, Moscow (1971).
[33] K. P. Belov, *Magnetic Transitions* [in Russian], Gos. Izdat. Fiz.-Mat. Lit., Moscow (1959).

This article was published in English in the original Russian journal. Reproduced here with stylistic changes by AIP.

ELECTRONIC PROPERTIES OF METALS AND ALLOYS

Anomalous diamagnetism in aluminum–lithium alloys

V. A. Desnenko, S. N. Dolya, N. V. Isaev, I. V. Svechkarev,* and A. V. Fedorchenko

B. Verkin Institute for Low Temperature Physics and Engineering, National Academy of Sciences of Ukraine, pr. Lenina 47, Kharkov 61103, Ukraine
(Submitted November 20, 2003)
Fiz. Nizk. Temp. **30**, 568–571 (May 2004)

In the region of the equilibrium solid solutions of lithium in aluminum an anomalous low-temperature peak of diamagnetism is observed which is due to the presence of a boundary point on a line of band degeneracy directly below the Fermi level. The position and structure of the peak in the average valence function are analogous to those studied previously in the aging systems Al–Mg and Al–Zn under suitable heat treatment. The value of the lithium impurity scattering parameter for the electron states in the vicinity of the point of degeneracy mentioned is estimated, and the linear relation of that parameter with impurity-related electrical resistance in aluminum alloys is established. © *2004 American Institute of Physics.*
[DOI: 10.1063/1.1739165]

INTRODUCTION AND STATEMENT OF THE PROBLEM ADDRESSED

In simple metal systems of the sp type, such as aluminum, the orbital component of the magnetic susceptibility often serves as a useful tool for diagnostics of the electronic structure, especially in cases when, because of thermal excitations or disorder in the crystal lattice, it is impossible to employ quantum oscillation or resonance methods.[1] In this case one uses the irregular behavior of the orbital susceptibility near points of electronic topological phase transitions,[2] caused by the coincidence of the Fermi level with critical energies of the electron spectrum, at which the topology of the Fermi surface changes. For example, in aluminum just below the Fermi level E_F there is a specific critical point with extremal energy E_c on a line of band degeneracy.[3] For boundary points of degeneracy of this type the electronic topological transition at $E_F = E_c$ and T, $H \to 0$, according to theoretical calculations,[3,4] is accompanied by divergence of the orbital diamagnetism on account of the interband contribution.

The corresponding peak of the anomalous diamagnetism has actually been observed[3,5] in alloys of aluminum with substitutional acceptor impurities of Mg and Zn at an average valence z of the alloy equal to the critical value $z_c = 2.945$, in the form a deep low-temperature dip, smoothed by the scattering of electrons on impurities, against the background of the appreciable paramagnetism of pure aluminum. A quantitative analysis of this feature in the behavior of the susceptibility is given in Ref. 3 on the basis of the results of a theoretical calculation of the orbital susceptibility for degenerate bands on the assumption that the disordered solid solutions of Mg and Zn in aluminum are homogeneous.

Unfortunately, in almost all binary systems of aluminum the concentration of an acceptor impurity corresponding to the average valence z_c, if it even falls in the solubility region, does so at rather high temperatures.[6] Obtaining uniform solid solutions in metastable alloys of aluminum at room temperatures requires special heat treatment with regimes that substantially influence the magnetic susceptibility of these alloys.[7] Thus the susceptibility can enrich the arsenal of tools for analysis of the mechanisms and kinetics of the accompanying structural changes. For this one needs reliable information about the behavior of the susceptibility near the diamagnetic anomaly in the system of stable solid solutions of aluminum, which can be taken as a standard, to convince oneself of its correspondence with the theoretical model, and to estimate the degree of uniformity of the solid solutions with Mg and Zn studied previously. As a candidate for the role of reference system in the present paper we have chosen the substitutional alloys of aluminum with lithium. This is the only system for which the topological transition under discussion can occur in the region of solid solutions stable at room temperature,[6,8] although the conclusions of some papers contradict that assumption.[6,9]

EXPERIMENTAL TECHNIQUE

Bars of six Al–Li alloys with concentrations $x(\mathrm{Li}) = 2$, 2.8, 3.8, 4.4, 7.4, and 10.7 at.% were melted from high-purity components: Al–5N and Li–4N. The polycrystalline samples with linear dimensions ~ 3 mm were cut out from the bars by an electrospark method, and the deformed surface was chemically etched off. The samples were subjected to a homogenizing anneal in a helium atmosphere for ~ 5 hours at a temperature of 530 °C, followed by rapid quenching in water. After the magnetic susceptibility measurements some of the samples were aged for around 3 hours at a temperature of 200 °C, and then slowly cooled at a rate of ~ 10 °C/h to room temperature, and the measurement procedure was repeated.

The susceptibility of the alloys was measured by a quantum magnetometer in a dc field of 200 Oe with an error not exceeding 5×10^{-9} e.m.u./g. The samples were placed in a

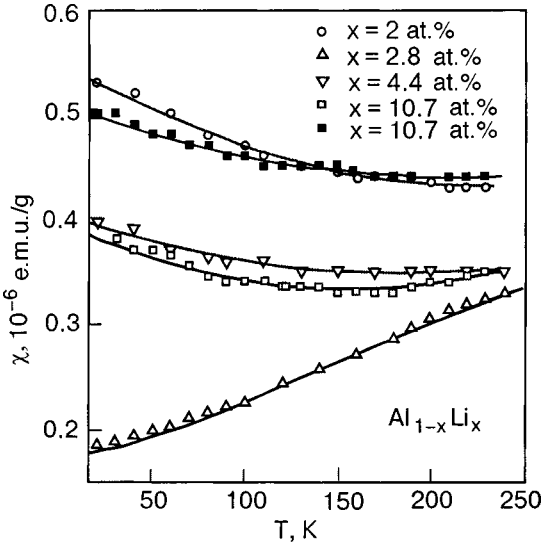

FIG. 1. Temperature dependence of the magnetic susceptibility of Al–Li alloys with different lithium concentrations (in at. %). The unfilled (□) and filled (■) squares pertain to quenched and aged samples, respectively.

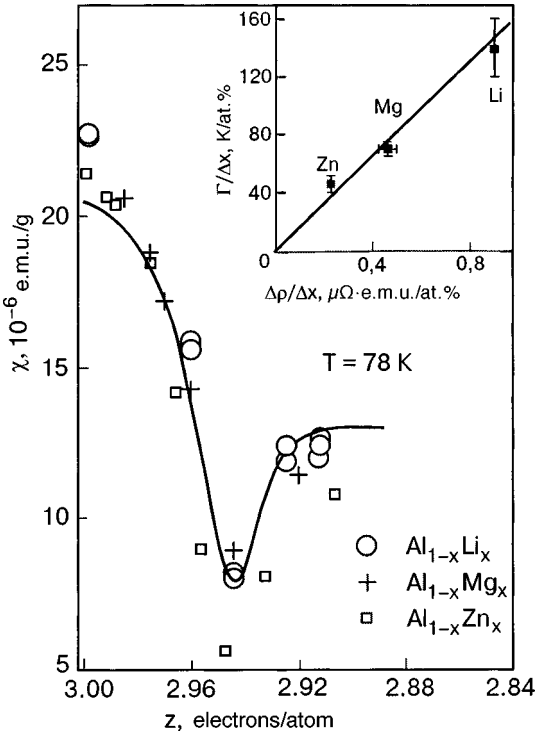

FIG. 2. Electronic part of the susceptibility of alloys of aluminum with Li (○), Mg (+) (Ref. 3), and Zn (□) (Ref. 5) at $T=78$ K versus the average valence z. The solid curve is the result of a theoretical calculation of the susceptibility of Al–Li alloys with the scattering taken into account (see text). The inset shows the relation of the impurity scattering parameter Γ to the resistivity ρ of the alloys.[8]

copper chamber in a compartment of the anticryostat and cooled by the dosed admission of cold gaseous helium into the anticryostat through a controlled valve. Together with a resistive heater on the upper part of the chamber, this system permitted regulation of the rate of cooling of the sample (usually 0.1–0.5 K/min) and the long-term maintenance of its temperature in the interval 4.2–250 K with an accuracy of ~ 0.3 K.

RESULTS OF MAGNETIC SUSCEPTIBILITY MEASUREMENTS

Examples of the temperature dependence of the magnetic susceptibility obtained for the Al–Li alloys are presented in Fig. 1. The dependence of the susceptibility on the lithium concentration near the extremum is shown in Fig. 2. The temperature of 78 K was chosen to permit comparison with analogous data available for the alloys Al–Mg (Ref. 3) and Al–Zn (Ref. 5), which are also shown in Fig. 2. For this same reason molar units are used for the susceptibility in Fig. 2, and the ionic diagmagnetism[10] was subtracted from the measured values, the impurity concentration is expressed in terms of the average valence of the alloys, and the concentrations $x(\mathrm{Li})=2$, 2.8, 3.8, and 4.4 at. % correspond to the valences $z=2.96$, 2.944, 2.924, and 2.912.

Up to concentrations of at least 4.4 at. % Li ($z>z_c$) the susceptibility of the quenched and aged samples agrees within the limits of error of the measurements. Aging was found to have a noticeable effect only for samples with concentrations $x\geqslant 7$ at. % Li ($z=2.86$); Fig. 1. The appearance of analogous differences in the study of the quenched and aged alloys had been observed previously in the Al–Cu system[7] upon transition through the solubility boundary (<2 at. % Cu, where the average valence is still far from the critical value z_c). Thus the solubility limit of Li and Al at room temperature, which is manifested in the magnetic properties, lies in the interval from 4.4 to 7.4 at %, in accordance with the value ~ 5 at. % Li given in Ref. 8. The peak of the diamagnetism in aluminum alloys with lithium falls in the region of stable homogeneous solid solutions and is observed at the same average valence z_c as in the Al–Mg and Al–Zn systems. The amplitude of the peak almost coincides with the value found in the alloys with magnesium and is considerably lower than the amplitude in alloys with Zn, although the lithium concentration required for realization of the peak is half as high.

ANALYSIS OF THE ANOMALOUS DIAMAGNETISM

In the analysis of the experimental data presented we shall use the concepts proposed in Ref. 3 as to the nature of the irregular behavior of the magnetic susceptibility of alloys of aluminum and the expression derived there for the dependence of the susceptibility on the level of the chemical potential $\chi(\mu)$. As we have said, the decisive factor in the occurrence of the substantial dependence of the susceptibility on the concentration of an acceptor impurity is the presence in the electron spectrum A1 of a boundary point on the line of band degeneracy, lying ~ 13 mRy below the Fermi level.[3,11] The scale of that dependence allows one to neglect the influence of all other irregular contributions to the susceptibility.[3] In the calculation of the orbital anomaly in Ref. 3 it was assumed that a fragment of the electron spectrum of Al near the actual point may be satisfactorily represented by a two-band **kp** Hamiltonian, the parameters of which are expressed in terms of the known Fourier components of the pseudopotential. The theory of orbital susceptibility[12] has been adapted for the nonstandard form of the Hamiltonian obtained, and the concentration and temperature dependences of the susceptibility of Al–Zn and

Al–Mg alloys near the anomalies are described by numerical calculations with a fitting of the value of the background contribution and the scattering parameter Γ. Here the position of the level of the chemical potential (or Fermi level) in the alloys was calculated from the value of z with the use of the electronic density of states of aluminum from Ref. 11, and the scattering was simulated by the introduction of an effective temperature that depends linearly on the concentration.

From a comparison of the data obtained in the Al–Li system with experiment and with a calculation for the Al–Mg and Al–Zn alloys (Fig. 2) one can conclude that the chosen heat treatment regimes for the last two systems apparently ensure sufficient homogeneity for these solid solutions. The behavior of the susceptibility of all the alloys presented near the peak is distinguished only by the individuality of the value of the impurity scattering parameter Γ, whereas the position of the boundary point of the band degeneracy relative to the Fermi level of pure aluminum in these alloys is practically the same, $E_c - E_F(\mathrm{Al}) = (-11 \pm 2)$ mRy. Such a value follows from the true positon of the peak $z_c = 2.945$ when its shift due to the smearing at finite values of T and Γ is taken into account.[3] It is in good agreement with the value -13 mRy mentioned above.

The theoretical curve of $\chi(z)$ given in Fig. 2 for the Al–Li alloys was obtained by smearing the corresponding dependence $\chi(\mu)$ from Ref. 3 by a Lorentzian, in which the level-broadening parameter due to the scattering, $d\Gamma/dx = (160 \pm 20)$ K/at. % Li, is chosen along with the constant background component for best agreement with the measured susceptibility. The difference of the scattering parameters for impurities can be estimated directly in terms of the effective temperature from the difference of the amplitude of the diamagnetic peak in the investigated alloy systems, using for calibration the temperature dependence of the amplitudes in Fig. 1 and in Refs. 3 and 5. Along with the absolute values of the scattering parameter $d\Gamma/dx$ given in Ref. 3 for Mg (70 K/at. %) and Zn (45 K/at. %) this procedure gives for lithium impurities in Al the ratio $d\Gamma/dx(\mathrm{Li}):d\Gamma/dx(\mathrm{Mg}) \approx 1.8:1$ and $d\Gamma/dx = 120 \pm 20$ K/at. %. The temperature dependence of the susceptibility expected for this parameter at the extremum agrees with experiment (the sample with 2.8 at. % Li in Fig. 1). For estimation we take the average value $d\Gamma/dx \approx 140$ K/at. % Li, bearing in mind the approximate nature of both methods of determining this quantity. For example, at the edge of the dependence $\chi(x)$ the region of averaging of the susceptibility over energy at the value obtained for Γ goes beyond the domain of applicability of the two-band model, [3] there exists some difference in the scattering parameter estimated using a Lorentzian and an effective temperature,[3] and in the calculation of $\chi(T)$ for the alloys the unknown temperature dependence of the level of the chemical potential μ is ignored. Eliminating these defects, which, as can be seen from the results, are not fundamental, would require considerable complication of the calculation, which is not justified at this stage.

The inset in Fig. 2 shows the relation between the values of Γ in the alloys under discussion with the influence of those impurities on the resistivity ρ of aluminum.[8,13] It turns out to be linear to within the error limits. The smallest scattering, strangely, is caused by zinc and not magnesium which is next to aluminum in a row of the periodic table. As a consequence of the fact that for the electron scattering processes governing the susceptibility anomaly the initial states are well localized in **k** space near the singular point, one can make a quantitative estimate of the scattering parameter, and the aforementioned strangeness in the influence of Zn and Mg can be linked to differences in the details of the structure of their pseudopotential form factors.[3]

CONCLUSION

This study has shown that the region of solubility of lithium in aluminum at room temperature, determined from the magnetic properties, exceeds 4.4 at. % and includes an electronic topological phase transition associated with the boundary point of a line of band degeneracy in the electron spectrum of Al. The peak of anomalous diamagnetism corresponding to the transition in stable homogeneous solid solutions of Al was realized for the first time. These reference data confirm the reliability of the form of the anomaly observed in the aging Al–Zn and Al–Mg alloys after a special heat treatment and its agreement with the theoretical model. The value of the electron scattering parameter for a lithium impurity near the boundary point was determined, and it was established that this parameter is linearly related to the resistivity of the alloys. On the basis of the available data, one can use the susceptibility for quantitative analysis of effects due to the influence of structural transformations in aging aluminum alloys on the degenerate electron states and establish the characteristic times and mechanisms of such transformations.

The authors are grateful to G. P. Mikitik, Yu. V. Sharlai, and V. V. Pustovalov for helpful discussions.

*E-mail: svechkarev@ilt.kharkov.ua

[1] I. V. Svechkarev, Izv. Akad. Nauk SSSR, Ser. Fiz. **42**, 1701 (1978).
[2] I. M. Lifshits, Zh. Éksp. Teor. Fiz. **38**, 1569 (1960) [Sov. Phys. JETP **11**, 1130 (1960)].
[3] S. A. Vorontsov and I. V. Svechkarev, Fiz. Nizk. Temp. **13**, 274 (1987) [Sov. J. Low Temp. Phys. **13**, 155 (1987)].
[4] G. P. Mikitik and I. V. Svechkarev, Fiz. Nizk. Temp. **15**, 295 (1989) [Sov. J. Low Temp. Phys. **15**, 165 (1989)].
[5] J. Mimault, J. Delafond, and A. Junqua, Phys. Status Solidi A **20**, 195 (1973).
[6] M. Hansen and K. Anderko, *Constitution of Binary Alloys* McGraw-Hill, New York (1958), Metallurgizdat, Moscow (1962) (Russ. Vol. I).
[7] A. E. Vol, *Structure and Properties of Binary Metallic Systems* [in Russian], Vol I, Fizmatgiz, Moscow (1959).
[8] A. J. McAlister, Bull. Alloy Phase Diagrams **3**, 177 (1982).
[9] J. Delafond, A. Junqua, and J. Mimault, Phys. Status Solidi A **15**, 553 (1973).
[10] P. W. Selwood, *Magnetochemistry*, 2nd ed., Interscience, New York (1956), Izd-vo Inostr. Lit., Moscow (1958).
[11] G. E. Grechnev, I. V. Svechkarev, and N. V. Ushakova, Fiz. Met. Metalloved. **61**, 202 (1986).
[12] H. Fukuyama, Prog. Theor. Phys. **45**, 704 (1971).
[13] B. N. Aleksandrov and V. V. Dukin, Fiz. Nizk. Temp. **3**, 633 (1977) [Sov. J. Low Temp. Phys. **3**, 308 (1977)].

Translated by Steve Torstveit